A. CARPINTERI

MECHANICAL DAMAGE AND CRACK GROWTH IN CONCRETE

MARTINUS NIJHOFF PUBLISHERS

Mechanical damage and crack growth in concrete: Plastic collapse to brittle fracture

ENGINEERING APPLICATION OF FRACTURE MECHANICS

Editor-in-Chief: George C. Sih

G.C. Sih and L. Faria (eds.), Fracture mechanics methodology: Evaluation of structure components integrity. 1984. ISBN 90-247-2941-6.

E.E. Gdoutos, Problems of mixed mode crack propagation. 1984. ISBN 90-247-3055-4.

A. Carpinteri and A.R. Ingraffea (eds.), Fracture mechanics of concrete: Material characterization and testing. 1984. ISBN 90-247-2959-9.

G.C. Sih and A. DiTommaso (eds.), Fracture mechanics of concrete: Structural application and numerical calculation. 1984. ISBN 90-247-2960-2.

A. Carpinteri, Mechanical damage and crack growth in concrete: Plastic collapse to brittle fracture. 1986. ISBN 90-247-3233-6.

Mechanical damage and crack growth in concrete

Plastic collapse to brittle fracture

By

Alberto Carpinteri

Istituto di Scienza delle Costruzioni
University of Bologna
Bologna, Italy

1986 **MARTINUS NIJHOFF PUBLISHERS**
a member of the KLUWER ACADEMIC PUBLISHERS GROUP
DORDRECHT / BOSTON / LANCASTER

Distributors

for the United States and Canada: Kluwer Academic Publishers, 190 Old Derby Street, Hingham, MA 02043, USA
for the UK and Ireland: Kluwer Academic Publishers, MTP Press Limited, Falcon House, Queen Square, Lancaster LA1 1RN, UK
for all other countries: Kluwer Academic Publishers Group, Distribution Center, P.O. Box 322, 3300 AH Dordrecht, The Netherlands

Library of Congress Cataloging in Publication Data

Carpinteri, A.
Mechanical damage and crack growth in concrete.

(Engineering application of fracture mechanics ;
Includes bibliographies.
1. Concrete--Cracking. I. Title. II. Series.
TA440.C318 1986 620.1'366 85-18848

ISBN-13: 978-94-010-8434-5 e-ISBN-13: 978-94-009-4350-6
DOI:10.1007/978-94-009-4350-6

Copyright

Martinus Nijhoff Publishers, P.O. Box 163, 3300 AD Dordrecht,
The Netherlands.

Contents

Series on engineering application of fracture mechanics

Fracture mechanics technology has received considerable attention in recent years and has advanced to the stage where it can be employed in engineering design to prevent against the brittle fracture of high-strength materials and highly constrained structures. While research continued in an attempt to extend the basic concept to the lower strength and higher toughness materials, the technology advanced rapidly to establish material specifications, design rules, quality control and inspection standards, code requirements, and regulations for safe operation. Among these are the fracture toughness testing procedures of the American Society of Testing Materials (ASTM), the American Society of Mechanical Engineers (ASME) Boiler and Pressure Vessel Codes for the design of nuclear reactor components, etc. Step-by-step fracture detection and prevention procedures are also being developed by the industry, government and university to guide and regulate the design of engineering products. This involves the interaction of individuals from the different sectors of the society that often presents a problem in communication. The transfer of new research findings to the users is now becoming a slow, tedious and costly process.

One of the practical objectives of this series on *Engineering Application of Fracture Mechanics* is to provide a vehicle for presenting the experience of real situations by those who have been involved in applying the basic knowledge of fracture mechanics in practice. It is time that the subject should be presented in a systematic way to the practicing engineers as well as to the students in universities, at least to all those who are likely to bear a responsibility for safe and economic design. Even though the current theory of linear elastic fracture mechanics (LEFM) is limited to brittle fracture behavior, it has already provided a remarkable improvement over the conventional methods not accounting for initial defects that are inevitably present in all materials and structures. The potential of the fracture mechanics technology, however, has not been fully recognized. There remains much to be done in constructing a quantitative theory of material damage that can reliably translate small specimen data to the design of large size structural components. The work of the physical metallurgists and the fracture mechanicians should also be brought together by reconciling the details of the material microstructure with the assumed continua of the computational methods. It is with the aim of developing a wider appreciation of the fracture mechanics technology applied to the design of engineering structures such as aircrafts, ships, bridges, pavements, pressure vessels, off-shore structures, pipelines, etc. that this series is being developed.

Undoubtedly, the successful application of any technology must rely on the soundness of the underlying basic concepts and mathematical models and how they reconcile with each other. This goal has been accomplished to a large extent by the book series on *Mechanics of Fracture* started in 1972. The seven published volumes offer a wealth of information on the effects of defects or cracks in cylindrical bars, thin and thick plates, shells, composites and solids in three dimensions. Both static and dynamic loads are considered. Each volume contains an introductory chapter that illustrates how the strain energy criterion can be used to analyze the combined influence of defect size, component geometry and size, loading, material properties, etc. The criterion is particularly effective for treating mixed mode fracture where the crack propagates in a non-self similar fashion. One of the major difficulties that continuously perplex the practitioners in fracture mechanics is the selection of an appropriate fracture criterion without which no reliable prediction of failure could be made. This requires much discernment, judgement and experience. General conclusion based on the agreement of theory and experiment for a limited number of physical phenomena should be avoided.

Looking into the future the rapid advancement of modern technology will require more sophisticated concepts in design. The micro-chips used widely in electronics and advanced composites developed for aerospace applications are just some of the more well-known examples. The more efficient use of materials in previously unexperienced environments is no doubt needed. Fracture mechanics should be extended beyond the range of LEFM. To be better understood is the entire process of material damage that includes crack initiation, slow growth and eventual termination by fast crack propagation. Material behavior characterized from the uniaxial tensile tests must be related to more complicated stress states. These difficulties could be overcome by unifying metallurgical and fracture mechanics studies, particularly in assessing the results with consistency.

This series is therefore offered to emphasize the applications of fracture mechanics technology that could be employed to assure the safe behavior of engineering products and structures. Unexpected failures may or may not be critical in themselves but they can often be annoying, time-wasting and discrediting of the technical community.

Bethlehem, Pennsylvania
1984

G.C. Sih
Editor-in-Chief

Editor-in-Chief's Preface

Following Volumes III and IV that dealt with the fracture mechanics of concrete emphasizing both material testing and structural application in general, it was felt that specimen size and loading rate effects for concrete require further attention. The only criterion that has thus far successfully linearized the highly nonlinear crack growth data of concrete is the strain energy density theory. In particular, the crack growth resistance curves plotting the strain energy density factor versus crack growth known as the *SR*-curves are straight lines as specimen size and loading steps or rates are altered. This allows the extrapolation of data and provides a useful design methodology.

This book is unique in that it is devoted specifically to the application of the strain energy density theory to civil engineering structural members made of concrete. Analyzed in detail is the strain softening behavior of concrete for a variety of different components including the influence of steel reinforcement. Permanent damage of the material is accounted for each increment of loading by invoking the mechanism of elastic unloading. This assumption is justified in concrete structures where the effective stiffness depends primarily on the crack growth rate and load history. Crack growth data are presented in terms of *SR*-curves with emphases placed on scaling specimen size which alone can change the mode of failure from plastic collapse to brittle fracture. Loading rate effects can also be scaled to control failure by yielding and fracture.

Because the materials in this book are mostly new, they should be of interest to those in research and application. The concept of *SR*-curves will have a far reaching consequence on concrete technology, particularly on future code requirements and regulations.

Bethlehem, Pennsylvania G.C. Sih
1984 Editor-in-Chief

Author's Preface

Structural elements can fail in many different ways. The ultimate load condition may be reached by a combination of plastic flow, slow or fast crack propagation, depending on the material strength, ductility and toughness, and the size of the structural components. Highly constrained and/or brittle materials may result in sudden crack formation and unstable crack propagation, whereas less constrained and/or more ductile materials are more likely to fail progressively by plastic yielding. In those situations, the presence of initial cracks do not play an important role in the failure process.

In many cases, however, the terminal condition is preceded by slow crack growth that continues even into the stage of global structure failure. There are other situations where slow crack growth may occur simultaneously with plastic flow and the final failure can still be catastrophic.

The current fracture mechanics literature contains a multitude of ideas, concepts, and criteria, that are not always consistent one with the other. Plastic Limit Analysis and Linear Elastic Fracture Mechanics are two theories that address failure of structural components with very ductile and very brittle behavior, respectively. They are unable to account for the slow crack growth and the softening behavior in concrete structures aside from the effect of material heterogeneity that is connected with the brittleness of concrete.

Remarkable scale effects have been found in fracture toughness testing of cementitious materials. The mechanical behavior can change from the very ductile to the very brittle simply by altering the size of geometrically similar specimens. Large specimens can fail by rapid crack propagation within the linear elastic range before softening takes place. On the other hand, small specimens tend to fail in a ductile manner with slow crack growth and softening leading to a complete stress relaxation.

In this book, a crack growth and material damage model is used in conjunction with the strain energy density theory of Sih to analyze the integrity of concrete structural members. A bilinear softening constitutive law is applied while the progressive damage of material is accounted for by changing the material elastic modulus and crack growth for each load step. The finite element method is employed consistently and repeatedly in both the stress and failure analysis.

As a consequence of the strain energy density theory, the rate of change of the strain energy density factor dS with respect to the crack growth rate da remained as a constant for each loading increment and specimen size, i.e., dS/da = constant. The straight line relationship between S and a known as the SR-curve rotates in a counterclockwise direction around a common point as the load increment is increased. These straight lines tend to shift parallel with one another when the size of geometrically similar specimens is increased. Hence, the influence of load increment and specimen size on subcritical crack growth and critical crack size for a given material can be easily determined from uniaxial data. Depending on the combined effect of structural size and geometry, crack growth may either lead to catastrophic failure or to crack arrest. Numerous examples are provided to illustrate how the strain energy density theory can be applied to predict different failure modes in concrete ranging from plastic collapse to brittle fracture.

The book is divided into eight chapters. The first chapter provides an historical review of the theories of Plastic Limit Analysis and Linear Elastic Fracture Mechanics. Independent of the material, they describe the extreme failure conditions of very small and very large structures, respectively. The intermediate stages are not covered by these two models. Mixed mode crack growth criteria are discussed briefly. The angle of crack initiation and the critical stress conditions are obtained by applying different crack growth criteria.

In the second chapter, microcracking, damage and strain-softening are discussed in connection with concrete-like materials. The fracture loci in the stress-intensity factor plane, K_I versus K_{II}, are related to the failure envelopes in the Mohr's plane, σ versus τ. The strain energy density theory is proposed as a basis for explaining such phenomena.

A cracked beam subjected to three-point bending is depicted in the third chapter for determining the crack growth rates of different concrete-like materials. SR-curves are developed for studying the load increment and specimen size effects.

In the fourth chapter, SR-curves are developed from the uniaxial data for a center cracked slab in tension with different initial crack lengths. The failure of a slab under eccentric compression is investigated in the fifth chapter. The edge crack is shown to grow with a decreasing rate as the zone of compressive stress is approached. A reinforced concrete beam is solved in the sixth chapter to investigate the influence of reinforcement on crack growth and material damage. An example involving crack growth and material damage for a panel subjected to seismic loadings is provided in the seventh chapter. The effects of loading step and size scaling of geometrically similar structural components are assessed quantitatively in chapters 3 to 7. The transition from plastic collapse to brittle fracture is accomplished by varying the size scale and is predicted consistently by the strain energy density theory.

In the eighth and final chapter, the problem of extrapolating experimental data from small fracture specimens to large structures is presented. A simple presentation of the aforementioned ductile-brittle transition due to specimen size is made by application of the concept of model scaling and physical similitude. Most of the size effects on fracture toughness and tensile strength of concrete which appeared in the literature for the last twenty years are reinterpreted in terms of dimensional analysis and statistics. The non-linearity in the constitutive stress-strain relation of the material and the shape of the preexisting defects are also considered. The damage model based on the strain energy density theory in this book is then compared with the cohesive model. The process zone at the crack tip of a concrete-like material may be simulated by assuming a damage zone in front of the stress-free crack tip, or by introducing a cohesive force distribution behind a fictitious crack tip.

This work was initiated at the Institute of Fracture and Solid Mechanics, Lehigh University, while the author was on sabbatical leave from the University of Bologna. It was completed at the Istituto di Scienza delle Costruzioni at the University of Bologna. The author wishes to express his gratitude to Professor George C. Sih for the very stimulating and fruitful discussions he had with him at Lehigh University and for providing valuable comments and support during the writing of this book.

Thanks are due to the Institute Secretaries, Mrs. Barbara DeLazaro and Mrs. Constance Weaver, for typing the manuscript and other assistance they provided during my stay at Lehigh. The preparation of the drawings by Miss Thea Bariselli at the Studio T-Line was greatly appreciated.

I am also grateful for the understanding and support provided by my wife Mariagiulia while I worked on this volume.

Alberto Carpinteri

Istituto di Scienza delle Costruzioni
University of Bologna, Italy
June 1984

1

Historical review: strength of materials and fracture mechanics

1.1. Classical theories of failure

Plasticity criteria. The mechanical behavior of most engineering materials under uniaxial tension consists of four stages as shown in Figure 1.1. They are linear elastic, strain-hardening, perfectly plastic and strain-softening. The strain-hardening and softening stage may be linearized in order to make the computations easier, Figure 1.1. Such an approximation does not lead to any serious loss in solution accuracy. The contribution of the individual stages, however, can vary over a wide range. For example, when a steel specimen is subjected to uniaxial tension, the linear elastic range is usually followed by perfect plasticity and then by strain-hardening. The strain-softening behavior is not significant and is represented by a nearly vertical drop in the stress-strain diagram, Figure 1.2(a). For a concrete specimen, the linear elastic range is immediately followed by strain-softening while the intermediate stages do not appear, Figure 1.2(b). Note that the elastic modulus for concrete is much lower than that for steel as well as the strain-softening modulus. These observations exhibit that the energy absorption* properties of steel and concrete vary at different stages. The former during the plastic and hardening stages, the latter during the softening stage.

In most engineering applications, simplifications of the non-linear constitutive law are required in order to obtain simple and useful information. The *Plastic limit analysis*, for example, assumes an elastic-perfectly plastic behavior, which, in fact, is a very realistic model for steel. On the other hand, an elastic-linear softening material agrees very well with concrete behavior. The elastic-perfectly plastic material can thus be considered a limiting case, Figure 1.3.

The *Theory of plasticity* was developed during the first half of the present century. Its object is the description of the elastic-plastic behavior when the local stress condition is multiaxial and the structural geometry is complex. Particular attention is paid to the ultimate situation just preceding the plastic

---

* The area under the stress and strain curve is assumed to be an indication of the capability of the material to absorb energy.

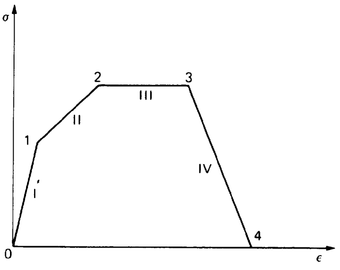

Fig. 1.1. Multilinear stress-strain relation.

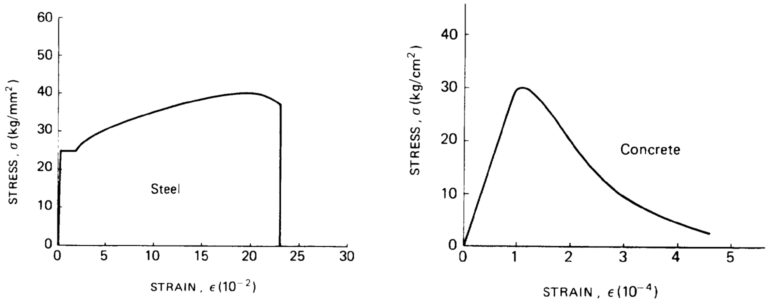

Fig. 1.2. Stress-strain relation for steel (a) and concrete (b).

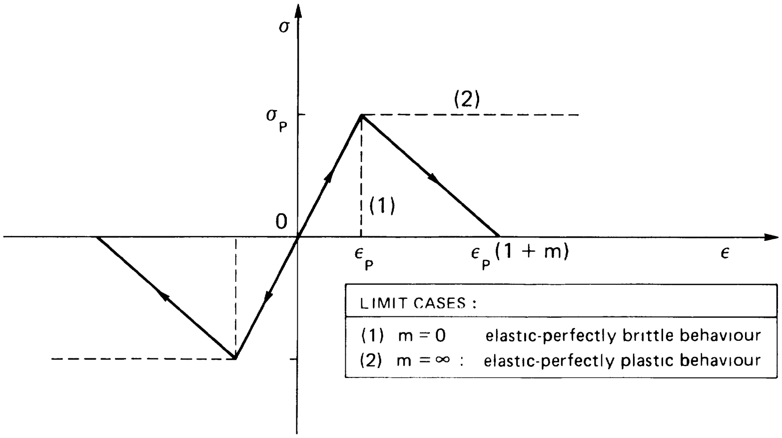

Fig. 1.3. Bilinear stress-strain relation under tensile and compressive load.

flow collapse, when the whole structure, or a part of it, undergoes very large displacement increments due to very small loading increments.

In the uniaxial tensile state, the material element is elastic when, Figure 1.3:

$$-\sigma_P < \sigma < \sigma_P \tag{1.1}$$

while it is plastic when:

$$\sigma = \pm\sigma_P \tag{1.2}$$

The case $|\sigma| > \sigma_P$ is impossible. The compressive and tensile yield strengths are about the same for steel. Analogously, in the bi-axial stress state (plane stress condition) the material element is elastic when

$$F(\sigma_1, \sigma_2) < 0 \tag{1.3}$$

with σ_1 and σ_2 being the principal stresses.

The condition of plasticity corresponds to

$$F(\sigma_1, \sigma_2) = 0 \tag{1.4}$$

The case $F(\sigma_1, \sigma_2) > 0$ is not included in *perfect plasticity.*

Equation (1.4) describes certain yield surface according to the assumed condition. The first criterion was proposed by Beltrami [1] at the end of the nineteenth century. It states that plastic flow occurs locally when the *strain energy density function* attains its critical value. The associated yield surface is:

$$F_B(\sigma_1, \sigma_2) = (\sigma_1^2 + \sigma_2^2 - 2\nu\sigma_1\sigma_2) - \sigma_P^2 = 0 \tag{1.5}$$

where ν is the Poisson ratio.

Then, von Mises [2] assumed that the plastic flow occurs when the *distortional strain energy density* reaches its critical value. The von Mises' yield surface is described by

$$F_M(\sigma_1, \sigma_2) = (\sigma_1^2 + \sigma_2^2 - \sigma_1\sigma_2) - \sigma_P^2 = 0 \tag{1.6}$$

This is the equation for an ellipse in the plane of the principal stresses, Figure 1.4. Such a criterion received various experimental confirmations.

Another well-known plasticity criterion is due to Tresca [3]. It assumes that plastic flow occurs when the *maximum tangential stress* attains its critical value:

$$F_T(\sigma_1, \sigma_2) = \max\{|\sigma_1|, |\sigma_2|, |\sigma_1 - \sigma_2|\} - \sigma_P = 0 \tag{1.7}$$

The yield locus given by equation (1.7) is an hexagon in the plane of the principal stresses, Figure 1.4.

Eventually, Hill [4] suggested a plasticity criterion based on the *maximum*

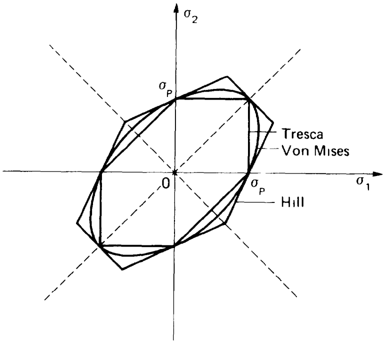

Fig. 1.4. Yield loci in the plane of the principal stresses.

principal deviatoric stress:

$$F_H(\sigma_1, \sigma_2) = \max\left\{\left|\frac{\sigma_1+\sigma_2}{2}\right|, \left|\sigma_1 - \frac{\sigma_2}{2}\right|, \left|\sigma_2 - \frac{\sigma_1}{2}\right|\right\} - \sigma_P = 0 \tag{1.8}$$

The yield locus in equation (1.8) is an hexagon in the plane of the principal stresses, Figure 1.4. The relations of the Tresca, Hill and von Mises yield envelopes are shown in Figure 1.4.

While the nature of plastic flow is clear, i.e., dilatation being collinear to the stress, in the uniaxial stress state, it is difficult to visualize the corresponding mechanical deformation in multiaxial stress states.

Normality of incremental plastic strain. Consider a material element in the initial stress state $\boldsymbol{\sigma}_0$. Suppose that in incremental change in stress state $(\boldsymbol{\sigma} - \boldsymbol{\sigma}_0)$ is experienced by the element and then removed in quasi-static manner. The well-known Drucker's Postulate [5] asserts that *the material is stable if the work performed in the loading cycle is non-negative.* For a stress state $\boldsymbol{\sigma}$ lying on the yield surface $F(\boldsymbol{\sigma}) = 0$, and for any admissible stress state $\boldsymbol{\sigma}_0$ lying in the elastic field or on its boundary, the condition

$$(\boldsymbol{\sigma} - \boldsymbol{\sigma}_0)\,\dot{\boldsymbol{\varepsilon}}_P \geqslant 0 \tag{1.9}$$

should hold with $\dot{\boldsymbol{\varepsilon}}_P$ being the incremental plastic strain corresponding to $\boldsymbol{\sigma}$. It is possible to give a geometric interpretation of $\boldsymbol{\sigma}$ and $\dot{\boldsymbol{\varepsilon}}_P$, Figure 1.5. The scalar product of equation (1.9) is always null or positive.

Since $\boldsymbol{\sigma}_0$ could be inside or on the yield surface, it follows that a regular point on the yield surface, has a unique tangent such that $\dot{\boldsymbol{\varepsilon}}_P$ *is normal to the yield locus* and *the yield locus is convex.* For a singular point on the yield locus, Figure 1.6(a), $\dot{\boldsymbol{\varepsilon}}_P$ cannot be uniquely defined by the normals. More than one $\dot{\boldsymbol{\varepsilon}}_P$ vector can correspond to the same $\boldsymbol{\sigma}$. On the other hand, in the

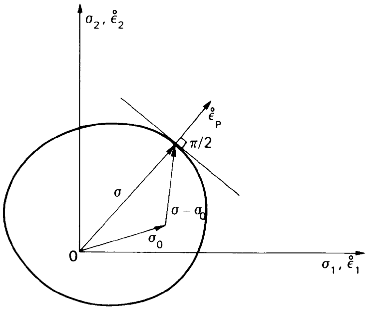

Fig. 1.5. Normality of incremental plastic strain.

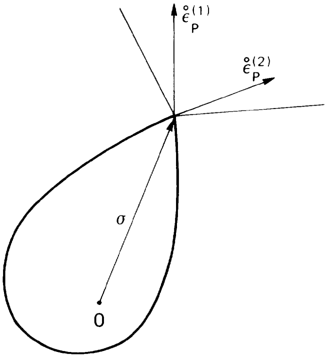

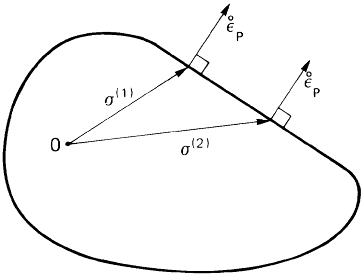

Fig. 1.6(a). Singular point on the yield surface.
Fig. 1.6(b). Yield surface not convex in the strict sense.

zones where the yield surface is linear (not convex in the strict sense) more than one $\boldsymbol{\sigma}$ vector can correspond to the same $\dot{\boldsymbol{\varepsilon}}_P$, Figure 1.6(b). The last two cases prevail in the Tresca's hexagon.

The elastic field includes the origin, and then equation (1.9) with $\boldsymbol{\sigma}_0 = 0$ yields

$$\boldsymbol{\sigma}\dot{\boldsymbol{\varepsilon}}_P = \dot{\phi}(\dot{\boldsymbol{\varepsilon}}_P) > 0 \qquad (1.10)$$

where $\dot{\phi}$ represents the work dissipated per unit volume and is only a function of the incremental plastic strain. This is valid even when the yield locus contains singularities and is not convex in the strict sense (linear segments). Then, the following hypothesis is equivalent to the Drucker's Postulate: *the work dissipated per unit volume is only a function of the incremental plastic strain.* From this, it is possible to deduce the *normality rule* and the *yield locus convexity* [6]. Equation (1.10), in fact, shows that any stress state $\boldsymbol{\sigma}$ able to produce incremental plastic strain $\dot{\boldsymbol{\varepsilon}}_P$ must lie on the plane normal

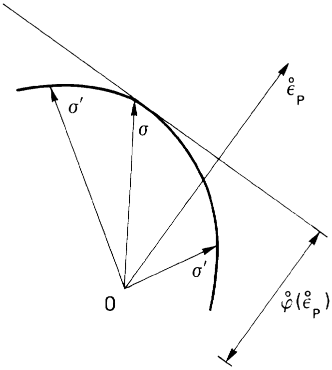

Fig. 1.7. Convexity of the yield locus.

to $\dot{\boldsymbol{\varepsilon}}_P$ and distant $\dot{\phi}(\dot{\boldsymbol{\varepsilon}}_P)$ from the origin, Figure 1.7. When $\boldsymbol{\varepsilon}_P$ rotates around 0, all these planes envelop the yield locus satisfying the convexity condition.

If $\dot{\boldsymbol{\sigma}}$ is the incremental stress corresponding to the incremental plastic strain $\dot{\boldsymbol{\varepsilon}}_P$, then:

$$\dot{\boldsymbol{\sigma}}\dot{\boldsymbol{\varepsilon}}_P \geqslant 0 \tag{1.11}$$

This can be obtained by assuming $\boldsymbol{\sigma}$ to be the initial stress state and $\dot{\boldsymbol{\sigma}}$ the incremental stress state. The condition

$$\dot{\boldsymbol{\sigma}}\dot{\boldsymbol{\varepsilon}}_P = 0 \tag{1.12a}$$

pertains to the elastic-perfectly plastic materials and

$$\dot{\boldsymbol{\sigma}}\dot{\boldsymbol{\varepsilon}}_P < 0 \tag{1.12b}$$

to strain-softening materials. This means that, while strain-hardening and perfectly plastic materials may be stable according to the Drucker's Postulate, strain-softening materials may not.

In Figure 1.8, the Tresca's yield locus and the related plastic flow mechanisms are illustrated. Along the segments AB, BC, DE and EF, only one of the two principal dilatations is activated, while along CD and FA one dilatation is positive and the other is negative; they are activated at the same time and to the same extent.

Theorems of limit analysis. Consider a rigid-perfectly plastic structure subjected to a proportional loading condition measured by the parameter λ, Figure 1.9. A stress field is statically admissible when it is in equilibrium with the external loading λ and $F \leqslant 0$ for each point of the structure. On the other

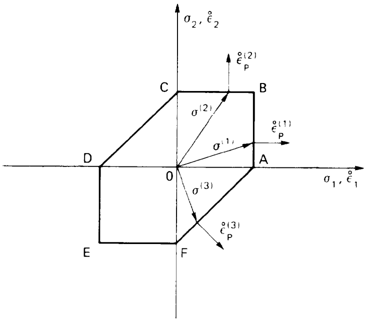

Fig. 1.8. Plastic flow mechanisms according to the Tresca's yield locus.

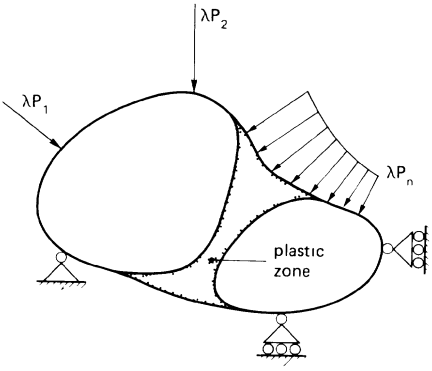

Fig. 1.9. Rigid-perfectly plastic structure subjected to a proportional loading condition.

hand, a plastic flow mechanism is kinematically admissible when the external constraints are satisfied and the corresponding dissipated work is positive.

The following theorems may be stated.

(a) *Maximum dissipated work theorem: Given a plastic flow mechanism* $\dot{\boldsymbol{\varepsilon}}_P$, *the work dissipated by the stress* $\boldsymbol{\sigma}$ *corresponding to such a mechanism in* Figure 1.7 *is higher than or equal to the work dissipated by any possible stress* $\boldsymbol{\sigma}'$:

$$\boldsymbol{\sigma}\dot{\boldsymbol{\varepsilon}}_P \geqslant \boldsymbol{\sigma}'\dot{\boldsymbol{\varepsilon}}_P \tag{1.13}$$

The inequality in equation (1.13) is valid for each point of the structure and hence from equation (1.10), it can be shown that

$$\int_V \phi(\dot{\boldsymbol{\varepsilon}}_P)\mathrm{d}V \geqslant \int_V \boldsymbol{\sigma}'\dot{\boldsymbol{\varepsilon}}_P\mathrm{d}V \tag{1.14}$$

(b) *Static theorem* (*upper bound theorem*): *The loading parameter* λ^-

corresponding to any statically admissible stress field is lower than or equal to the limit load parameter λ_P. Let $\boldsymbol{\sigma}^-$ be a statically admissible stress field and λ^- the corresponding external loading parameter. If $\boldsymbol{\sigma}$ is the limit stress field, then $\dot{\mathbf{u}}$ and $\dot{\boldsymbol{\varepsilon}}_P$ are the corresponding incremental displacement and incremental plastic strain at limit load, respectively. The application of the *Virtual Work Principle* gives

$$\int_V \boldsymbol{\sigma}^- \dot{\boldsymbol{\varepsilon}}_P \mathrm{d}V = \sum_i \lambda^- P_i \dot{\mathbf{u}}_i \tag{1.15a}$$

$$\int_V \boldsymbol{\sigma} \dot{\boldsymbol{\varepsilon}}_P \mathrm{d}V = \sum_i \lambda_P P_i \dot{\mathbf{u}}_i \tag{1.15b}$$

The inequality in equation (1.13) then leads to

$$\int_V (\boldsymbol{\sigma} - \boldsymbol{\sigma}^-) \dot{\boldsymbol{\varepsilon}}_P \mathrm{d}V \geqslant 0 \tag{1.16}$$

and hence

$$\lambda_P \geqslant \lambda^- \tag{1.17}$$

(c) *Kinematic theorem (lower bound theorem): The loading parameter* λ^+ *corresponding to any kinematically admissible plastic flow mechanism is higher than or equal to the limit load parameter* λ_P. Let $\dot{\mathbf{u}}^+$ and $\dot{\boldsymbol{\varepsilon}}^+$ be the fields of incremental displacement and incremental plastic strain respectively related to a kinematically admissible plastic flow mechanism. The limit stress field is $\boldsymbol{\sigma}$. The loading parameter λ^+ corresponding to the kinematically admissible plastic flow mechanism is given by

$$\int_V \dot{\phi}(\dot{\boldsymbol{\varepsilon}}^+) \mathrm{d}V = \sum_i \lambda^+ P_i \dot{\mathbf{u}}_i^+ \tag{1.18}$$

The application of the *Virtual Work Principle* to the limit stress field $\boldsymbol{\sigma}$ and to the kinematically admissible mechanism $\dot{\boldsymbol{\varepsilon}}^+$ gives

$$\int_V \boldsymbol{\sigma} \dot{\boldsymbol{\varepsilon}}^+ \mathrm{d}V = \sum_i \lambda_P P_i \dot{\mathbf{u}}_i^+ \tag{1.19}$$

From equation (1.14), it is found that

$$\int_V \dot{\phi}(\dot{\boldsymbol{\varepsilon}}^+)\mathrm{d}V \geqslant \int_V \boldsymbol{\sigma}\dot{\boldsymbol{\varepsilon}}^+\mathrm{d}V \tag{1.20}$$

Equations (1.18), (1.19) and (1.20) thus yield

$$\lambda_P \leqslant \lambda^+ \tag{1.21}$$

(d) *Mixed theorem: If the loading parameter* λ *corresponds to a statically admissible stress field as well as to a kinematically admissible plastic flow mechanism,* equations (1.17) *and* (1.21) give

$$\lambda = \lambda_P \tag{1.22}$$

(e) *Material addition: A size increase of a perfectly plastic structure cannot produce a decrease in the limit load.* The sum of the limit stress field in the original structure with an identically null stress field in the added material portion constitutes a statically admissible stress field. This means that the limit load of the latter structure is higher than or equal to that of the former.

Elastic-plastic beam behavior. The elastic-plastic behavior of a beam will be analyzed. The classical theory of Bernoulli assumes that plane cross-sections before bending remain plane after bending. The case of the symmetric cross-section in Figure 1.10 will be considered. Let Y be the bending axis and X the neutral axis. The variations of the longitudinal dilatations ϵ and the stresses σ with y are shown in Figure 1.10. In the elastic range, Figure 1.10(a), the well-known equations

$$\sigma = \frac{M}{I}y, \qquad \epsilon = \frac{\sigma}{E} \tag{1.23a}$$

and

$$\sigma_{\max} = \frac{M}{W}, \qquad W = \frac{I}{b/2} \tag{1.23b}$$

are obtained and they hold for $\sigma_{\max} < \sigma_P$. Here M is the bending moment, E the Young's modulus, I the moment of inertia and b the depth of the cross-section.

When $M > \sigma_P W$, elastic-plastic bending occurs. The ϵ diagram is linear, whereas the absolute value of stress σ cannot exceed the yield strength, σ_P. The stress diagram is then shown in Figure 1.10(b). If d is the distance between the X-axis and the beam fibers where $|\epsilon| = \epsilon_P$, the equilibrium

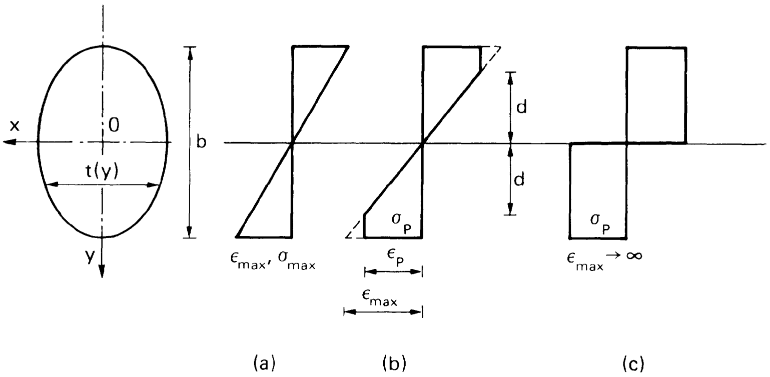

(a) (b) (c)

Fig. 1.10. Elastic-plastic flexural beam behavior: cross section with two axes of symmetry.

condition is

$$M = \iint_A \sigma y \, dA = 2\int_0^d \sigma_P \frac{y}{d} y t(y) \, dy + 2\int_d^{b/2} \sigma_P y t(y) \, dy \tag{1.24}$$

Recalling that the curvature is given by

$$R = \frac{\epsilon_{max}}{b/2} = \frac{\epsilon_P}{d} \tag{1.25}$$

equation (1.24) can be rewritten as

$$M = 2\sigma_P \left[\frac{R}{\epsilon_P} \int_0^{\epsilon_P/R} y^2 t(y) \, dy + \int_{\epsilon_P/R}^{b/2} y t(y) \, dy \right] \tag{1.26}$$

When the curvature R increases, the bending moment M tends to a limit value, M_P:

$$\lim_{R \to \infty} M = 2\sigma_P \int_0^{b/2} y t(y) \, dy = 2\sigma_P S = M_P \tag{1.27}$$

The limit value M_P is called *plastic moment.* It is equal to the product of the yield strength by twice the statical moment of half-section related to the X-axis. When the whole cross section is yielded, the σ diagram appears as that shown in Figure 1.10(c) with a discontinuity on the X-axis. It is interesting to compare the moment at incipient yield $M_e = \sigma_P W$, with the plastic moment $M_P = 2\sigma_P S$. For a rectangular cross section we have $M_P/M_e = 1.5$, while for the commercial I-beams this ratio is about 1.15.

Consider now a rectangular beam cross section and a material having the same strain-softening behavior in tension and in compression, Figure 1.3. When the material is elastic-perfectly plastic ($m \to \infty$), the bending moment in the non-linear stage is given by a special case of equation (1.26):

$$M = \frac{\sigma_P b^2}{4}\left[1 - \frac{1}{3}\left(\frac{R_e}{R}\right)^2\right] \tag{1.28}$$

R_e being the limit elastic curvature $2\epsilon_P/b$. When the material is *elastic-perfectly brittle* ($m = 0$), the result is

$$M = \frac{\sigma_P b^2}{6}\left(\frac{R_e}{R}\right)^2 \tag{1.29}$$

Finally, when the material is *elastic-linear softening*, Figure 1.3, the following relations hold

$$M = \frac{\sigma_P b^2}{6}\left(\frac{R_e}{R}\right)^2\left[1 + \tfrac{3}{2}m\left(1 + \frac{m}{3}\right)\right], \qquad \text{for } \frac{R_e}{R} \leqslant \frac{1}{m+1},$$

$$M = \frac{\sigma_P b^2}{6}\left[\frac{3}{2} - \frac{1}{2}\left(\frac{R_e}{R}\right)^2 - \frac{1}{m}\left(\frac{R}{R_e} - 1\right)\left(1 - \frac{R_e}{R}\right)\left(1 + \frac{1}{2}\frac{R_e}{R}\right)\right],$$

$$\text{for } \frac{R_e}{R} > \frac{1}{m+1} \tag{1.30}$$

Therefore, the maximum allowable bending moment lies between 1/6 $\sigma_P b^2$ and 1/4 $\sigma_P b^2$. The variations of the bending moment with curvature are shown in Figure 1.11.

Consider now a cross section with only one axis of symmetry that coincides with the bending axis, Figure 1.12. The neutral axis remains perpendicular to the symmetry axis, although its position is not fixed during the loading process. In the limit case of a completely yielded cross section as given in Figure 1.12, the condition

$$\sigma_P A_1 = \sigma_P A_2 \tag{1.31}$$

holds with A_1 and A_2 being the areas of the cross section located above and below the plastic neutral axis, n_p, respectively. Therefore, the plastic moment is

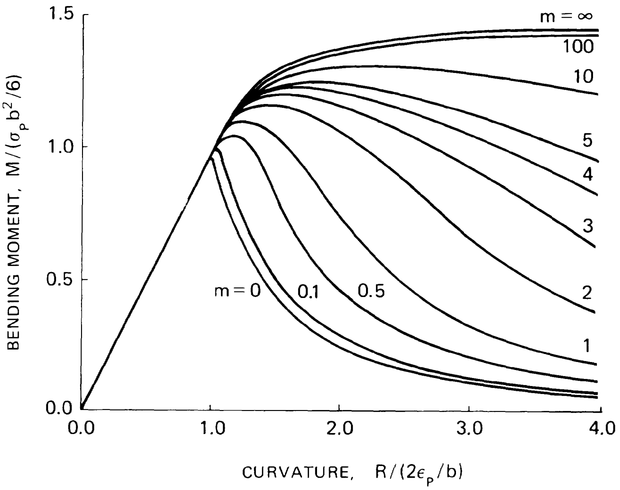

Fig. 1.11. Variations of the bending moment with curvature for an elastic-softening material.

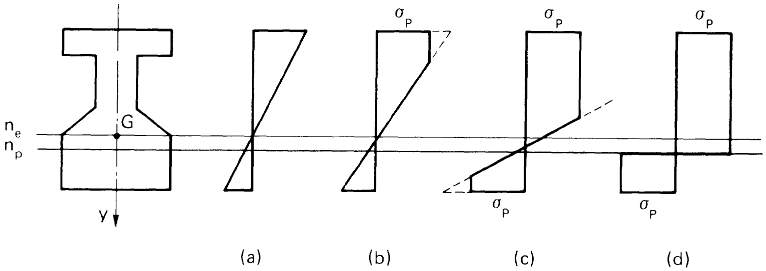

Fig. 1.12. Elastic-plastic flexural beam behavior: cross section with one axis of symmetry.

$$M_P = \sigma_P \frac{A}{2} (d_1 + d_2) \tag{1.32}$$

where d_1 and d_2 are the distances of the neutral axis n_p from the centroids of the half-sections. When $M_e < M < M_P$, the neutral axis is between n_e and n_p as shown in Figure 1.12.

In general, a beam can be loaded by a combination of bending moments, M_x and M_y, torsional moment, M_z, shear forces, S_x and S_y, and axial force, F_z. They can produce curvatures R_x and R_y, rotation θ_z, shear deformations η'_x and η'_y, and axial dilatation ϵ_z respectively. It is possible to prove the theorems of normality of incremental plastic strain and convexity of yield locus by replacing the stress vector, $\boldsymbol{\sigma}$, with the six-dimensional loading vector, $\mathbf{Q}$, and the incremental plastic strain vector, $\dot{\boldsymbol{\epsilon}}_P$, with the plastic flow vector, $\dot{\mathbf{q}}_P$.

Consider the case of eccentric axial force. For a rectangular cross section loaded by the axial force F on the Y-axis with eccentricity e, four stages of development prevail as F is increased. Referring to Figures 1.13(a), (b), (c) and (d), they correspond respectively to elastic, elastic–plastic yielded only on one side, elastic–plastic yielded on both sides and limit condition with complete yielding. Figure 1.13(d) can be decomposed as shown in Figures 1.14 such that Figure 1.14(a) represents the resultant force F, and Figure 1.14(b) the resultant moment $M = Fe$. If δ is the extension indicated in Figure 1.14, then

$$N = \sigma_P t(b - 2\delta) \tag{1.33a}$$

and

$$M = \sigma_P t\delta(b - \delta) \tag{1.33b}$$

The plastic axial force and bending moment are

$$N_P = \sigma_P tb \tag{1.34a}$$

$$M_P = \sigma_P \frac{tb^2}{4} \tag{1.34b}$$

respectively. The following ratios can be defined:

$$\tilde{N} = \frac{N}{N_P} = 1 - 2\left(\frac{\delta}{b}\right) \tag{1.35a}$$

$$\tilde{M} = \frac{M}{M_P} = 4\left(\frac{\delta}{b}\right)\left(1 - \frac{\delta}{b}\right) \tag{1.35b}$$

such that

$$\tilde{M} = 1 - \tilde{N}^2 \tag{1.36}$$

The yield locus in the plane $\tilde{M}$ versus $\tilde{N}$ is given in Figure 1.15 and is convex.

Limit analysis of frames. The limit load for frames can be obtained by the application of the Mixed Theorem. A kinematically admissible plastic flow mechanism is used. This corresponds to a statically admissible bending moment that may be regarded as the plastic limit condition.

Consider the portal frame of Figure 1.16(a) subjected to a horizontal load

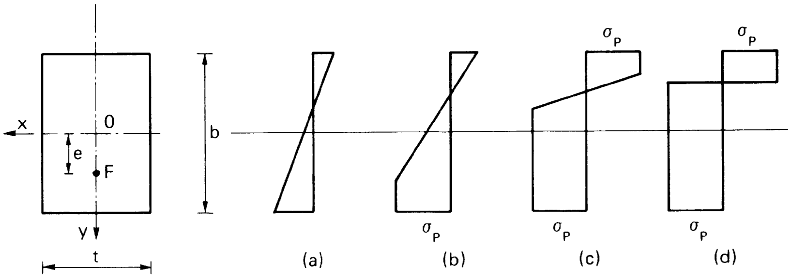

Fig. 1.13. Elastic-plastic behavior of a beam subjected to an eccentric axial force.

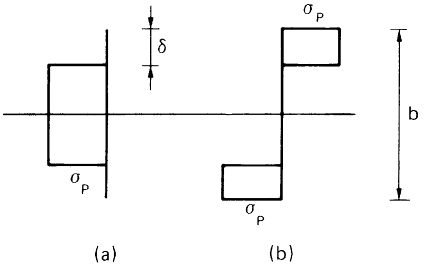

Fig. 1.14. Resultant force and moment of an eccentric axial force, refer to Figure 1.13.

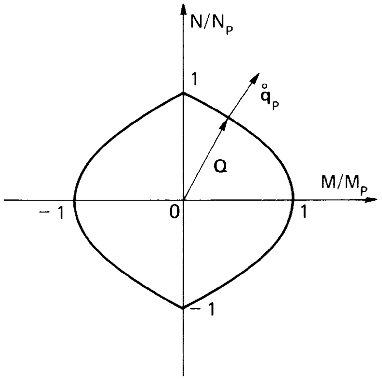

Fig. 1.15. Yield locus in the plane of bending mement vs. axial force.

P_1. Plastic hinges are formed at 1, 2, 4 and 5 by the incremental horizontal plastic displacement $\dot{u}_1$ in Figure 1.16(b). The application of the Virtual Work Principle at plastic collapse gives:

$$P_1 l\dot{\theta} = M_P 4\dot{\theta} \tag{1.37}$$

from which P_1 is obtained:

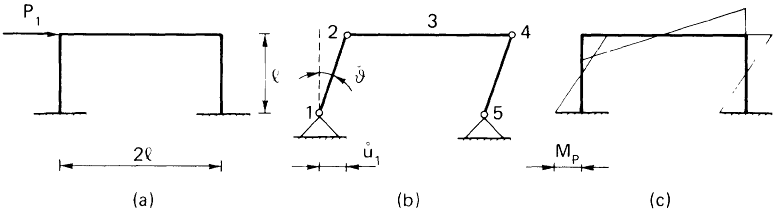

Fig. 1.16. Portal frame subjected to a horizontal load.

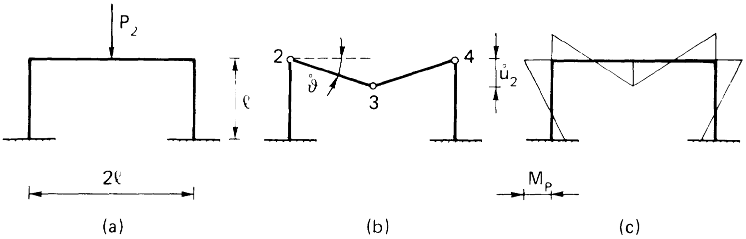

Fig. 1.17. Portal frame subjected to a vertical load.

$$P_1 = 4\frac{M_P}{l} \tag{1.38}$$

The assumed plastic flow mechanism in Figure 1.16(b) corresponds to the bending moment diagram in Figure 1.16(c), which is statically admissible. For the Mixed Theorem, therefore, equation (1.38) gives the limit load.

Let the portal frame be subjected to a vertical load P_2 in Figure 1.17(a). Plastic hinges are now formed at 2, 3 and 4 by the incremental vertical plastic displacement $\dot{u}_2$ in Figure 1.17(b). The application of the Virtual Work Principle at plastic collapse renders

$$P_2 = 4\frac{M_P}{l} \tag{1.39}$$

The corresponding bending moment diagram is given in Figure 1.17(c) which is statically admissible. Equation (1.39) therefore gives the limit load as a result of the Mixed Theorem.

The case when the portal frame is subjected to P_1 and P_2 is shown in Figure 1.18(a). Plastic hinges at 1, 3, 4 and 5 are formed by the incremental plastic displacements $\dot{u}_1 = \dot{u}_2$, Figure 1.18(b). The Virtual Work Principle leads to

$$P_1 l\dot{\theta} + P_2 l\dot{\theta} = 6M_P\dot{\theta} \tag{1.40}$$

and hence

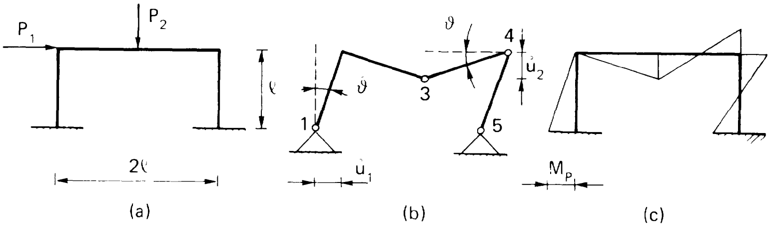

Fig. 1.18. Portal frame subjected to a horizontal and a vertical load.

$$P_1 + P_2 = 6\frac{M_P}{l} \tag{1.41}$$

The bending moment diagram is shown in Figure 1.18(c), which is statically admissible only when

$$\frac{1}{2} \leqslant \left|\frac{P_2}{P_1}\right| \leqslant 2 \tag{1.42}$$

Equations (1.38), (1.39), (1.41) and (1.42) give the plastic flow locus in Figure 1.19. All four quadrants are considered, i.e., forces P_1 and P_2 can invert their way. The locus is convex and the normality rule is valid for the whole structure. In fact, when the $|P_2/P_1|$ ratio is small, the lateral mechanism in Figure 1.16(b) is activated and the incremental plastic displacement vector

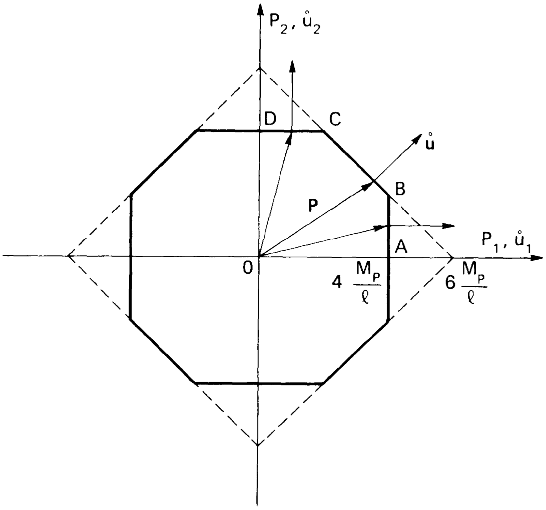

Fig. 1.19. Plastic flow locus for the portal frame in Figure 1.18.

$\dot{\mathbf{u}}$ is normal to the side AB of the yield locus so that $\dot{u}_2 = 0$. By increasing the $|P_2/P_1|$ ratio in equation (1.42), the mixed mechanism in Figure 1.18(b) is activated and the incremental plastic displacement vector is normal to the side BC of the yield locus and hence $\dot{u}_1 = \dot{u}_2$. For $|P_2/P_1| > 2$, the vertical mechanism in Figure 1.17(b) is activated and the incremental plastic displacement vector is normal to the side CD of the yield locus with $\dot{u}_1 = 0$.

1.2. Crack tip stress intensity factor and energy release rate

Griffith's model. The theoretical strength of metallic materials is about one tenth of the Young's modulus, E. Such high values are rarely found in practice. In fact, materials fail prematurely due to the existence of microcracks, flaws and other stress concentration causes. Brittle materials usually fail at a stress level of $\sigma \simeq E/1{,}000$. The theoretical strength of $\sigma_{\text{th}} \simeq E/10$ is achieved only in opportunely prepared materials, as, for example, the glass fibres.

Inglis [9] provided the solution of a solid weakened by an elliptical cavity subjected to a uniform stress σ normal to the major semi-axis of the ellipse. The maximum normal stress at the immediate vicinity $y = 0$ and $x \to a$ is

$$\sigma_{\max} = \sigma\left(1 + 2\frac{a}{b}\right) = \sigma\left(1 + 2\sqrt{\frac{a}{\rho}}\right) \simeq 2\sigma\sqrt{\frac{a}{\rho}} \tag{1.43}$$

where a and b are the major and minor semi-axis of the ellipse, respectively

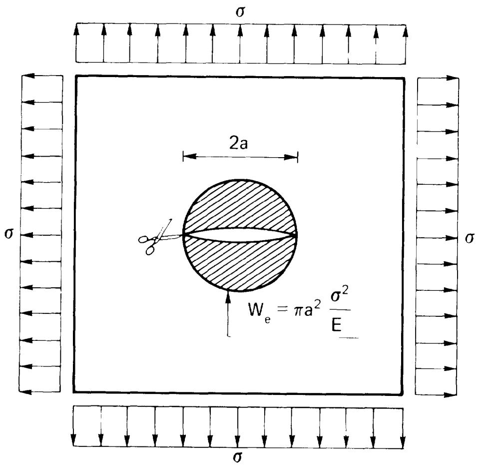

Fig. 1.20. Griffith's crack in an infinite slab subjected to a uniform stress field.

and $\rho = b^2/a$ is the radius of curvature at the end of the major axis.

Griffith [10] developed the concept that a pre-existing crack can propagate when the elastic energy released during the crack extension is equal to or higher than the surface energy required to create the newly formed crack surface. Based on the Inglis' stress solution, he considered the limit case when the ellipse degenerates into a slit, Figure 1.20, and showed that the elastic energy released by the body with a slit of length $2a$ is

$$W_e = \pi a^2 \frac{\sigma^2}{E} \tag{1.44}$$

The surface energy required to create the total crack surface is

$$W_s = 4a\gamma \tag{1.45}$$

with γ being the unit surface energy*. Incipient fracture is assumed to occur when the potential energy, $V(a) = W_s(a) - W_e(a)$, is stationary or decreases, i.e.,

$$\frac{\mathrm{d}V}{\mathrm{d}a} = 4\gamma - 2\pi a \frac{\sigma^2}{E} = 0 \tag{1.46}$$

which leads to

$$\sigma_{cr} = \sqrt{\frac{2\gamma E}{\pi a_{cr}}} \tag{1.47}$$

If the initial crack length is given, $a = a_0$, a corresponding value $\sigma_{cr}(a_0)$ exists, Figure 1.21. As the critical crack length a_{cr} tends to increase, the fracture stress σ_{cr} decreases, and the fracture process results to be unstable.

Irwin's model. Irwin [12] proposed a mathematical crack model referring the near stress field to three fracture modes, Figure 1.22. They are the opening, sliding and tearing mode and often referred to respectively as Mode I, II and III crack extension. The corresponding stress fields are

$$\sigma_x = \frac{K_I}{(2\pi r)^{1/2}} \cos \frac{\theta}{2} \left(1 - \sin \frac{\theta}{2} \sin \frac{3}{2}\theta\right) \tag{1.48a}$$

---

* Equation (1.45) is computed from the definition of surface tension for a liquid and not that of breaking the atomic bonds of a solid. Refer to [11] for a clarification of the physical implication of the Griffith original derivation [10] although the functional form for the critical stress σ_{cr} in equation (1.47) is correct.

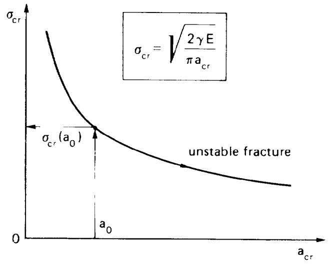

Fig. 1.21. Variation of the crack propagation stress with the semi-length of the crack.

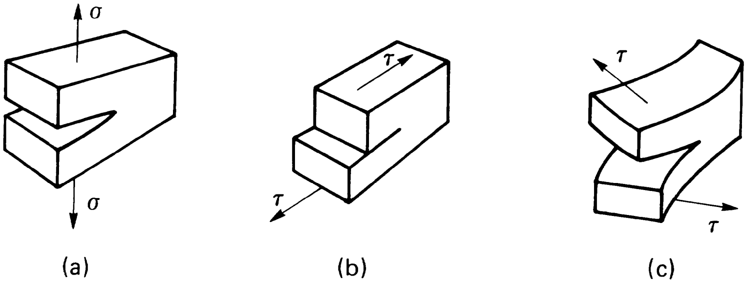

Fig. 1.22. Fracture modes: opening (a), sliding (b) and tearing (c).

$$\sigma_y = \frac{K_I}{(2\pi r)^{1/2}} \cos\frac{\theta}{2}\left(1 + \sin\frac{\theta}{2}\sin\frac{3}{2}\theta\right) \tag{1.48b}$$

$$\tau_{xy} = \frac{K_I}{(2\pi r)^{1/2}} \sin\frac{\theta}{2}\cos\frac{\theta}{2}\cos\frac{3}{2}\theta \tag{1.48c}$$

for Mode I and

$$\sigma_x = -\frac{K_{II}}{(2\pi r)^{1/2}} \sin\frac{\theta}{2}\left(2 + \cos\frac{\theta}{2}\cos\frac{3}{2}\theta\right) \tag{1.49a}$$

$$\sigma_y = \frac{K_{II}}{(2\pi r)^{1/2}} \cos\frac{\theta}{2}\sin\frac{\theta}{2}\cos\frac{3}{2}\theta \tag{1.49b}$$

$$\tau_{xy} = \frac{K_{II}}{(2\pi r)^{1/2}} \cos\frac{\theta}{2}\left(1 - \sin\frac{\theta}{2}\sin\frac{3}{2}\theta\right) \tag{1.49c}$$

for Mode II. The stress notations are shown in Figure 1.23 with r and θ being the local polar coordinates. K_I and K_{II} are known as the stress intensity

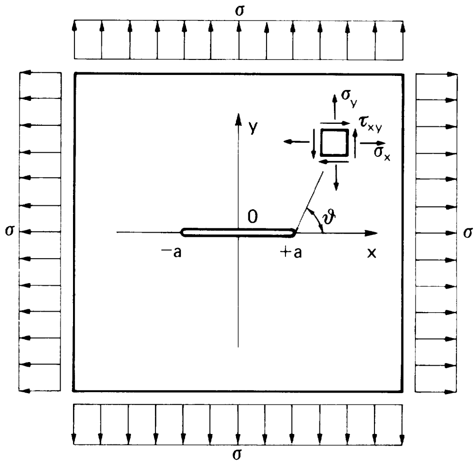

Fig. 1.23. Stress notations in the crack tip vicinity.

factors. Mode III pertains to anti-plane shear and is associated with the local shear stresses:

$$\tau_{xz} = -\frac{K_{III}}{(2\pi r)^{1/2}} \sin\frac{\theta}{2} \tag{1.50a}$$

$$\tau_{yz} = \frac{K_{III}}{(2\pi r)^{1/2}} \cos\frac{\theta}{2} \tag{1.50b}$$

where K_{III} is the Mode III stress intensity factor.

Strain energy release rate. If an infinite slab contains a crack of initial length $2a$ that extends to the length $2(a + \mathrm{d}a)$, the variation of potential elastic energy may be computed to define a generalized force G_I and related to K_I:

$$G_I = \frac{K_I^2}{E} \tag{1.51}$$

For the Griffith crack, $K_I = \sigma\sqrt{\pi a}$ and hence equations (1.47) and (1.51) may be combined to give

$$G_{IC} = 2\gamma \tag{1.52}$$

at incipient fracture. Since under in-plane shear as shown in Figure 1.24, the

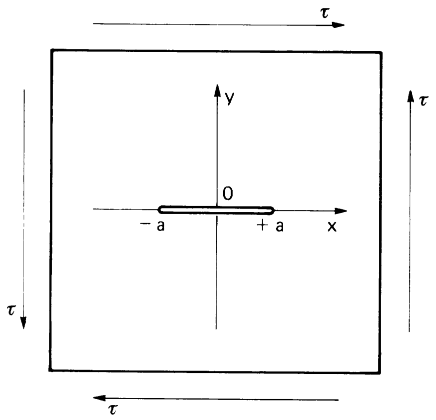

Fig. 1.24. Griffith's crack in an infinite slab subjected to pure shear at the infinity.

crack does not grow in a self-similar manner, there is no relation similar to that given by equation (1.51) for Mode II.

1.3. Other fracture criteria

Since the Griffith model applies only to self-similar crack growth, it cannot be conveniently applied to situations where the crack turns or curves under general loading conditions.

Maximum stress criterion. This criterion was proposed by Erdogan and Sih [13] in 1963 and is based on the assumption that the crack initiates from its tip in a direction normal to the maximum circumferential stress σ_θ. With reference to the polar coordinates, equations (1.48) and (1.49) may be added and expressed in the form

$$\sigma_r = \frac{1}{(2\pi r)^{1/2}} \cos\frac{\theta}{2}\left[K_I\left(1+\sin^2\frac{\theta}{2}\right)+K_{II}\left(\frac{3}{2}\sin\theta-2\tan\frac{\theta}{2}\right)\right] \tag{1.53a}$$

$$\sigma_\theta = \frac{1}{(2\pi r)^{1/2}} \cos\frac{\theta}{2}\,[K_I(1+\cos\theta)-3K_{II}\sin\theta] \tag{1.53b}$$

$$\tau_{r\theta} = \frac{1}{2(2\pi r)^{1/2}} \cos\frac{\theta}{2}\,[K_I\sin\theta+K_{II}(3\cos\theta-1)] \tag{1.53c}$$

The fracture initiation angle θ may be found by letting $\tau_{r\theta}(\theta)$ equal to zero, i.e.,

$$2(2\pi r)^{1/2}\tau_{r\theta}(\theta) \;=\; 0 \tag{1.54}$$

which corresponds to the principal plane. Equation (1.53c) gives

$$\cos\frac{\theta}{2}\,[K_I\sin\theta + K_{II}(3\cos\theta - 1)] \;=\; 0 \tag{1.55}$$

which can be satisfied by setting $\cos\theta/2 = 0$ that corresponds to the stress free surface conditions of $\theta = \pm\pi$ or by letting

$$K_I\sin\theta + K_{II}(3\cos\theta - 1) \;=\; 0 \tag{1.56}$$

which yields the crack initiation angle θ. For a crack of length $2a$ subjected to stresses applied biaxially, Figure 1.25, the stress intensity factors are

$$K_I \;=\; \sigma_\beta\sqrt{\pi a} \tag{1.57a}$$

$$K_{II} \;=\; \tau_\beta\sqrt{\pi a} \tag{1.57b}$$

with σ_β and τ_β being respectively the normal and shear stress with respect to the line crack. Mohr circle analysis gives

$$K_I \;=\; \left(\frac{\sigma_1+\sigma_2}{2} + \frac{\sigma_1-\sigma_2}{2}\cos 2\beta\right)\sqrt{\pi a} \tag{1.58a}$$

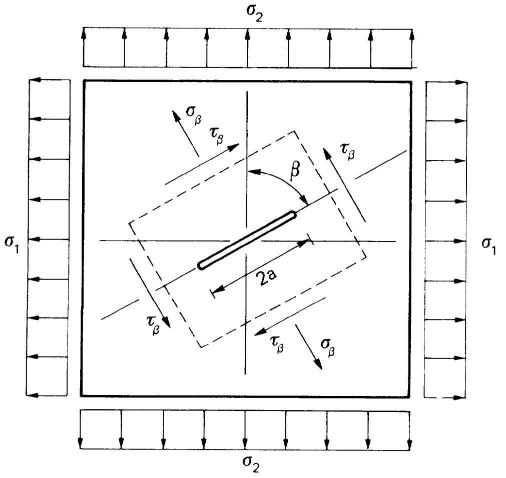

Fig. 1.25. Inclined crack subjected to a biaxial stress field.

$$K_{II} = \left(\frac{\sigma_2 - \sigma_1}{2} \sin 2\beta\right)\sqrt{\pi a} \tag{1.58b}$$

If s is the ratio σ_1/σ_2 of the principal stresses, then equations (1.58) can be rewritten as

$$K_I = \sigma_2\sqrt{\pi a}\,[s + (1 - s)\sin^2\beta] \tag{1.59a}$$

$$K_{II} = \sigma_2\sqrt{\pi a}\,(1 - s)\sin\beta\cos\beta \tag{1.59b}$$

Equations (1.56) and (1.59) further lead to an expression that relates the crack propagation angle, θ, and crack inclination angle, β:

$$[s + (1 - s)\sin^2\beta]\sin\theta + [\tfrac{1}{2}(1 - s)\sin 2\beta](3\cos\theta - 1) = 0 \tag{1.60}$$

Equation (1.60) can be transformed into:

$$2(1 - s)\sin 2\beta\left(\tan\frac{\theta}{2}\right)^2 - 2[s + (1 - s)\sin^2\beta]\left(\tan\frac{\theta}{2}\right) - (1 - s)\sin 2\beta = 0 \tag{1.61}$$

The solution of interest is reported in Figure 1.26 for different ratios s.

If $s = 1$, it is always $\theta = 0$, since the stress field at the infinity is uniform, and then the crack extension is collinear due to the symmetry. If $s = 0$, there is a discontinuity for $\beta = 0$. In fact $\theta(\beta = 0, s = 0) = 0$ due to the symmetry, while

$$\lim_{\beta \to 0^+} \theta(\beta, s = 0) \simeq 70^\circ$$

If s is small but different from zero, the discontinuity disappears and is replaced by a rapid variation, represented by a very steep branch in Figure 1.26. From a mathematical point of view, this is a typical case of *non-uniform convergence* of function $\theta(s, \beta)$ in $\beta = 0$ and for $s \to 0^+$.

While equation (1.54) determines the direction of maximum stress, the additional condition may be introduced as a criterion of instability:

$$\sqrt{2\pi r}\,\sigma_\theta = K_{IC} \tag{1.62}$$

Introducing the dimensionless stress-intensity factors

$$K_I^* = K_I/K_{IC}, \qquad K_{II}^* = K_{II}/K_{IC} \tag{1.63}$$

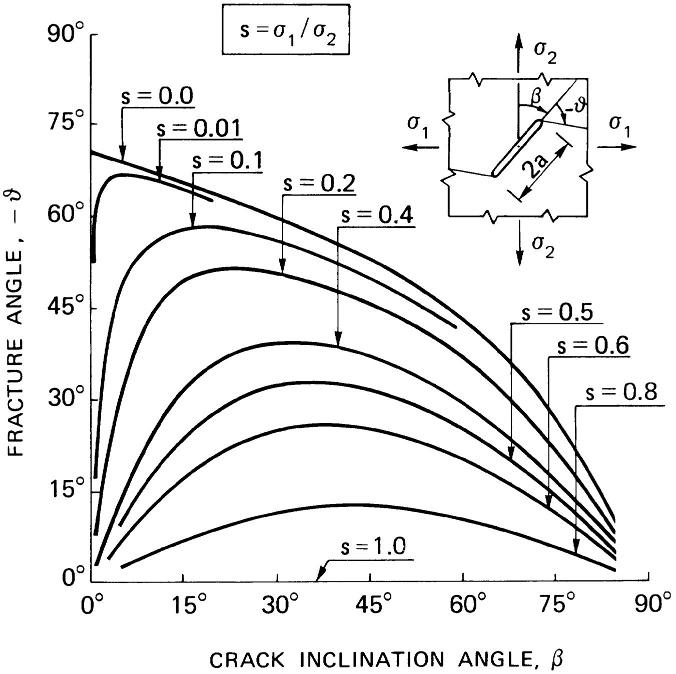

Fig. 1.26. Crack branching angle as a function of the crack inclination angle, Maximum stress criterion.

the fracture locus may be plotted in the K_I^* versus K_{II}^* plane. Solving

$$K_I^* \sin\theta + K_{II}^*(3\cos\theta - 1) = 0 \tag{1.64a}$$

$$K_I^* \cos^2\frac{\theta}{2} - \frac{3}{2}K_{II}^* \sin\theta = \frac{1}{\cos\frac{\theta}{2}} \tag{1.64b}$$

for K_I^* and K_{II}^* by varying θ, all the points of the locus are defined. They are symmetric with respect to the K_I^*-axis and valid only in the half-plane $K_I^* \geqslant 0$, Figure 1.27.

In the foregoing treatment, a core region of finite size r_0 surrounding the crack tip has been assumed such that r in equation (1.53) is larger than r_0 and the crack tip stresses always remain finite. The size of this region can be determined analytically [14]. The fracture locus also varies with the ratio r_0/a [15].

Minimum strain energy density criterion. The strain energy density function at the crack tip is of the form [16, 17]

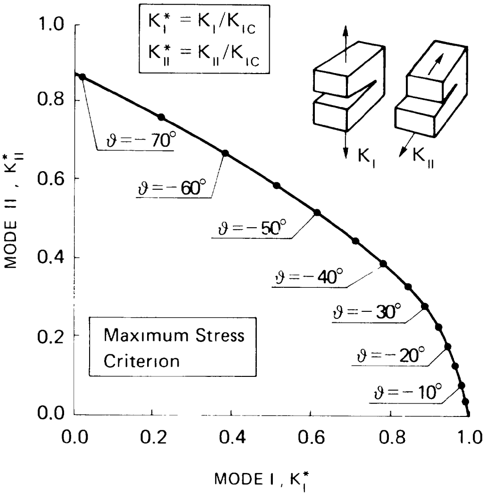

Fig. 1.27. Fracture locus in the plane of the stress-intensity factors, Maximum stress criterion.

$$\left(\frac{\mathrm{d}W}{\mathrm{d}V}\right) = \frac{1}{r}(a_{11}K_I^2 + 2a_{12}K_IK_{II} + a_{22}K_{II}^2 + a_{33}K_{III}^2) \tag{1.65}$$

where the volume of the differential element is $\mathrm{d}V = r\mathrm{d}r\mathrm{d}\theta$. The coefficients a_{ij} for plane strain are

$$a_{11} = \frac{1}{16\pi G}[(3 - 4\nu - \cos\theta)(1 + \cos\theta)] \tag{1.66a}$$

$$a_{12} = \frac{1}{16\pi G}(2\sin\theta)[\cos\theta - 1 + 2\nu] \tag{1.66b}$$

$$a_{22} = \frac{1}{16\pi G}[4(1 - \nu)(1 - \cos\theta) + (1 + \cos\theta)(3\cos\theta - 1)] \tag{1.66c}$$

$$a_{33} = \frac{1}{4\pi G} \tag{1.66d}$$

The function $\mathrm{d}W/\mathrm{d}V$ thus possesses a $1/r$ singularity at the crack tip. A *strain energy density factor* S can thus be defined as a function of θ

$$\left(\frac{\mathrm{d}W}{\mathrm{d}V}\right) = \frac{S(\theta)}{r} \tag{1.67}$$

Sih [16, 17] proposed the following criterion in 1973:

(a) The crack initiation direction is assumed to correspond with the minimum strain energy density factor:*

$$\frac{\partial S}{\partial \theta} = 0, \qquad \frac{\partial^2 S}{\partial \theta^2} > 0 \qquad \text{for } \theta = \theta_0 \tag{1.68}$$

(b) The crack starts to propagate when S reaches a critical value, S_c at

$\theta = \theta_0$.

Unlike the maximum stress criterion, the quantity S alone determines the material fracture resistance and the direction of crack initiation. For Mode I crack extension, $K_{II} = K_{III} = 0$; $\theta_0 = 0$ and therefore $a_{11} = (1 - 2\nu)/4\pi G$. The critical value of the strain energy density factor, S_c, can be related to the critical value of the stress-intensity factor, K_{IC}:

$$S_c = \frac{(1 - 2\nu)(1 + \nu)}{2\pi E} K_{IC}^2, \text{ for plane strain} \tag{1.69}$$

In the case of mixed mode in-plane loading, $K_I \neq 0$, $K_{II} \neq 0$ and $K_{III} = 0$. By the application of equations (1.65) and (1.66), an expression for finding the stationary values of S is obtained:

$$\frac{\partial S}{\partial \theta} = K_I^2 \frac{1}{8G} \sin\theta(\cos\theta - 1 + 2\nu) + 2K_I K_{II} \frac{1}{8G} [2\cos^2\theta + (2\nu - 1)\cos\theta - 1] + K_{II}^2 \frac{1}{8G} \sin\theta(-3\cos\theta + 1 - 2\nu) = 0 \tag{1.70}$$

This results in a fourth order equation:

$$2(1 - \nu)K_I K_{II}\left(\tan\frac{\theta}{2}\right)^4 + (3K_{II}^2 - K_I^2)\left(\tan\frac{\theta}{2}\right)^3 + [(2\nu - 1)(K_I^2 - K_{II}^2) - 6K_I K_{II}]\left(\tan\frac{\theta}{2}\right)^2 + [K_I^2 - 3K_{II}^2]\left(\tan\frac{\theta}{2}\right) + [(2\nu - 1)(K_I^2 - K_{II}^2) + 2K_I K_{II}\nu] = 0 \tag{1.71}$$

---

* In general, the strain energy density function $\mathrm{d}W/\mathrm{d}V$ should be used instead of S, particularly in situations where the material is nonlinear [18–20].

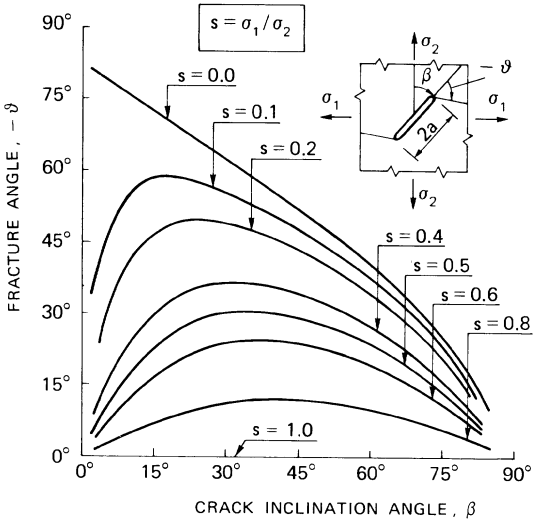

Fig. 1.28. Crack branching angle as a function of the crack inclination angle, Minimum strain energy density criterion.

The two factors, K_I and K_{II}, are functions of the loading ratio s, and crack inclination angle β.

Substituting equations (1.59) into (1.71), it is possible to obtain the crack inclination angle, β, as a function of θ. The results are displayed graphically in Figure 1.28 for $\nu = 0.3$.

The crack growth conditions are

$$\frac{\partial S}{\partial \theta} = 0 \tag{1.72a}$$

$$S(K_I, K_{II}) = S_c \tag{1.72b}$$

Equations (1.72) can be restated as

$$K_I^{*2} \sin\theta(\cos\theta - 1 + 2\nu) + K_{II}^{*2} \sin\theta(-3\cos\theta + 1 - 2\nu)$$
$$+ 2K_I^* K_{II}^* [2\cos^2\theta + (2\nu - 1)\cos\theta - 1] = 0 \tag{1.73a}$$

$$[(3 - 4\nu - \cos\theta)(1 + \cos\theta)]K_I^{*2} + 4\sin\theta[\cos\theta - (1 - 2\nu)]K_I^* K_{II}^*$$
$$+ [4(1 - \nu)(1 - \cos\theta) + (1 + \cos\theta)(3\cos\theta - 1)]K_{II}^{*2}$$
$$- 4(1 - 2\nu) = 0 \tag{1.73b}$$

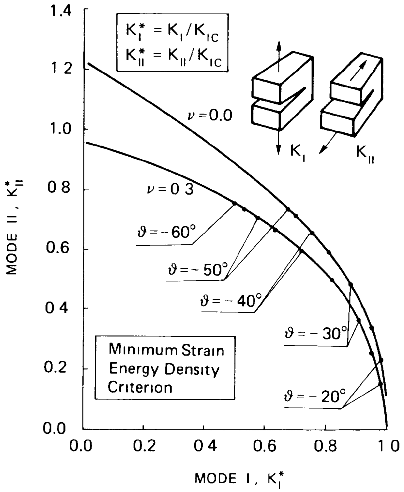

Fig. 1.29. Fracture locus in the plane of the stress-intensity factors, Minimum strain energy density criterion.

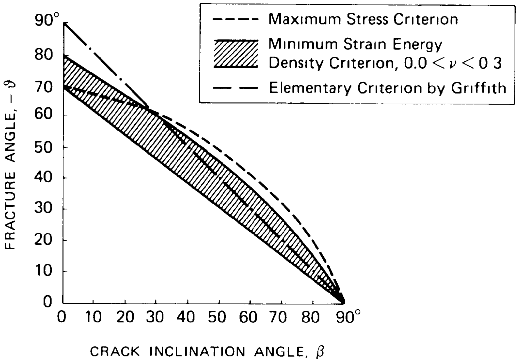

Fig. 1.30. Crack branching angle vs. crack inclination angle, comparison between the various theories.

Equations (1.73) yield the fracture locus in the plane K_I^* versus K_{II}^* for each value of the Poisson ratio ν. The fracture loci for $\nu = 0.0$ and 0.3 are reported in Figure 1.29. The results can be compared with those obtained from the maximum circumferential stress criterion in Figure 1.27.

In Figure 1.30, the curves $\theta(\beta)$ obtained from the various theories are summarized. The straight line connecting the points $-\theta = 90°$ and $\beta = 90°$ corresponds to the simple assumption of Griffith that the crack propagates orthogonally to the direction of the uniaxial applied stress. Care, however, should be exercised when comparing these results with experiments which often contain scatters that are not properly understood and misinterpreted.

There is always the temptation to concoct and to modify theories [21, 22] in order to agree with experiments. Frequently, errors originated from the stress analyses [23–25] are carried into the failure criterion.

The strain energy density criterion [18–20] will be employed throughout this book as it can be applied consistently to account for load time history effects regardless of geometry, material or loading type. The relationship in equation (1.67) will hold in general except that S can no longer be expressed in terms of the stress intensity factors if the material behaves nonlinearly.* Sih has shown in [20] that the qualitative features of the crack growth resistance curves derived from the strain energy density theory for concrete are preserved when the energy dissipation mechanisms of the material are altered. The plots of strain energy density factors S versus the half or full crack length, say a, will be referred to as the SR-curves. They are discussed in [20] for the cases of elastic and plastic unloading during crack growth in concrete beams that exhibit softening.

Crack tip cohesive forces. Based on the argument that the stress at the crack tip must be finite, the maximum value it can reach is the yield strength σ_P as shown in Figure 1.31(a). If the material softens elastically, the stress can go to zero as the crack tip is approached, Figure 1.31(b). A fictitious crack longer than the actual one can be considered with cohesive forces applied at the tip. In this way, the non-linear effects during crack growth can be easily simulated.

Barenblatt [26] applied the aforementioned concept by considering attractive atomic forces in a very small region near the crack tip. This annuls the stress-singularity due to mechanical loads. Dugdale [27] proposed a mathematically similar but conceptually different model of finite crack tip stress. His argument is based on material that attains a yield limit at the crack tip. A more elegant interpretation of these concepts was made by Rice [28] who assumed the restraining stress σ as a function of the separation distance, δ, Figure 1.32 (a). A path independent integral was employed to show that the energy J_c necessary to produce a unit free surface can be written as, Figure 1.32(b):

$$J_c = \int_0^{\delta_c} \sigma(\delta)\,d\delta \tag{1.74}$$

where J_c represents the area under the σ versus δ curve, Figure 1.32(a). For a linear elastic material, it can be shown that $J_c = G_{IC} = K_{IC}^2/E$. Such a relationship has recently been studied by Hillerborg, Modeer and Petersson [29, 30] using a *fictitious crack model* with cohesive forces at the crack tip and the finite element method. When the softening σ versus δ law becomes perfectly plastic, equation (1.74) yields the well-known relation between the

---

* May be a function of all the space variables.

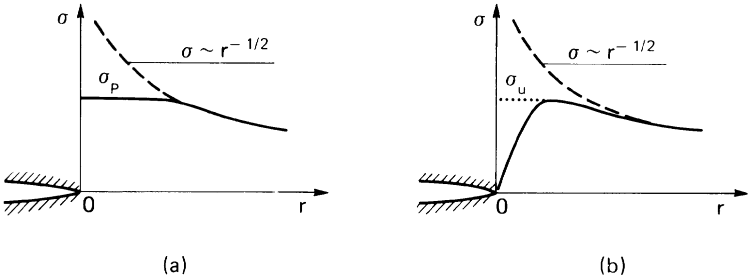

Fig. 1.31. Stress limitation in the crack tip vicinity: perfectly plastic (a) and softening (b) material.

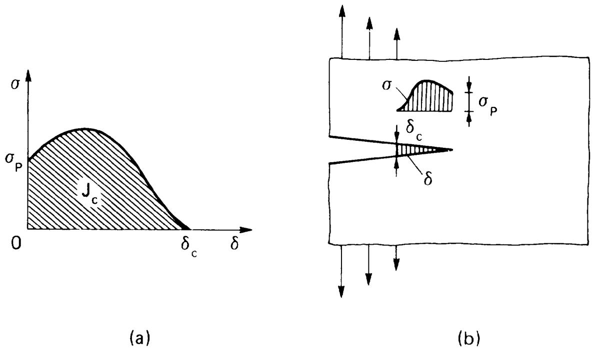

Fig. 1.32. Cohesive stresses at the crack tip: restraining stress as a function of the separation distance (a) and of the distance from the crack tip (b).

energy required to create a unit crack growth, J_c, the critical crack opening displacement, δ_c, and the yield strength, σ_P, i.e.

$$\delta_c = J_c/\sigma_P \tag{1.75}$$

The cohesive force models are limited to self-similar cracks and, since equations (1.74) and (1.75) are derived from the path independent J-integral also to elastic materials that do not undergo plastic deformation or any other kind of irreversible deformation.

References

1. Beltrami, E., Rendiconti Reale Istituto Lombardo, serie II, tomo XVIII, pp. 704–714 (1885).

2. von Mises, R., Göttinger Nachrichten, Kl 582 (1913).
3. Tresca, H., Comptes Rendus, Acad. Sci., Paris, 59, p. 754 (1864).
4. Hill, R., Phil. Mag., 41, p. 733 (1950).
5. Drucker, D.C., Quart. Appl. Math., 7, pp. 411–418 (1950).
6. Massonnet, C. and Save, M., Calcul Plastique des Constructions, Vol. 2, Centre Belgo-Luxembourgeois d'information de l'acier, Bruxelles (1972).
7. Muskhelishvili, N.I., Some Basic Problems of the Mathematical Theory of Elasticity, P. Noordhoff Ltd., Groningen, The Netherlands (1963).
8. Timoshenko, S., Theory of Elasticity, McGraw-Hill, New York and London (1934).
9. Inglis, C.E., Trans. Roy. Inst. Naval Architects, 60, p. 219 (1913).
10. Griffith, A.A., Phil. Trans. Roy. Soc. London, A 221, p. 163 (1921).
11. Sih, G.C., Some basic problems in fracture mechanics and new concepts, Engineering Fracture Mechanics, 5, pp. 365–377 (1973).
12. Irwin, G.R., Journ. Appl. Mech., 24, p. 361 (1957).
13. Erdogan, F. and Sih, G.C., On the crack extension in plates under plane loading and transverse shear, Journal of Basic Engineering, pp. 519–527 (1963).
14. Kipp, M.E. and Sih, G.C., The strain energy density failure criterion applied to notched elastic solids, International Journal of Solids and Structures, 11, pp. 153–173 (1975).
15. Carpinteri, A., DiTommaso, A. and Viola, E., Collinear stress effect on the crack branching phenomenon, Materials and Structures (RILEM), 12, pp. 439–446 (1979).
16. Sih, G.C. and Macdonald, B., Fracture mechanics applied to engineering problems – strain energy density fracture criterion, Engineering Fracture Mechanics, 6, pp. 361–386 (1974).
17. Sih, G.C., Introductory Chapters of Mechanics of Fracture, Vol. I to VII, edited by G.C. Sih, Martinus and Nijhoff Publishers, The Hague, 1972 to 1981.
18. Carpinteri, A. and Sih, G.C., Damage accumulation and crack growth in bilinear materials with softening: application of strain energy density theory, J. of Theoretical and Applied Fracture Mechanics, Vol. 1, No. 2, pp. 145–160 (1984).
19. Sih, G.C., Mechanics of material damage in concrete, Fracture Mechanics of Concrete: Material Characterization and Testing, edited by A. Carpinteri and A.R. Ingraffea, Martinus Nijhoff Publishers, The Hague, pp. 1–29 (1984).
20. Sih, G.C., Non-linear response of concrete: interaction of size, loading step and material property, Applications of Fracture Mechanics to Cementitious Composites, edited by S.P. Shah, Martinus Nijhoff Publishers, The Hague, pp. 3–23 (1984).
21. Sih, G.C. and Gdoutos, E.E., Discussion on a modified strain-energy density criterion applied to crack propagation by P.S. Theocaris and N.P. Andrianopoulos, J. Appl. Mech., 49, pp. 678–679 (1982).
22. Sih, G.C., Moyer, E.T., Jr. and Gdoutos, E.E., Discussion on the Mises elastic-plastic boundary as the core region in fracture criteria by P.S. Theocaris and N.P. Andrianopoulos, Engng. Fract. Mech., 18, No. 3, pp. 731–734 (1983).
23. Sih, G.C. and Madenci, E., Discussion on a further examination on the application of the strain energy density theory to the angled crack problem by K.J. Chang, Trans. ASME, J. Appl. Mech., 50, pp. 234–236 (1983).
24. Sih, G.C. and Tzou, D.Y., Discussion on criteria for brittle fracture in biaxial tension by S.K. Maiti and R.A. Smith, J. of Engin. Fract. Mech., 21, No. 5, pp. 977–981 (1985).
25. Tzou, D.Y. and Sih, G.C., Discussion on subsurface crack propagation due to surface traction in sliding wear by H.C. Sin and N.P. Suh, J. of Applied Mechanics, 52, pp. 237–238 (1985).
26. Barenblatt, G.J., The mathematical theory of equilibrium crack in the brittle fracture, Advance in Applied Mechanics, 7, pp. 55–125 (1962).

27. Dugdale, D.S., Yielding of steel sheets containing slits, Journal of Mechanics and Physics of Solids, 8, pp. 100–104 (1960).
28. Rice, J.R., Path independent integral and approximate analysis of strain concentration by notches and cracks, Journal of Applied Mechanics, 35, pp. 379–386 (1968).
29. Hillerborg, A., Modeer, M. and Petersson, P.E., Analysis of crack formation and crack growth in concrete by means of fracture mechanics and finite elements, Cement and Concrete Research, 6, pp. 773–782 (1976).
30. Petersson, P.E., Crack growth and development of fracture zones in plain concrete and similar materials, Report TVBM-1006, Division of Building Materials, Lund Institute of Technology (1981).

2

Fracture of concrete and brittle materials

2.1. Crack surface friction

When surfaces are in contact, load can be transmitted in the normal direction by compressive forces and in the tangential direction by shear or friction. In the case of cracks or lines of discontinuities in concrete, the chances are that they will be oriented at some angles with the load. This leads to rubbing or sliding of adjacent surfaces, an influence that will be discussed in this chapter.

Mohr–Coulomb friction model. An early criterion applied to study the failure behavior of soil and concrete is that of Mohr–Coulomb. It assumes that the shear stress τ on the fracture plane is induced by friction:

$$\tau = c + \mu\sigma \tag{2.1}$$

in which c is the material cohesion, σ is the compression orthogonal to the fracture plane and μ is the friction coefficient being related to the friction angle φ by the relation $\mu = \tan\varphi$. The generalization of equation (2.1) takes the form

$$\tau = f(\sigma) \tag{2.2}$$

In the plane σ versus τ, equation (2.2) can be considered as the envelope of the Mohr's circumferences related to the conditions of incipient fracture, Figure 2.1. The criterion can also be expressed in terms of the principal stresses σ_1, σ_2 and σ_3. For the case shown in Figure 2.2 where $\sigma_1 > \sigma_2 > \sigma_3$:

$$\sin\varphi = \frac{\frac{1}{2}(\sigma_1 - \sigma_3)}{c\cot\varphi - \frac{1}{2}(\sigma_1 + \sigma_3)} \tag{2.3}$$

which may be written as

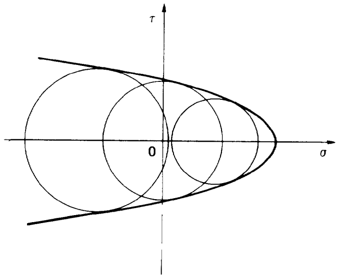

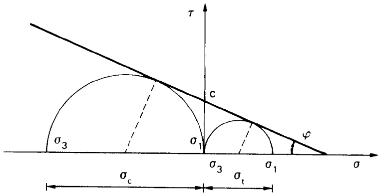

Fig. 2.1. Envelope of the Mohr's circumferences related to the conditions of incipient fracture.
Fig. 2.2. Mohr–Coulomb friction criterion.

$$\frac{\sigma_1}{\sigma_t} - \frac{\sigma_3}{\sigma_c} = 1 \tag{2.4}$$

provided that

$$\sigma_t = 2c \cos \varphi/(1 + \sin \varphi) \tag{2.5a}$$

$$\sigma_c = 2c \cos \varphi/(1 - \sin \varphi) \tag{2.5b}$$

are defined as the uniaxial tensile and compressive strengths respectively, Figure 2.2. This is a two parameter criterion as only two of the four parameters c, φ, σ_t, σ_c are needed to characterize the material strength. It is convenient to use the two parameters σ_c and m:

$$m = \frac{\sigma_c}{\sigma_t} = \frac{1 + \sin \varphi}{1 - \sin \varphi} \tag{2.6}$$

The fracture locus in the plane σ_1 versus σ_3 obtained from equation (2.4) is an irregular hexagon. Its shape depends on the friction angle φ or on the ratio m. When $\sigma_c = \sigma_t$, i.e., when $\varphi = 0$ and $m = 1$, the hexagon coincides with that of Tresca's criterion. Note that the friction coefficient μ increases with m, Figure 2.3.

Griffith's hoop stress criterion. Griffith [1] in 1924 attributed the considerably lower strength of brittle materials to the existence of inherent microcracks. These stress raisers lead to crack growth and the eventual failure of the body as a result of macrocracking. He used the maximum hoop stress σ_η along the contour of the elliptic crack in Figure 2.4 as the criterion of failure [1]:

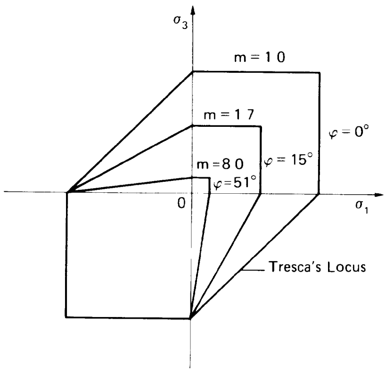

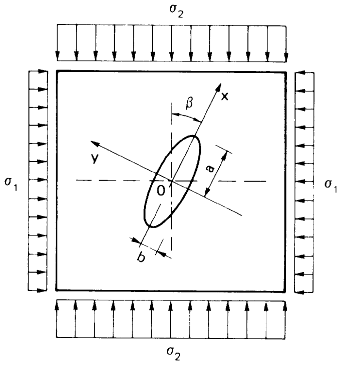

Fig. 2.3. Mohr–Coulomb fracture locus in the plane of the extreme principal stresses.
Fig. 2.4. Elliptic crack in an infinite slab subjected to a biaxial compressive loading condition.

$$\sigma_\eta = \frac{1}{2\xi_0}\,[(\sigma_1+\sigma_2)-(\sigma_1-\sigma_2)\cos 2\beta]$$

$$\pm\,\{\tfrac{1}{2}\,[(\sigma_1^2+\sigma_2^2)-(\sigma_1^2-\sigma_2^2)\cos 2\beta]\}^{1/2} \qquad (2.7)$$

The critical orientation β_{cr}, for which we have the maximum stress among the maximum stresses related to the various orientations, can be found by differentiating equation (2.7) with respect to β and by setting the result equal to zero:

$$\cos 2\beta_{cr} = \frac{\sigma_1-\sigma_2}{2(\sigma_1+\sigma_2)} \qquad (2.8)$$

The elliptical coordinate ξ_0 in equation (2.7) is related to the semiaxes a and b of the ellipse in Figure 2.4:

$$(a^2-b^2)\cosh\xi_0 = a \qquad (2.9)$$

Equation (2.8) is valid only when $(\sigma_2/\sigma_1) \geqslant -\frac{1}{3}$ or $(\sigma_1/\sigma_2) \geqslant -\frac{1}{3}$. Otherwise, the solution is $\beta = 0$ or $\beta = \pi/2$ depending on the stress ratio. Substituting equation (2.8) into (2.7) the results is

$$(\sigma_\eta)_{\max} = -\frac{(\sigma_1-\sigma_2)^2}{4\xi_0(\sigma_1+\sigma_2)} \qquad (2.10)$$

where $(\sigma_\eta)_{\max}$ is the maximum tensile stress along the elliptic contours.

Suppose that many elliptic cracks are randomly oriented and that σ_{th}

denotes the theoretical strength at the edge of the most vulnerable crack. Then, equation (2.10) may be set equal to σ_{th} at incipient fracture:

$$\sigma_{th} = -\frac{(\sigma_1 - \sigma_2)^2}{4\xi_0(\sigma_1 + \sigma_2)} \tag{2.11}$$

On the other hand, if the slab is subjected to uniaxial tensile stress with $\sigma_2 < 0$ and $\sigma_1 = 0$, then equation (2.7) becomes

$$\sigma_\eta = \frac{\sigma_2}{\xi_0}\left\{\tfrac{1}{2}(1 + \cos 2\beta) \pm [\tfrac{1}{2}(1 + \cos 2\beta)]^{1/2}\right\} \tag{2.12}$$

Differentiating σ_η with respect to β and setting the result equal to zero, it is possible to obtain the solution $\beta = 0$ with the maximum hoop stress given by

$$(\sigma_\eta)_{\max} = \frac{2\sigma_2}{\xi_0} \tag{2.13}$$

The allowable applied stress σ_{cr} can thus be obtained by letting $(\sigma_\eta)_{\max} = \sigma_{th}$, i.e.,

$$\sigma_{cr} = -\frac{\sigma_{th}\xi_0}{2} \tag{2.14}$$

Combining equations (2.11) and (2.14), it is found that

$$\frac{(\sigma_1 - \sigma_2)^2}{(\sigma_1 + \sigma_2)} = 8\sigma_{cr} \tag{2.15}$$

In the special case of uniaxial compression, equation (2.15) yields a compressive strength equal to eight times the tensile strength σ_{cr}. The condition in equation (2.15) is valid only for $(\sigma_2/\sigma_1) \geqslant -\frac{1}{3}$ and $(\sigma_1/\sigma_2) \geqslant -\frac{1}{3}$. The fracture locus of equation (2.15) is displayed in Figure 2.5. The Mohr–Coulomb criterion also gives a ratio of $\sigma_c/\sigma_t = 8.0$ when $\varphi \simeq 51°$ in equation (2.6).

Griffith cracks with friction. McClintock and Walsh [2] proposed the idea that narrow elliptical cracks can close. This gives rise to shear stress on the crack due to friction that tends to increase the strength because of the reduction of stress concentration at the ends of the crack. Let the normal stress on the crack surface be σ_ξ which is assumed to be a function of only the applied stress normal to the crack, σ_β. When the applied stress σ_β reaches some critical compressive value σ_{cr}^*, the crack closes at the ends. A further

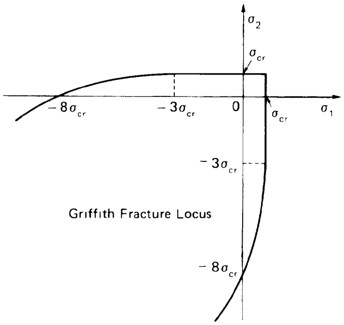

Fig. 2.5. Griffith fracture locus in the plane of the principal stresses.

increase in σ_β causes a corresponding increase in σ_ξ. Hence, a relationship between the compressions σ_β and σ_ξ can be established:

$$\sigma_\xi = 0, \qquad \text{for } \sigma_\beta \leqslant \sigma_{cr}^* \tag{2.16a}$$

$$\sigma_\xi = \sigma_\beta - \sigma_{cr}^* \qquad \text{for } \sigma_\beta \geqslant \sigma_{cr}^* \tag{2.16b}$$

The frictional shear stress, τ_f, is obtained by assuming that a frictional stress must be overcome to activate crack growth, i.e.,

$$\tau_f = \mu\sigma_\xi \tag{2.17}$$

The modified condition of incipient fracture is therefore

$$\sigma_1[(1+\mu^2)^{1/2} - \mu] - \sigma_2[(1+\mu^2)^{1/2} + \mu] = 4\sigma_{cr}\left(1 + \frac{\sigma_{cr}^*}{\sigma_{cr}}\right)^{1/2} - 2\mu\sigma_{cr}^* \tag{2.18}$$

where σ_{cr} refers to the critical applied stress in the absence of friction effects. From equation (2.18), the ratio m of compressive to tensile strength is obtained

$$m = \frac{\sigma_c}{\sigma_t} = \frac{4\left(1 + \frac{\sigma_{cr}^*}{\sigma_{cr}}\right)^{1/2} - 2\mu\sigma_{cr}^*}{(1+\mu^2)^{1/2} - \mu} \tag{2.19}$$

Since $\sigma_{cr}^* \simeq 0$, when $\mu \simeq 1$, it follows that $\sigma_c \simeq 10\sigma_t$. For friction angles between 45° and 50°, this result is in agreement with that by Griffith. The

McClintock and Walsh's hoop stress elliptical crack model, however, cannot be used to explain the behavior of a line crack because it makes use of the linear theory of elasticity that does not account for large rotation at the point where the maximum hoop stress criterion is applied. Figure 2.6 shows that the tangent line undergoes a 90° rotation when the ellipse shrinks to a line crack.

A more realistic explanation of the large discrepancies of compressive and tensile strength of brittle materials has been given by Sih [3, 4] based on the strain energy density criterion. He showed that σ_c/σ_t can vary from 10 to 10^3 depending on the relative orientations of the flaws with reference to the uniaxial tensile and compressive stress. Unless flaw orientations are considered, the test data on the failure of brittle materials can involve large scatters, particularly the measurement of σ_c and σ_t.

Stress intensity factors. Instead of using the stress on the elliptical crack boundary as the criterion of incipient fracture, the stress intensity factor concept for a line crack ($b = 0$ in Figure 2.4) may be adopted. Let K_I^* and K_{II}^* denote the dimensionless stress intensity factors corresponding to Mode I and II crack extension. They are defined as

$$K_I^* = \frac{\sigma_\beta\sqrt{\pi a}}{K_{IC}} \tag{2.20a}$$

$$K_{II}^* = \frac{\tau_\beta\sqrt{\pi a}}{K_{IC}} \tag{2.20b}$$

in which σ_β and τ_β can be related to a uniaxial stress state defined as $\sigma_1 = 0$ and $\sigma_2 = \sigma_{cr}$, Figure 2.7, i.e.,

$$\sigma_\beta = \frac{\sigma_{cr}}{2}(1 - \cos 2\beta) \tag{2.21a}$$

$$\tau_\beta = \frac{\sigma_{cr}}{2}\sin 2\beta \tag{2.21b}$$

When both K_I^* and K_{II}^* are present, the direction of crack initiation is not

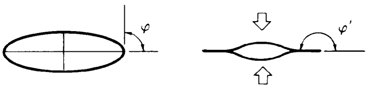

(a) (b)

Fig. 2.6. Large rotation after shrinking of the elliptic crack.

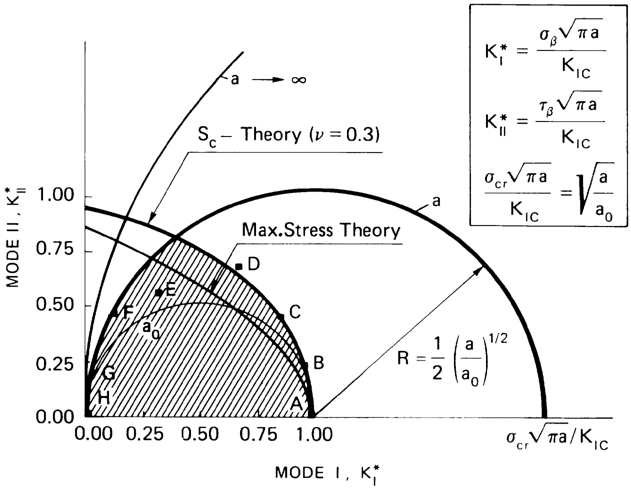

Fig. 2.7. Fracture loci in the plane of the dimensionless stress-intensity factors.

known ahead of time. The strain energy density theory* in [5, 6] or the S_c-theory can be most conveniently applied in this case. Plotted in Figure 2.7 are the K_I^* versus K_{II}^* curves predicted by the S_c-theory for $\nu = 0.3$ and data of PMMA plates [7] with $K_{IC} = 9.3\,\text{kg/mm}^{3/2}$. Agreement is seen with the data points $A, B, \ldots, D$ for large β while the points $E, F, \ldots, H$ had an opposite trend corresponding to small β. Such a deviation is due to the inadequacy of the single crack model** that cannot account for the change in nonhomogeneity of the system due to the interaction of load with the presence of microcracks in PMMA as β is reduced. It should be remembered that the stress intensity factor concept is limited to linear elastic behavior and cannot be applied to explain the data points $E, F, \ldots, H$ in Figure 2.7 where nonlinearity effects cannot be neglected.

Fictitious macrocrack model. A fictitious macrocrack of length $2a_0$ will be assumed to model the multitude of randomly oriented and distributed microcracks. A schematic of the model is shown in Figure 2.8(a) where a state of biaxial tension is considered. The situation in Figure 2.8(b) represents

---

* Other criteria such as the maximum normal stress, energy release rate, etc., are fundamentally unsound although they may yield predictions that do not deviate significantly from experiments for specific problems. They do become problematic in general and cannot be conveniently applied to all materials, loading conditions and component geometries.

** Different results will be predicted by the strain energy density theory if the stress analysis were to include the effects of material nonlinearity and the presence of many cracks oriented and located at different positions.

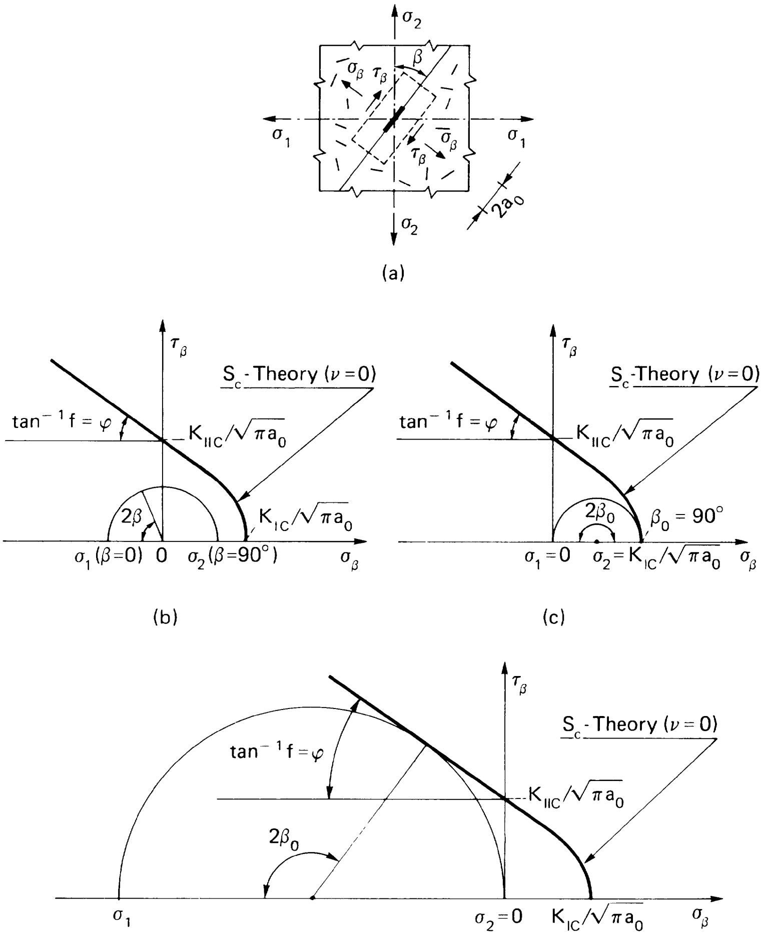

Fig. 2.8. Fracture envelopes in the Mohr's plane, σ_β versus τ_β, related to the condition of incipient micro-cracking.

all the possible stress states (σ_β, τ_β) that do not result in crack propagation. Fracture occurring in a direction normal to σ_β with $\tau_\beta = 0$ at $\beta_0 = 90°$ is shown in Figure 2.8(c) while Figure 2.8(d) pertains to uniaxial fracture under compression for the fictitious crack inclined at an angle 90°–(φ/2).

By neglecting the effect of σ_2 and assuming that σ_1 and σ_3 are respectively the maximum and minimum principal stresses, the model can be applied to three dimensional stress states even though only K_I and K_{II} are used. Frictional effects may also be included by assuming that crack propagation occurs when [8]

$$\tau_\beta - \mu|\sigma_\beta| = \frac{K_{IIC}}{\sqrt{\pi a_0}} \tag{2.22}$$

or

$$|K_{II}| = K_{IIC} + \mu|K_I|, \qquad \text{for } K_I < 0 \tag{2.23}$$

Figure 2.9 gives a plot of σ_1 versus σ_3 for four different values of the angle of friction between the crack surfaces. The concavity of the envelope in the τ_β versus σ_β plane is equivalent to the concavity of the σ_1 versus σ_3 locus in the tension-compression quadrants. Such a concavity is similar to that of the Drucker Postulate [9]. Considered here is the effect of friction-resistant materials. Several authors have observed this concavity in biaxial experimental investigations on concrete specimens [10, 11]. Their results can be explained by application of the Strain Energy Density Theory [5, 6] for $\sigma_\beta > 0$ and including the friction effects for $\sigma_\beta < 0$ [8]. In Figures 2.10 and 2.11, it is evident that by increasing the ratio of compressive to tensile strength, the concavity of the experimental locus becomes more pronounced. This can be theoretically explained by observing the trend of the loci reported in Figure 2.9. The concavity of the envelope tends to increase as the ratio of compressive

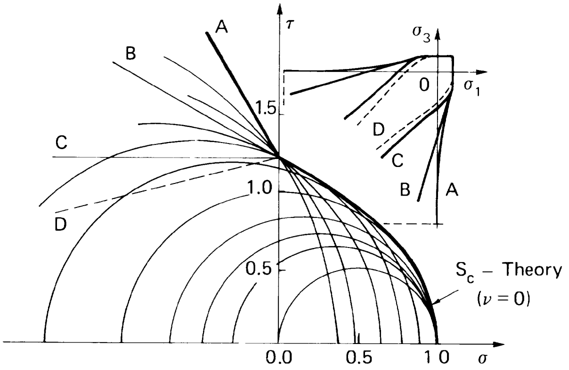

Fig. 2.9. Fracture envelopes for four different values of the angle of friction between the crack surfaces.

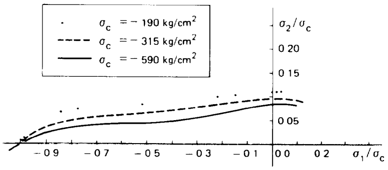

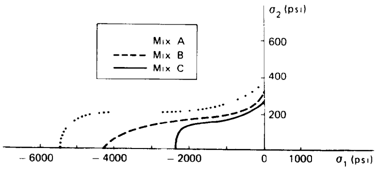

Fig. 2.10. Experimental fracture loci in the tension-compression quadrant [10].
Fig. 2.11. Experimental fracture loci in the tension-compression quadrant [11].

to tensile strength is increased provided that the fracture criterion applied for $\sigma_\beta \geqslant 0$ is always the same. The Strain Energy Density Theory, for $\nu = 0$, seems to agree accurately with the experimental results.

2.2. Statistical theories

It is well-known that all materials contain inherent flaws. Their distribution is not deterministic and can be treated in a statistical fashion. In what follows, some elementary notion of the probabilistic approach for predicting the strength of materials will be considered.

Probability density and cumulative distribution. For a ductile material, the variability in strength of nominally identical specimens is generally not more than 4 to 8% of its mean strength, while in a brittle material the variation can be as high as 100% of the mean strength. Moreover, brittle material behavior is sensitive to changes in the specimen size*. Considered will be the *weakest link concept* of Weibull [12] which assumes that the probability of finding a critical imperfection in a given material tends to increase with the volume.

To start with, consider the bell-shaped curve in Figure 2.12 that represents the *probability density*, p, of the random quantity X. It means that the probability of obtaining a value of such a quantity included between x and $x + \mathrm{d}x$ is equal to $p(x)\mathrm{d}x$. If x_1 and x_2 are the extremes of the interval where it is possible to find the X value, we have

$$\int_{x_1}^{x_2} p(x)\mathrm{d}x = 1 \tag{2.24}$$

The mean value of the distribution $p(x)$ is defined as follows:

$$\bar{x} = \frac{\int_{x_1}^{x_2} xp(x)\mathrm{d}x}{\int_{x_1}^{x_2} p(x)\mathrm{d}x} = \int_{x_1}^{x_2} xp(x)\mathrm{d}x \tag{2.25}$$

The product, $p(x)\mathrm{d}x$, represents the area, $\mathrm{d}A$, of the elementary rectangle of Figure 2.12. Hence,

$$\bar{x} = \frac{\int_A x\mathrm{d}A}{\int_A \mathrm{d}A} = \frac{S_y}{A} = x_G \tag{2.26}$$

where A is the area included between the curve $p(x)$ and the X-axis, S_y the

---

* Such effect can be explained by the joined application of Fracture Mechanics and Statistics. This will be considered in detail in chapter 8.

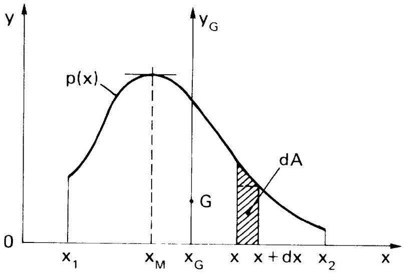

Fig. 2.12. Probability density function.

statical moment of this area with respect to the Y-axis and x_G the abscissa of the centroid of area A.

In the same way, it is possible to prove that the standard deviation, Σ, is equal to the radius of inertia of area A with respect to the Y_G-axis, Figure 2.12:

$$\Sigma^2 = \int_{x_1}^{x_2} (x - \bar{x})^2 p(x) \mathrm{d}x \tag{2.27}$$

The *cumulative distribution* in Figure 2.13 is the probability that the variable, X, is less than or equal to some given value x:

$$P(x) = \text{probability } (X \leqslant x) \tag{2.28}$$

With reference to Figure 2.12, it is the area under the curve $p(x)$, between x_1 and x, i.e.,

$$P(x) = \int_{x_1}^{x} p(x) \mathrm{d}x \tag{2.29}$$

The cumulative distribution is thus the integral function of the probability

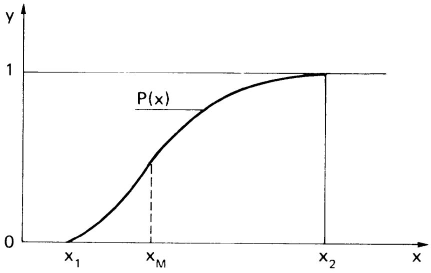

Fig. 2.13. Cumulative distribution related to Figure 2.12.

density, so that the probability density is the derivative of the cumulative distribution given by

$$p(x) = \frac{\mathrm{d}P}{\mathrm{d}x} \tag{2.30}$$

Weibull's theory. In the Weibull analysis, the material is considered to be statistically isotropic and homogeneous. The idea of the 'weakest link of a chain' is then adopted which is contrary to the concept that the failure of one element causes redistribution of load among the other elements, with total failure taking place only when the entire system is no longer capable of bearing load.

Let $P_1(\sigma)$ be the cumulative distribution of probability of failure by stress σ for one link. Therefore the probability of survival at σ for one link is equal to $[1-P_1(\sigma)]$. For an entire chain of N links, the probability of failure based on the weakest link concept is

$$P_N(\sigma) = 1-[1-P_1(\sigma)]^N \tag{2.31}$$

With the knowledge that

$$\lim_{n\to\infty}\left(1-\frac{x}{n}\right)^n = \exp(-x) \tag{2.32}$$

equation (2.31) can be approximated as

$$1-P_N(\sigma) = \exp[-NP_1(\sigma)] \tag{2.33}$$

Since the number of links, N, is proportional to the volume, V, the probability of failure can be expressed as

$$P_f = 1-\exp[-V\Phi(\sigma)] \tag{2.34}$$

where $V\Phi(\sigma) = NP_1(\sigma)$. In equation (2.34), $\Phi(\sigma)$ is an unknown function and Weibull assumed an empirical form for this function given by

$$\Phi(\sigma) = \left(\frac{\sigma-\sigma_u}{\sigma_0}\right)^m, \qquad \text{for } \sigma > \sigma_u \tag{2.35a}$$

and

$$\Phi(\sigma) = 0, \qquad \text{for } \sigma \leqslant \sigma_u \tag{2.35b}$$

where σ_u is the stress at which there is no probability of failure and is called the 'threshold stress'. The quantity σ_0 is a normalizing factor and m is a material parameter or the *Weibull modulus.* If the threshold stress is assumed to be zero, the probability of failure by a uniaxial tensile stress σ in the cumulative distribution form is

$$P_f = 1 - \exp\left[-V\left(\frac{\sigma}{\sigma_0}\right)^m\right] \tag{2.36}$$

The mean strength can then be obtained by using the probability of failure in the probability density form

$$\bar{\sigma}_f = \int_0^\infty \sigma \frac{\mathrm{d}P_f}{\mathrm{d}\sigma}\mathrm{d}\sigma = \int_0^1 \sigma \mathrm{d}P_f \tag{2.37}$$

If the probability of survival P_s is equal to $(1 - P_f)$, it can be seen from Figure 2.14 that

$$\bar{\sigma}_f = \int_0^\infty P_s \mathrm{d}\sigma \tag{2.38}$$

Therefore

$$\bar{\sigma}_f = \int_0^\infty \exp\left[-V\left(\frac{\sigma}{\sigma_0}\right)^m\right]\mathrm{d}\sigma = \frac{\sigma_0}{V^{1/m}}\Gamma\left(1+\frac{1}{m}\right) \tag{2.39}$$

where Γ is the 'Gamma-function' defined as

$$\Gamma(z) = \int_0^\infty t^{z-1}\mathrm{e}^{-t}\mathrm{d}t$$

Equation (2.36) can be modified to include the stress variation due to non-uniform uniaxial stress field as follows:

$$P_f = 1 - \exp\left[-\int_V\left(\frac{\sigma}{\sigma_0}\right)^m \mathrm{d}V\right] \tag{2.40}$$

For the three point bending specimen in Figure 2.15, the longitudinal stresses σ are different at different points of the beam and hence

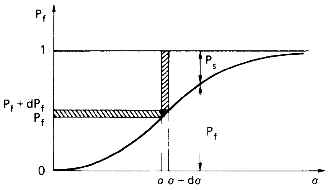

Fig. 2.14. Cumulative distribution of the probability of failure.

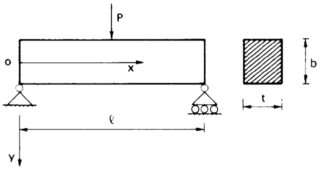

Fig. 2.15. Three point bending specimen.

$$P_f = 1 - \exp\left[-2t\left(\frac{\sigma_{\max}}{\sigma_0}\right)^m \int_0^{l/2}\int_0^{b/2}\left(\frac{4xy}{lb}\right)^m \mathrm{d}x\,\mathrm{d}y\right] \tag{2.41}$$

where $\sigma_{\max}$ is the maximum stress occurring at the bottom fiber. Integrating the above equation and using equation (2.38), it is found that

$$\bar{\sigma}_f = \frac{\sigma_0}{V^{1/m}}\,\Gamma\left(1 + \frac{1}{m}\right)[2(m+1)^2]^{1/m} \tag{2.42}$$

The above expression is similar to equation (2.39). The only difference is the factor: $f(m) = [2(m+1)^2]^{1/m}$. For any flexural loading system [13], $\bar{\sigma}_f$ takes the form

$$\bar{\sigma}_f = \frac{\sigma_0}{V^{1/m}}\,\Gamma\left(1 + \frac{1}{m}\right)f(m) \tag{2.43}$$

where f is a function of m alone and depends on the particular loading system. Equation (2.43) can be put into the logarithmic form:

$$\ln \bar{\sigma}_f = \ln\left[\sigma_0\Gamma\left(1 + \frac{1}{m}\right)f(m)\right] - \frac{1}{m}\ln V \tag{2.44}$$

It follows from equation (2.44) that the average strength decreases when the specimen volume is increased. Equation (2.36) can also be put into the logarithmic form

$$\ln \ln \left(\frac{1}{1-P_f}\right) = \ln \frac{V}{\sigma_0^m} + m \ln \sigma \tag{2.45}$$

Both equations (2.44) and (2.45) are useful for the experimental determination of the Weibull modulus, m. The former can be applied only when a set of specimens of different size are tested while the latter can be utilized with a set of identical specimens as illustrated by the straight line plot in Figure 2.16 [14]. The physical meaning of the Weibull modulus, m, will be discussed in chapter 8.

Safety factor. The factor of safety, $\bar{s}$, is defined as the ratio of the mean strength to the strength at a given probability of failure:

$$\bar{s} = \bar{\sigma}_f/\sigma_f \tag{2.46}$$

From equations (2.36) and (2.43), an alternative form for P_f can be obtained:

$$P_f = 1 - \exp\left\{-\left[\Gamma\left(1+\frac{1}{m}\right) f(m)\right]^m \left(\frac{\sigma_f}{\bar{\sigma}_f}\right)^m\right\} \tag{2.47}$$

From equation (2.46) it follows that

$$P_f = 1 - \exp\left\{-\left[\Gamma\left(1+\frac{1}{m}\right) f(m) \frac{1}{\bar{s}}\right]^m\right\} \tag{2.48}$$

Since $P_f = 1 - P_s$, the above equation leads to

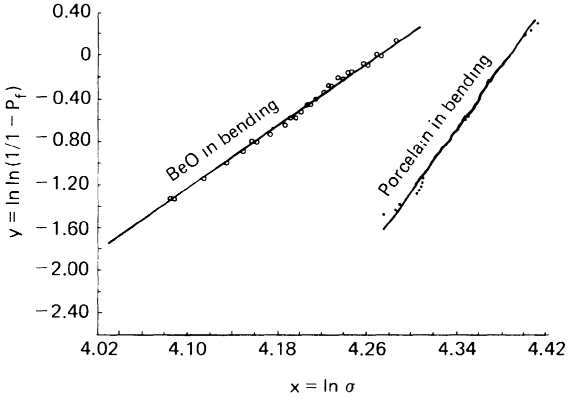

Fig. 2.16. Experimental plots related to equation (2.45) [14].

$$\bar{s} = \frac{\Gamma\left(1 + \frac{1}{m}\right) f(m)}{\left[\ln \frac{1}{P_s}\right]^{1/m}} \tag{2.49}$$

The safety factor is independent of the volume of the structural element. It is only a function of the probability of survival and of the Weibull modulus. Figure 2.17 shows that $\bar{s}$ tends to 1 for large values of m. This means that materials with high values of m are safer than those with low values of m. The Weibull modulus will be shown in chapter 8 to depend on the shape and the size-distribution of micro-defects, as well as on the ductility of the material.

2.3. Mechanical damage and strain-softening behavior of concrete

The mechanical damage of concrete-like materials tends to decrease load carrying capacity and stiffness of the material. These two effects can be described together by considering strain-softening. Let the specimen in Figure 2.18(a) be subjected to cyclic compression. The stress-strain diagram is given in Figure 2.18(b). The Young's modulus and the maximum bearable stress decrease with increasing the number of loading cycles. The σ versus ϵ envelope describes the strain-softening behavior of the material. The same behavior can be found even if a concrete specimen is tested in tension with monotonic strain variation by using a strain-controlled testing machine. It is important to emphasize that the permanent plastic deformations in

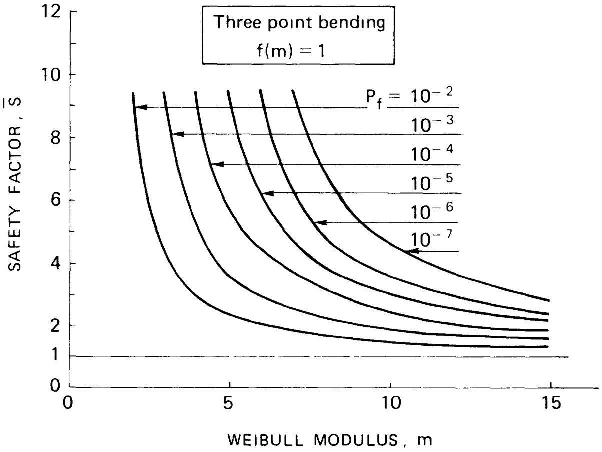

Fig. 2.17. Variation of safety factor with Weibull modulus for the three point bending specimen.

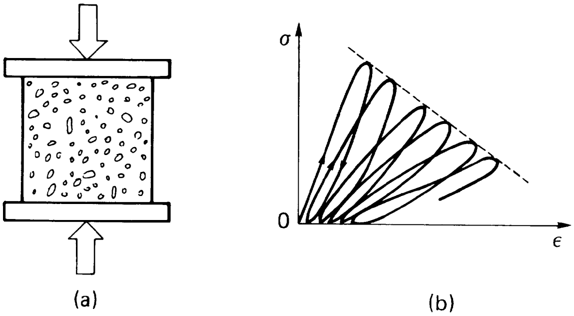

Fig. 2.18. Concrete specimen (a) subjected to repeated compression (b).

concrete-like materials are relatively small so that unloading can be assumed to return to the origin.

Several authors have considered damage theories without considering the orientation of preexisting and new developing microcracks. More recently, Krajcinovic and Fonseca [15] have considered damage as a multitude of flat, plane microcracks. The shape of the microcracks turns out to be of little significance while the crack density played an important role. Their results correlated well with experiments [16].

Delameter, Herrmann and Barnett [17] considered an infinite elastic solid containing a doubly periodic rectangular array of slit-like cracks shown in Figure 2.19 subjected to a uniform stress. A state of plane strain was assumed. The cracks were represented as suitable distributions of dislocations determined from a singular integral equation. The computation of the change in strain energy due to the presence of the cracks led to the determination of effective elastic constants. The cracked sheet behaved as an orthotropic solid. The effective Young's modulus orthogonal to the cracks is given in Figure 2.20 as a function of the crack spacing in both the x and y directions.

The mechanical damage, i.e., the decrease in Young's modulus, is related to the strain-softening material behavior as well as to the smeared microcracking. On the other hand, it can also be included in a fracture mechanics description of macrocrack growth. Near the tip of a crack, in fact, the stress concentration produces a degradation of the local elastic modulus and this material damage interacts with the crack growth process. The decrease in the elastic modulus leads to a stress relaxation at the crack tip. This can be associated with the strain energy density absorbed locally and dissipated nonuniformly for each increment of crack growth. A finite element analysis of this damage process coupled with the strain energy density criterion will be applied in the subsequent chapters.

Damage and strain-softening. Decrease in elastic modulus and load relaxation at the crack tip are closely connected. As proposed by Janson and Hult

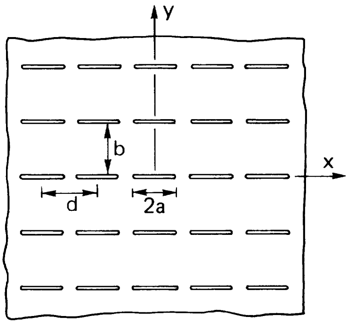

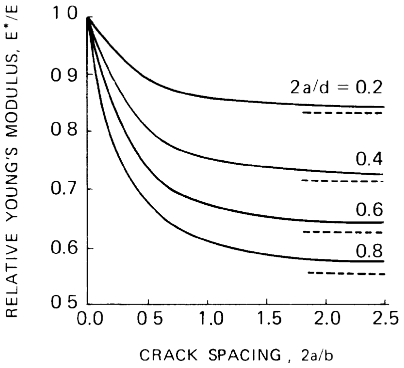

Fig. 2.19. Infinite elastic sheet containing a doubly periodic rectangular array of slit-like cracks.

Fig. 2.20. Effective Young's modulus orthogonal to the cracks as a function of the crack spacing.

[18–20], they can be jointly described through a simple analytical model that consists of a sheet containing a crack and loaded in Mode I. The material is assumed to exhibit time-independent continuous damage when loaded and damage affects only the stress in a narrow region ahead of the crack corresponding to the Dugdale zone [21]. The stress field in the crack tip region is approximated as uniaxial so that a simple analysis can be performed. Let P be the transmitted load, A the macroscopic area and A_{eff} the microscopically load carrying area. Broberg [22] defined $\sigma = P/A$, $\sigma_{\mathrm{eff}} = P/A_{\mathrm{eff}}$ and

$$\omega = \ln (A/A_{\mathrm{eff}}) \tag{2.50}$$

For small ω, the Kachanov definition [23] gives

$$\omega = \frac{A - A_{\mathrm{eff}}}{A} \tag{2.51}$$

The relation

$$\sigma = \sigma_{\mathrm{eff}} \exp(-\omega) \tag{2.52}$$

can thus be established. Assuming that damage depends on strain according to a power relation, then

$$\omega = K\epsilon^m \tag{2.53}$$

Alternatively, damage can also be defined in terms of the local decrease in elastic modulus:

$$\omega = \ln (E/E_{\text{eff}}) \tag{2.54}$$

From equations (2.53) and (2.54), it is seen that

$$E_{\text{eff}} = E \exp(-K\epsilon^m) \tag{2.55}$$

and hence

$$\sigma = E_{\text{eff}}\epsilon = E\epsilon \exp(-K\epsilon^m) \tag{2.56}$$

Near the crack tip where the strain is very high, the stress is assumed to vanish:

$$\lim_{\epsilon\to\infty} \sigma = \lim_{\epsilon\to\infty} E\epsilon \exp(-K\epsilon^m) = 0 \tag{2.57}$$

The above model therefore yields a strain-softening behavior, Figure 2.21.

Assume that damage does not alter the strain distribution around the crack. The relation

$$\sigma_{\text{eff}} = E\epsilon \tag{2.58}$$

holds such that σ_{eff} and ϵ vary as $r^{-1/2}$ and the damage parameter ω as $r^{-m/2}$ where r is the distance from the crack tip. Close to the crack tip, equation (2.56) yields

$$\sigma \propto r^{-1/2} \exp(-Kr^{-m/2}) \tag{2.59}$$

A zone can be identified close to the crack tip, within which the stress σ decreases while σ_{eff}, ϵ and ω increase.

Later on, a more refined model similar to that of Janson and Hult [18–20] will be presented. Damage will be assumed to depend on the absorbed strain energy density and not on the uniaxial strain ϵ as in equation (2.53). The Kachanov ratio ω in equation (2.51), however, will be shown to have the unit

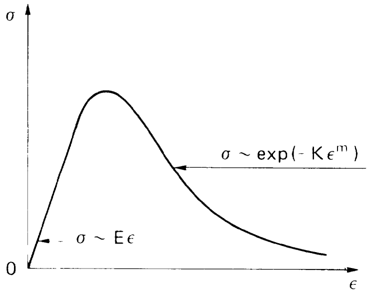

Fig. 2.21. Strain-softening constitutive behavior.

value when the strain energy density in a unit volume of material reaches the critical value, $(\mathrm{d}W/\mathrm{d}V)_c$. This corresponds to the elastic modulus being zero and the material can no longer carry any load. The slow crack growth process will also be addressed as in the works of [24–26].

Damage and fracture. It is possible to associate damage with crack formation and propagation by assuming that a strain localization [27, 28] occurs and a stress-displacement law governs the mechanical behavior of the body. More precisely, when a concrete specimen is tested in uniaxial tension, damage is assumed to occur in the ***fracture zone***, Figure 2.22, as the strain ϵ exceeds the strain capacity, ϵ_u. Bazant and Oh [29] showed that such a zone has a characteristic constant width w_0, so that the opening w of the fracture zone can be expressed by the product

$$w = w_0 \epsilon_d \tag{2.60}$$

where ϵ_d is the strain within the damage zone. Using equation (2.60), it is possible to transform the strain localization theory into that based on cohesive force. The only necessary assumption is that the fracture zone width, w_0, is actually a material constant. This was shown for the case of concrete by Bazant and Oh [29]. A very extensive statistical investigation showed that w_0 is about three times the maximum aggregate size.

By observing tensile tests on concrete specimens, it is possible to assert that the damage zone becomes more and more localized as the loading capacity decreases. While the material within the fracture zone softens, Figure 2.22, the stress and strain outside the fracture zone still behave in a proportional manner. As a result, strains accumulate in the fracture zone while the remaining part of the body unloads itself. Hillerborg, Modeer and Petersson [30] assumed that the original width of the fracture zone is equal

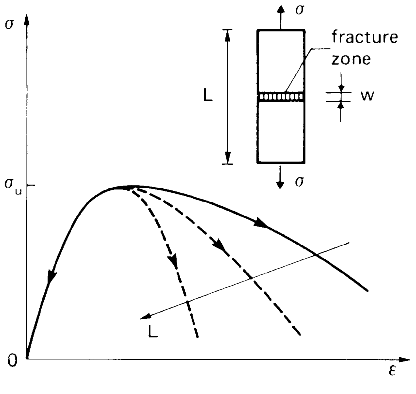

Fig. 2.22. Localization of the fracture zone.

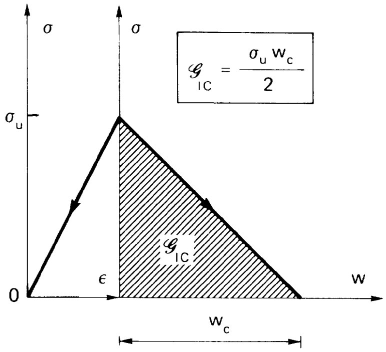

Fig. 2.23. Stress-strain and stress-displacement constitutive laws.

to zero. It is different from zero only during the stage when it is being developed. Stress at the softening stage will, therefore, be a function of this width, w, Figure 2.23. This simple hypothesis explains the size effects for the descending branch of the global σ versus ϵ curve which appears to vary with specimen size [31] as shown in Figure 2.22. Another remarkable consequence of this hypothesis is that it is possible to have similarity in the physical fracture behavior only when the value w_c of total stress relaxation is proportional to the structural size, L. In this case, the fracture energy $G_{IC} = \sigma_u w_c/2$, is proportional to L, Figure 2.23, and the global collapse dilatation, $\epsilon_c \simeq w_c/L$, is constant as the size L is varied.

The change of the abscissa as the unstable stage begins, Figure 2.23, is important and will be discussed in more detail subsequently. The dilatation is a dimensionless quantity, while the width w of the fracture zone has the dimension of length, $[L]$. Size (or scale) effects in Fracture Mechanics originate from this transition. The area under the σ versus ϵ curve represents the energy dissipated per unit volume, thus having the physical dimension of stress, $[F]\,[L]^{-2}$. It is well-known that the classical strength criteria such as those advanced by Beltrami using the strain energy density and von Mises using the distortion energy density, are equivalent to imposing limits on certain stress quantity. On the other hand, the area under a σ versus w curve, Figure 2.23, represents the energy dissipated per unit area, thus having the dimensions of surface energy, $[F]\,[L]^{-1}$.

Several authors have assumed a crack propagation model similar to that by Hillerborg, Modeer and Petersson [30, 32]. Gerstle, Ingraffea and Gergely [33] generalized the Fictitious Crack Model by Hillerborg to mixed mode crack problems and considered both normal and shear stresses on the crack surface as functions of both discontinuities in normal and tangential displacements. Bazant and Oh [29] transformed the σ versus w descending law into a σ versus ϵ softening law. They simply divided the crack opening displacement w by using the characteristic width w_0 of the crack band that forms the fracture process zone. Wecharatana and Shah [34] showed that the value w_c of the critical crack opening displacement strongly affects the length of the process zone. It is, however, not sensitive to the shape of the σ versus w diagram. Visalvanich and Naaman [35] proposed a generalized σ versus w law for fiber reinforced mortar and plain concrete that agreed with the experimental results. Gjϕrv and Lϕland [31] combined the damage model by Janson and Hult [18] with the fictitious crack model by Hillerborg, Modeer and Petersson [30].

Statistical continuous damage theory. The connection between the Continuous Damage Theory and the Statistical Strength Theories [36] will now be discussed. According to the Kachanov damage definition given in equation (2.51), the macroscopical stress is

$$\sigma = E\epsilon(1-\omega) \tag{2.61}$$

If $p_f(\sigma)$ is the failure probability density function, the damage due to the uniaxial tensile stress σ can be defined as

$$\omega = \frac{\int_0^{\sigma} p_f(\sigma)\mathrm{d}\sigma}{\int_0^{\infty} p_f(\sigma)\mathrm{d}\sigma} = P_f(\sigma) \tag{2.62}$$

where $P_f(\sigma)$ is the cumulative distribution function of the probability of failure. In the case of Weibull distribution, damage can be expressed as

$$\omega = 1-\exp\left[-\left(\frac{E\epsilon}{\sigma_0}\right)^m\right] \tag{2.63}$$

Equation (2.63) can be obtained from equation (2.36) by considering a unit volume of material. When $m = 1$ and for small values of ϵ, equation (2.63) reduces to

$$\omega = \frac{E\epsilon}{\sigma_0} \tag{2.64}$$

This corresponds to a uniform band-limited probability density of failure, Figure 2.24.

From equations (2.61) and (2.64), the softening stress-strain relationship is obtained:

$$\sigma = E\epsilon\left(1-\frac{E\epsilon}{\sigma_0}\right) \tag{2.65}$$

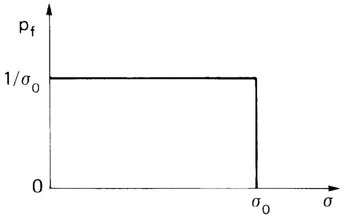

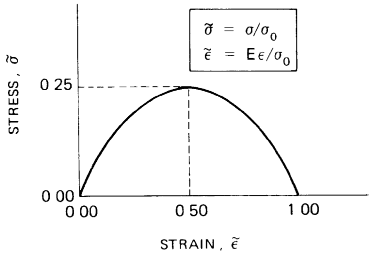

Fig. 2.24. Uniform band-limited probability density of failure.

Fig. 2.25. Softening stress-strain relation in the case of a uniform band-limited probability density of failure.

In the case of a uniform band-limited probability density $p_f(\sigma)$, this is a second degree parabola symmetric about the axis $\epsilon = \epsilon_u$, Figure 2.25. Defining failure as the inability of a tensile specimen to support additional load increments, ϵ_u is found as

$$\epsilon_u = \frac{\sigma_0}{2E} \tag{2.66}$$

In general, equations (2.61) and (2.63) yield the softening stress-strain relationship

$$\sigma = E\epsilon \exp\left[-\left(\frac{E\epsilon}{\sigma_0}\right)^m\right] \tag{2.67}$$

which is similar to equation (2.56). In this case, the ultimate strain, ϵ_u, is a function of the Weibull modulus, m. The stress-strain curves for three different values of the Weibull modulus, m, are displayed in Figure 2.26.

2.4. Strain energy density theory

Despite the large number of publications in recent years dealing with the selection of failure criteria to predict nonlinear fracture phenomena, the majority of the works have centered on specific problem areas and have not led to a better understanding of the physics of the problem. In particular, the influence of specimen geometry and slow crack growth remain as two of the most discussed topics and yet with very little understanding. A consistent method for explaining these phenomena has been developed by application of the strain energy density theory [5]. Refer to [24, 37–39] that address specimen geometry effects and to [40–42] that treat slow crack growth.

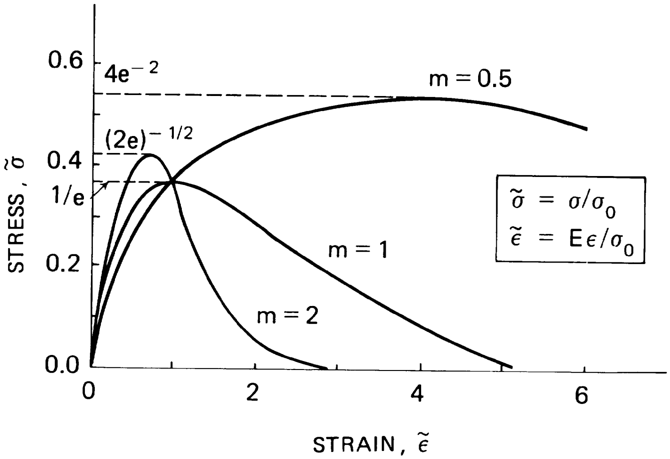

Fig. 2.26. Softening stress-strain relations by varying the Weibull modulus m.

Geometry effects and stable crack growth. By geometry effects, it is meant that the mechanical behavior of the structure can change dramatically with the structural geometry, initial crack configuration and/or structural scale. While the first two of these three effects can be analyzed by applying the traditional theory in Solid Mechanics, the last one is more difficult and can be explained only by invoking the concepts of Physical Similitude and Model Scaling [43, 44]. It is known that by keeping the shape constant and varying only the scale or size, the structure behavior can change from brittle to ductile.

Stable crack growth often occurs prior to global instability of the structure. It is different from unstable crack propagation. While the latter is a global or structural instability and may be predicted by the critical value of the strain energy density factor, S_c, the former is a local or microstructural instability and depends on the critical value of the strain energy density, $(dW/dV)_c$, a quantity that can be obtained as the area under the true stress and true strain curve. Stable crack growth may occur under both monotonic and repeated loadings. It can take place prior to or after unstable crack propagation. The fundamental laws governing the transition from slow to rapid crack propagation, and vice versa, should be very general and applicable to very simple as well as to very complicated structures so that they can be applied to extrapolate the results obtained from small specimens for predicting the behavior of large structures.

Strain energy density concept. Perhaps, one of the most general failure criteria advanced to date is the strain energy density theory. It focuses attention on the fluctuation of the energy from a unit volume of material to the next throughout a medium. The peaks and valleys of this function in mathematical terms are the stationary values. They have been shown in [37–42] to be associated with the process of material damage. The theory is based on the general assumption that *progressive material damage can be uniquely related to the rate at which energy is dissipated in a unit volume of material* [45]. Since the theory applies to any material in general, strain-softening materials are also included. A fundamental relation used is*

$$\frac{dW}{dV} = \frac{S}{r} \tag{2.68}$$

in which S is the strain energy density factor with r measured from the location of failure initiation. For the case of a line crack, failure will initiate from the tip as shown in Figure 2.27 which is surrounded by the radius r_0 of the core region. It serves as a limiting continuum length. The factor S is the area under the dW/dV versus r plot in Figure 2.27. Crack initiation occurs when dW/dV reaches a critical value, $(dW/dV)_c$.

The above concept will be incorporated into the finite element stress analysis for analyzing the failure of plain or reinforced concrete slabs subjected to tension, bending or eccentric compression. Slow crack growth prior to global instability will be calculated for each load increment. Specimen size and loading rate effects will be exhibited by the SR-Curves.

Mechanical damage and strain-softening. Material damage at the crack tip and crack growth increments will be computed by using the bilinear elastic-softening stress-strain relation in Figure 2.28. Stress may increase linearly with strain up to the point of ultimate strength, U, as shown in Figure 2.28. From there on, the strain may increase while the stress decreases down to zero at F, Figure 2.28. If the loading is relaxed at A in Figure 2.28, unloading is then assumed to occur along the line AO, so that a new loading path OAF is obtained. No permanent deformation is accounted for. There is, however, a permanent degradation of the elastic modulus. The slope of the line AO tends to decrease as the point A approaches F. When A coincides with F, the effective modulus E^* vanishes, and complete separation of the material occurs. On the other hand, when A is on the elastic branch OU, unloading occurs along the same line and no degradation of the material takes place.

The present model accounts for mechanical damage by decrease in the elastic modulus, E, as dictated by the strain energy density theory [47, 48]. For a non-damaged material element, the critical value of the strain energy

---

* For isothermal systems, dW/dV can be computed from the stress components σ_{ij} and strain components ϵ_{ij} by the expression

$$\frac{dW}{dV} = \int_0^{\epsilon_{ij}} \sigma_{ij} d\epsilon_{ij}$$

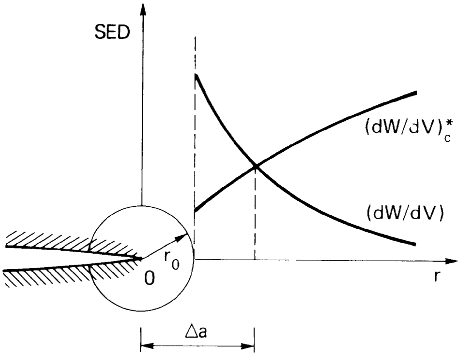

Fig. 2.27. Crack growth increment Δa according to the Strain Energy Density Theory.

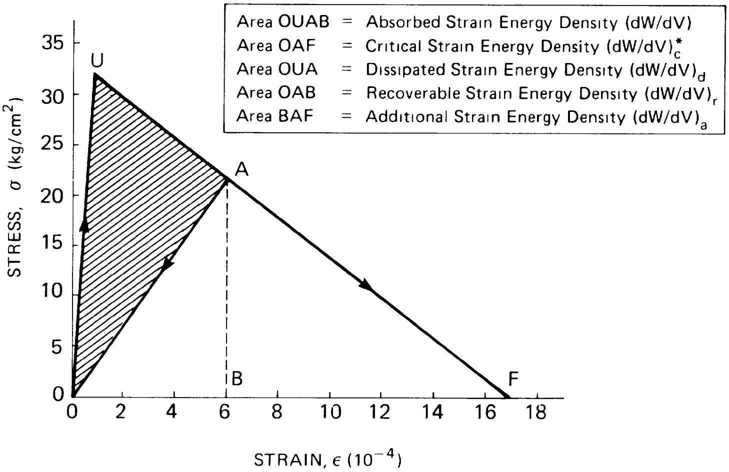

Fig. 2.28. Bilinear elastic-softening stress-strain relation.

density function, $(\mathrm{d}W/\mathrm{d}V)_c$, is equal to the area *OUF*, Figure 2.28. The material element at *A* is damaged with $(\mathrm{d}W/\mathrm{d}V)_d$ being the area *OUA* as that portion of the energy dissipated. The recoverable strain energy density, $(\mathrm{d}W/\mathrm{d}V)_r$ is the area *OAB* while *BAF* represents the additional strain energy density, $(\mathrm{d}W/\mathrm{d}V)_a$. In this way, the decreased critical strain energy density, $(\mathrm{d}W/\mathrm{d}V)_c^*$ can be expressed as

$$\left(\frac{\mathrm{d}W}{\mathrm{d}V}\right)_c^* = \left(\frac{\mathrm{d}W}{\mathrm{d}V}\right)_c - \left(\frac{\mathrm{d}W}{\mathrm{d}V}\right)_d = \left(\frac{\mathrm{d}W}{\mathrm{d}V}\right)_r + \left(\frac{\mathrm{d}W}{\mathrm{d}V}\right)_a \tag{2.69}$$

The intersection of $(\mathrm{d}W/\mathrm{d}V)_c^*$ with $(\mathrm{d}W/\mathrm{d}V)$ determines the amount of crack growth, Figure 2.27.

The above model can be extended to three-dimensional stress conditions using the current value of the absorbed strain energy density, $(\mathrm{d}W/\mathrm{d}V)$, as a measure of damage. In other words, the effective elastic modulus, E^*, and the decreased critical value of strain energy density, $(\mathrm{d}W/\mathrm{d}V)_c^*$, can be considered as functions of the absorbed strain energy density, $(\mathrm{d}W/\mathrm{d}V) = (\mathrm{d}W/\mathrm{d}V)_r + (\mathrm{d}W/\mathrm{d}V)_d$. Such functions in the uniaxial case are

$$OUAB \text{ area} \rightarrow AO \text{ slope, i.e., } \left(\frac{\mathrm{d}W}{\mathrm{d}V}\right) \rightarrow E^* \tag{2.70a}$$

$$OUAB \text{ area} \rightarrow OAF \text{ area, i.e., } \left(\frac{\mathrm{d}W}{\mathrm{d}V}\right) \rightarrow \left(\frac{\mathrm{d}W}{\mathrm{d}V}\right)_c^* \tag{2.70b}$$

Stress and strain during softening at A, Figure 2.28, can be expressed in terms of stress and strain at the ultimate and fracture conditions, i.e.,

$$\sigma = E^*\epsilon = \frac{\sigma_u \epsilon_f}{(\epsilon_f - \epsilon_u) + \dfrac{\sigma_u}{E^*}} \tag{2.71}$$

By means of equations (2.70), it is simple to express the absorbed strain energy density, $(\mathrm{d}W/\mathrm{d}V)$, and the decreased critical value, $(\mathrm{d}W/\mathrm{d}V)_c^*$, as functions of the quantities, σ_u, ϵ_u, ϵ_f, and of the effective elastic modulus, E^*:

$$\left(\frac{\mathrm{d}W}{\mathrm{d}V}\right) = \tfrac{1}{2}(\sigma\epsilon + \sigma_u\epsilon - \sigma\epsilon_u) \tag{2.72a}$$

$$\left(\frac{\mathrm{d}W}{\mathrm{d}V}\right)_r = \tfrac{1}{2}\sigma\epsilon \tag{2.72b}$$

$$\left(\frac{\mathrm{d}W}{\mathrm{d}V}\right)_d = \left(\frac{\mathrm{d}W}{\mathrm{d}V}\right) - \left(\frac{\mathrm{d}W}{\mathrm{d}V}\right)_r = \tfrac{1}{2}(\sigma_u\epsilon - \sigma\epsilon_u) \tag{2.72c}$$

$$\left(\frac{\mathrm{d}W}{\mathrm{d}V}\right)_c^* = \left(\frac{\mathrm{d}W}{\mathrm{d}V}\right)_c - \left(\frac{\mathrm{d}W}{\mathrm{d}V}\right)_d = \tfrac{1}{2}(\sigma_u\epsilon_f - \sigma_u\epsilon + \sigma\epsilon_u) \tag{2.72d}$$

The effective modulus E^* in equation (2.70a) can be discretized into 25 different values

$$E^*(n) = \frac{(26-n)}{25}E, \quad n = 1,2,\ldots,25 \tag{2.73}$$

Three different materials are considered in Figure 2.29. They have the same Young's modulus, E, the same ultimate stress, σ_u, and strain, ϵ_u while differing only in the fracture strain, ϵ_f. The 25 values of E^* and $(\mathrm{d}W/\mathrm{d}V)_c^*$ are plotted in Figures 2.30 and 2.31 as a function of the absorbed strain energy density, $(\mathrm{d}W/\mathrm{d}V)$, for three different materials. Mechanical damage of the material is thus accounted for in discrete increments. When the absorbed strain energy

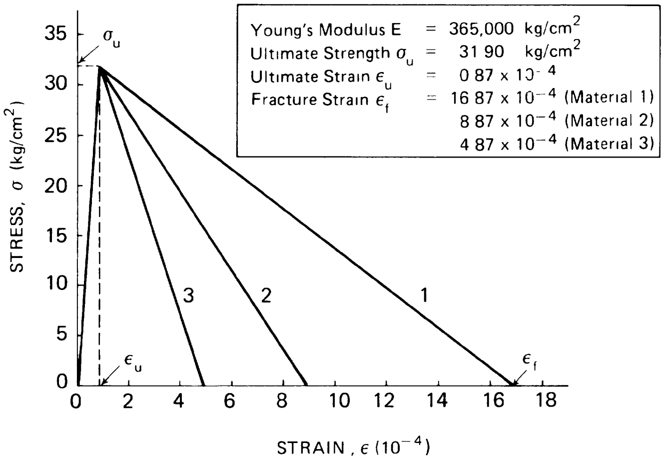

Fig. 2.29. Stress-strain curves for three different materials.

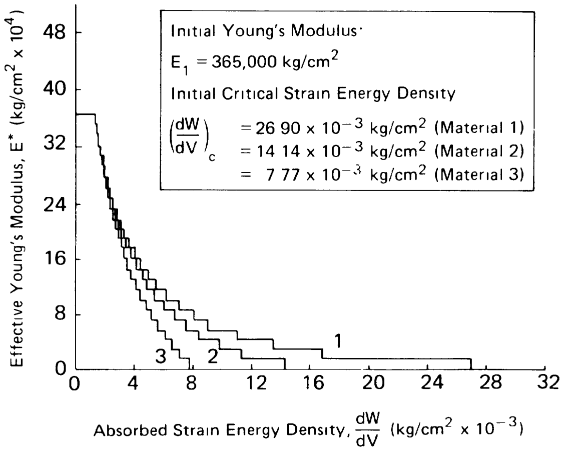

Fig. 2.30. Effective Young's modulus versus absorbed strain energy density.

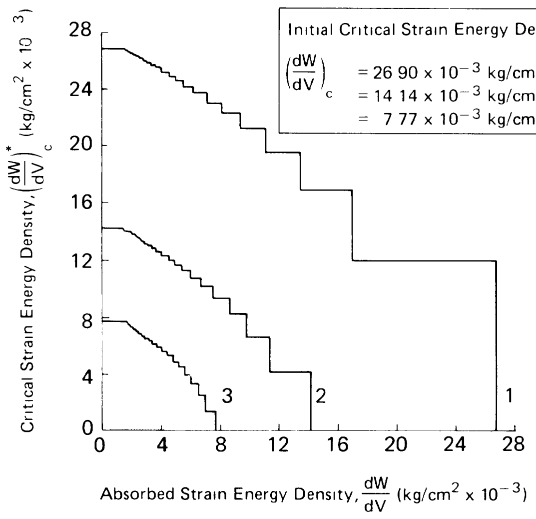

Fig. 2.31. Critical strain energy density versus absorbed strain energy density.

density is equal to the critical value, $(\mathrm{d}W/\mathrm{d}V)_c$, E^* and $(\mathrm{d}W/\mathrm{d}V)_c^*$ both vanish. Below the value $(\mathrm{d}W/\mathrm{d}V)_u = \frac{1}{2}\sigma_u\epsilon_u = 1.39 \times 10^{-3}$ kg/cm^2, damage does not occur and the elastic modulus and critical value of strain energy density correspond to their initial values.

In Table 2.1, the results for two different cases of $\Delta\epsilon = \epsilon_u/2$ and $\epsilon_u/4$ are

TABLE 2.1
Results for two different strain-controlled tensile loading simulations (Material 3 in Figure 2.29).

1st Numerical simulation ($\Delta\epsilon = \epsilon_u/2$)			
Increment $j = 1, 2,$ etc.	Stress σ_j (kg/cm^2)	Strain ϵ_j (10^{-4})	Damage material
1	31.75	0.870	1
2	22.86	1.305	14
3	22.86	1.740	17
4	19.05	2.175	20
5	3.81	2.610	25
2nd Numerical simulation ($\Delta\epsilon = \epsilon_u/4$)			
1	31.75	0.8700	1
2	28.57	1.0875	8
3	26.67	1.3050	12
4	24.45	1.5225	15
5	22.86	1.7400	17
6	22.86	1.9575	18
7	19.05	2.1750	20
8	3.49	2.3925	25

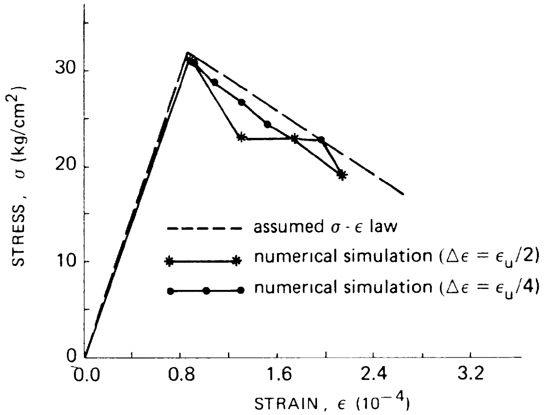

Fig. 2.32. Theoretical stress-strain variation and numerical simulations (Material 3 in Figure 2.29).

reported for Material 3 defined in Figure 2.29. The loading is strain-controlled. Progressive damage of the material is evaluated and reported for the 25 segments referred to in equation (2.73). The results are displayed in Figure 2.32 and compared with the assumed theoretical σ versus ϵ constitutive law of Material 3. It can be shown that, when the effective elastic modulus, E^*, varies continuously and the loading increment, $\Delta\epsilon$, tends to zero, the theoretical bilinear σ versus ϵ variation (dashed line of Figure 2.32) can be reproduced exactly by the numerical damage-simulation.

Slow crack growth versus fast crack propagation. In order to evaluate the crack growth increment at each loading step, the Strain Energy Density Theory will be applied, as proposed by Sih [3–5]. Subcritical crack growth is assumed to follow the condition

$$\left(\frac{\mathrm{d}W}{\mathrm{d}V}\right)_c \quad \text{or} \quad \left(\frac{\mathrm{d}W}{\mathrm{d}V}\right)_c^* = \frac{S_1}{r_1} = \frac{S_2}{r_2} = \ldots = \frac{S_j}{r_j} = \ldots = \frac{S_c}{r_c} \quad \text{or} \quad \frac{S_c^*}{r_c^*} \tag{2.74}$$

If the process leads to global instability, then the inequalities

$$S_1 < S_2 < \ldots < S_j < \ldots < S_c \text{ or } S_c^* \tag{2.75a}$$

$$r_1 < r_2 < \ldots < r_j < \ldots < r_c \text{ or } r_c^* \tag{2.75b}$$

will hold. In situations where fracture comes to arrest, the following shall apply:

$$S_1 > S_2 > \ldots > S_j > \ldots > S_0 \text{ or } S_0^* \tag{2.76a}$$

$$r_1 > r_2 > \ldots > r_j > \ldots > r_0 \text{ or } r_0^* \tag{2.76b}$$

The unstable crack growth increment is $\Delta a = r_c^*$ and crack arrest increment $\Delta a = r_0^*$. At the onset of rapid crack propagation, S_c is related to K_{IC} by equation (1.69).

References

1. Griffith, A.A., The theory of rupture, Proc. 1st Int. Congress Appl. Mech., Delft, pp. 55–93 (1924).
2. McClintock, F.A. and Walsh, J.B., Friction on Griffith cracks in rocks under pressure, Proceedings 4th National Congress Applied Mechanics, Berkeley, pp. 1015–1021 (1962).
3. Sih, G.C., Some basic problems in fracture mechanics and new concepts, J. of Engin. Fract. Mech., Vol. 5, pp. 365–377 (1973).
4. Sih, G.C., Strain energy density factor applied to mixed mode crack problems, Int. J. of Fract., Vol. 10, pp. 305–321 (1974).
5. Sih, G.C., Introductory Chapters in Mechanics of Fracture, Vol. I to VII, edited by G.C. Sih, Martinus Nijhoff Publishers, The Hague, 1973–1981.
6. Sih, G.C. and Macdonald, B., Fracture mechanics applied to engineering problems – strain energy density fracture criterion, Engineering Fracture Mechanics, 6, pp. 361–386 (1974).
7. Carpinteri, A., Crack dominante e microcracks nei materiali fragili, Giornale del Genio Civile, fasc. 1-2-3, pp. 67–82 (1978).
8. Carpinteri, A., DiTommaso, A. and Viola, E., Stato limite di frattura nei materiali fragili, Giornale del Genio Civile, fasc. 4-5-6, pp. 201–224 (1978).
9. Drucker, D.C., Quart. Appl. Math., 7, pp. 411–418 (1950).
10. Kupfer, H., Hilsdorf, H. and Rusch, H., Behavior of concrete under biaxial stresses, Journal of the American Concrete Institute, 65 (1969).
11. McHenry, D. and Karni, J., Strength of concrete under combined tensile and compressive stress, Journal of the American Concrete Institute, 54, pp. 829–840 (1958).
12. Weibull, W., A statistical theory of the strength of materials, Swedish Royal Institute for Engineering Research, Stockholm (1939).
13. Jayatilaka, A.S., Fracture of Engineering Brittle Materials, Applied Science Publishers LTD, London (1979).
14. Freudenthal, A.M., Statistical approach to brittle fracture, Fracture: An Advanced Treatise, edited by H. Liebowitz, Vol. II, pp. 592–619 (1968).
15. Krajcinovic, D. and Fonseka, G.U., The continuous damage theory of brittle materials. Part 1: General theory, Journal of Applied Mechanics, 48, pp. 809–815 (1981).
16. Fonseka, G.U. and Krajcinovic, D., The continuous damage theory of brittle materials. Part 2: Uniaxial and plane response modes, Journal of Applied Mechanics, 48, pp. 816–824 (1981).
17. Delameter, W.R., Herrmann, G. and Barnett, D.M., Weakening of an elastic solid by a rectangular array of cracks, Journal of Applied Mechanics, 42, pp. 74–80 (1975).
18. Janson, J. and Hult, J., Fracture mechanics and damage mechanics – a combined approach, Journal de Mecanique Appliquee, 1, pp. 69–84 (1977).

19. Janson, J., Dugdale-crack in a material with continuous damage formation, Engineering Fracture Mechanics, 9, pp. 891–899 (1977).
20. Janson, J., Damage model of crack growth and instability, Engineering Fracture Mechanics, 10, pp. 795–806 (1978).
21. Dugdale, D.S., Yielding of steel sheets containing slits, Journal of the Mechanics and Physics of Solids, 8, pp. 100–104 (1960).
22. Broberg, H., Damage measures in creep deformation and rupture, Swedish Solid Mechanics Reports (1974).
23. Kachanov, L.M., Time to failure under creep conditions, AN SSSR, OTN, 8 (1958).
24. Carpinteri, A. and Sih, G.C., Damage accumulation and crack growth in bilinear materials with softening: application of strain energy density theory, J. of Theoretical and Applied Fracture Mechanics, Vol. 1, No. 2, pp. 145–160 (1984).
25. Sih, G.C., Mechanics of material damage in concrete, Fracture Mechanics of Concrete: Material Characterization and Testing, edited by A. Carpinteri and A.R. Ingraffea, Martinus Nijhoff Publishers, The Hague, pp. 1–29 (1984).
26. Sih, G.C., Non-linear response of concrete: interaction of size, loading step and material property, Applications of Fracture Mechanics to Cementitious Composites, edited by S.P. Shah, Martinus Nijhoff Publishers, The Hague, pp. 3–23 (1984).
27. Rice, J.R., Path independent integral and approximate analysis of strain concentration by notches and cracks, Journal of Applied Mechanics, 35, pp. 379–386 (1968).
28. Rice, J.R., The localization of plastic deformation, Theoretical and Applied Mechanics, Proceedings of the 14th IUTAM Congress, Delft, pp. 207–220 (1976).
29. Bazant, Z.P. and Oh, B.H., Concrete fracture via stress-strain relations, Report 81-10/665c, Center for Concrete and Geomaterials, Northwestern University (1981).
30. Hillerborg, A., Modeer, M. and Petersson, P.E., Analysis of crack formation and crack growth in concrete by means of fracture mechanics and finite elements, Cement and Concrete Research, 6, pp. 773–782 (1976).
31. Gjørv, O.E. and Løland, K.E., Ductility of concrete and tensile behavior, Rapport BML 80.613, Institutt for Bygningsmateriallaere, Universitetet i Trondheim (1980).
32. Petersson, P.E., Crack growth and development of fracture zones in plain concrete and similar materials, Report TVBM-1006, Division of Building Materials, Lund Institute of Technology (1981).
33. Gerstle, W.H., Ingraffea, A.R. and Gergely, P., The fracture mechanics of bond in reinforced concrete, Report 82-7, Department of Structural Engineering, Cornell University (1982).
34. Wecharatana, M. and Shah, S.P., Predictions of nonlinear fracture process zone in concrete, Journal of Engineering Mechanics, American Society of Civil Engineers, 109, pp. 1231–1246 (1983).
35. Visalvanich, K. and Naaman, A.E., Fracture modeling of fiber reinforced cementitious composites, Report 82-1, Department of Materials Engineering, University of Illinois at Chicago Circle (1982).
36. Krajcinovic, D. and Silva, M.A.G., Statistical aspects of the continuous damage theory, International Journal of Solids and Structures, 18, pp. 551–562 (1982).
37. Sih, G.C., Mechanics of crack growth: geometrical size effect in fracture, Fracture Mechanics in Engineering Application, edited by G.C. Sih and S.R. Valluri, Sijthoff and Noordhoff, pp. 3–29 (1979).
38. Sih, G.C. and Tzou, D.Y., Mechanics of nonlinear crack growth: effect of specimen size and loading step, Proceedings on Modeling Problems in Crack Tip Mechanics, edited by J.T. Pindera, Martinus Nijhoff Publishers, The Hague, pp. 155–169 (1984).
39. Sih, G.C. and Chao, C.K., Size effect of cylindrical specimens with fatigue cracks, J. of Theoretical and Applied Fracture Mechanics, Vol 1, No. 3, pp. 239–247 (1984).

40. Sih, G.C., Analytical aspects of macro-fracture mechanics, Analytical and Experimental Fracture Mechanics, edited by G.C. Sih and M. Mirabile, Sijthoff and Noordhoff, pp. 3–15 (1981).
41. Sih, G.C. and Madenci, E., Crack growth resistance characterized by the strain energy density function, J. of Engin. Fract. Mech., Vol. 18, pp. 1159–1171 (1983).
42. Sih, G.C. and Tzou, D.Y., Crack-extension resistance of polycarbonate material, J. of Theoretical and Applied Fracture Mechanics, Vol. 2, No. 3 (in press).
43. Carpinteri, A., Size effect in fracture toughness testing: a dimensional analysis approach, Analytical and Experimental Fracture Mechanics, edited by G.C. Sih and M. Mirabile, Sijthoff and Noordhoff, pp. 785–797 (1981).
44. Carpinteri, A., Notch sensitivity in fracture testing of aggregative materials, Engineering Fracture Mechanics, 16, pp. 467–481 (1982).
45. Sih, G.C., The strain energy density concept and criterion, Special Issue in Fracture Mechanics Dedicated to G.R. Irwin, ed. A.K. Rao, J. of Aeronautical Society of India, Vol. 37, No. 1 pp. 43–60 (1985).
46. Kipp, M.E. and Sih, G.C., The strain energy density failure criterion applied to notched elastic solids, International Journal of Solids and Structures, Vol. 11, pp. 153–173 (1975).
47. Sih, G.C. and Matic, P., Mechanical response of materials with physical defects. Part 1: Modelling of material damage for center cracked panel, Report AFOSR-TR-81-1, Institute of Fracture and Solid Mechanics, Lehigh University (1981).
48. Sih, G.C. and Matic, P., Mechanical response of materials with physical defects. Part 2: Combined modelling of material damage and crack propagation for center cracked panel, Report AFOSR-TR-82-2, Institute of Fracture and Solid Mechanics, Lehigh University (1982).

3

Three-point bending of slab with edge crack

3.1. Step-by-step analysis of material damage and crack growth

A beam with square cross-section simply supported at the ends, cracked and loaded in the middle is considered in Figure 3.1 with the initial sizes shown. Geometrically similar specimens will also be considered by multiplying all the dimensions by the same constant factor in order to investigate the effect of scaling on the mechanics of fracture.

Because of symmetry, only left half of the specimen in Figure 3.1 needs to be analyzed. The finite element mesh used for the specimen is given in Figure 3.2. The Axisymmetric/Planar Elastic Structures (APES) finite element program [1] is applied at each loading increment. This is a computer program that incorporates the 12-noded quadrilateral isoparametric elements allowing for cubic displacement fields and quadratic stress and strain fields within each element. The r^{-1} strain energy density singularity in the vicinity of the crack tip is embedded in the solution by the use of 1/9 to 4/9 nodal spacing on the element sides adjacent to the crack tip. A total of 309 nodes and 52 elements are used and a condition of plane strain is assumed.

The damage-crack model developed in [2–4] will be employed in which elastic unloading is assumed. The load is transmitted to the specimen via the deflection δ, Figure 3.3, such that the softening stage can be traced by controlling the strain in the test. The P versus δ relationship in Figure 3.3 corresponds to that for Material 1 in Figure 2.29 and for a constant deflection increment, $\Delta\delta = 4 \times 10^{-3}$ cm. For the first step, the stiffness is only 6.21% lower than the original one. Such a decrease is mostly due to material damage at the crack tip. At the second step, the departure from linearity becomes more significant. The P versus δ curve begins to bend appreciably to the right at the third step and reaches a maximum. The segments AD and DT in Figure 3.3 represent the decreases in the secant stiffness due to material damage and crack growth, respectively. At the fourth step, the load P decreases and the tangent stiffness becomes negative. This is due to the widening of the damage zone and crack extension, which make the specimen more and more flexible. At this state, the contributions of material damage and crack growth to the secant stiffness decrease are almost the same. At the fifth and sixth

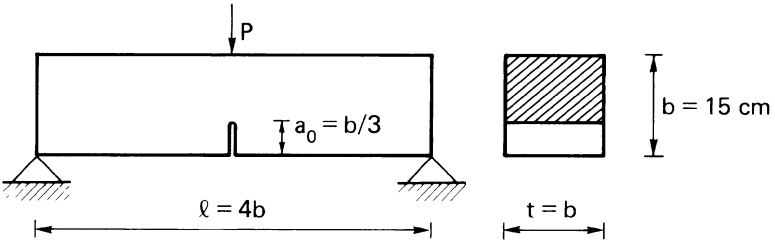

Fig. 3.1. Three-point bending fracture specimen.

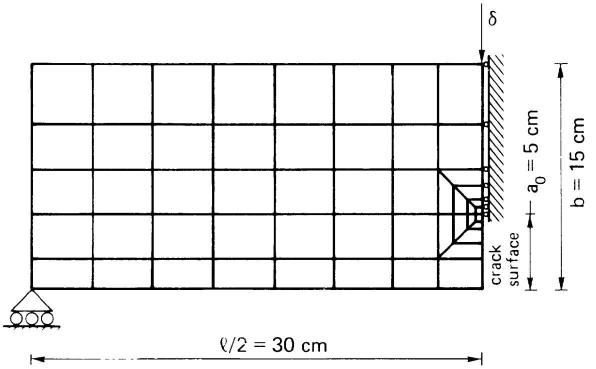

Fig. 3.2. Finite element idealization of the three-point bending fracture specimen in Figure 3.1.

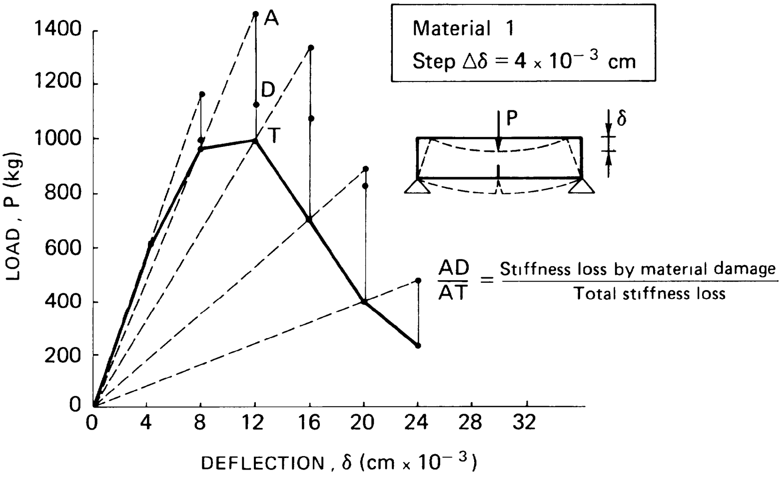

Fig. 3.3. Typical schematic relation of load versus deflection of three-point bending specimen.

steps, the load continues to decrease while the influence of crack growth increases sharply. When $\delta = 24 \times 10^{-3}$ cm, the load carried by the specimen is only one fifth of the maximum, while the crack has extended two thirds of the specimen width, b.

Each loading step is the result of two applications of the APES program. More precisely, point A in Figure 3.3 is obtained by a linear extrapolation from the preceeding point on the P versus δ curve. The point A then drops down to D due to material damage followed by point D going further down to T as a result of crack growth. Finite element meshes are adjusted for each crack growth increment. In Figure 3.4, the meshes and the deformed configurations related to the case of deflection increment $\Delta\delta = 1 \times 10^{-3}$ cm, are illustrated.

The five cases analyzed in this chapter are summarized in Table 3.1. The three materials in Figure 2.29 and three different loading increments are considered. The load-deflection values and the crack growth increments are reported in Table 3.2. In Figures 3.5 to 3.9, the sequences of the meshes utilized in the loading process description are displayed for each one of the cases in Table 3.1. The number n inside each element indicates the level of damage according to equation (2.73). The undamaged elements with $\mathrm{d}W/\mathrm{d}V < \frac{1}{2}\sigma_u \epsilon_u$ are not numbered. In compression, the material is assumed to be elastic, with the initial Young's modulus, E.

In what follows, the damage around the crack tip will be analyzed. Referring to the ith element in accordance with Kachanov's [5] idea of reduction in the elastic modulus, the parameter d_i may be defined:

$$d_i = \frac{E - E_i^*}{E} \tag{3.1}$$

A damage zone prevails such that the coordinates of its center are given by

$$x_D = \frac{\sum\limits_i x_i d_i A_i}{\sum\limits_i d_i A_i} \; ; \quad y_D = \frac{\sum\limits_i y_i d_i A_i}{\sum\limits_i d_i A_i} \tag{3.2}$$

where x_i and y_i are the coordinates of the centroid and A_i the area of the ith finite element. It follows that the following components of the inertia tensor may be defined:

$$I_{xx} = \sum_i (y_i - y_D)^2 d_i A_i \tag{3.3a}$$

$$I_{xy} = I_{yx} = \sum_i (x_i - x_D)(y_i - y_D) d_i A_i \tag{3.3b}$$

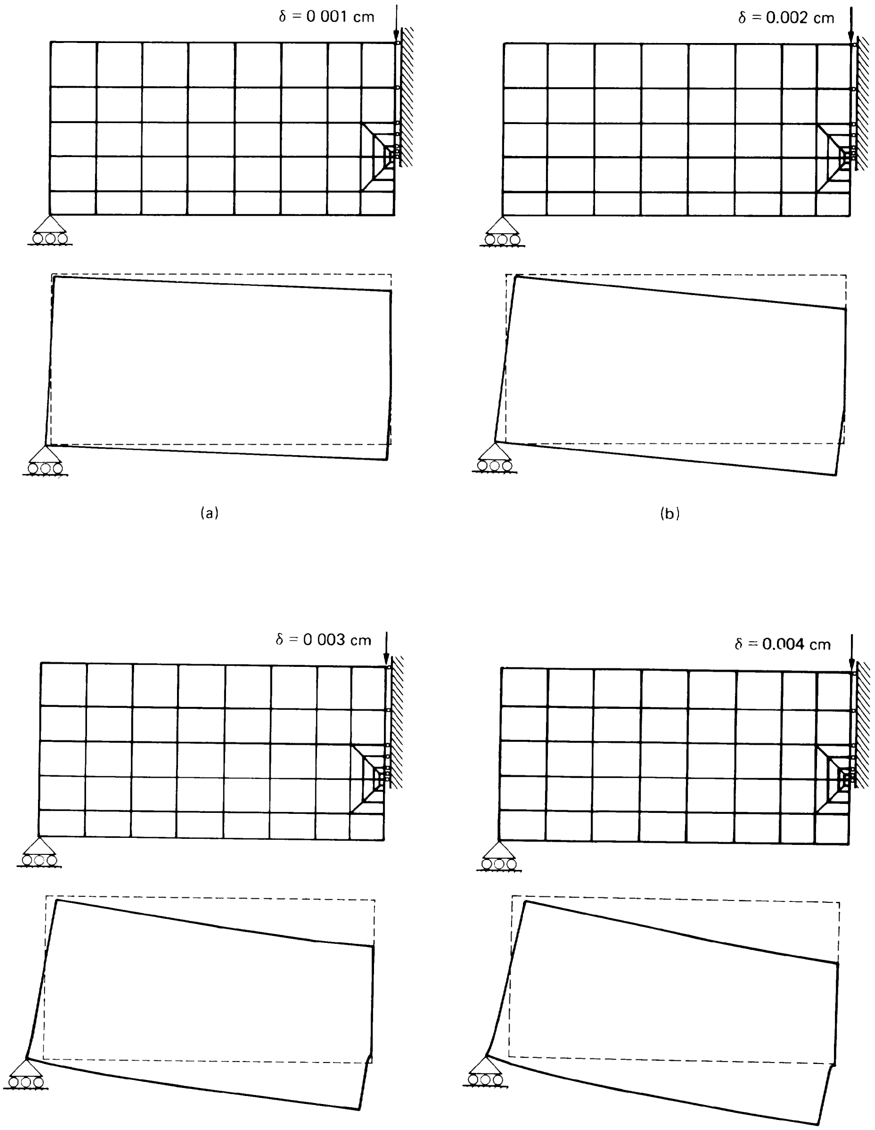

(a) (b)

(c) (d)

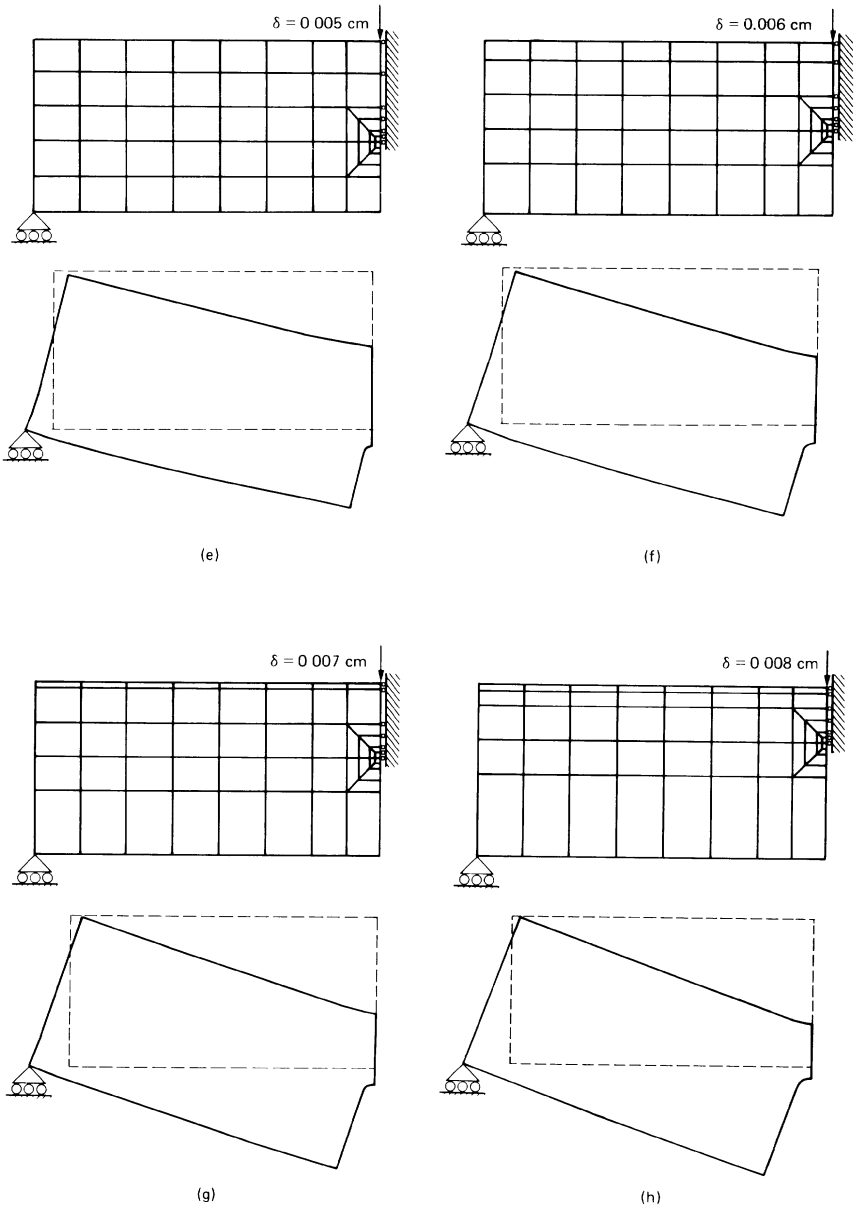

(e) (f)

(g) (h)

Fig. 3.4. Finite element meshes and deformed configurations related to Case No. 5 in Table 3.1.

TABLE 3.1.
The five cases analyzed in this chapter, changing material properties and deflection increments.

Case no.	Material	Deflection increment $\Delta\delta$ (10^{-3} cm)	Symbol
I (1)	1	4	●
II (2)	2	4	⊙
III (3)	3	4	○
IV (4)	3	2	□
V (5)	3	1	△

TABLE 3.2.
Load, deflection and crack growth increment at each loading increment and for each case in Table 3.1.

Case no. (1)			
Increment $j = 1, 2$, etc.	Load P_j (kg)	Deflection δ_j (10^{-3} cm)	Crack growth increment Δa_j (cm)
1	574	4	0.088
2	967	8	0.089
3	996	12	0.476
4	706	16	1.346
5	400	20	1.667
6	238	24	1.603
Case no. (2)			
1	564	4	0.157
2	828	8	0.480
3	572	12	1.688
4	276	16	2.000
Case no. (3)			
1	528	4	0.420
2	582	8	1.408
3	287	12	2.190
Case no. (4)			
1	302	2	0.069
2	521	4	0.421
3	566	6	0.809
4	384	8	1.533
5	166	10	2.000
Case no. (5)			
1	152	1	0.023
2	301	2	0.069
3	426	3	0.166
4	483	4	0.444
5	500	5	0.506
6	392	6	1.110
7	273	7	1.208
8	119	8	1.629

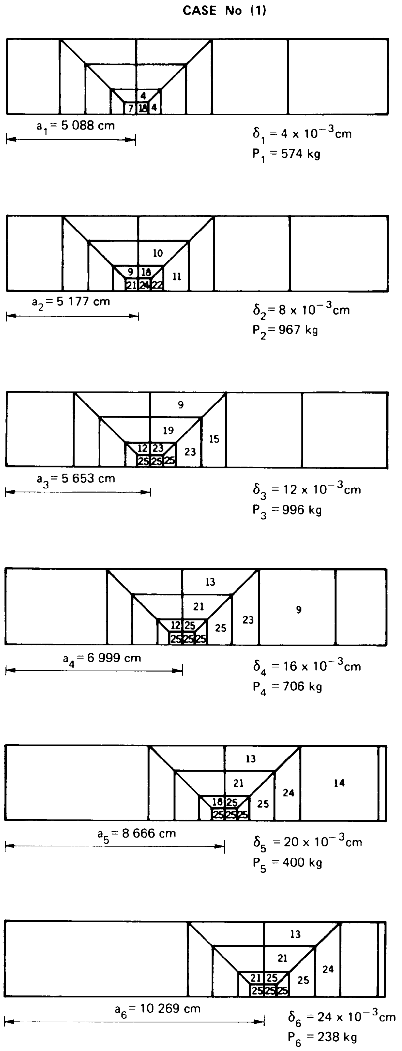

Fig. 3.5. Sequences of the meshes utilized in the loading process description; the number n inside each element indicates the level of damage according to equation (2.73). Case No. 1 in Table 3.1.

$$I_{yy} = \sum_i (x_i - x_D)^2 d_i A_i \qquad (3.3c)$$

The trajectories of the damage center and the principal damage directions during the loading process are plotted in Figure 3.10 for each one of the cases in Table 3.1. These results are in close agreement with the predictions

CASE No (2)

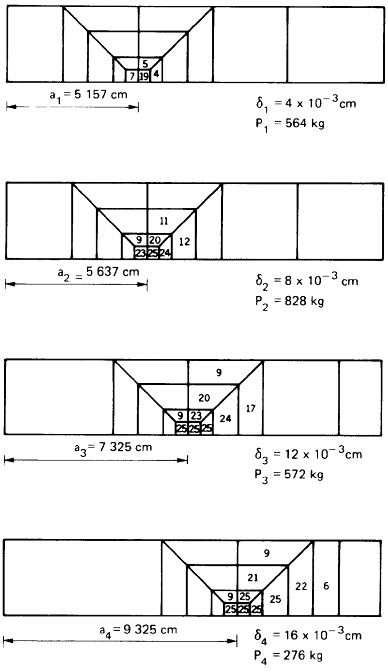

Fig. 3.6. The same as in Figure 3.5. Case No. 2 in Table 3.1.

CASE No (3)

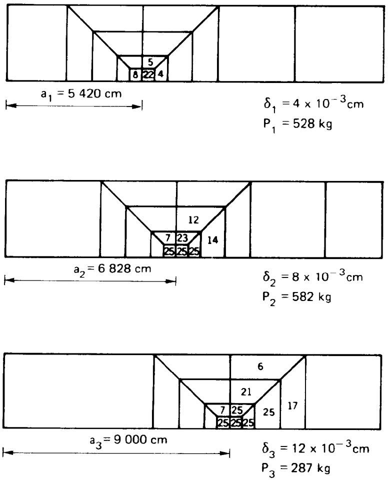

Fig. 3.7. The same as in Figure 3.5. Case No. 3 in Table 3.1.

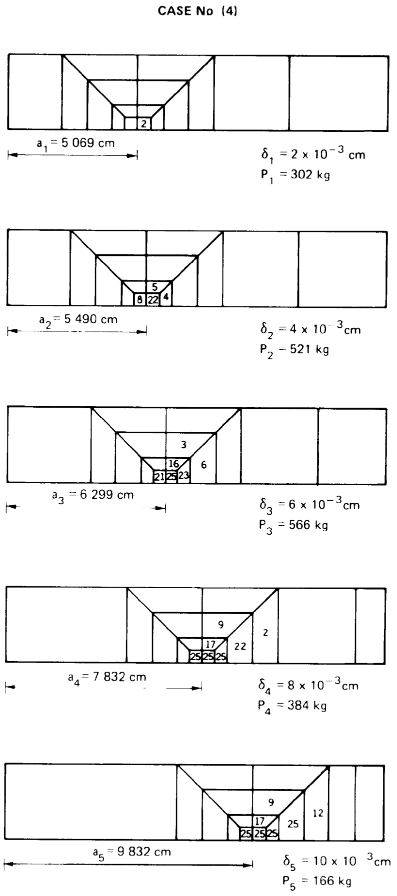

Fig. 3.8. The same as in Figure 3.5. Case No. 4 in Table 3.1.

made from the strain energy density theory. Computing the strain energy density factor, S, as a function of θ measured from the line of expected crack growth as shown in Figure 3.10, the relative minimum of S can be shown to correspond with $\theta = 0^\circ$ and the relative maximum with $\theta_0 = \cos^{-1}(1 - 2\nu)$. According to the S-criterion [6, 7], the former refers to the direction of macrocrack growth and the latter to the direction of maximum yielding.* For $\nu = 0.1$, an angle of $\theta_0 = 36.8^\circ$ is predicted. The agreement is quite good for small values of r. This is to be expected as the asymptotic

---

* The yield criterion based on $(\mathrm{d}W/\mathrm{d}V)_{\max}$ will be in conflict with the results obtained from plasticity which adopts the von Mises yield condition using the distortion energy component only. The present model based on elastic unloading [2, 3] presents no conceptual difficulties.

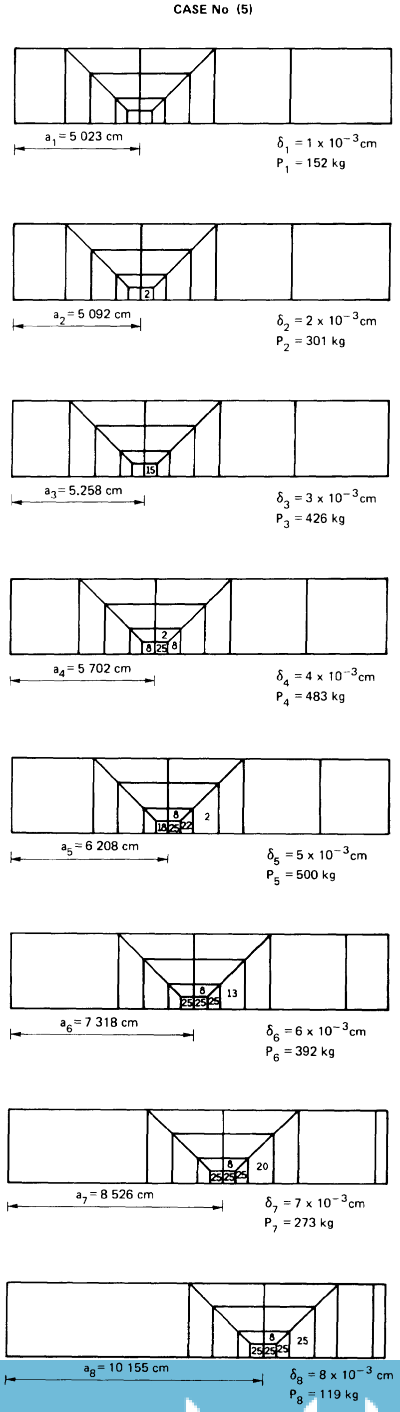

Fig. 3.9. The same as in Figure 3.5. Case No. 5 in Table 3.1.

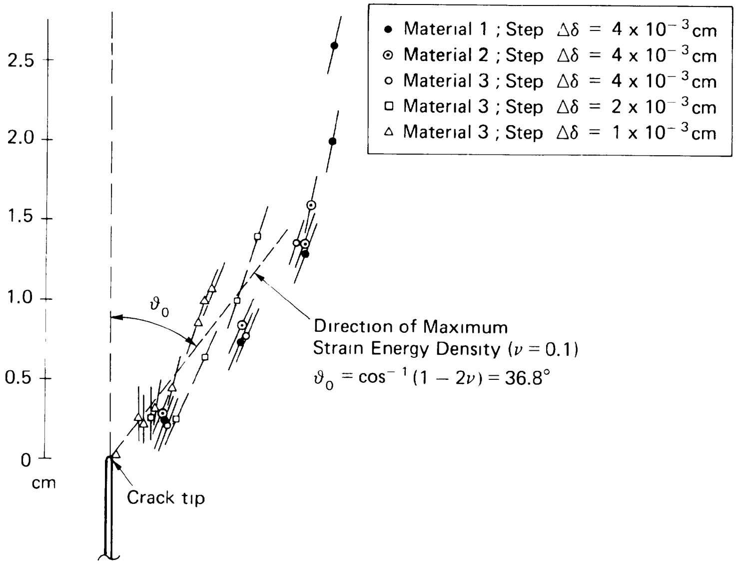

Fig. 3.10. Trajectories of the damage center and principal damage directions during the loading process of a three-point bending fracture specimen.

stress solution is limited to $r/a < 0.1$. Yielding can thus be viewed as damage with loss of material stiffness.

The distributions of the strain energy density function, $(\mathrm{d}W/\mathrm{d}V)$, and of the effective critical strain energy density function, $(\mathrm{d}W/\mathrm{d}V)_c^*$, over the whole ligament are given in Figure 3.11. They relate to the second loading increment pertaining to Case (3). While $(\mathrm{d}W/\mathrm{d}V)$ decreases away from the crack tip inside each finite element, $(\mathrm{d}W/\mathrm{d}V)_c^*$ increases monotonically. In consistence with Beltrami's criterion, the present analysis assumes that the material elements fail when $(\mathrm{d}W/\mathrm{d}V) \geqslant (\mathrm{d}W/\mathrm{d}V)_c^*$. The crack growth increment Δa is then determined from the intersection of $\mathrm{d}W/\mathrm{d}V$ with $(\mathrm{d}W/\mathrm{d}V)_c^*$ curves, Figure 3.11. The positive jumps of the strain energy density function, $(\mathrm{d}W/\mathrm{d}V)$, are due to the fact that the less damaged elements have a higher stiffness and, therefore, a higher load-bearing capacity. Such jumps represent a discrete softening effect ahead of the crack tip.

3.2. Effect of material properties

The numerical results will be discussed in connection with the σ versus ϵ curves in Figure 2.29. The load-deflection responses for the deflection increment $\Delta\delta = 4 \times 10^{-3}$ cm, are displayed in Figure 3.12. The shape of the curves is similar. The difference is that the area under them is approximately proportional to the area under the corresponding σ versus ϵ curve.

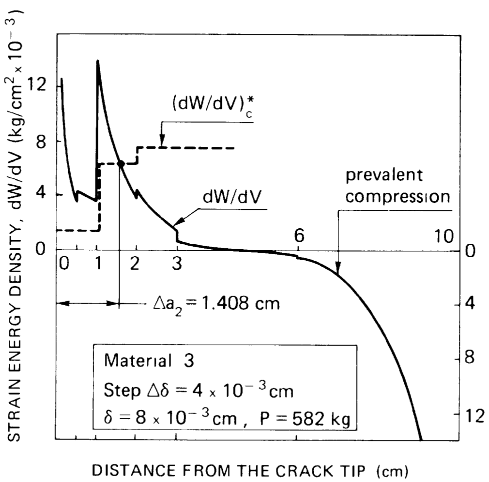

Fig. 3.11. Distributions of the strain energy density function, (dW/dV), and of the effective critical strain energy density function, $(dW/dV)^*_c$, over the whole ligament of a three-point bending fracture specimen.

In Figure 3.13, the ratio of stiffness loss by material damage to total stiffness loss (by material damage and crack growth) appears as a function of the imposed deflection, δ. Such a ratio is equal to the ratio AD/AT in Figure 3.3. The general trend is that it tends to zero for very small as well as for very large deflections. For intermediate deflections, these curves present a maximum which increases by increasing the critical strain energy density of the material,

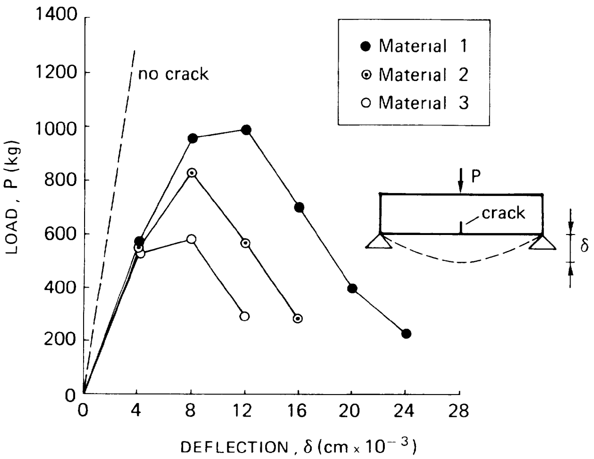

Fig. 3.12. Load-deflection diagrams for three different materials (see Figure 2.29) and $\Delta\delta = 4 \times 10^{-3}$ cm.

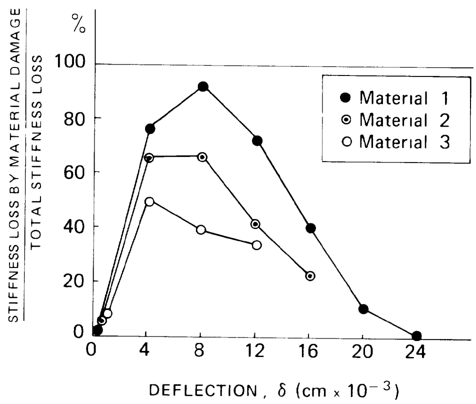

Fig. 3.13. Ratio of stiffness loss by material damage to total stiffness loss as a function of the imposed deflection, for three different materials (see Figure 2.29) and $\Delta\delta = 4 \times 10^{-3}$ cm.

$(\mathrm{d}W/\mathrm{d}V)_c$. In fact, for $\epsilon_f \to \infty$, the material becomes elastic-perfectly plastic and only material damage occurs, since $(\mathrm{d}W/\mathrm{d}V)_c$ and $(\mathrm{d}W/\mathrm{d}V)_c^*$ tend to infinity. It is therefore impossible for crack growth to occur.

In Figure 3.14, the load P is plotted against the crack growth, $(a - a_0)$. At the beginning, the load increases while the crack grows. Then, after reaching a maximum, the load decreases. The peaks represent the transition between stable and unstable structural behavior. For a relatively large structure, crack instability precedes the traditional structural instability and Linear Elastic Fracture Mechanics can be applied. When the structure is relatively small, as in the case of fracture toughness specimens, structural collapse precedes unstable crack propagation. It is interesting to observe that after the first 2 cm of crack growth the post-collapse structural behavior is not significantly affected by the variation in $(\mathrm{d}W/\mathrm{d}V)_c$, Figure 3.14.

In Figure 3.15, the values of the strain energy density factor, S, are plotted against the crack growth, $(a - a_0)$. These are known as the SR-curves which are straight lines. The results correspond to small crack growth increments during which time P is still increasing in a stable fashion. The straight line relationship between S and a is essential as it allows the development of simple design rules.

The higher $(\mathrm{d}W/\mathrm{d}V)_c$ is, the steeper the S versus a line variation appears to be. The S versus a lines tend to rotate counterclockwise as $(\mathrm{d}W/\mathrm{d}V)_c$ increases for the tougher material. Since the S_c values for Materials 1, 2 and 3 are different, their intersections with the S versus a lines will also differ. It can easily be shown that more subcritical crack growth could be attained by Material 1 if this possessed the highest S_c value. The strain energy density factor rate, $\mathrm{d}S/\mathrm{d}a$, has the same physical dimensions as those of the

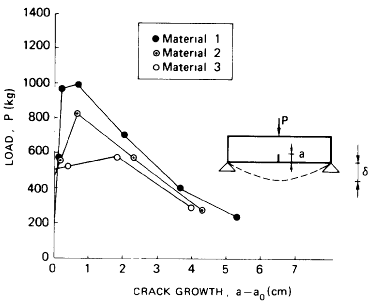

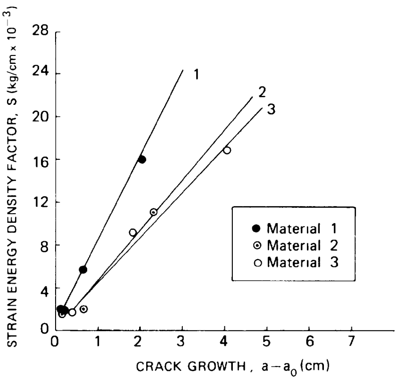

Fig. 3.14. Load-crack growth diagrams for three different materials (see Figure 2.29) and $\Delta\delta = 4 \times 10^{-3}$ cm.

Fig. 3.15. Strain energy density factor versus crack growth for three different materials (see Figure 2.29) and $\Delta\delta = 4 \times 10^{-3}$ cm.

strain energy density function. It always has a lower value than the corresponding $(\mathrm{d}W/\mathrm{d}V)_c$, Table 3.3. The ratio $(\mathrm{d}S/\mathrm{d}a)/(\mathrm{d}W/\mathrm{d}V)_c$ decreases as material damage as compared with crack growth becomes more dominant.

In Figure 3.16, the maximum load $P_{\max}$, is plotted against the softening strain $(\epsilon_f - \epsilon_u)$, and the case $(\epsilon_f - \epsilon_u) = 1 \times 10^{-4}$ is included for which a condition of elastic-perfectly brittle collapse is attained at the ligament. The points corresponding to $(\epsilon_f - \epsilon_u) = 8 \times 10^{-4}$ and 16×10^{-4} are above the elastic-perfectly plastic limit load. This is due to the reduction of structural size. In this case, the Limit Analysis concept in Section 1.1 can be applied. It states that a size increase of a perfectly plastic structure cannot produce a decrease in the limit load.

3.3. Load step influence on crack growth

The load step effects contribute to the increase in the strength of cement composites when the loading rate is increased. This effect will be illustrated by varying the load step in the analysis. In Figure 3.17, the load-deflection curves are displayed for Material 3 and three different deflection increments as $\Delta\delta = 4 \times 10^{-3}$, 2×10^{-3}, and 1×10^{-3} cm. The maximum load, $P_{\max}$,

TABLE 3.3.
Comparison between strain energy density factor rate, $\mathrm{d}S/\mathrm{d}a$, and critical value of the strain energy density function, $(\mathrm{d}W/\mathrm{d}V)_c$.

Material	1	2	3
$(\mathrm{d}W/\mathrm{d}V)_c$ [kg/cm² × 10⁻³]	26.90	14.14	7.77
$\mathrm{d}S/\mathrm{d}a$ [kg/cm² × 10⁻³]	7.54	4.60	4.15

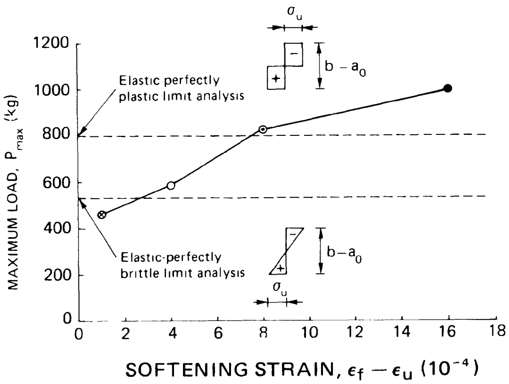

Fig. 3.16. Maximum load versus softening strain.

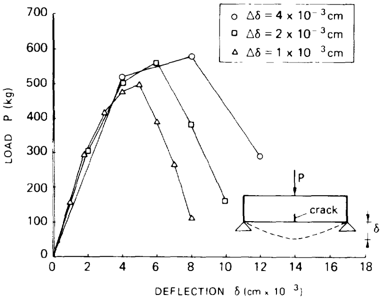

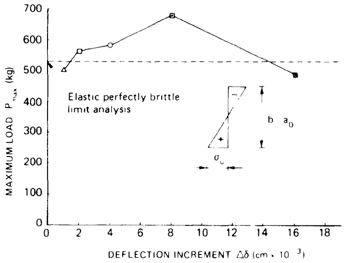

Fig. 3.17. Load-deflection diagrams for Material 3 (see Figure 2.29) and three different loading increments.

Fig. 3.18. Maximum load versus deflection increment with Material 3 (see Figure 2.29).

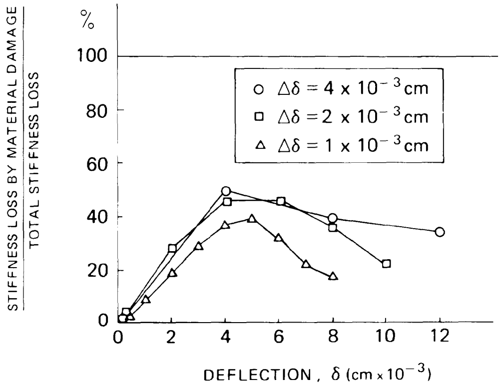

Fig. 3.19. Ratio of stiffness loss by material damage to total stiffness loss as a function of the imposed deflection and for three different loading increments (Material 3 in Figure 2.29).

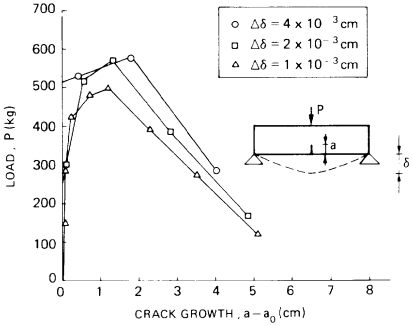

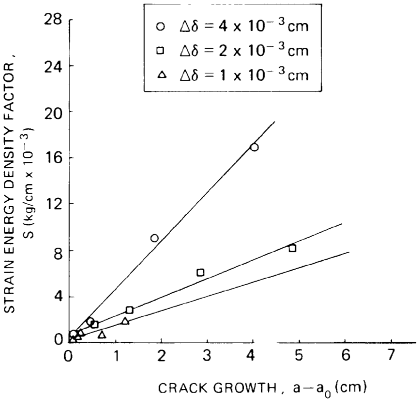

Fig. 3.20. Load-crack growth diagrams for three different loading increments and Material 3 (see Figure 2.29).

Fig. 3.21. Strain energy density factor versus crack growth for three different loading increments and Material 3 (see Figure 2.29).

increases by increasing the deflection increment. In Figure 3.18, $P_{\max}$ is plotted against the step $\Delta\delta$ and the cases $\Delta\delta = 8 \times 10^{-3}$ and 16×10^{-3} cm, are also included. In this range, $P_{\max}$ tends to increase and then decrease. The 36% difference between the maxima with $\Delta\delta = 8 \times 10^{-3}$ cm and $\Delta\delta = 1 \times 10^{-3}$ cm reflects the well known increase in flexural strength of cement and mortar when the strain rate increases [8].

In Figure 3.19, the ratio of stiffness loss by material damage to total stiffness loss is plotted as a function of the deflection, δ. It renders the same trends as discussed earlier in section 3.2, i.e., damage exceeds crack growth only for intermediate crack lengths. Moreover, the stiffness loss by crack growth tends to overcome that by material damage when the load step, $\Delta\delta$, decreases.

In Figure 3.20, the load, P, is plotted against the crack growth, $(a - a_0)$. The peaks of these curves represent the transition between stable and unstable structural behavior and not necessarily between stable and unstable crack propagation. Also, the load-crack growth diagram is not significantly affected by the load step, $\Delta\delta$, in the post-collapse condition. In Figure 3.21, the values of the strain energy density factor, S, are plotted against the crack growth. The higher the deflection increment, $\Delta\delta$, is, the steeper is the S versus a line.

3.4. Scaling of geometrically similar specimens

Because material damage and crack growth occur in a non-self-similar fashion for each step of loading, specimens of different sizes appear to behave differently. This well-known size effect will be analyzed by the results obtained on the three-point bending specimen. A dimensionless load parameter may be defined as

$$\frac{P}{\left(\dfrac{\mathrm{d}W}{\mathrm{d}V}\right)_c b^2} = \Pi\left[\frac{\delta}{b}, \frac{E}{\left(\dfrac{\mathrm{d}W}{\mathrm{d}V}\right)_c}, \frac{\sigma_u}{\left(\dfrac{\mathrm{d}W}{\mathrm{d}V}\right)_c}, \nu, \frac{l}{b}, \frac{t}{b}, \frac{a_0}{b}\right] \tag{3.4}$$

This is similar to the Buckingham's theorem for physical similitude and model scaling. In equation (3.4) the material toughness, $(\mathrm{d}W/\mathrm{d}V)_c$, and specimen width, b, have been used as the fundamental quantities. The dimensionless load parameter may be regarded as a function of the dimensionless deflection parameter δ/b only, if all others are kept constant.

In the same way, it is possible to define a dimensionless strain energy density factor:

$$\frac{S}{\left(\dfrac{\mathrm{d}W}{\mathrm{d}V}\right)_c b} = \Sigma\left[\frac{a}{b}, \frac{E}{\left(\dfrac{\mathrm{d}W}{\mathrm{d}V}\right)_c}, \frac{\sigma_u}{\left(\dfrac{\mathrm{d}W}{\mathrm{d}V}\right)_c}, \nu, \frac{l}{b}, \frac{t}{b}, \frac{a_0}{b}\right] \tag{3.5}$$

By assuming the function Σ to be linear in a/b [9, 10], the following is obtained:

$$\frac{S}{\left(\dfrac{\mathrm{d}W}{\mathrm{d}V}\right)_c b} = \frac{\mathrm{d}S/\mathrm{d}a}{(\mathrm{d}W/\mathrm{d}V)_c} \cdot \frac{a - a_0}{b} + \frac{S_0}{\left(\dfrac{\mathrm{d}W}{\mathrm{d}V}\right)_c b} \tag{3.6}$$

which may be rearranged into the form

$$\frac{S}{\left(\dfrac{\mathrm{d}W}{\mathrm{d}V}\right)_c b} = A\left(\frac{a}{b}\right) + B \tag{3.7}$$

The constants A and B are dimensionless and scale independent. It follows that the slope of the S versus a diagram is constant, i.e., $\mathrm{d}S/\mathrm{d}a =$ constant and that the intercept, S_0, is proportional to the scale b.

Figures 3.22(a) to (e) inclusive give the straight line plots of S versus $(a - a_0)$ for different combinations of materials and load steps with b varying from 15 cm upwards. The critical crack growth decreases with increasing specimen size. For Case (3), with $S_c = 8 \times 10^{-3}$ kg/cm, the limiting size $b = 222$ cm is obtained, Figure 3.22(c). Beyond this size, stable crack growth

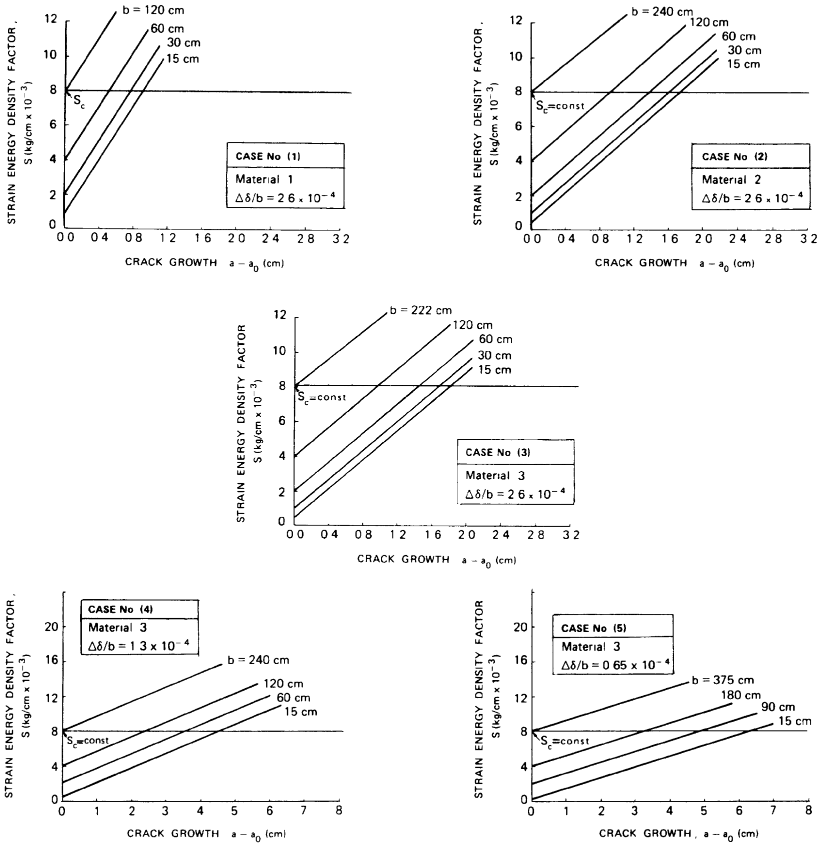

Fig. 3.22. (a) Straight line plots of strain energy density factor versus crack growth, varying the specimen size scale. Case No. 1 in Table 3.1. (b) The same as in Figure 3.22(a). Case No. 2 in Table 3.1. (c) The same as in Figure 3.22(a). Case No. 3 in Table 3.1. (d) The same as in Figure 3.22(a). Case No. 4 in Table 3.1. (e) The same as in Figure 3.22(a). Case No. 5 in Table 3.1.

ceases to occur and failure corresponds to unstable crack-propagation or catastrophic fracture.

The relations between $P/(\mathrm{d}W/\mathrm{d}V)_c b^2$ and δ/b are summarized in Figures 3.23. The vertical lines with arrows indicate the limiting values of δ/b as the critical strain energy density factor, $S_c = 8 \times 10^{-3}$ kg/cm, is reached. This corresponds to $K_{IC} = 144.35$ kg/cm$^{3/2}$ which is typical of concrete [11, 12]. It is clear that crack instability occurs for smaller dimensionless deflections of the specimen as size b is increased. Without considering unstable crack propagation, in case (3) the maximum load can be estimated from the relation

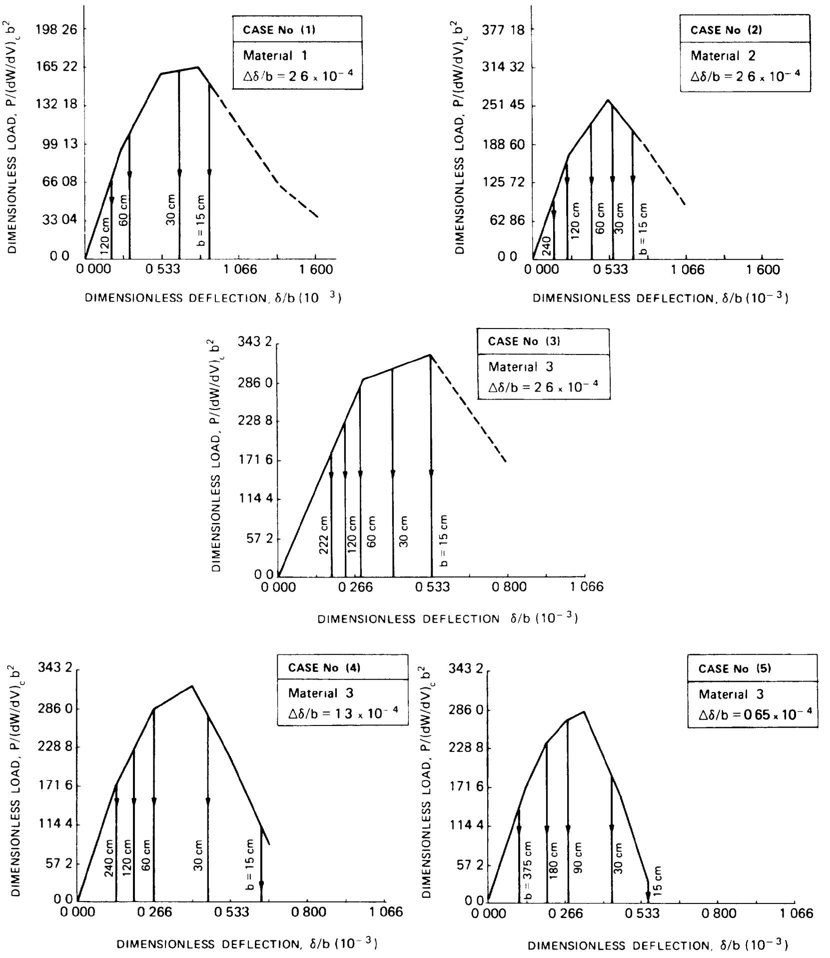

Fig. 3.23. (a) Dimensionless load-deflection diagram. Case No. 1 in Table 3.1. (b) Dimensionless load-deflection diagram. Case No. 2 in Table 3.1. (c) Dimensionless load-deflection diagram. Case No. 3 in Table 3.1. (d) Dimensionless load-deflection diagram. Case No. 4 in Table 3.1. (e) Dimensionless load-deflection diagram. Case No. 5 in Table 3.1.

$$P_{\max} = 332.90 \left(\frac{\mathrm{d}W}{\mathrm{d}V}\right)_c b^2 \tag{3.8}$$

Case (3) shows that structural instability occurs before unstable crack propagation only for $b \leqslant 15$ cm, Figure 3.23(c). For $b = 30$ cm, softening behavior is not present and the crack starts spreading in an unstable manner when the load P is still in the ascending stage. The critical length, a_{cr}, for each size can

TABLE 3.4(a–e).
(a) Maximum load for different size scales and according to the various theories: Strain Energy Density Theory, Linear Elastic Fracture Mechanics, Limit Analysis. Case No. 1 in Table 3.1. (b) The same as in Table 3.4(a). Case No. 2 in Table 3.1. (c) The same as in Table 3.4(a). Case No. 3 in Table 3.1. (d) The same as in Table 3.4(a). Case No. 4 in Table 3.1. (e) The same as in Table 3.4(a). Case No. 5 in Table 3.1.

Case no. (1)

Size b, cm	15	30	60	120
$P^{(1)}_{max}$ (SEDT), kg	1000	3920	10400	28380
$P^{(2)}_{max}$ (LEFM), kg	1254	3548	10034	28380
$P^{(3)}_{max}$ (Limit analysis), kg	531	2124	8496	33984
$P^{(1)}_{max}/P^{(2)}_{max}$ ratio	0.80	1.10	1.04	1.00
$P^{(3)}_{max}/P^{(2)}_{max}$ ratio	0.42	0.60	0.85	1.20

Case no. (2)

Size b, cm	15	30	60	120	240
$P^{(1)}_{max}$ (SEDT), kg	825	3400	11137	32000	80270
$P^{(2)}_{max}$ (LEFM), kg	1254	3548	10034	28380	80270
$P^{(3)}_{max}$ (Limit analysis), kg	531	2124	8496	33984	136000
$P^{(1)}_{max}/P^{(2)}_{max}$ ratio	0.66	0.96	1.11	1.13	1.00
$P^{(3)}_{max}/P^{(2)}_{max}$ ratio	0.42	0.60	0.85	1.20	1.69

Case no. (3)

Size b, cm	15	30	60	120	222
$P^{(1)}_{max}$ (SEDT), kg	575	2170	7625	25600	71480
$P^{(2)}_{max}$ (LEFM), kg	1254	3548	10034	28380	71480
$P^{(3)}_{max}$ (Limit analysis), kg	531	2124	8496	33984	136000
$P^{(1)}_{max}/P^{(2)}_{max}$ ratio	0.46	0.61	0.76	0.90	1.00
$P^{(3)}_{max}/P^{(2)}_{max}$ ratio	0.42	0.60	0.85	1.20	1.90

Case no. (4)

Size b, cm	15	30	60	120	240
$P^{(1)}_{max}$ (SEDT), kg	562	2250	7826	25600	80270
$P^{(2)}_{max}$ (LEFM), kg	1254	3548	10034	28380	80270
$P^{(3)}_{max}$ (Limit analysis), kg	531	2124	8496	33984	136000
$P^{(1)}_{max}/P^{(2)}_{max}$ ratio	0.45	0.63	0.78	0.90	1.00
$P^{(3)}_{max}/P^{(2)}_{max}$ ratio	0.42	0.60	0.85	1.20	1.69

Case no. (5)

Size b, cm	15	30	90	180	375
$P^{(1)}_{max}$ (SEDT), kg	500	2000	17190	61200	156800
$P^{(2)}_{max}$ (LEFM), kg	1254	3548	18400	52140	156800
$P^{(3)}_{max}$ (Limit analysis), kg	531	2124	19116	76500	332000
$P^{(1)}_{max}/P^{(2)}_{max}$ ratio	0.40	0.56	0.93	1.17	1.00
$P^{(3)}_{max}/P^{(2)}_{max}$ ratio	0.42	0.60	1.04	1.47	2.12

be found from the S versus a plots on Figure 3.22(c). A similar set of curves are produced for Material 3 with $\Delta\delta/b = 0.65 \times 10^{-4}$ and they are given in Figures 3.22(e) and 3.23(e). They basically show that, with the same critical value S_c, the limiting specimen size is increased from $b = 222$ to 375 cm as the ratio $\Delta\delta/b$ is changed from 2.6×10^{-4} to 0.65×10^{-4}. The interaction of loading step with specimen size is exhibited.

It is now apparent that the quantity $S_c/(\mathrm{d}W/\mathrm{d}V)_c b$ must also enter into the dimensional analysis in equation (3.4). In fact, for estimating $P_{\max}$, it suffices to consider

$$\frac{P_{\max}}{\left(\dfrac{\mathrm{d}W}{\mathrm{d}V}\right)_c b^2} = \Pi(S^*) \tag{3.9}$$

in which S^* is a dimensionless quantity:

$$S^* = \frac{S_c}{\left(\dfrac{\mathrm{d}W}{\mathrm{d}V}\right)_c b} = \frac{r_c}{b} \tag{3.10}$$

Hence, all geometically similar structures can be regarded as governed by S^*. This dimensionless quantity can be used to predict the load versus deflection behavior of all specimen sizes. The amount of subcritical crack growth is obviously size-dependent in addition to other influences such as loading steps and material properties [4].

It is also of interest to discuss the present findings in relation to the maximum load $P^{(2)}_{\max}$ resulting from the well-known ASTM-formula [13]:

$$K_I = \frac{Pl}{tb^{3/2}} f\left(\frac{a_0}{b}\right) \tag{3.11}$$

where

$$f\left(\frac{a_0}{b}\right) = 2.9\left(\frac{a_0}{b}\right)^{1/2} - 4.6\left(\frac{a_0}{b}\right)^{3/2} + 21.8\left(\frac{a_0}{b}\right)^{5/2}$$

$$- 37.6\left(\frac{a_0}{b}\right)^{7/2} + 38.7\left(\frac{a_0}{b}\right)^{9/2} \tag{3.12}$$

The predicted values of $P^{(3)}_{\max}$ from a linear elastic limit analysis can be

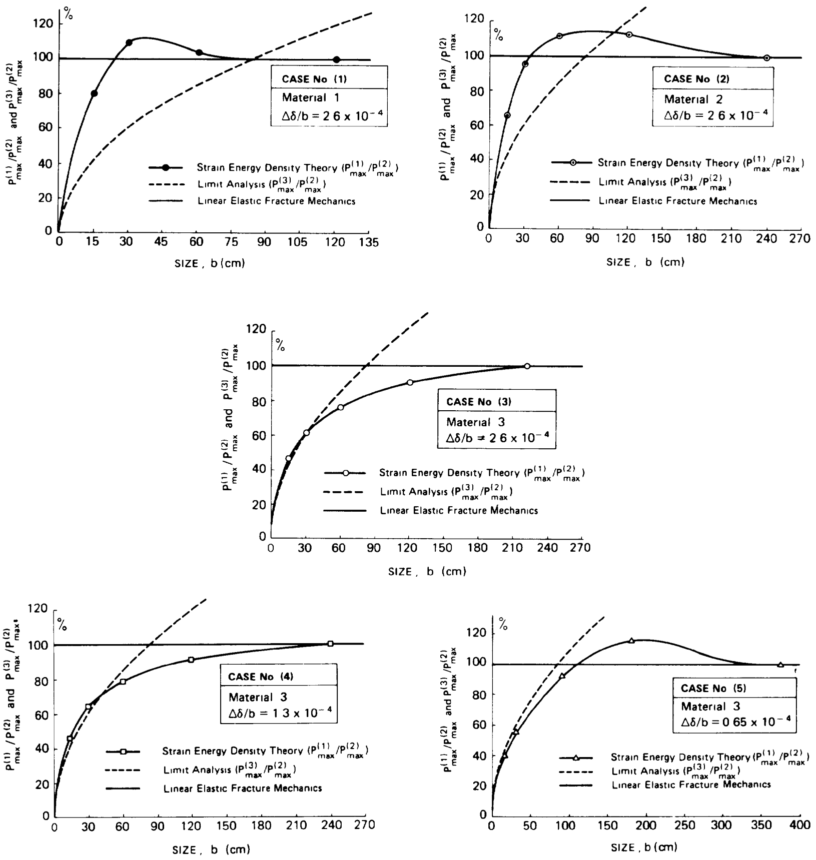

Fig. 3.24. (a) Maximum load predicted by Strain Energy Density Theory and by Limit Analysis referred to the critical load from LEFM. Case No. 1 in Table 3.1. (b) The same as in Figure 3.24(a). Case No. 2 in Table 3.1. (c) The same as in Figure 3.24(a). Case No. 3 in Table 3.1. (d) The same as in Figure 3.24(a). Case No. 4 in Table 3.1. (e) The same as in Figure 3.24(a). Case No. 5 in Table 3.1.

computed as

$$P^{(3)}_{\max} = \frac{2}{3}\,\frac{\sigma_u t(b-a_0)^2}{l} \tag{3.13}$$

where the ligament size at collapse is assumed to be $(b - a_0)$. All the maximum loads obtained by the various approaches are reported in Tables 3.4. Normalizing the results $P^{(1)}_{\max}$ and $P^{(3)}_{\max}$, obtained by the present approach and by the limit analysis respectively, with $P^{(2)}_{\max}$, recommended by ASTM, and plotting the ratios against b, Figures 3.24 give a comparison between the various theories. The horizontal line $P^{(1)}_{\max}/P^{(2)}_{\max}$ and $P^{(3)}_{\max}/P^{(2)}_{\max}$ equal to 100% represents the limiting case of ASTM where failure coincides totally with brittle fracture. The curves of Figures 3.24 give the maximum failure load involving both structural collapse and brittle fracture. When the specimen size is small, the simple formula in equation (3.13) gives good prediction based on ultimate strength only. On the other hand, when the specimen size is large, the ASTM-formula in equation (3.11) gives good prediction based on Linear Elastic Fracture Mechanics only. The two extreme situations have thus been connected [14, 15].

References

1. Hilton, P.D., Gifford, L.N. and Lomacky, O., Finite element fracture mechanics of two-dimensional and axisymmetric elastic and elastic-plastic cracked structures, Report No. 4493, Naval Ship Research and Development Center (1975).
2. Sih, G.C. and Matic, P., Mechanical response of materials with physical defects. Part 1: Modelling of material damage for center cracked panel, Report AFOSR-TR-81-1, Institute of Fracture and Solid Mechanics, Lehigh University (1981).
3. Sih, G.C. and Matic, P., Mechanical response of materials with physical defects. Part 2: Combined modelling of material damage and crack propagation for center cracked panel, Report AFOSR-TR-82-2, Institute of Fracture and Solid Mechanics, Lehigh University (1982).
4. Carpinteri, A. and Sih, G.C., Damage accumulation and crack growth in bilinear materials with softening: application of strain energy density theory, Journal of Theoretical and Applied Fracture Mechanics, Vol. 1, No. 2, pp. 145–160 (1984).
5. Kachanov, L.M., Time to failure under creep conditions, AN SSSR, OTN, 8 (1958).
6. Sih, G.C., Some basic problems in fracture mechanics and new concepts, Engineering Fracture Mechanics, 5, pp. 365–377 (1973).
7. Sih, G.C. and Macdonald, B., Fracture mechanics applied to engineering problems – strain energy density fracture criterion, Engineering Fracture Mechanics, 6, pp. 361–386 (1974).
8. Mindess, S. and Nadeau, J.S., Effect of loading rate on the flexural strength of cement and mortar, American Ceramic Society Bulletin, 56, pp. 429–430 (1977).
9. Sih, G.C. and Madenci, E., Crack growth resistance characterized by the strain energy density function, Engineering Fracture Mechanics, 18, pp. 1159–1171 (1983).
10. Sih, G.C., Mechanics of material damage in concrete, Fracture Mechanics of Concrete: Material Characterization and Testing, edited by A. Carpinteri and A.R. Ingraffea, Martinus Nijhoff Publishers, pp. 1–29 (1984).
11. Carpinteri, A., Static and energetic fracture parameters for rocks and concretes, Materials & Structures (RILEM), 14, pp. 151–162 (1981).
12. Carpinteri, A., Application of fracture mechanics to concrete structures, Journal of the Structural Division, American Society of Civil Engineers, 103, pp. 833–848 (1982).
13. Standard Method of Test for Plane Strain Fracture Toughness of Metallic Materials, E 399-74, ASTM.
14. Carpinteri, A., Size effect in fracture toughness testing: a dimensional analysis approach, Analytical and Experimental Fracture Mechanics, edited by G.C. Sih and M. Mirabile, Sijthoff and Noordhoff, pp. 735–747 (1981).

15. Carpinteri, A., Notch sensitivity in fracture testing of aggregative materials, Engineering Fracture Mechanics, 16, pp. 467–481 (1982).

4

Center cracked slab in tension

4.1. Introduction

A center cracked slab in tension is analyzed, Figure 4.1. The sizes shown in Figure 4.1 with $t = 15$ cm will be scaled such that all dimensions will be multiplied by a constant factor. The slab is assumed to be made of Material 3 defined in Figure 2.29. On account of symmetry, only one fourth of the slab is analyzed. The finite element mesh used for the specimen is shown in Figure 4.2. As in chapter 3, the APES finite element program [1] will be used.

The damage-crack growth model of Sih and Matic [2, 3] will be applied to the tension test specimen subjected to a strain-controlled loading process. The cases investigated are summarized in Table 4.1. Three different initial crack lengths and three different strain increments are considered. The stress-strain values and the crack growth increments are given in Table 4.2, while the values of crack length and strain energy density factor are reported in Table 4.3. In Table 4.4, the level of damage in each element is given according to equation (2.73) for each strain increment.

The trajectories of the damage center, defined in chapter 3, are shown in Figure 4.3 for each one of the cases in Table 4.1. The variation in initial crack

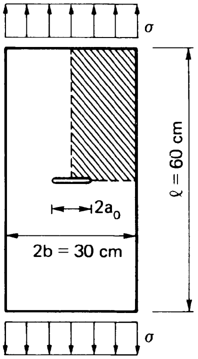

Fig. 4.1. Center cracked slab in tension.

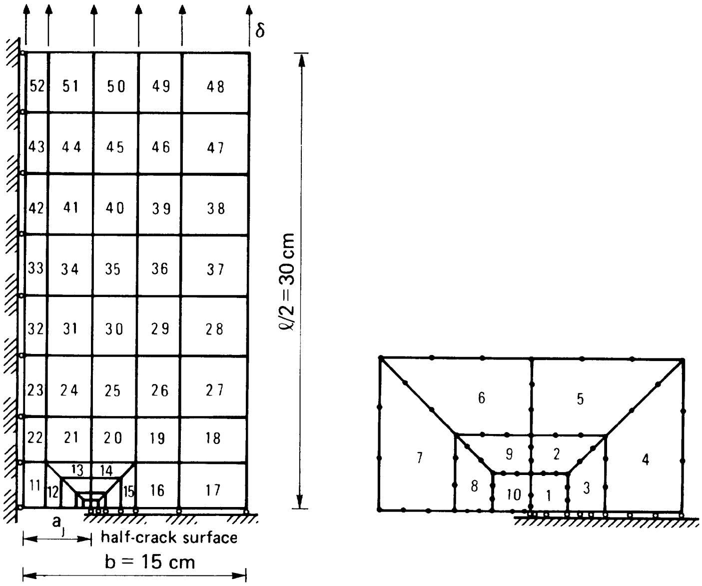

(a) (b)

Fig. 4.2. Finite element idealization of the center cracked slab in Figure 4.1 (a); zoom area (b).

length and loading step do not appear to influence the trajectory. Similar to the results in Figure 3.10, the direction of maximum strain energy density coincides with that of maximum damage, especially for small values of distance r from the crack tip.

4.2. Influence of initial crack length

The numerical results will be discussed by varying the initial crack length. The stress-strain responses for the strain increment $\Delta\epsilon = 1.67 \times 10^{-5}$, are displayed

TABLE 4.1.
The five cases analyzed in this chapter, changing initial crack length and loading increments

Case no.	Initial crack length a_0/b	Strain increment $\Delta\epsilon$ (10^{-5})	Symbol
I (1)	0.3	1.67	●
II (2)	0.4	1.67	⊙
III (3)	0.5	1.67	○
IV (4)	0.3	3.33	□
V (5)	0.3	6.67	△

TABLE 4.2.
Stress, strain and crack growth increment at each loading increment and for each case in Table 4.1

Case No. (1)

Increment $j = 1, 2,$ etc.	Stress σ_j (kg/cm^2)	Strain ϵ_j (10^{-5})	Crack growth increment Δa_j (cm)
1	5.65	1.67	0.036
2	11.22	3.33	0.106
3	16.35	5.00	0.388
4	19.88	6.67	0.774
5	17.10	8.33	1.959
Case No. (2)			
1	5.33	1.67	0.044
2	10.50	3.33	0.142
3	14.94	5.00	0.435
4	16.28	6.67	1.432
5	9.95	8.33	2.731
Case No. (3)			
1	4.92	1.67	0.051
2	9.58	3.33	0.201
3	13.23	5.00	0.455
4	12.72	6.67	1.588
Case No. (4)			
1	11.24	3.33	0.106
2	21.22	6.67	0.458
3	18.48	10.00	2.881
4	2.05	13.33	6.707
Case No. (5)			
1	21.40	6.67	0.449
2	11.08	13.33	4.637

in Figure 4.4. The load carrying capacity decreases as the initial crack length is increased. In Figure 4.5, the ratio of stiffness loss by material damage to total stiffness loss (by material damage and crack growth) is plotted against the strain, ϵ. Such a ratio increases from zero, at low strain, to a plateau at about 50%. The difference in initial crack length does not influence this behavior.

In Figure 4.6, the stress σ is displayed against the crack growth, $2(a-a_0)$. For the first steps, the stress increases while the crack grows. After reaching a maximum, the stress decreases and attains the value zero when the whole ligament is separated.

In Figure 4.7, the strain energy density factor, S, is plotted against the crack growth $2(a-a_0)$. The values of S for small crack growths give a linear S versus a variation. The slopes of the S versus a lines increased with the value

TABLE 4.3.
Crack length and strain energy density factor at each loading increment and for each case in Table 4.1.

Case No. (1) Increment $j = 1, 2$, etc.	Crack length $2a_j$ (cm)	Strain energy density factor S_j (kg/cm × 10^{-3})
1	9.072	0.280
2	9.284	0.748
3	10.060	1.304
4	11.548	1.130
5	15.466	2.860
Case No. (2)		
1	12.088	0.342
2	12.372	0.924
3	13.242	0.635
4	16.106	3.503
5	21.568	6.936
Case No. (3)		
1	15.102	0.396
2	15.504	1.183
3	16.414	0.664
4	19.590	6.352
Case No. (4)		
1	9.212	0.748
2	10.128	0.669
3	15.890	4.808
4	29.304	9.792
Case No. (5)		
1	9.898	0.655
2	19.172	21.005

of the initial crack length. With longer initial cracks the crack instability is reached after shorter stable crack growths.

4.3. Loading step variation

In Figure 4.8, the stress-strain curves are displayed for the dimensionless initial crack length $a_0/b = 0.3$ and three different strain increments of $\Delta\epsilon = 1.67 \times 10^{-5}$, 3.33×10^{-5} and 6.67×10^{-5}. The maximum stress tends to increase slightly by increasing the strain increment. The ratio of stiffness loss by material damage to total stiffness loss as a function of strain, ϵ, is given in Figure 4.9. The influence of material damage increases when the crack advances and a stationary value of the ratio is eventually reached. The stress

TABLE 4.4(a).
Level of damage according to equation (2.73) in each finite element and at each loading increment. Case No. 1 in Table 4.1.

Damage element	Increment $j = 1, 2$, etc.				
reference number	1	2	3	4	5
1	–	10	23	25	25
2	–	–	7	14	14
3	–	–	9	25	25
4	–	–	–	14	25
5	–	–	–	8	13
6	–	–	–	–	–
7	–	–	–	–	–
8	–	–	–	–	–
9	–	–	–	–	–
10	–	–	7	21	25
11	–	–	–	–	–
12	–	–	–	–	–
13	–	–	–	–	–
14	–	–	–	4	10
15	–	–	–	5	20
16	–	–	–	–	12
17	–	–	–	–	3
18	–	–	–	–	5
19	–	–	–	–	8
20	–	–	–	–	4
21	–	–	–	–	–
22	–	–	–	–	–
23	–	–	–	–	–
24	–	–	–	–	–
25	–	–	–	–	–
26	–	–	–	–	3
27	–	–	–	–	5
28	–	–	–	–	2

TABLE 4.4(b)
The same as in Table 4.4(a). Case No. 2 in Table 4.1.

Damage element	Increment $j = 1, 2$, etc.				
reference number	1	2	3	4	5
1	–	14	25	25	25
2	–	–	9	15	15
3	–	–	14	25	25
4	–	–	3	18	25
5	–	–	3	11	15
6	–	–	–	–	–
7	–	–	–	–	–
8	–	–	–	–	–
9	–	–	–	–	–
10	–	–	11	25	25
11	–	–	–	–	–

TABLE 4.4(b) (CONTINUED)

Damage element reference number	Increment *j* = 1, 2, etc. 1	2	3	4	5
12	–	–	–	–	–
13	–	–	–	–	–
14	–	–	–	6	12
15	–	–	–	10	24
16	–	–	–	2	16
17	–	–	–	–	4
18	–	–	–	–	11
19	–	–	–	–	11
20	–	–	–	–	4
21	–	–	–	–	–
22	–	–	–	–	–
23	–	–	–	–	–
24	–	–	–	–	–
25	–	–	–	–	–
26	–	–	–	–	5
27	–	–	–	–	10
28	–	–	–	–	3

TABLE 4.4(c)
The same as in Table 4.4(a). Case No. 3 in Table 4.1.

Damage element reference number	Increment *j* = 1, 2, etc. 1	2	3	4
1	–	17	25	25
2	–	2	12	17
3	–	–	18	25
4	–	–	6	22
5	–	–	5	13
6	–	–	–	–
7	–	–	–	–
8	–	–	–	–
9	–	–	–	–
10	–	–	15	25
11	–	–	–	–
12	–	–	–	–
13	–	–	–	–
14	–	–	–	7
15	–	–	–	13
16	–	–	–	3
17	–	–	–	–
18	–	–	–	–
19	–	–	–	2
20	–	–	–	–
21	–	–	–	–
22	–	–	–	–
23	–	–	–	–
24	–	–	–	–

TABLE 4.4(c). (CONTINUED)

Damage element reference number	Increment $j = 1, 2$, etc. 1	2	3	4
25	–	–	–	–
26	–	–	–	–
27	–	–	–	2

TABLE 4.4(d).
The same as in Table 4.4(a). Case No. 4 in Table 4.1

Damage element reference number	Increment $j = 1, 2$, etc. 1	2	3	4
1	10	25	25	25
2	–	15	25	25
3	–	18	25	25
4	–	8	25	25
5	–	9	21	25
6	–	–	–	–
7	–	–	–	–
8	–	–	–	–
9	–	4	5	14
10	–	15	25	25
11	–	–	–	–
12	–	–	–	–
13	–	–	–	–
14	–	3	16	21
15	–	2	21	25
16	–	–	14	25
17	–	–	8	25
18	–	–	9	25
19	–	–	12	25
20	–	–	10	16
21	–	–	–	–
22	–	–	–	–
23	–	–	–	–
24	–	–	–	–
25	–	–	4	8
26	–	–	8	16
27	–	–	9	20
28	–	–	7	13
29	–	–	5	8
30	–	–	–	3
31	–	–	–	–
32	–	–	–	–
33	–	–	–	–
34	–	–	–	–
35	–	–	–	–
36	–	–	3	3
37	–	–	5	5
38	–	–	3	3

TABLE 4.4(d) (CONTINUED)

Damage element	Increment $j = 1, 2$, etc.			
reference number	1	2	3	4
39	–	–	2	2
40	–	–	–	–
41	–	–	–	–
42	–	–	–	–
43	–	–	–	–
44	–	–	–	–
45	–	–	–	–
46	–	–	2	2
47	–	–	2	2
48	–	–	2	2
49	–	–	2	2
50	–	–	–	–
51	–	–	–	–
52	–	–	–	–

TABLE 4.4(e).
The same as in Table 4.4(a). Case No. 5 in Table 4.1.

Damage element	Increment $j = 1, 2$, etc.	
reference number	1	2
1	25	25
2	17	25
3	15	25
4	7	25
5	9	25
6	–	6
7	–	–
8	–	–
9	6	15
10	14	25
11	–	–
12	–	–
13	–	3
14	3	23
15	2	25
16	–	21
17	–	16
18	–	17
19	–	20
20	–	18
21	–	2
22	–	–
23	–	–
24	–	3
25	–	13
26	–	16
27	–	17

TABLE 4.4(e) (CONTINUED)

Damage element reference number	Increment $j = 1, 2$, etc.	
	1	2
28	–	16
29	–	13
30	–	10
31	–	6
32	–	3
33	–	6
34	–	8
35	–	10
36	–	12
37	–	14
38	–	12
39	–	11
40	–	10
41	–	9
42	–	8
43	–	9
44	–	10
45	–	10
46	–	11
47	–	11
48	–	11
49	–	11
50	–	10
51	–	10
52	–	10

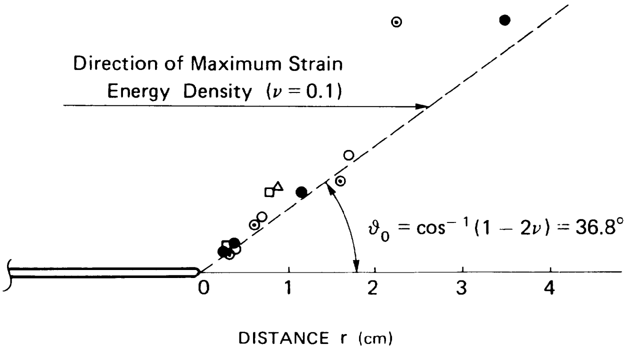

Fig. 4.3. Trajectories of the damage center during the loading process of a center cracked slab in tension.

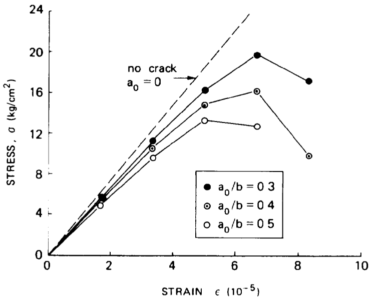

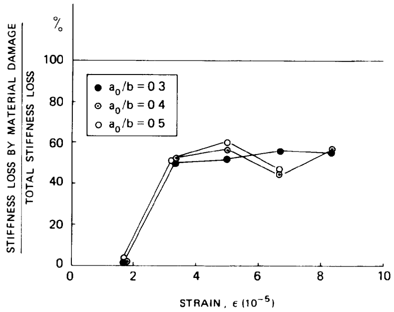

Fig. 4.4. Stress-strain diagrams for three different initial crack lengths and $\Delta\epsilon = 1.67 \times 10^{-5}$.

Fig. 4.5. Ratio of stiffness loss by material damage to total stiffness loss as a function of strain, for three different initial crack lengths and $\Delta\epsilon = 1.67 \times 10^{-5}$.

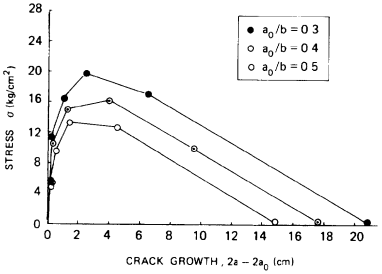

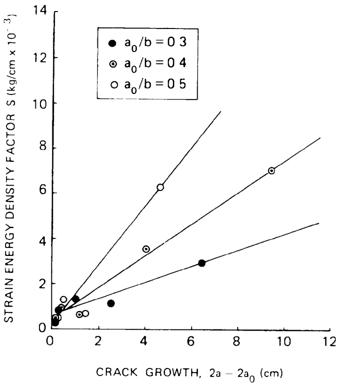

Fig. 4.6. Stress-crack growth diagrams for three different initial crack lengths and $\Delta\epsilon = 1.67 \times 10^{-5}$.

Fig. 4.7. Strain energy density factor versus crack growth for three different initial crack lengths and $\Delta\epsilon = 1.67 \times 10^{-5}$.

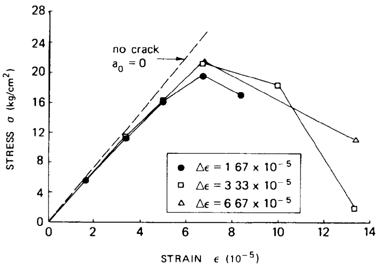

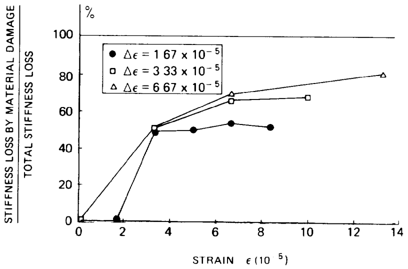

Fig. 4.8. Stress-strain diagrams for $a_0/b = 0.3$ and three different loading increments.

Fig. 4.9. Ratio of stiffness loss by material damage to total stiffness loss as a function of strain, for three different loading increments and $a_0/b = 0.3$.

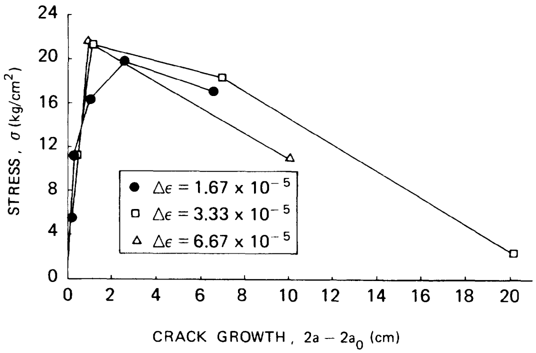

Fig. 4.10. Stress-crack growth diagrams for three different loading increments and $a_0/b = 0.3$.

σ as a function of crack growth $2(a - a_0)$ is shown in Figure 4.10. Note that the results are not sensitive to changes in the load step $\Delta\epsilon$.

In Figure 4.11, the values of strain energy density factor, S, are plotted against crack growth. An increase in the strain increment $\Delta\epsilon$ tends to increase the slope of the S versus a line. As in the case of the three point bending test in chapter 3, larger load steps tend to decrease subcritical crack growth and enhance global instability.

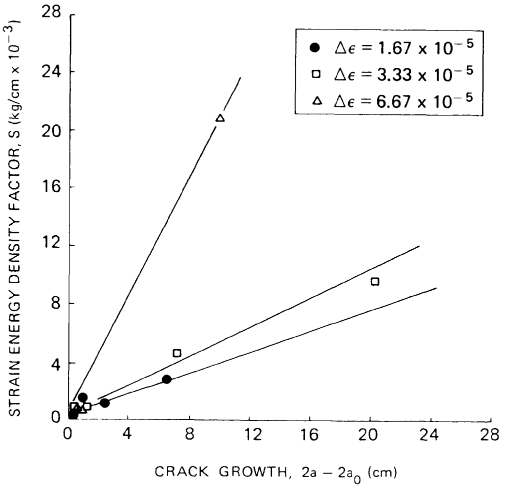

Fig. 4.11. Strain energy density factor versus crack growth for three different loading increments and $a_0/b = 0.3$.

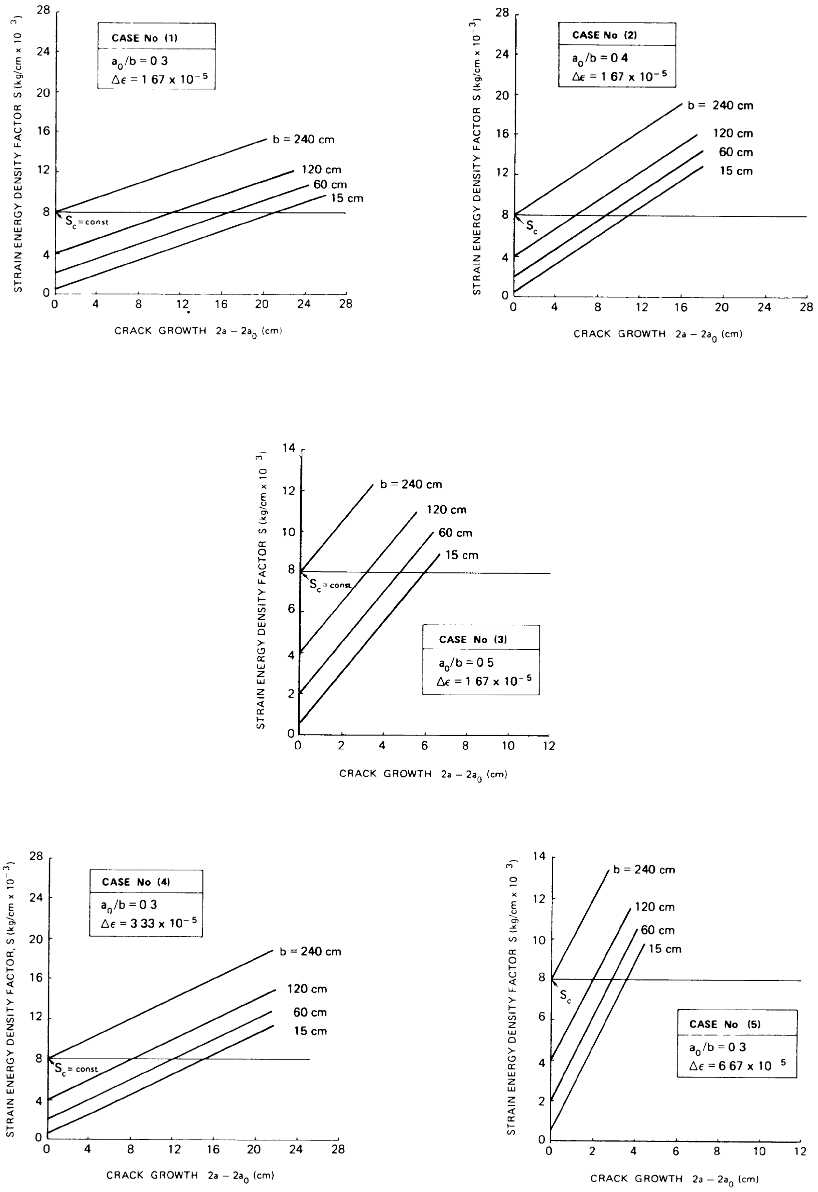

Fig. 4.12. (a) Straight line plots of strain energy density factor versus crack growth, varying the specimen size scale. Case No. 1 in Table 4.1. (b) The same as in Figure 4.12(a). Case No. 2 in Table 4.1. (c) The same as in Figure 4.12(a). Case No. 3 in Table 4.1. (d) The same as in Figure 4.12(a). Case No. 4 in Table 4.1. (e). The same as in Figure 4.12(a). Case No. 5 in Table 4.1.

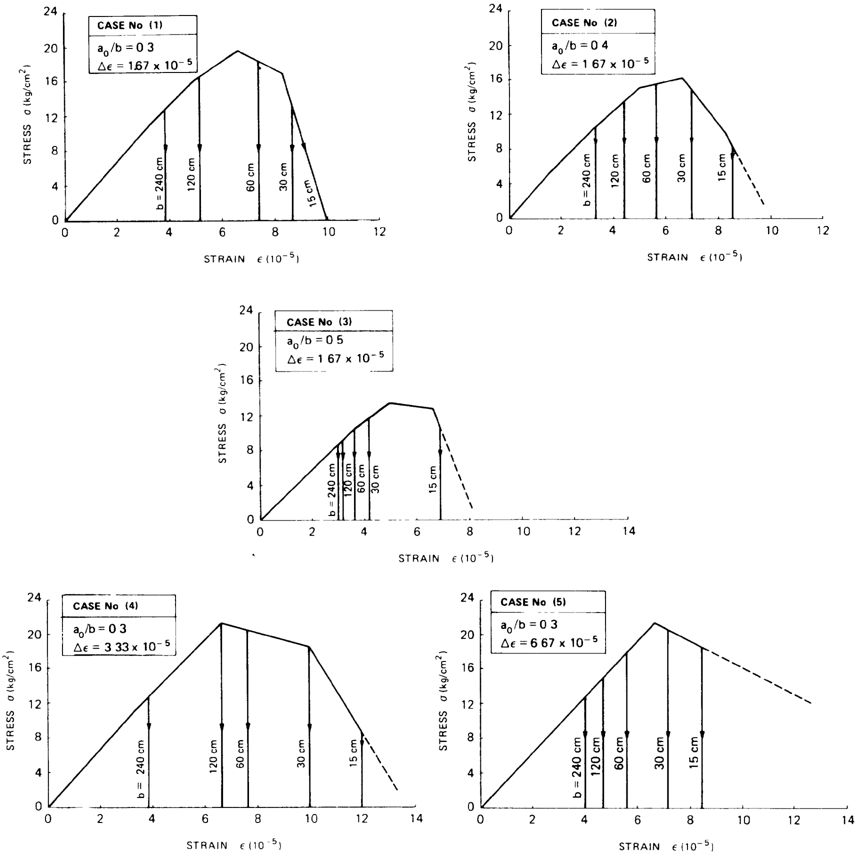

Fig. 4.13. (a) Stress-strain diagrams, varying the specimen size scale. Case No. 1 in Table 4.1. (b) The same as in Figure 4.13(a). Case No. 2 in Table 4.1. (c) The same as in Figure 4.13(a). Case No. 3 in Table 4.1. (d) The same as in Figure 4.13(a). Case No. 4 in Table 4.1. (e) The same as in Figure 4.13(a). Case No. 5 in Table 4.1.

4.4. Size scale effect of center cracked slab

Figures 4.12(a) to (e) inclusive give the straight line plots of S versus crack growth for different cases by increasing b from 15 cm and larger. As in section 3.4, the critical crack growth decreases with increasing specimen size. For Case (1), with $S_c = 8 \times 10^{-3}$ kg/cm, the limiting size is $b = 240$ cm, Figure 4.12(a). Beyond this size, stable crack growth ceases to occur and failure corresponds to unstable crack propagation or catastrophic fracture. Figures 4.13(a) to (e) inclusive show the relations between stress and strain. The vertical lines with arrows indicate the limiting values of ϵ as the critical

TABLE 4.5.
(a) Maximum stress for different size scales and according to the various theories: Strain Energy Density Theory, Linear Elastic Fracture Mechanics, Limit Analysis. Case No. 1 in Table 4.1. (b) The same as in Table 4.5(a). Case No. 2 in Table 4.1. (c) The same as in Table 4.5(a). Case No. 3 in Table 4.1. (d) The same as in Table 4.5(a). Case No. 4 in Table 4.1. (e) The same as in Table 4.5(a). Case No. 5 in Table 4.1.

Case no. (1)

Size b, cm	15	30	60	120	240
$\sigma^{(1)}_{\max}$ (SEDT), kg/cm^2	19.88	19.88	19.88	16.72	9.13
$\sigma^{(2)}_{\max}$ (LEFM), kg/cm^2	36.35	25.70	18.18	12.85	9.13
$\sigma^{(3)}_{\max}$ (Limit analysis), kg/cm^2	22.33	22.33	22.33	22.33	22.33
$\sigma^{(1)}_{\max}/\sigma^{(2)}_{\max}$ ratio	0.55	0.77	1.09	1.30	1.00
$\sigma^{(3)}_{\max}/\sigma^{(2)}_{\max}$ ratio	0.61	0.87	1.23	1.73	2.44

Case no. (2)

Size b, cm	15	30	60	120	240
$\sigma^{(1)}_{\max}$ (SEDT), kg/cm^2	16.28	16.28	15.45	13.38	7.43
$\sigma^{(2)}_{\max}$ (LEFM), kg/cm^2	29.70	21.03	14.87	10.51	7.43
$\sigma^{(3)}_{\max}$ (Limit analysis), kg/cm^2	19.14	19.14	19.14	19.14	19.14
$\sigma^{(1)}_{\max}/\sigma^{(2)}_{\max}$ ratio	0.55	0.77	1.03	1.27	1.00
$\sigma^{(3)}_{\max}/\sigma^{(2)}_{\max}$ ratio	0.64	0.91	1.29	1.82	2.57

Case no. (3)

Size b, cm	15	30	60	120	240
$\sigma^{(1)}_{\max}$ (SEDT), kg/cm^2	13.23	11.47	10.31	9.05	6.23
$\sigma^{(2)}_{\max}$ (LEFM), kg/cm^2	24.93	17.63	12.46	8.81	6.23
$\sigma^{(3)}_{\max}$ (Limit analysis), kg/cm^2	15.95	15.95	15.95	15.95	15.95
$\sigma^{(1)}_{\max}/\sigma^{(2)}_{\max}$ ratio	0.53	0.65	0.83	1.03	1.00
$\sigma^{(3)}_{\max}/\sigma^{(2)}_{\max}$ ratio	0.63	0.90	1.28	1.81	2.56

Case no. (4)

Size b, cm	15	30	60	120	240
$\sigma^{(1)}_{\max}$ (SEDT), kg/cm^2	21.22	21.22	21.22	21.22	9.13
$\sigma^{(2)}_{\max}$ (LEFM), kg/cm^2	36.35	25.70	18.18	12.85	9.13
$\sigma^{(3)}_{\max}$ (Limit analysis), kg/cm^2	22.33	22.33	22.33	22.33	22.33
$\sigma^{(1)}_{\max}/\sigma^{(2)}_{\max}$ ratio	0.58	0.82	1.16	1.65	1.00
$\sigma^{(3)}_{\max}/\sigma^{(2)}_{\max}$ ratio	0.61	0.87	1.23	1.73	2.44

Case no. (5)

Size b, cm	15	30	60	120	240
$\sigma^{(1)}_{\max}$ (SEDT), kg/cm^2	21.40	21.40	18.00	15.08	9.13
$\sigma^{(2)}_{\max}$ (LEFM), kg/cm^2	36.35	25.70	18.18	12.85	9.13
$\sigma^{(3)}_{\max}$ (Limit analysis), kg/cm^2	22.33	22.33	22.33	22.33	22.33
$\sigma^{(1)}_{\max}/\sigma^{(2)}_{\max}$ ratio	0.59	0.83	0.99	1.17	1.00
$\sigma^{(3)}_{\max}/\sigma^{(2)}_{\max}$ ratio	0.61	0.87	1.23	1.73	2.44

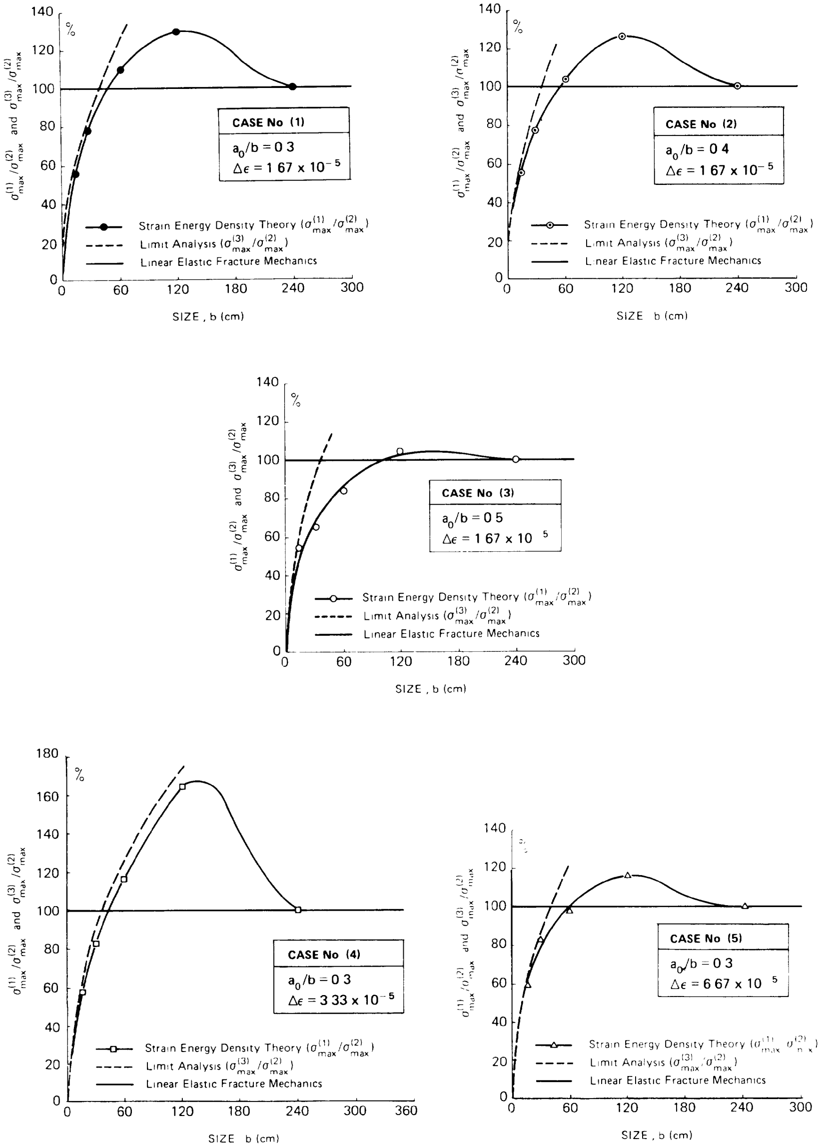

Fig. 4.14. (a) Maximum stress predicted by Strain Energy Density Theory and by Limit Analysis referred to the critical stress from LEFM. Case No. 1 in Table 4.1. (b). The same as in Figure 4.14(a). Case No. 2 in Table 4.1. (c) The same as in Figure 4.14(a). Case No. 3 in Table 4.1. (d) The same as in Figure 4.14(a). Case No. 4 in Table 4.1. (e) The same as in Figure 4.14(a). Case No. 5 in Table 4.1.

strain energy density factor, $S_c = 8 \times 10^{-3}$ kg/cm, is reached. Crack instability occurs for smaller strains as the size b is increased. This is obvious, since the initial crack length a_0 also increases for a given ratio of a_0/b. Case (1) shows that structural instability occurs before unstable crack propagation only for $b \lesssim 80$ cm, Figure 4.13(a). For $b = 120$ cm, the softening behavior is not present and the crack starts spreading in an unstable manner while the stress σ is still in the ascending stage.

It is also interesting to consider the maximum stress, $\sigma^{(2)}_{\max}$, resulting from the Linear Elastic Fracture Mechanics solution [5]:

$$K_I = \sigma\sqrt{\pi a_0}\left(\sec\frac{\pi a_0}{2b}\right)^{1/2} \tag{4.1}$$

Let $\sigma^{(3)}_{\max}$ denote the result predicted from the limit analysis:

$$\sigma^{(3)}_{\max} = \sigma_u\left(1 - \frac{a_0}{b}\right) \tag{4.2}$$

where the ligament size at collapse is assumed to be $2(b - a_0)$. All the maximum stresses obtained by the different approaches are reported in Tables 4.5. Normalizing the stresses $\sigma^{(1)}_{\max}$ and $\sigma^{(3)}_{\max}$, obtained by the present approach and by the limit analysis respectively, with $\sigma^{(2)}_{\max}$, obtained through Linear Elastic Fracture Mechanics, the results for the different failure modes are displayed in Figures 4.14(a) to (e) inclusive. The transition from plastic collapse to brittle fracture can be achieved simply by changing the specimen size.

The strain energy density theory has thus enabled the predictions of all failure modes between the two extremes of brittle fracture and plastic collapse. Smaller specimen tests can thus be performed to predict the behavior of larger specimens or structural components. Moreover, the predictions were made only using the uniaxial stress and strain data, an accomplishment that has not been achieved by the other failure criteria.

References

1. Hilton, P.D., Gifford, L.N. and Lomacky, O., Finite element fracture mechanics of two-dimensional and axisymmetric elastic and elastic-plastic cracked structures, Report No. 4493, Naval Ship Research and Development Center (1975).
2. Sih, G.C. and Matic, P., Mechanical response of materials with physical defects. Part 1: Modelling of material damage for center cracked panel, Report AFOSR-TR-81-1, Institute of Fracture and Solid Mechanics, Lehigh University (1981).
3. Sih, G.C. and Matic, P., Mechanical response of materials with physical defects. Part 2: Combined modelling of material damage and crack propagation for center

cracked panel, Report AFOSR-TR-82-2, Institute of Fracture and Solid Mechanics, Lehigh University (1982).

4. Carpinteri, A. and Sih, G.C., Damage accumulation and crack growth in bilinear materials with softening: application of strain energy density theory, J. of Theoretical and Appl. Fract. Mechanics, Vol. 1, No. 2, pp. 145–160 (1984).
5. Sih, G.C., Handbook of Stress-Intensity Factors for Researchers and Engineers, Lehigh University (1973).

5

Off-center compression of slab with edge crack

5.1. Preliminary information

Further application of the strain energy density theory will be made to the problem of a slab with an edge crack subjected to off-center compression with *b* specified as illustrated in Figure 5.1 and *t* equal to *b*. The material properties for the slab correspond to those of Material 3 in Figure 2.29. The grid pattern for the finite element meshes is shown in Figure 5.2 such that only one-half of the problem needs to be analyzed on account of symmetry. Referring to the damage-crack growth model based on Strain Energy Density Theory in [1], the crack growth resistance curves will be developed by specifying the vertical displacement δ as the applied load.

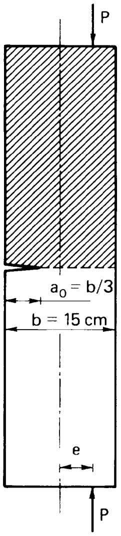

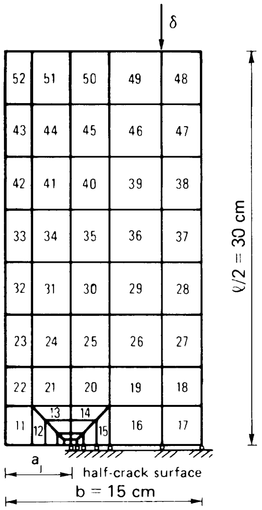

Fig. 5.1. Off-center compression of slab with edge crack.

Fig. 5.2. Finite element idealization of the cracked slab with off-center compression in Figure 5.1. The zoom area is the same as in Figure 4.2(b).

TABLE 5.1.
The five cases analyzed in this chapter, changing load eccentricity and loading increments.

Case no.	Eccentricity e/b	Displacement increment $\Delta\delta$ (10^{-3} cm)	Symbol
I (1)	0.30	4	●
II (2)	0.35	4	○
III (3)	0.40	4	○
IV (4)	0.40	2	□
V (5)	0.40	1	△

Table 5.1 summarizes the different cases to be investigated. Three different eccentricities, e/b, and three different loading (displacement) increments are considered. The load-displacement values and the crack growth increments are specified in Table 5.2, while the crack lengths and the strain energy density factors are reported in Table 5.3. The damage level according to equation (2.73) is described in Tables 5.4(a) to (e) inclusive for each loading step.

5.2. Load eccentricity effect

Numerical results will be presented to study the influence of load eccentricity, e/b. The load-displacement responses for the case $\Delta\delta = 4 \times 10^{-3}$ cm, are displayed in Figure 5.3. The softening behavior is absent when the loading eccentricity is very small. The compressive stress field in the ligament tends to arrest the crack inhibiting material damage.

Shown in Figure 5.4 is the ratio of stiffness loss by material damage to total stiffness loss (by material damage and crack growth) as a function of the displacement, δ. This ratio tends to zero for small and large displacements. For intermediate displacements, these curves present a maximum which tends to increase by decreasing the load eccentricity, e/b. In Figure 5.5, the load P is given as a function of the crack growth, $(a - a_0)$. For large loading eccentricities, $e/b = 0.35$ and 0.40, the load increases and then decreases after reaching a maximum. The maximum represents the structural instability. For small loading eccentricities, $e/b = 0.30$, the unstable stage disappears and the crack stops since the compressive stress field dominates.

When the axial force, P, is compressive, a bending moment $M = Pe$ is created that tends to open the crack. The total stress-intensity factor can be obtained by applying the superposition principle:

$$K_I = K_I^{(M)} - K_I^{(P)} \tag{5.1}$$

in which [2, 3]

TABLE 5.2.
Load, displacement and crack growth increment at each loading increment and for each case in Table 5.1.

Case no. (1)

Increment $j = 1, 2,$ etc.	Load P_j (kg)	Displacement δ_j (10^{-3} cm)	Crack growth increment Δa_j (cm)
1	4134	4	0.037
2	8256	8	0.140
3	12306	12	0.500
4	16176	16	0.500
5	19715	20	0.500
6	23094	24	0.000
7	27902	28	0.000
Case no. (2)			
1	3519	4	0.097
2	6976	8	0.500
3	10296	12	1.000
4	13284	16	1.000
5	11365	20	2.000
Case no. (3)			
1	2847	4	0.221
2	5900	8	0.975
3	8532	12	1.579
4	10132	16	2.000
Case no. (4)			
1	1516	2	0.000
2	3018	4	0.238
3	4470	6	0.500
4	5836	8	1.000
5	7145	10	1.042
6	8280	12	1.006
Case no. (5)			
1	758	1	0.000
2	1516	2	0.000
3	2271	3	0.066
4	3014	4	0.248
5	3729	5	0.500
6	4428	6	0.500
7	5107	7	0.527
8	5733	8	1.000

$$K_I^{(M)} = \frac{M}{b^{3/2}t} Y_M(\xi) \tag{5.2a}$$

$$K_I^{(P)} = \frac{P}{b^{1/2}t} Y_P(\xi) \tag{5.2b}$$

TABLE 5.3.
Crack length and strain energy density factor at each loading increment and for each case in Table 5.1.

Increment $j = 1, 2,$ etc.	Crack length a_j (cm)	Strain energy density factor S_j (kg/cm $\times 10^{-3}$)
Case no. (1)		
1	5.037	0.287
2	5.177	0.953
3	5.677	2.265
4	6.177	2.157
5	6.677	2.035
6	6.677	0.000
7	6.677	0.000
Case no. (2)		
1	5.097	0.714
2	5.597	2.132
3	6.597	4.410
4	7.597	3.680
5	9.597	9.240
Case no. (3)		
1	5.221	1.398
2	6.191	5.187
3	7.770	8.890
4	9.770	12.240
Case no. (4)		
1	5.000	0.000
2	5.238	1.587
3	5.738	2.182
4	6.738	4.560
5	7.780	6.387
6	8.786	4.024
Case no. (5)		
1	5.000	0.000
2	5.000	0.000
3	5.066	0.501
4	5.314	1.614
5	5.814	2.752
6	6.314	1.995
7	6.841	1.771
8	7.841	4.415

where $\xi = a/b$ is the relative crack length and the functions Y_M and Y_P, for $0 \leqslant \xi \leqslant 0.7$, are given by

$$Y_M(\xi) = 6 \times (1.99\xi^{1/2} - 2.47\xi^{3/2} + 12.97\xi^{5/2} - 23.17\xi^{7/2} + 24.80\xi^{9/2}) \tag{5.3a}$$

TABLE 5.4(a).
Level of damage according to equation (2.73) in each finite element and at each loading increment. Case No. 1 in Table 5.1.

Damage element reference number	Increment $j = 1, 2$, etc. 1	2	3	4	5	6	7
1	–	12	25	25	25	25	25
2	–	–	–	19	25	25	–
3	–	–	4	9	13	–	–
4	–	–	–	–	–	–	–
5	–	–	–	–	15	–	–
6	–	–	–	–	2	4	15
7	–	–	–	–	–	–	7
8	–	–	–	–	–	–	7
9	–	–	–	10	14	14	25
10	–	3	13	13	13	19	25
11	–	–	–	–	–	–	–
12	–	–	–	–	–	–	–
13	–	–	–	–	–	–	–
14	–	–	–	–	–	–	–
15	–	–	–	–	–	–	–
16	–	–	–	–	–	–	–
17	–	–	–	–	–	–	–
18	–	–	–	–	–	–	–
19	–	–	–	–	–	–	–
20	–	–	–	–	–	–	–
21	–	–	–	–	–	–	–
22	–	–	–	–	–	–	–
23	–	–	–	–	3	5	7
24	–	–	–	–	–	–	–
25	–	–	–	–	–	–	–
26	–	–	–	–	–	–	–
27	–	–	–	–	–	–	–
28	–	–	–	–	–	–	–
29	–	–	–	–	–	–	–
30	–	–	–	–	–	–	–
31	–	–	–	–	–	–	–
32	–	–	–	5	11	16	21
33	–	–	–	6	12	17	22
34	–	–	–	–	–	–	–
35	–	–	–	–	–	–	–
36	–	–	–	–	–	–	–
37	–	–	–	–	–	–	–
38	–	–	–	–	–	–	–
39	–	–	–	–	–	–	–
40	–	–	–	–	–	–	–
41	–	–	–	–	–	–	–
42	–	–	–	3	7	8	8
43	–	–	–	–	–	–	–
44	–	–	–	–	–	–	–
45	–	–	–	–	–	–	–
46	–	–	–	–	–	–	–

TABLE 5.4(a) (CONTINUED)

Damage element reference number	Increment $j = 1, 2$, etc. 1	2	3	4	5	6	7
47	–	–	–	–	–	–	–
48	–	–	–	–	–	–	–
49	–	–	–	–	–	–	–
50	–	–	7	19	25	25	–
51	–	–	–	–	–	–	–
52	–	–	–	–	–	–	–

TABLE 5.4(b).
The same as in Table 5.4(a). Case No. 2 in Table 5.1.

Damage element reference number	Increment $j = 1, 2$, etc. 1	2	3	4	5
1	7	25	25	25	25
2	–	6	25	25	25
3	–	10	25	25	25
4	–	–	7	17	25
5	–	–	2	21	25
6	–	–	–	11	13
7	–	–	–	–	–
8	–	–	–	–	–
9	–	3	12	12	16
10	–	17	25	25	25
11	–	–	–	–	–
12	–	–	–	–	–
13	–	–	–	–	5
14	–	–	–	2	24
15	–	–	–	–	–
16	–	–	–	–	–
17	–	–	–	–	–
18	–	–	–	–	–
19	–	–	–	–	–
20	–	–	–	–	–
21	–	–	–	–	–
22	–	–	–	–	–
23	–	–	–	–	2
24	–	–	–	–	–
25	–	–	–	–	–
26	–	–	–	–	–
27	–	–	–	–	–
28	–	–	–	–	–
29	–	–	–	–	–
30	–	–	–	–	–
31	–	–	–	–	–
32	–	–	4	10	15
33	–	–	5	12	17
34	–	–	–	–	–
35	–	–	–	–	–

TABLE 5.4(b) (CONTINUED)

Damage element reference number	Increment $j = 1, 2$, etc. 1	2	3	4	5
36	–	–	–	–	–
37	–	–	–	–	–
38	–	–	–	–	–
39	–	–	–	–	–
40	–	–	–	–	–
41	–	–	–	–	–
42	–	–	2	6	9
43	–	–	–	–	–
44	–	–	–	–	–
45	–	–	–	–	–
46	–	–	–	–	–
47	–	–	–	–	–
48	–	–	–	–	–
49	–	–	–	–	–
50	–	–	4	19	25
51	–	–	–	–	–
52	–	–	–	–	–

TABLE 5.4(c).
The same as in Table 5.4(a). Case No. 3 in Table 5.1.

Damage element reference number	Increment $j = 1, 2$, etc. 1	2	3	4
1	15	25	25	25
2	–	15	25	25
3	–	19	25	25
4	–	–	18	25
5	–	–	14	25
6	–	–	6	15
7	–	–	–	–
8	–	–	–	–
9	–	9	15	19
10	2	22	25	25
11	–	–	–	–
12	–	–	–	–
13	–	–	–	5
14	–	–	–	11
15	–	–	7	–
16	–	–	–	–
17	–	–	–	–
18	–	–	–	–
19	–	–	–	–
20	–	–	–	–
21	–	–	–	–
22	–	–	–	–
23	–	–	–	–
24	–	–	–	–

TABLE 5.4(c) (CONTINUED)

Damage element reference number	Increment $j = 1, 2$, etc. 1	2	3	4
25	–	–	–	–
26	–	–	–	–
27	–	–	–	–
28	–	–	–	–
29	–	–	–	–
30	–	–	–	–
31	–	–	–	–
32	–	–	4	7
33	–	–	5	10
34	–	–	–	–
35	–	–	–	–
36	–	–	–	–
37	–	–	–	–
38	–	–	–	–
39	–	–	–	–
40	–	–	–	–
41	–	–	–	–
42	–	–	–	3
43	–	–	–	–
44	–	–	–	–
45	–	–	–	–
46	–	–	–	–
47	–	–	–	–
48	–	–	–	–
49	–	–	–	–
50	–	–	5	21
51	–	–	–	5
52	–	–	–	–

TABLE 5.4(d).
The same as in Table 5.4(a). Case No. 4 in Table 5.1.

Damage element reference number	Increment $j = 1, 2$, etc. 1	2	3	4	5	6
1	–	13	25	25	25	25
2	–	–	5	20	25	25
3	–	–	8	25	25	25
4	–	–	–	3	16	22
5	–	–	–	–	14	25
6	–	–	–	–	–	4
7	–	–	–	–	–	–
8	–	–	–	–	–	–
9	–	–	–	6	6	6
10	–	7	20	25	25	25
11	–	–	–	–	–	–
12	–	–	–	–	–	–
13	–	–	–	–	–	–

TABLE 5.4(d) (CONTINUED)

Damage element reference number	Increment $j = 1, 2$, etc. 1	2	3	4	5	6
14	–	–	–	–	–	3
15	–	–	–	–	2	–
16	–	–	–	–	–	–
17	–	–	–	–	–	–
18	–	–	–	–	–	–
19	–	–	–	–	–	–
20	–	–	–	–	–	–
21	–	–	–	–	–	–
22	–	–	–	–	–	–
23	–	–	–	–	–	–
24	–	–	–	–	–	–
25	–	–	–	–	–	–
50	–	–	–	–	2	13

TABLE 5.4(e).
The same as in Table 5.4(a). Case No. 5 in Table 5.1.

Damage element reference number	Increment $j = 1, 2$, etc. 1	2	3	4	5	6	7	8
1	–	–	4	14	23	25	25	25
2	–	–	–	–	–	9	18	21
3	–	–	–	–	3	14	23	25
4	–	–	–	–	–	–	–	7
5	–	–	–	–	–	–	–	4
6	–	–	–	–	–	–	–	–
7	–	–	–	–	–	–	–	–
8	–	–	–	–	–	–	–	–
9	–	–	–	–	–	–	–	–
10	–	–	–	7	15	21	25	25

$$Y_P(\xi) = 1.99\xi^{1/2} - 0.41\xi^{3/2} + 18.70\xi^{5/2} - 38.48\xi^{7/2} + 53.85\xi^{9/2} \tag{5.3b}$$

Equation (5.1) can thus be written as

$$K_I = \frac{P}{b^{1/2}t}\left[\frac{e}{b}Y_M(\xi) - Y_P(\xi)\right] \tag{5.4}$$

From the critical condition $K_I = K_{IC}$, the dimensionless axial force at incipient fracture can be obtained as a function of the crack depth, ξ, and the eccentricity e/b:

$$\frac{P_c}{K_{IC}b^{1/2}t} = \frac{1}{\frac{e}{b}Y_M(\xi) - Y_P(\xi)} \tag{5.5}$$

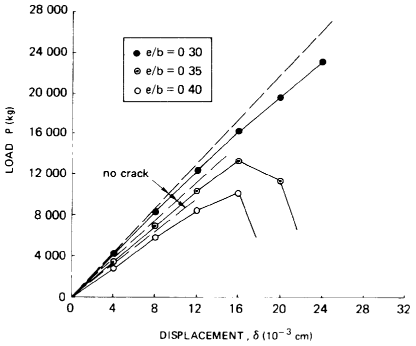

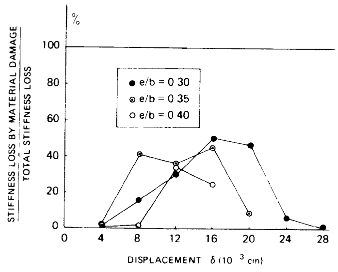

Fig. 5.3. Load-displacement diagrams for three different load eccentricities and $\Delta\delta = 4 \times 10^{-3}$ cm.

Fig. 5.4. Ratio of stiffness loss by material damage to total stiffness loss as a function of displacement, for three different load eccentricities and $\Delta\delta = 4 \times 10^{-3}$ cm.

The curves in Figure 5.6 give a graphical representation of equation (5.5) and show that for a fixed eccentricity e/b, the fracture process becomes stable after initiation. According to Linear Elastic Fracture Mechanics that accounts only for unstable crack propagation, fracture will be catastrophic in nature once the load P becomes critical. It cannot explain the nonuniform crack growth rate phenomenon owing to the effect of compression ahead of the crack. For large eccentricities, $e/b = 0.35$ and 0.40, a softening behavior is predicted that is in contrast to the stable solution obtained by Linear Elastic

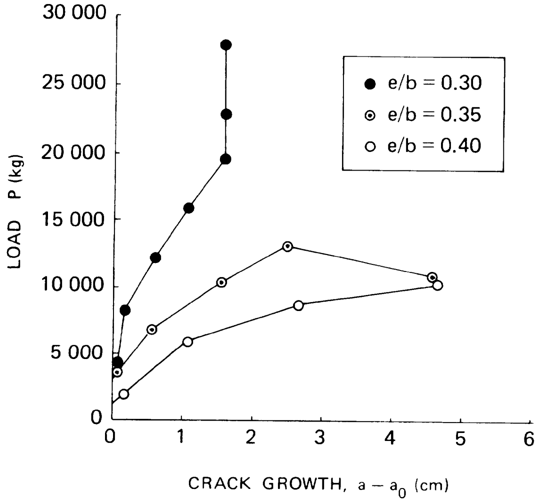

Fig. 5.5. Load-crack growth diagrams for three different load eccentricities and $\Delta\delta = 4 \times 10^{-3}$ cm.

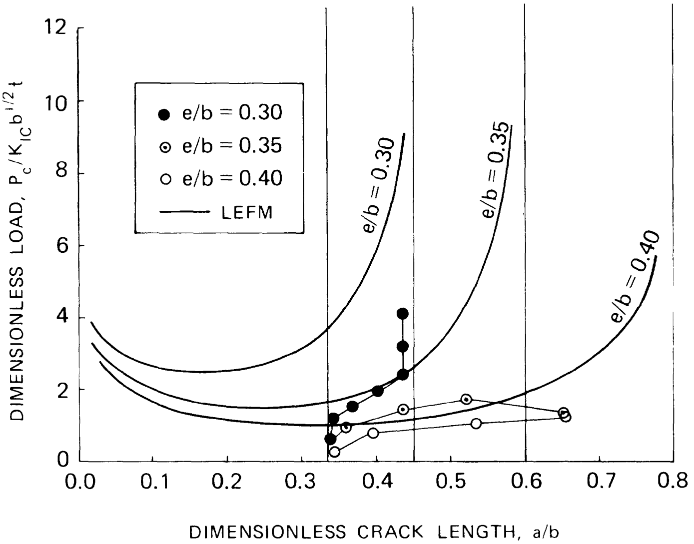

Fig. 5.6. Dimensionless load-crack length diagrams and comparison with Linear Elastic Fracture Mechanics.

Fracture Mechanics [4, 5]. On the other hand, it is interesting to observe that the crack arrest predicted by Linear Elastic Fracture Mechanics (see vertical asymptotes of Figure 5.6), is confirmed by the Strain Energy Density Theory for small eccentricities ($e/b = 0.30$).

In Figure 5.7, the values of the strain energy density factor, S, are plotted against the crack growth, $(a - a_0)$. For large eccentricities, $e/b = 0.35$ and 0.40, they increase when the crack advances, whereas for small eccentricities, $e/b = 0.30$, they increase and then decrease in a quasi-linear manner. This is due to the stability effect of compression which tends to close the crack as it

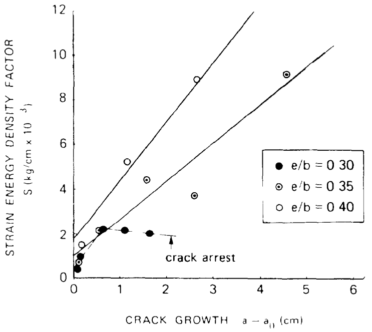

Fig. 5.7. Strain energy density factor versus crack growth for three different load eccentricities and $\Delta\delta = 4 \times 10^{-3}$ cm.

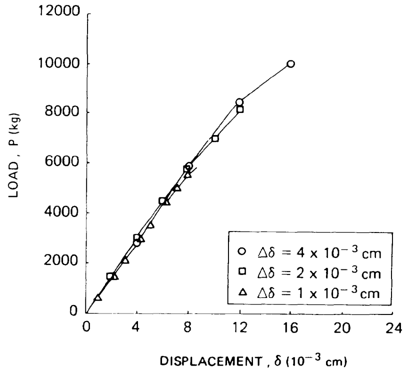

Fig. 5.8. Load-displacement diagrams for $e/b = 0.40$ and three different loading increments.

grows. The slope of the S versus a lines increases with the eccentricity ratio e/b. Obviously, subcritical crack growth will be suppressed as e/b is increased. For $S_c = 8 \times 10^{-3}$ kg/cm, the critical crack lengths $a_c = 9.2$ and 7.3 cm correspond respectively to $e/b = 0.35$ and 0.40. Unstable crack propagation fails to occur when e/b is reduced to 0.30 or smaller.

5.3. Variation in loading step

In Figure 5.8, the load-displacement curves are given for $e/b = 0.40$, while the displacement increment $\Delta\delta$ takes the values of 4×10^{-3}, 2×10^{-3} and 1×10^{-3} cm. The maximum load increases by increasing the displacement

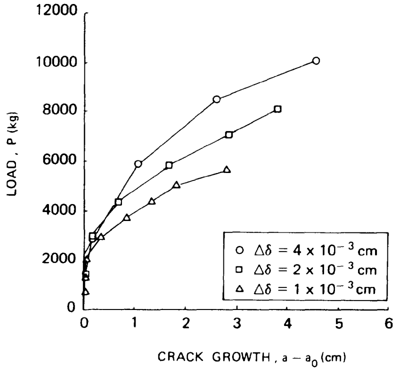

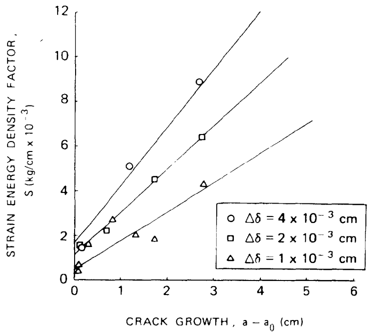

Fig. 5.9. Load-crack growth diagrams for three different loading increments and $e/b = 0.40$.

Fig. 5.10. Strain energy density factor versus crack growth for three different loading increments and $e/b = 0.40$.

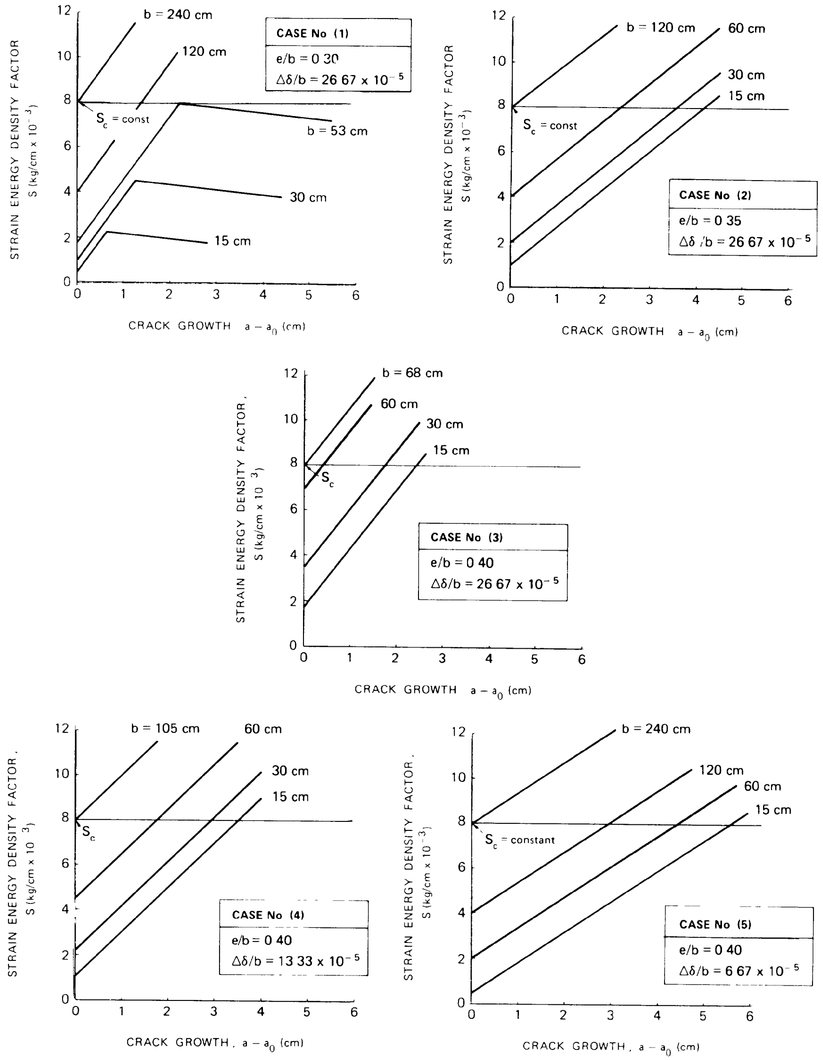

Fig. 5.11. (a) Bilinear plots of strain energy density factor versus crack growth, varying the size scale of the slab. Case No. 1 in Table 5.1. (b) Straight line plots of strain energy density factor versus crack growth, varying the size scale of the slab. Case No. 2 in Table 5.1. (c) The same as in Figure 5.11(b). Case No. 3 in Table 5.1. (d) The same as in Figure 5.11(b). Case No. 4 in Table 5.1. (e) The same as in Figure 5.11(b). Case No. 5 in Table 5.1.

increment. The solution in this case is not sensitive to changes in the load step. The variations of P with $(a - a_0)$ are shown in Figure 5.9. These curves are affected by the loading step, even during the stable stage of increasing load. The SR-curves for three different displacement steps $\Delta\delta$ are given in

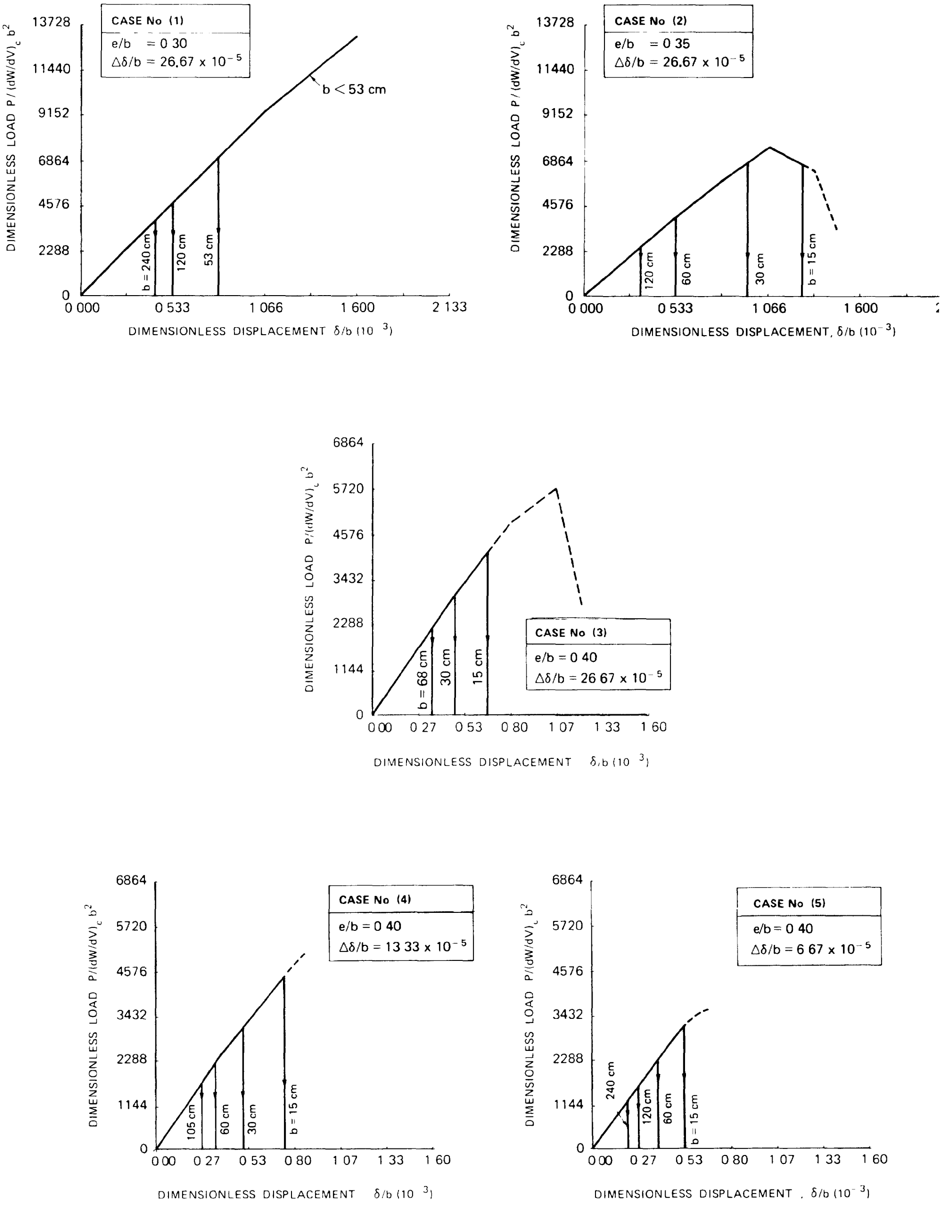

Fig. 5.12. (a) Dimensionless load-displacement diagrams, varying the size scale of the slab. Case No. 1 in Table 5.1. (b) The same as in Figure 5.12(a). Case No. 2 in Table 5.1. (c) The same as in Figure 5.12(a). Case No. 3 in Table 5.1. (d) The same as in Figure 5.12(a). Case No. 4 in Table 5.1. (e) The same as in Figure 5.12(a). Case No. 5 in Table 5.1.

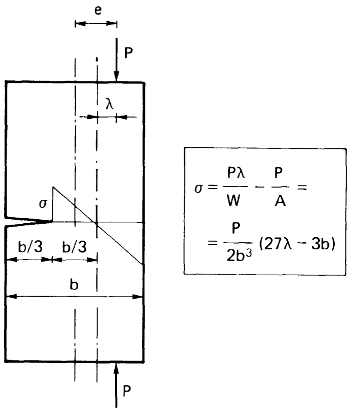

Fig. 5.13. Linear elastic limit analysis at the ligament.

Figure 5.10. These curves rotate slightly in the counterclockwise direction as $\Delta\delta$ is increased. For a constant S_c, the effect of increasing $\Delta\delta$ tends to reduce slow crack growth or to enhance brittle fracture.

5.4. Scaling in size

Figure 5.11(a) shows the bilinear S versus a variations with the size b. Crack instability occurs only for $b \geqslant 53$ cm. This is based on a critical value of $S_c = 8 \times 10^{-3}$ kg/cm. Figures 5.11(b), (c), (d) and (e), on the other hand, show a linear S versus a relationship and the curves shift upwards by increasing the structural size b. The limiting size beyond which the stable crack growth does not occur decreases when the loading eccentricity and/or the loading step increase. Figures 5.12(a) to (e) inclusive represent the relations between $P/(\mathrm{d}W/\mathrm{d}V)_c b^2$ and δ/b. The vertical lines with arrows indicate the limiting values of δ/b as the critical strain energy density factor, $S_c = 8 \times 10^{-3}$ kg/cm, is reached. The maximum load $P^{(2)}_{\max}$ can be obtained from the Linear Elastic Fracture Mechanics solution in equation (5.5). The load $P^{(3)}_{\max}$, obtained from the linear elastic limit analysis at the ligament is

$$P^{(3)}_{\max} = \frac{2\sigma_u b^3}{27\lambda - 3b} \tag{5.6}$$

where $\lambda = e - (b/6)$, Figure 5.13.

Tables 5.5(a) to (e) inclusive report the maximum loads obtained through the different assumptions and for various sizes, while Figures 5.14(a) to (e) inclusive give a graphical display of results obtained from the different theories. The strain energy density theory again predicts the entire range of failure modes from brittle fracture to plastic collapse.

TABLE 5.5.
(a) Maximum load for different size scales and according to the various theories: Strain Energy Density Theory, Linear Elastic Fracture Mechanics, Limit Analysis. Case No. 1 in Table 5.1. (b) The same as in Table 5.5(a). Case No. 2 in Table 5.1. (c) The same as in Table 5.5(a). Case No. 3 in Table 5.1. (d) The same as in Table 5.5(a). Case No. 4 in Table 5.1. (e) The same as in Table 5.5(a). Case No. 5 in Table 5.1.

Case no. (1)

Size b, cm	53	120	240
$P^{(1)}_{\max}$ (SEDT), kg	150 000	566 000	1 740 000
$P^{(2)}_{\max}$ (LEFM), kg	180 700	616 000	1 740 000
$P^{(3)}_{\max}$ (Limit analysis), kg	350 000	1 800 000	7 206 000
$P^{(1)}_{\max}/P^{(2)}_{\max}$ ratio	0.83	0.92	1.00
$P^{(3)}_{\max}/P^{(2)}_{\max}$ ratio	1.94	2.92	4.14

Case no. (2)

Size b, cm	15	30	60	120
$P^{(1)}_{\max}$ (SEDT), kg	13 284	48 000	112 000	285 000
$P^{(2)}_{\max}$ (LEFM), kg	12 580	35 600	100 600	285 000
$P^{(3)}_{\max}$ (Limit analysis), kg	7 717	30 870	123 480	494 000
$P^{(1)}_{\max}/P^{(2)}_{\max}$ ratio	1.06	1.35	1.11	1.00
$P^{(3)}_{\max}/P^{(2)}_{\max}$ ratio	0.61	0.87	1.23	1.73

Case no. (3)

Size b, cm	15	30	60	68
$P^{(1)}_{\max}$ (SEDT), kg	7 000	21 000	65 270	80 400
$P^{(2)}_{\max}$ (LEFM), kg	8 180	23 500	66 600	80 400
$P^{(3)}_{\max}$ (Limit analysis), kg	4 376	17 500	70 000	90 000
$P^{(1)}_{\max}/P^{(2)}_{\max}$ ratio	0.85	0.89	0.98	1.00
$P^{(3)}_{\max}/P^{(2)}_{\max}$ ratio	0.53	0.74	1.05	1.12

Case no. (4)

Size b, cm	15	30	60	105
$P^{(1)}_{\max}$ (SEDT), kg	7 525	22 000	64 000	151 500
$P^{(2)}_{\max}$ (LEFM), kg	8 180	23 500	66 600	151 500
$P^{(3)}_{\max}$ (Limit analysis), kg	4 376	17 500	70 000	219 000
$P^{(1)}_{\max}/P^{(2)}_{\max}$ ratio	0.92	0.94	0.96	1.00
$P^{(3)}_{\max}/P^{(2)}_{\max}$ ratio	0.53	0.74	1.05	1.44

Case no. (5)

Size b, cm	15	60	120	240
$P^{(1)}_{\max}$ (SEDT), kg	5 500	64 000	181 000	523 500
$P^{(2)}_{\max}$ (LEFM), kg	8 180	66 600	185 000	523 500
$P^{(3)}_{\max}$ (Limit analysis), kg	4 376	70 000	286 000	1 145 000
$P^{(1)}_{\max}/P^{(2)}_{\max}$ ratio	0.67	0.96	0.98	1.00
$P^{(3)}_{\max}/P^{(2)}_{\max}$ ratio	0.53	1.05	1.55	2.19

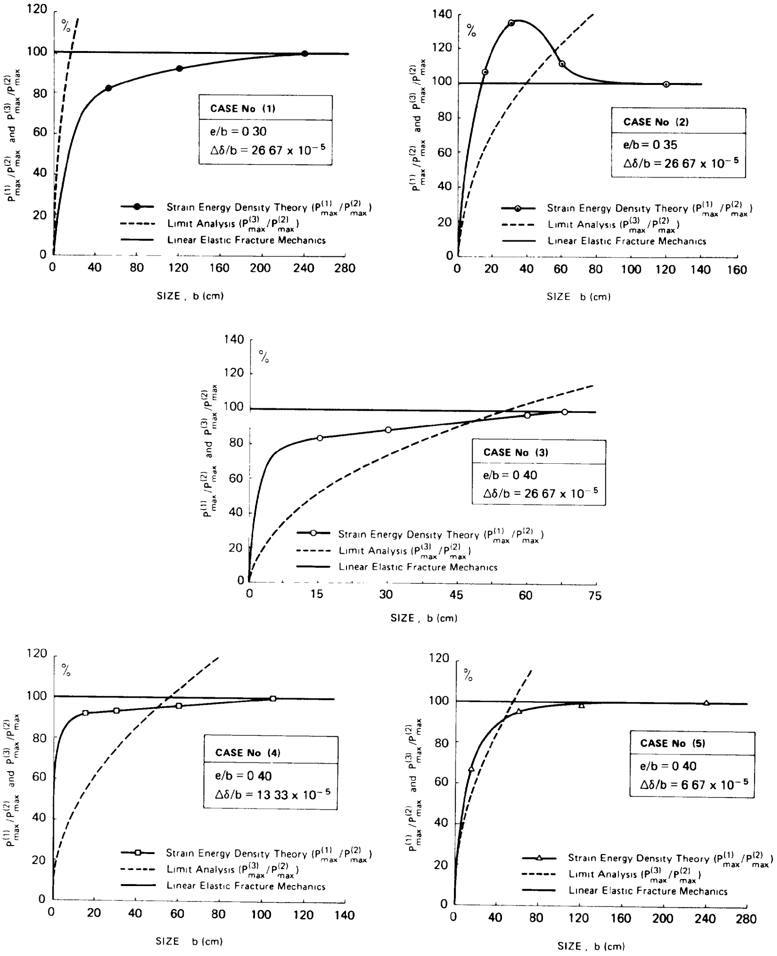

Fig. 5.14. (a) Maximum load predicted by Strain Energy Density Theory and by Limit Analysis referred to the critical load from LEFM. Case No. 1 in Table 5.1. (b) The same as in Figure 5.14(a). Case No. 2 in Table 5.1. (c) The same as in Figure 5.14(a). Case No. 3 in Table 5.1. (d) The same as in Figure 5.14(a). Case No. 4 in Table 5.1. (e) The same as in Figure 5.14(a). Case No. 5 in Table 5.1.

References

1. Carpinteri, A. and Sih, G.C., Damage accumulation and crack growth in bilinear materials with softening: application of strain energy density theory, J. of Theoretical and Applied Fract. Mech., Vol. 1, No. 2, pp. 145–160 (1984).
2. Okamura, H., Watanabe, K. and Takano, T., Applications of the compliance concept in fracture mechanics, Special Technical Publication 536, American Society for Testing and Materials, pp. 423–438 (1973).

3. Okamura, H., Watanabe, K. and Takano, T., Deformation and strength of cracked member under bending moment and axial force, Engineering Fracture Mechanics, 7, pp. 531–539 (1975).
4. Carpinteri A., DiTommaso, A. and Viola, E., Sulla capacitá portante limite di pareti lapidee lesionate, Proceedings of the 5th Italian Congress of Theoretical and Applied Mechanics, Palermo, Vol. 2, pp. 93–104 (1980).
5. Carpinteri, Al. and Carpinteri, An., Softening and fracturing process in masonry arches, Proceedings of the 6th International Brick Masonry Conference, Roma, pp. 502–510 (1982).

6

Steel reinforced beam with crack in bending

6.1. Traditional approach

Linear elastic analysis. Reinforced concrete is a composite material of mortar, aggregates and steel bars. Concrete presents a *relatively* high compressive strength, whereas its tensile strength is low. This is why steel bars are embedded in order to carry the tensile load. Concrete and steel adhere well. They possess the same coefficient of thermal expansion, $\alpha_0 \simeq 1.2 \times 10^{-5}\,^\circ\mathrm{C}^{-1}$ such that they can expand together without exerting differential displacements.

The basic assumptions for the statics of reinforced concrete are [1]:

(1) Concrete behaves as a linear elastic material with compressive loads and as a nontraction-bearing material with tensile loads.
(2) Steel behaves as a linear elastic material with both compressive and tensile loads.
(3) The steel bars cannot slip inside concrete; therefore, the expansions of both materials are the same.
(4) The cross-sections remain plane.

In beam bending, the neutral axis divides the cross-section into two parts: one part is in tension and the other in compression, Figure 6.1. The steel bars are therefore installed below the neutral axis such that the concrete is compressed while the steel is stretched. The condition of axial equilibrium for the rectangular cross-section in Figure 6.1 is

$$\sigma_s A_s = \sigma_c t x/2 \tag{6.1}$$

where σ_s is the stress in steel, σ_c is the maximum compressive stress in the upper extremity of the concrete beam, A_s is the steel area, t is the thickness of the beam and x is the unknown distance of the neutral axis from the upper extremity of the beam. Moment equilibrium yields

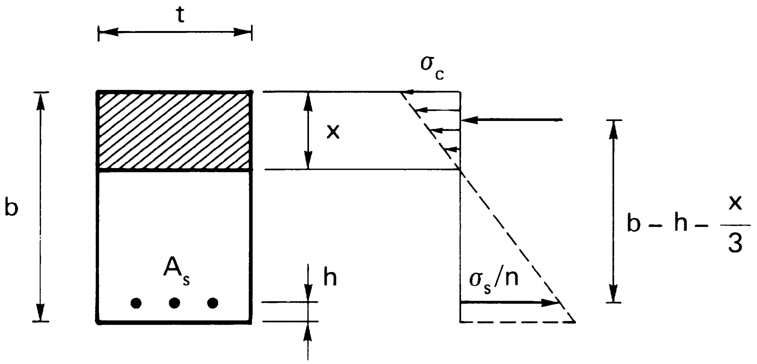

Fig. 6.1. Reinforced concrete beam cross-section.

$$M = \sigma_s A_s \left(b - h - \frac{x}{3}\right) \tag{6.2}$$

where M is the bending moment applied to the cross-section and $(b - h - (x/3))$ the moment arm. The beam depth is b and h is the distance of the steel bars measured from the lower extremity of the beam. The proportionality condition in strain gives

$$\frac{\epsilon_s}{\epsilon_c} = \frac{b - h - x}{x} \tag{6.3}$$

where ϵ_s is the dilatation of the steel bars and ϵ_c the strain of concrete in the upper extremity of the cross-section, Figure 6.1. If the stresses are introduced in equation (6.3), the result is

$$\sigma_s = n\sigma_c \frac{b - h - x}{x} \tag{6.4}$$

where n is the ratio of elastic modulus of steel, E_s, to elastic modulus of concrete, $E_c (n \simeq 10)$. Combining equations (6.1) and (6.4), it follows that

$$n\sigma_c A_s \frac{b - h - x}{x} = \sigma_c tx/2 \tag{6.5}$$

from which

$$\tfrac{1}{2}tx^2 - nA_s(b - h - x) = 0 \tag{6.6}$$

The root x of the quadratic equation (6.6) gives the position of the neutral axis which guarantees the balance of moment. The steel area A_s must be considered n times larger. From equations (6.1) and (6.2), it is then possible to obtain the stresses in concrete and steel as functions of the distance x:

$$\sigma_c = \frac{2M}{tx\left(b-h-\dfrac{x}{3}\right)} \tag{6.7a}$$

$$\sigma_s = \frac{M}{A_s\left(b-h-\dfrac{x}{3}\right)} \tag{6.7b}$$

Alternatively, the unknowns x, b, A_s may be solved. Equation (6.4) may be transformed into

$$x = \frac{n\sigma_c}{\sigma_s + n\sigma_c}(b-h) \tag{6.8}$$

Hence, equations (6.1) and (6.8) may be used to give

$$A_s = \frac{n\sigma_c^2}{2\sigma_s(\sigma_s + n\sigma_c)}t(b-h) \tag{6.9}$$

By means of equations (6.8) and (6.9), equation (6.2) becomes

$$M = \left(1-\frac{\alpha}{3}\right)\beta\sigma_s t(b-h)^2 \tag{6.10}$$

with b as an unknown. The quantities α and β are

$$\alpha = \frac{n\sigma_c}{\sigma_s + n\sigma_c} \tag{6.11a}$$

$$\beta = \frac{n\sigma_c^2}{2\sigma_s(\sigma_s + n\sigma_c)} \tag{6.11b}$$

Once the beam depth b has been obtained, equations (6.8) and (6.9) give the neutral axis position and the steel area A_s.

Limit design. According to the linear elastic analysis, the stress in steel σ_s and in concrete σ_c are a fraction of the yield strength. For a reinforced concrete beam, the linear elastic analysis can drastically underestimate carrying capacity and ductility.

The stress-strain relationship suggested by the international regulations [2] for concrete in compression is shown in Figure 6.2. The σ versus ϵ curve is parabolic up to the attainment of the yield strength σ_0 with strain $\epsilon_0 = 2 \times 10^{-3}$ following the line OA, i.e.,

$$\sigma = \sigma_0 \left[2\left(\frac{\epsilon}{\epsilon_0}\right) - \left(\frac{\epsilon}{\epsilon_0}\right)^2 \right] \tag{6.12}$$

A perfectly plastic behavior then follows up to the ultimate strain, $\epsilon_u = 3.5 \times 10^{-3}$, when crushing occurs.

Consider the rectangular cross-section in Figure 6.3. Let it be loaded by a bending moment, M, and suppose that the section remains plane, so that the strain diagram is linear, Figure 6.3(a). The stress diagram in Figure 6.3(b) is not linear and is related to equation (6.12). The resultant compressive force, F_c, may be determined by means of an integration:

$$F_c = \int_0^x \sigma(\epsilon(y))t\,dy = k_s \sigma_0 t x \tag{6.13}$$

The distance of the stress resultant from the upper extremity of the beam, d, can be found from

$$F_c d = \int_0^x \sigma(\epsilon(y))ty\,dy \tag{6.14}$$

which leads to

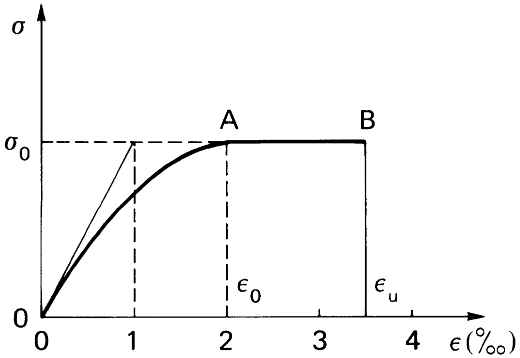

Fig. 6.2. Stress-strain relationship suggested by the international regulations for concrete in compression.

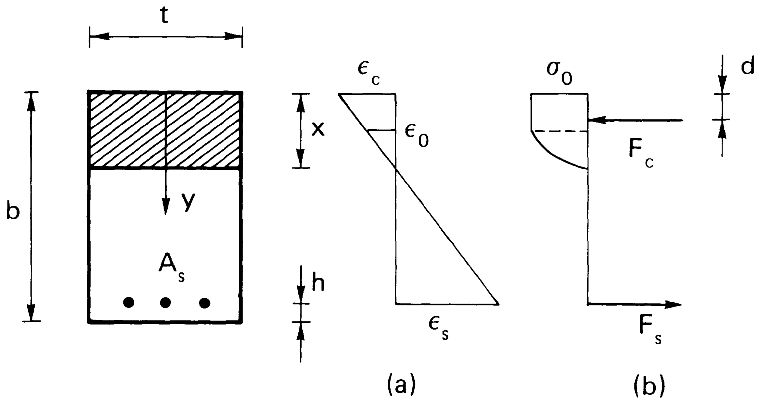

Fig. 6.3. Reinforced concrete beam cross-section: stress and strain distributions for limit design.

$$d = k_d x \tag{6.15}$$

Instead of the diagram σ versus ϵ in Figure 6.2, a simpler bilinear relationship *OAB* can be used:

$$k_s = 1 - \frac{\epsilon_0}{2\epsilon_c} \tag{6.16}$$

When the strain in the upper extremity of the beam, ϵ_c, reaches the ultimate value, $\epsilon_u = 3.5 \times 10^{-3}$, equation (6.16) gives $k_s = 0.714$.

The condition of axial equilibrium for the rectangular cross-section in Figure 6.3 is

$$\sigma_s A_s = k_s \sigma_0 t x \tag{6.17}$$

while moment equilibrium renders

$$M = k_s \sigma_0 t x (b - h - k_d x) \tag{6.18}$$

The distance of the neutral axis from the upper extremity of the beam x can be related to the beam depth b by means of equation (6.3). More explicitly equations (6.17) and (6.18) can be written as

$$\sigma_s A_s = k_s(\epsilon_c, \epsilon_s)\sigma_0 t \frac{\epsilon_c}{\epsilon_s + \epsilon_c}(b - h) \tag{6.19}$$

and

$$M = k_s(\epsilon_c, \epsilon_s)\sigma_0 t \frac{\epsilon_c}{\epsilon_s + \epsilon_c}(b-h)^2 \left[1 - k_d(\epsilon_c, \epsilon_s)\cdot\frac{\epsilon_c}{\epsilon_s + \epsilon_c}\right] \tag{6.20}$$

The limit moment M can be obtained from equations (6.19) and (6.20) by assuming that collapse occurs when the steel begins to yield. Once the values σ_s and ϵ_s are fixed, equation (6.19) gives ϵ_c. If ϵ_c is lower than 3.5×10^{-3}, the limit moment can then be found from equation (6.20). Otherwise, the upper limit will be fixed at $\epsilon_c = 3.5 \times 10^{-3}$ from which ϵ_s is obtained by using eqation (6.19). Similarly M, ϵ_c and ϵ_s can be given and b and A_s can be solved by assuming that the concrete fractures at the same time when the steel reaches its yield limit.

6.2. Linear elastic fracture mechanics

Preliminary remarks. In the traditional analysis of a reinforced concrete beam, the tension part of concrete is assumed not to support traction while the compression part is assumed to behave elastically or elastic-plastically. Such an analysis does not take into account the stiffness variation and the stress concentration due to the presence of cracks. Traditionally, the influence of cracks in masonry or concrete is treated by empirical means. Such an approach has no predictive capability.

In this section, five different collapse conditions are considered:

(1) crack propagation in concrete;
(2) tensile strength collapse in concrete;
(3) crushing collapse in concrete;
(4) yielding of steel;
(5) slippage of steel bars.

The collapse conditions depend on the mechanical and geometrical properties of the beam. The process of concrete fracture and steel plastic flow will depend on a number of parameters [3–5] such as percentage of steel, A_s/A, yield strength of steel, f_y, fracture toughness of concrete, K_{IC} and beam depth, b.

Reaction of reinforcement. Consider a reinforced concrete beam element with a rectangular cross-section of thickness t and depth b, subjected to a bending moment, M. The steel reinforcement is at a distance h from the external surface. A through-thickness edge crack of depth $a \geqslant h$ is assumed to exist in the stretched position shown in Figure 6.4. The cracked concrete beam element is subjected to the bending moment, M, and the eccentric axial force, F. It is well-known that a bending moment, M^*, induces a stress-intensity factor at the crack tip equal to [6, 7]:

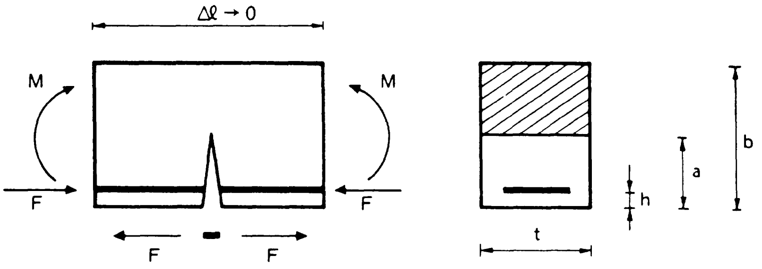

Fig. 6.4. Cracked reinforced beam element.

$$K_I = \frac{M^*}{b^{3/2}t} Y_M(\xi) \tag{6.21}$$

where $\xi = a/b$ is the relative crack depth and Y_M is the function:

$$Y_M(\xi) = 6 \times (1.99\xi^{1/2} - 2.47\xi^{3/2} + 12.97\xi^{5/2} - 23.17\xi^{7/2} + 24.80\xi^{9/2}) \tag{6.22}$$

for $\xi \leqslant 0.7$. In the same way, an axial force F^*, can be associated with the stress intensity factor [6, 7]:

$$K_I = \frac{F^*}{b^{1/2}t} Y_F(\xi), \tag{6.23}$$

in which

$$Y_F(\xi) = 1.99\xi^{1/2} - 0.41\xi^{3/2} + 18.70\xi^{5/2} - 38.48\xi^{7/2} + 53.85\xi^{9/2} \tag{6.24}$$

for $\xi \leqslant 0.7$. The bending moment M^* produces a local rotation φ equal to [6, 7]

$$\varphi = \lambda_{MM} M^* \tag{6.25}$$

in which

$$\lambda_{MM} = \frac{2}{b^2 tE} \int_0^{\xi} Y_M^2(\xi) \mathrm{d}\xi \tag{6.26}$$

The axial tensile force F^* yields the rotation [6, 7]

$$\varphi = \lambda_{MF} F^* \tag{6.27}$$

in which

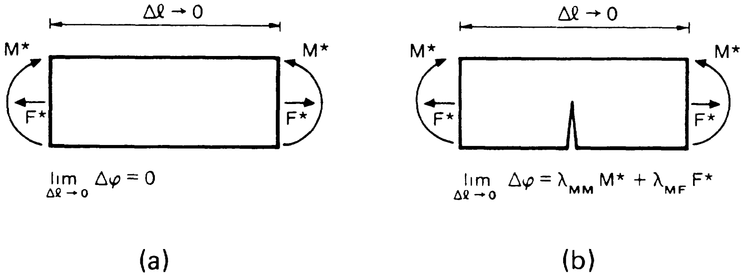

Fig. 6.5. Local rotation in uncracked (a) and cracked (b) beam cross-section.

$$\lambda_{MF} = \frac{2}{btE}\int_0^{\xi} Y_M(\xi)Y_F(\xi)\mathrm{d}\xi \tag{6.28}$$

The uncracked section acts as a perfectly fixed joint, Figure 6.5(a), while the cracked section is an elastic joint rotating under the action of the bending moment M^* and the axial force F^* shown in Figure 6.5(b), i.e.

$$\varphi = \lambda_{MM}M^* + \lambda_{MF}F^* \tag{6.29}$$

For the statically undeterminate system in Figure 6.4, the total moment is

$$M^* = M - F\left(\frac{b}{2} - h\right) \tag{6.30}$$

while the axial force is

$$F^* = -F \tag{6.31}$$

Until the steel begins to yield or slip, the global rotation due to the bending moment M^* and to the closing force F^* is equal to zero:

$$\varphi = \lambda_{MM}M^* + \lambda_{MF}F^* = 0 \tag{6.32}$$

Equation (6.32) is the condition that determines F. Inserting equations (6.30) and (6.31) into equation (6.32), the result is

$$\lambda_{MM}\left[M - F\left(\frac{b}{2} - h\right)\right] - \lambda_{MF}F = 0 \tag{6.33}$$

Finally, it is possible to show that

$$\frac{Fb}{M} = \frac{1}{\left(\frac{1}{2} - \frac{h}{b}\right) + r(\xi)} \tag{6.34}$$

where

$$r(\xi) = \frac{\int_0^{\xi} Y_M(\xi) Y_F(\xi) \mathrm{d}\xi}{\int_0^{\xi} Y_M^2(\xi) \mathrm{d}\xi} \tag{6.35}$$

The statically undetermined reaction of the reinforcement, against the relative crack depth for $h/b = 1/10, 1/20$ is shown in Figure 6.6. The decrease of the reaction by increasing the crack depth can be explained by observing that both the compliances λ_{MM} and λ_{MF} increase with an increasing crack length with λ_{MF} increasing more rapidly than λ_{MM}.

Reinforcement plastic flow or slippage. Equation (6.34) shows that the force F transmitted by the reinforcement increases linearly with the bending moment M up to the limit $F_P = f_y A_s$. Before the steel yields, cracks grow in concrete as slippage is allowed between concrete and steel. The effect of slippage can also be included by defining a fictitious yield strength $\bar{f}_y$ for steel that is smaller than the true value f_y.

A perfectly plastic behavior of the reinforcement will be considered, Figure 6.7. From equation (6.34), it is possible to obtain the moment of plastic flow for the reinforcement:

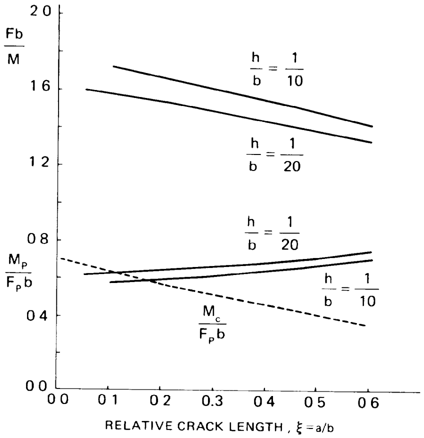

Fig. 6.6. Reaction of reinforcement and bending moment of reinforcement plastic flow, due to yielding of steel or to slippage of bar.

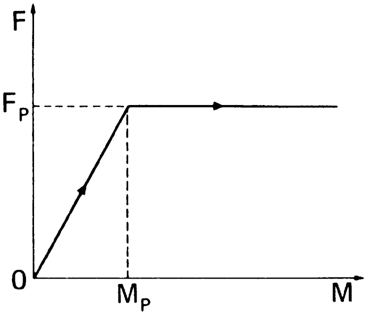

Fig. 6.7. Force transmitted by reinforcement against applied moment.

$$M_P = F_P b\left[\left(\frac{1}{2}-\frac{h}{b}\right)+r(\xi)\right] \tag{6.36}$$

The plot of moment against the relative crack depth for $h/b = 1/10,\ 1/20$, is given in Figure 6.6. The moment of reinforcement plastic flow M_P is seen to increase with the crack depth ξ. If the concrete has a low crushing strength, f_c, and steel has a relatively high yield strength, f_y, then the concrete crushes before the steel yields. If M_c is the moment required to crush the concrete it follows then

$$\frac{M_c}{F_P b} = \frac{f_c/f_y}{A_s/A}\ \frac{(1-\xi)\left(2+\xi-3\dfrac{h}{b}\right)}{6} \tag{6.37}$$

where F_P and M_c are defined in Figures 6.7 and 6.8. The dashed line in Figure 6.6 represents the solution of equation (6.37) for $f_c = 200\,\text{kg/cm}^2$, $f_y = 3600\,\text{kg/cm}^2$, $A_s/A = 0.024$ and $h/b = 0.1$. The collapse of concrete comes before the steel can yield. This occurs for sufficiently high values of crack depth ($\xi \geqslant 0.175$).

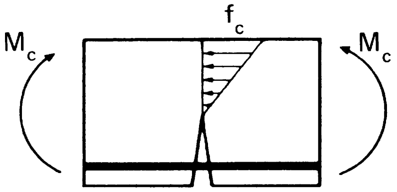

Fig. 6.8. Assumption of linear stress variation through the ligament.

Rigid-hardening behavior. The mechanical behavior of the cracked reinforced concrete beam is rigid until $M \leqslant M_P$ for $\varphi = 0$. When $M > M_P$, φ is given by

$$\varphi = \lambda_{MM}\left[M - F_P\left(\frac{b}{2} - h\right)\right] - \lambda_{MF}F_P \tag{6.38}$$

The M versus φ diagram in Figure 6.9 describes the rigid-linear hardening behavior given by equation (6.38). The hardening line is parallel to the M versus φ diagram related to the same cracked beam without reinforcement shown by the broken line. The hardening coefficient λ_{MM}^{-1} versus the relative crack depth ξ is also plotted in Figure 6.9. By increasing the crack depth, ξ, the hardening line becomes more and more inclined until a perfectly plastic behavior is reached. As ξ tends to zero, the hardening line becomes nearly vertical before it behaves as for a rigid body. Some M versus φ diagrams for $h/b = 1/20$ are also shown in Figure 6.10 with ξ varying between 0.05 and 0.50. The moment of steel plastic flow increases very little by increasing ξ while the slope of the hardening line decreases sharply.

Stability of concrete fracture and steel yielding. After the steel flows plastically, the stress-intensity factor acting at the crack tip is equal to the sum of equations (6.21) and (6.23) with

$$M^* = M - F_P\left(\frac{b}{2} - h\right) \tag{6.39}$$

and

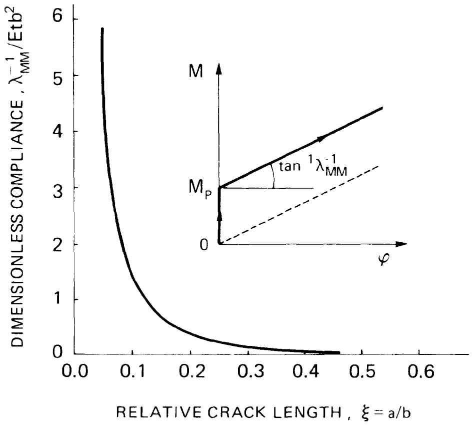

Fig. 6.9. Hardening coefficient against relative crack depth.

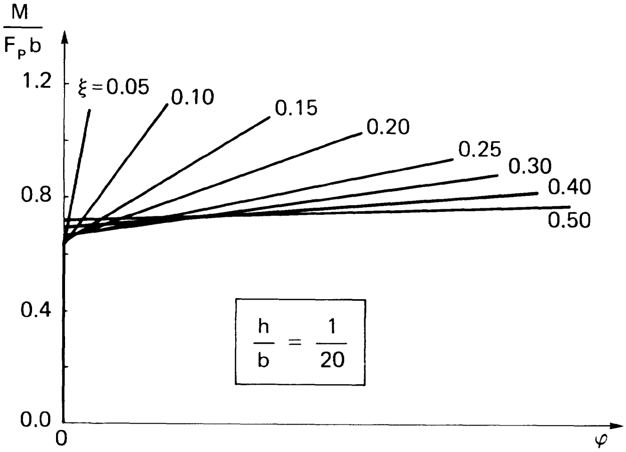

Fig. 6.10. Moment versus rotation diagrams for different crack depths.

$$F^* = -F_P \tag{6.40}$$

It follows that

$$K_I = \frac{1}{b^{3/2}t}\, Y_M(\xi)\left[M - F_P\left(\frac{b}{2} - h\right)\right] - \frac{F_P}{b^{1/2}t}\, Y_F(\xi) \tag{6.41}$$

When K_I in equation (6.41) is set equal to the concrete fracture toughness K_{IC}, the moment M_F at incipient fracture becomes

$$M_F = \frac{K_{IC}b^{3/2}t}{Y_M(\xi)} + \frac{F_P b}{Y_M(\xi)}\left[Y_F(\xi) + Y_M(\xi)\cdot\left(\frac{1}{2} - \frac{h}{b}\right)\right] \tag{6.42}$$

The fracture moment of concrete M_F is plotted against the relative crack depth ξ in Figure 6.11. The non-dimensional number N_P is

$$N_P = \frac{f_y b^{1/2}}{K_{IC}} \cdot \frac{A_s}{A} \tag{6.43}$$

For $h/b = 1/20$ and N_P close to zero, M_F decreases as the crack extends and a typical phenomenon of unstable fracture occurs. For higher N_P values, a stable branch follows the unstable one of the curve. Even for $N_P = 1$, the minimum of the curve is evident and takes place for $\xi \simeq 0.35$. For higher N_P values, the crack depth ξ for which the minimum occurs is lower, while the stable branch becomes steeper and steeper. For $N_P \gtrsim 8.5$, the unstable

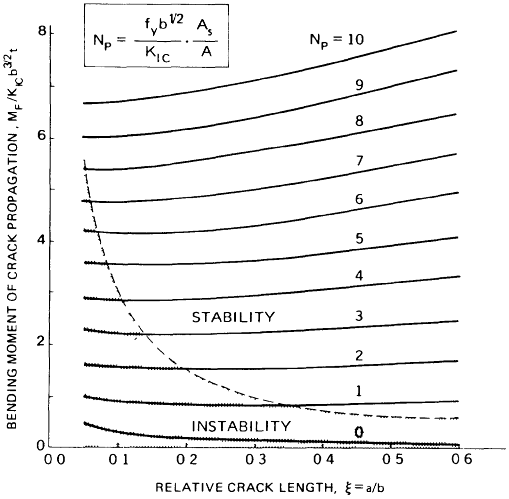

Fig. 6.11. Bending moment of crack propagation versus relative crack depth ($h/b = 1/20$).

branch disappears and only the stable branch remains. A similar behavior has been discussed in section 5.2 for a cracked masonry wall subjected to an eccentric axial compression. The locus of the minima is represented by a dashed line in Figure 6.11. This line divides the diagram into an upper zone where the fracture is stable, and a lower one where the process is unstable. Fracture in reinforced concrete is therefore stable when the beam is sufficiently reinforced with sufficiently small cross-section, or when the crack is sufficiently deep.

For $h/b = 1/10$, the curves are similar to those in Figure 6.11. The only differences are

(1) the curves shift downwards, i.e., crack propagation occurs for lower moments, and
(2) the dashed line shifts upwards, i.e., the stable zone of the diagram shrinks.

For a reinforced concrete beam with $f_y = 2400\,\text{kg/cm}^2$, $K_{IC} = 80\,\text{kg/cm}^{3/2}$, $b = 30\,\text{cm}$ and $A_s/A = 0.010$, the non-dimensional number in equation (6.43) is $N_P = 1.64$. Figure 6.11 therefore shows that the fracture is at the metastable state.

From equations (6.36) and (6.42), a relation between M_F and M_P can be established:

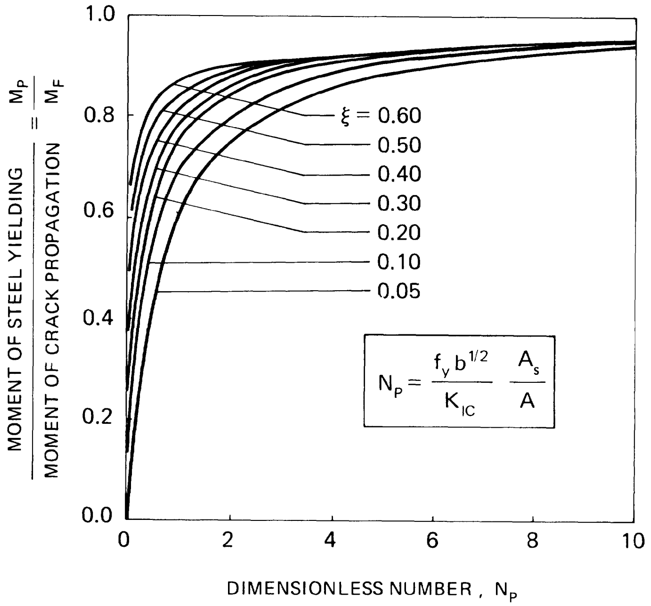

Fig. 6.12. Ratio between moment of steel plastic flow and moment of crack propagation in concrete ($h/b = 1/20$).

$$\frac{M_P}{M_F} = \frac{\left[\frac{1}{2} - \frac{h}{b} + r(\xi)\right] Y_M(\xi)}{\frac{1}{N_P} + Y_F(\xi) + Y_M(\xi)\left(\frac{1}{2} - \frac{h}{b}\right)} \tag{6.44}$$

In Figure 6.12, the ratio M_P/M_F against the non-dimensional number N_P is given for different crack depths ξ and $h/b = 1/20$. This diagram shows that when high N_P corresponds to deep cracks, the events of crack propagation and plastic flow in steel are then close to one another.

In Figure 6.13 M versus φ diagrams are shown, for $h/b = 1/20$, $\xi = 0.1$, and $N_P = 0.0$, 0.1, 0.3, 0.7 and 3.0. This corresponds to five different steel areas.

The rigid behavior ($0 \leqslant M \leqslant M_P$) is followed by the linear hardening behavior ($M_P < M \leqslant M_F$). The latter stops when crack propagation occurs. If the fracture process is unstable, $M(\varphi)$ contains a discontinuity and drops from value M_F to value F_Pb with a negative jump, Figures 6.13(a), (b) and (c). A complete and instaneous separation of the concrete cross-section occurs. While the rotation φ is constant, the new moment F_Pb can be estimated according to the scheme in Figure 6.14, where each beam segment is subjected to the traction F_P of the reinforcement and to the contact compression F_P,

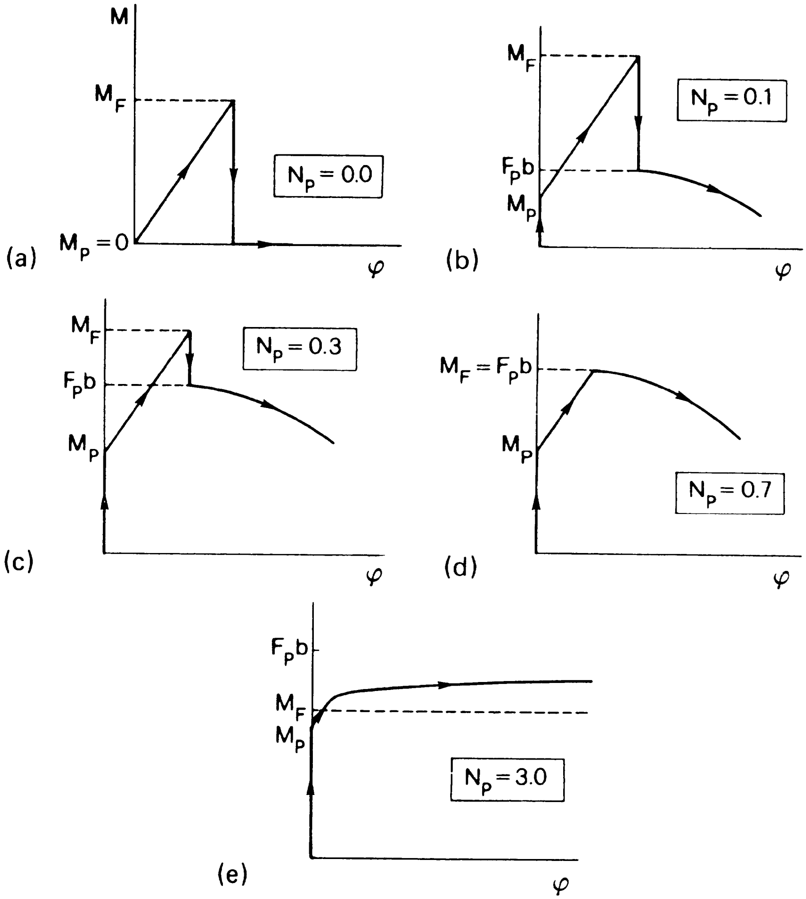

Fig. 6.13. Mechanical behavior of reinforced concrete beams for different nondimensional numbers N_P ($h/b = 1/20$; $\xi = 0.10$).

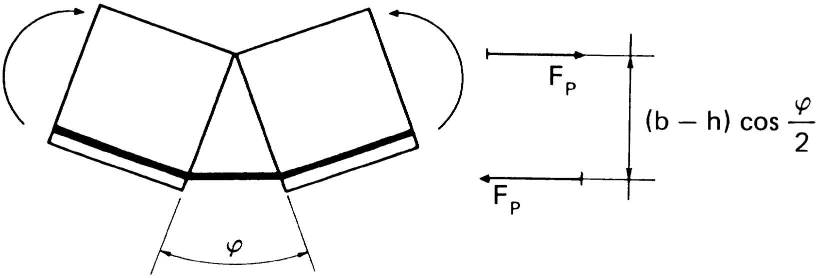

Fig. 6.14. Statical scheme after concrete separation.

i.e., to the moment $F_P(b-h) \simeq F_P b$. An increase in φ without considering any other phenomenon of instability results in a decrease in the bending moment as shown in Figure 6.14:

$$M = F_P b \cos\frac{\varphi}{2} \tag{6.45}$$

If the fracture phenomenon is stable, $M(\varphi)$ does not contain any discontinuity and describes a hardening behavior, Figure 6.13(e). The envelope is shown in Figure 6.10.

In Figure 6.13(a), the case $N_P = 0$ is considered, i.e., a beam without reinforcement. The plastic flow moment M_P is naturally equal to zero as well as the moment $F_P b$ which occurs immediately after the complete separation of concrete. The case $N_P = 0.1$ is described in Figure 6.13(b), i.e., a beam reinforced weakly. The ratio $M_P/F_P b$ can be determined from Figure 6.6 and M_P/M_F from Figure 6.12. The slope of the hardening line depends only on the crack length, besides the elastic modulus of concrete and the cross-section sizes, Figure 6.9. The case $N_P = 0.3$ is considered in Figure 6.13(c) with a higher ratio of M_P/M_F. The ratio $M_P/F_P b$, is independent of N_P, Figure 6.6, and remains unchanged. In Figure 6.13(d), the case $N_P = 0.7$ is reported. For this value, $M_F = F_P b$, and the discontinuity vanishes. Finally, Figure 6.13(e) treats the case $N_P = 3$. The fracture moment M_F is only slightly higher than the plastic moment M_P and the moment $F_P b$ is obtainable only with a positive jump of the function. Figure 6.11 shows that the fracture process for $N_P = 3$ and $\xi \geqslant 0.14$ is stable. Therefore, the concrete does not separate instantaneously.

Note that for $N_P \leqslant 0.7$ it is $F_P b \leqslant M_F$ and a discontinuity appears in the diagram $M(\varphi)$, Figures 6.13(a) to (d). On the other hand, for $N_P \leqslant 0.7$, the curves in Figure 6.11 lie completely in the unstable zone.

6.3. Non-linear model with material damage and softening

Effect of reinforcement on load transfer. The three-point bent beam in chapter 3 will be reinforced with a steel bar on the tension side, Figure 6.15. The finite element mesh used for the left side of the structure is shown in Figure 6.16. The damage-crack growth model of Sih and Matic [8, 9] is again applied to derive the SR-curves with particular emphasis placed on the influence of reinforcement. The horizontal displacement of the point of reinforcement reaction F is assumed to be zero until F reaches the plastic limit, $F_P = f_y A_s$. Then, the constant force F_P is transmitted to the cracked beam.

The cases analyzed are summarized in Table 6.1. Material 3 in Figure 2.29

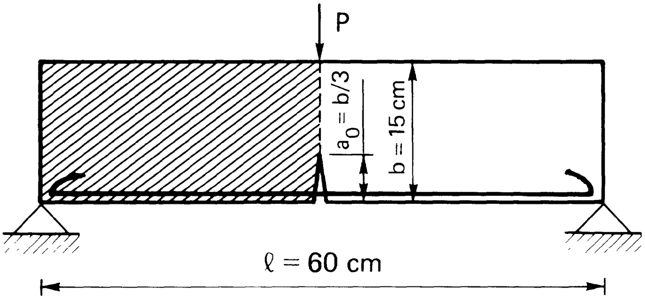

Fig. 6.15. Steel reinforced beam with crack in bending.

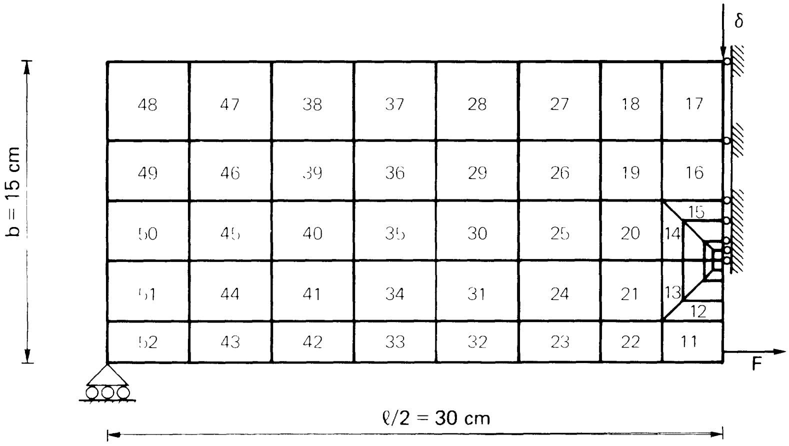

Fig. 6.16. Finite element idealization of the steel reinforced beam with crack in Figure 6.15. The zoom area is the same as in Figure 4.2(b).

and three different yield forces are used. The load-deflection values and the crack growth increments are reported in Table 6.2. The crack lengths and strain energy density factors can be found in Table 6.3 while the reinforcement reactions and the related plastic crack openings are given in Table 6.4. The damage level within the finite elements is described in Tables 6.5(a) to (c) as defined by equation (2.73) for increasing loads. Note that element 11

TABLE 6.1.
The three cases analyzed in this chapter, changing the yield force F_P.

Case no.	Yield force, F_P (kg)	Symbol
I (1)	1296	●
II (2)	648	⊙
III (3)	324	○

TABLE 6.2.
Load, deflection and crack growth increment at each loading increment and for each case in Table 6.1.

Increment $j = 1, 2,$ etc.	Load P_j (kg)	Deflection δ_j (10^{-3} cm)	Crack growth increment Δa_j (cm)
Case no. (1)			
1	608	3	0.060
2	1116	6	0.383
3	1062	9	1.332
4	528	12	2.253
Case no. (2)			
1	608	3	0.060
2	1113	6	0.383
3	1206	9	1.104
4	889	12	2.162
Case no. (3)			
1	591	3	0.060
2	892	6	0.551
3	814	9	1.438
4	532	12	2.127

TABLE 6.3.
Crack length and strain energy density factor at each loading increment and for each case in Table 6.1.

Increment $j = 1, 2,$ etc.	Crack length a_j (cm)	Strain energy density factor S_j (kg/cm × 10^{-3})
Case no. (1)		
1	5.060	0.466
2	5.443	1.900
3	6.775	10.283
4	9.028	17.100
Case no. (2)		
1	5.060	0.466
2	5.443	1.900
3	6.547	8.026
4	8.709	16.258
Case no. (3)		
1	5.060	0.466
2	5.611	3.890
3	7.049	8.469
4	9.176	13.464

TABLE 6.4.
Reaction of the reinforcement and plastic crack opening at each loading increment and for each case in Table 6.1.

Increment $j = 1, 2,$ etc.	Reinforcement reaction F_j (kg)	Plastic crack opening w_j (10^{-3} cm)
Case no. (1)		
1	$365 < F_P (1296)$	0
2	$656 < F_P$	0
3	$465 < F_P$	0
4	$260 < F_P$	0
Case no. (2)		
1	$365 < F_P (648)$	0
2	$648 = F_P$	0.038
3	$648 = F_P$	2.153
4	$648 = F_P$	6.202
Case no. (3)		
1	$324 = F_P$	0.141
2	$324 = F_P$	1.908
3	$324 = F_P$	4.867
4	$324 = F_P$	8.830

experiences a severe damage as the reinforcement transmits the force F to the beam. This is particularly noticeable for Cases (1) and (2) where the beam is more reinforced.

The load-deflection responses for the deflection increment $\Delta\delta = 3 \times 10^{-3}$ cm are presented in Figure 6.17. At first, the P versus δ curve rises as the steel area increases. It then drops when the steel area is so large that element 11 begins to experience considerable damage, Figure 6.16.

In Figure 6.18, the ratio of stiffness loss by material damage to total stiffness loss is given as a function of the imposed deflection, δ. The general trend is that this ratio tends to zero for very small as well as for very large deflections. For intermediate deflections, these curves yield a maximum that increases with increasing plastic force, F_P, which is equivalent to increasing the steel area. In Figure 6.19, the load P is plotted against the crack growth $(a - a_0)$. The load first increases as the crack grows. Structural instability then begins. The values of the strain energy density factor, S, are plotted against the crack growth $(a - a_0)$ in Figure 6.20. They increase when the crack grows and the variation is steeper for larger steel areas. This implies that for a given value of S_c subcritical crack growth reduces as the reinforcement is increased, and crack instability occurs earlier.

Scaling in size. Figures 6.21 give the S versus a plots as the beam depth, b is varied. As for the non-reinforced beams, the critical crack growth decreases

TABLE 6.5(a).
Level of damage according to equation (2.73) in each finite element and at each loading increment. Case No. 1 in Table 6.1.

Damage element	Increment $j = 1, 2$, etc.			
reference number	1	2	3	4
1	–	20	25	25
2	–	4	15	22
3	–	–	21	25
4	–	–	2	25
5	–	–	4	15
6	–	–	–	–
7	–	–	–	–
8	–	–	–	–
9	–	–	–	–
10	–	5	21	25
11	–	9	22	25
12	–	–	–	–
13	–	–	–	–
14	–	–	–	3
15	–	–	–	4

TABLE 6.5(b).
The same as in Table 6.5(a). Case No. 2 in Table 6.1.

Damage element	Increment $j = 1, 2$, etc.			
reference number	1	2	3	4
1	–	20	25	25
2	–	4	19	25
3	–	–	24	25
4	–	–	8	24
5	–	–	8	18
6	–	–	–	–
7	–	–	–	–
8	–	–	–	–
9	–	–	5	5
10	–	5	24	25
11	–	9	12	12
12	–	–	–	–
13	–	–	–	–
14	–	–	–	3
15	–	–	–	5

TABLE 6.5(c).
The same as in Table 6.5(a). Case No. 3 in Table 6.1.

Damage element	Increment $j = 1, 2$, etc.			
reference number	1	2	3	4
1	–	25	25	25
2	–	12	25	25
3	–	10	25	25

TABLE 6.5(c) (CONTINUED)

Damage element	Increment $j = 1, 2,$ etc.			
reference number	1	2	3	4
4	–	–	17	25
5	–	–	11	16
6	–	–	–	–
7	–	–	–	–
8	–	–	–	–
9	–	3	3	3
10	–	14	25	25
11	–	–	–	–
12	–	–	–	–
13	–	–	–	–
14	–	–	–	–
15	–	–	–	15

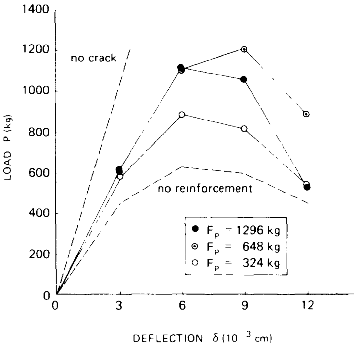

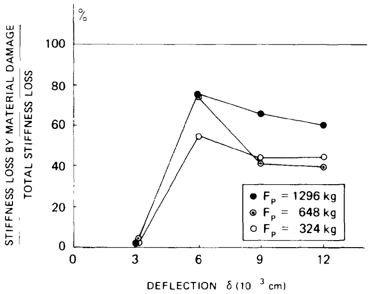

Fig. 6.17. Load-deflection diagrams for three different yield forces.

Fig. 6.18. Ratio of stiffness loss by material damage to total stiffness loss as a function of deflection, for three different yield forces.

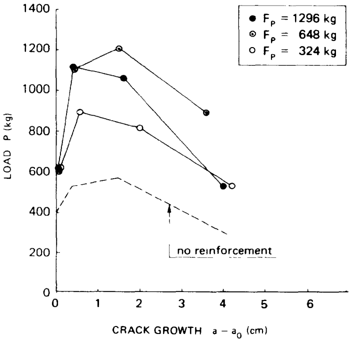

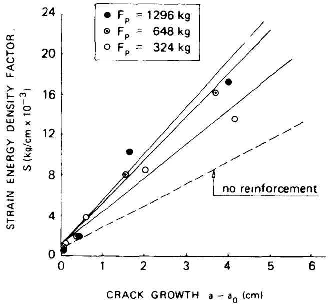

Fig. 6.19. Load-crack growth diagrams for three different yield forces.

Fig. 6.20. Strain energy density factor versus crack growth for three different yield forces.

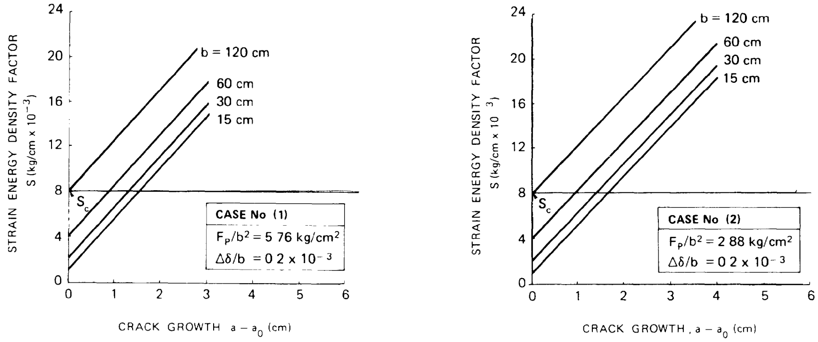

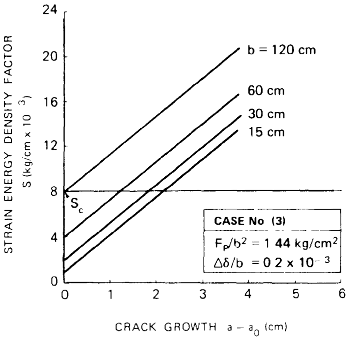

Fig. 6.21. (a) Straight line plots of strain energy density factor versus crack growth, varying the beam size scale. Case No. 1 in Table 6.1. (b) The same as in Figure 6.21(a). Case No. 2 in Table 6.1. (c) The same as in Figure 6.21(a). Case No. 3 in Table 6.1.

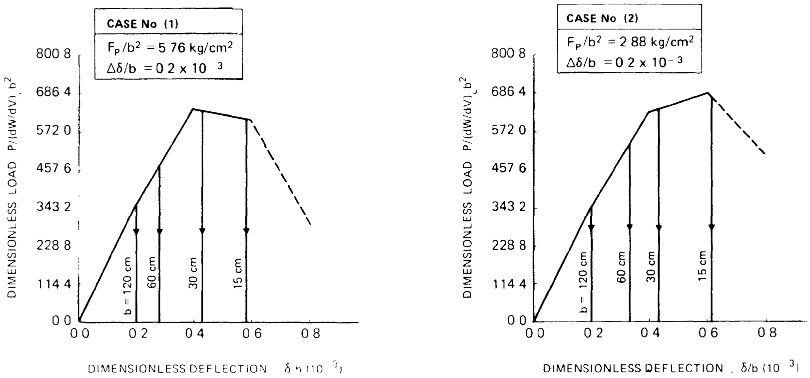

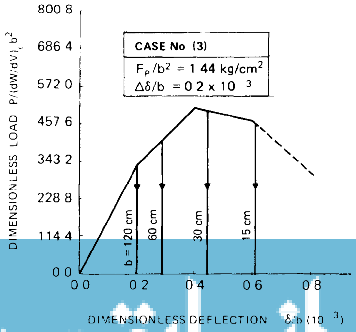

Fig. 6.22. (a) Dimensionless load-deflection diagrams, varying the beam size scale. Case No. 1 in Table 6.1. (b) The same as in Figure 6.22(a). Case No. 2 in Table 6.1. (c) The same as in Figure 6.22(a). Case No. 3 in Table 6.1.

TABLE 6.6.
(a) Maximum load for different size scales and according to the various theories: Strain Energy Density Theory, Linear Elastic Fracture Mechanics, Limit Analysis. Case No. 1 in Table 6.1. (b) The same as in Table 6.6(a). Case No. (2) in Table 6.1. (c) The same as in Table 6.6(a). Case No. (3) in Table 6.1.

Case no. (1)

Size b, cm	15	30	60	120
$P^{(1)}_{max}$ (SEDT), kg	1 116	4 464	13 200	38 400
$P^{(2)}_{max}$ (LEFM), kg	2 155	7 250	25 125	89 535
$P^{(3)}_{max}$ (Limit analysis), kg	1 543	6 174	24 696	98 784
$P^{(1)}_{max}/P^{(2)}_{max}$ ratio	0.52	0.62	0.53	0.43
$P^{(3)}_{max}/P^{(2)}_{max}$ ratio	0.72	0.85	0.98	1.10

Case no. (2)

Size b, cm	15	30	60	120
$P^{(1)}_{max}$ (SEDT), kg	1 206	4 460	15 040	38 400
$P^{(2)}_{max}$ (LEFM), kg	1 662	5 278	17 240	57 995
$P^{(3)}_{max}$ (Limit analysis), kg	1 037	4 149	16 600	66 384
$P^{(1)}_{max}/P^{(2)}_{max}$ ratio	0.73	0.84	0.87	0.66
$P^{(3)}_{max}/P^{(2)}_{max}$ ratio	0.62	0.79	0.96	1.14

Case no. (3)

Size b, cm	15	30	60	120
$P^{(1)}_{max}$ (SEDT), kg	892	3 568	11 360	36 800
$P^{(2)}_{max}$ (LEFM), kg	1 415	4 290	13 280	42 160
$P^{(3)}_{max}$ (Limit analysis), kg	785	3 141	12 564	50 256
$P^{(1)}_{max}/P^{(2)}_{max}$ ratio	0.63	0.83	0.86	0.87
$P^{(3)}_{max}/P^{(2)}_{max}$ ratio	0.55	0.73	0.95	1.19

with increasing specimen size. The limiting size is approximately $b = 120$ cm, and this result is independent of the steel percentage, F_P/b^2.

In Figures 6.22, the relations between the dimensionless load and dimensionless deflection are shown. The vertical lines with arrows indicate that the limiting value of δ/b corresponds to S reaching the critical value $S_c = 8 \times 10^{-3}$ kg/cm.

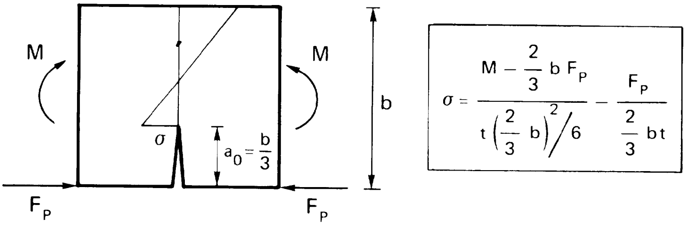

$$\sigma = \frac{M - \frac{2}{3}\,b\,F_P}{t\left(\frac{2}{3}\,b\right)^2\Big/6} - \frac{F_P}{\frac{2}{3}\,bt}$$

Fig. 6.23. Linear elastic limit analysis at the ligament.

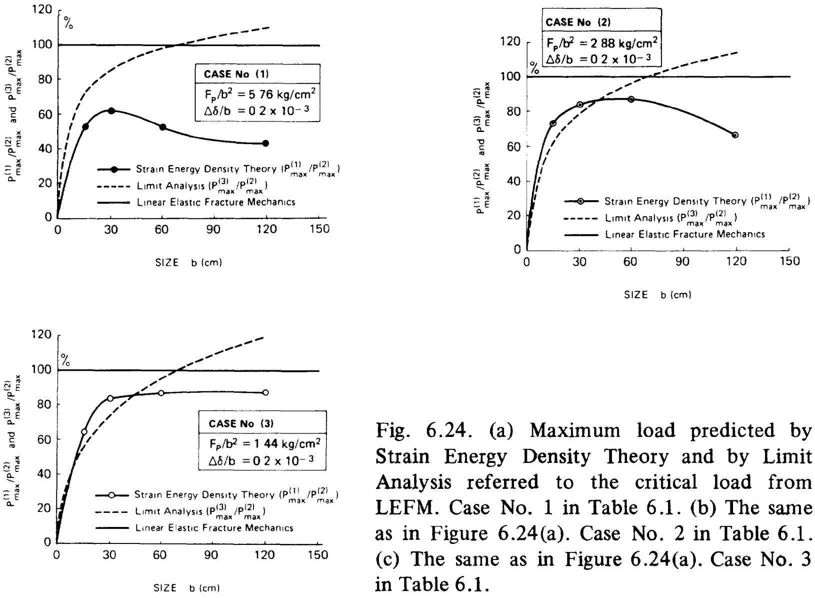

Fig. 6.24. (a) Maximum load predicted by Strain Energy Density Theory and by Limit Analysis referred to the critical load from LEFM. Case No. 1 in Table 6.1. (b) The same as in Figure 6.24(a). Case No. 2 in Table 6.1. (c) The same as in Figure 6.24(a). Case No. 3 in Table 6.1.

Summarized in Table 6.6 are the maximum loads $P^{(1)}_{max}$, obtained by the non-linear damage model, $P^{(2)}_{max}$, given by the Linear Elastic Fracture Mechanics approach in section 6.2. [see equation (6.42)], and $P^{(3)}_{max}$, obtained through a linear elastic limit analysis at the ligament (Figure 6.23). Unlike the results corresponding to no steel reinforcement, Figures 6.24(a) to (c) inclusive show that the reinforced beam does not fail by brittle fracture. The strain energy density curve never reaches the Linear Elastic Fracture Mechanics limit of K_{IC} that corresponds to catastrophic failure, even when the beam size is increased. For small size beams, the Strain Energy Density Theory prediction is very close to that of limit analysis. On the other hand, the maximum load, for $b \to \infty$, is a constant fraction of the Linear Elastic Fracture Mechanics solution [3, 4]. Such a fraction increases for decreasing steel percentages, F_P/b^2, and tends to unity when F_P/b^2 tends to zero, Figure 6.24(c).

References

1. Leonhardt, F. and Mönnig, E., Le Basi del Dimensionamento nelle Costruzioni in Cemento Armato, Vol. 1, Edizioni Tecniche (1978).
2. Codice-modello CEB/FIP per le strutture in cemento armato, AITEC, Roma (1978).
3. Carpinteri, A., A fracture mechanics model for reinforced concrete collapse, Proceedings of the IABSE Colloquium on Advanced Mechanics of Reinforced Concrete, Delft, pp. 17–30 (1981).

4. Carpinteri, A., Stability of fracturing process in R.C. beams, Journal of Structural Engineering, American Society of Civil Engineers, 110, pp. 544–558 (1984).
5. Carpinteri, Al. and Carpinteri, An., Hysteretic behavior of R.C. beams, Journal of Structural Engineering, American Society of Civil Engineers, 110, pp. 2073–2084 (1984).
6. Okamura, H., Watanabe, K. and Takano, T., Applications of the compliance concept in fracture mechanics, Special Technical Publication 536, American Society for Testing and Materials, pp. 423–438 (1973).
7. Okamura, H., Watanabe, K. and Takano, T., Deformation and strength of cracked member under bending moment and axial force, Engineering Fracture Mechanics, 7, pp. 531–539 (1975).
8. Sih, G.C. and Matic, P., A pseudo linear analysis of yielding and crack growth: strain energy density criterion, Defects, Fracture and Fatigue, edited by G.C. Sih and J.W. Provan, Martinus Nijhoff Publishers, The Hague, pp. 223–232 (1982).
9. Carpinteri, A. and Sih, G.C., Damage accumulation and crack growth in bilinear materials with softening: application of strain energy density theory, Journal of Theoretical and Applied Fracture Mechanics, Vol. 1, No. 2, pp. 145–160 (1984).

7

Panel with opening and diagonal cracks

7.1. Infilled frames and seismic loadings

The presence of panels in framed structures enhances stiffness, strength and ductility. Stiffened frames also give rise to higher natural frequencies with corresponding changes in mode shapes. Stafford Smith [1, 2] analyzed the lateral stiffening of infilled frames. In reality, this problem can be very difficult because of the partial debonding between frame and panel as a result of monolateral constraint. More schematically, the presence of a panel in a frame may be simulated by a diagonal strut, Figure 7.1. The stiffness of this fictitious strut depends on the geometric and mechanical features of the panel in relation to those of the frame. Simplified models may be developed by resorting to the theory of beams on elastic foundation.

The global stiffness of the frame-panel system in Figure 7.1(a) depends on the extension and distribution of the contact forces. When the frame stiffness increases, the contact zone extends and then the effective panel stiffness increases accordingly. This is why a large increase in global lateral stiffness can be achieved with a relatively small increase in frame stiffness.

Stafford Smith [2] defined the relative panel-frame stiffness as

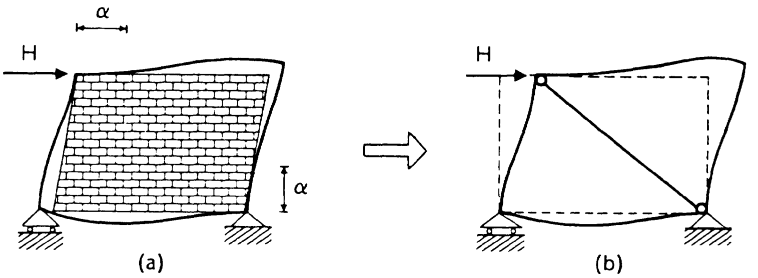

Fig. 7.1. Infilled frame (a) and simulation of the panel by a diagonal strut (b).

$$\lambda h = \sqrt[4]{\frac{E_p h^3 t}{4EI}} \tag{7.1}$$

where E_p, h and t are the elastic modulus, height and thickness of the panel respectively. The flexural rigidity of the pilasters is EI. The extension, α, of the contact zone in Figure 7.1 (a), is given approximately by

$$\frac{\alpha}{h} = \frac{\pi}{2} \frac{1}{\lambda h} \tag{7.2}$$

which when combined with equation (7.1) yields

$$\frac{\alpha}{h} = \frac{\pi}{2} \sqrt[4]{\frac{4EI}{E_p h^3 t}} \tag{7.3}$$

The relative width of the fictitious strut, w/d, is plotted as a function of the parameter λh in Figure 7.2 obtained by a numerical calculation performed in [3]. Stafford Smith suggests that a conservative estimate of the lateral displacements of an infilled frame can be carried out considering the global structure as a network, where the panels are replaced by diagonal struts with relative width $w/d = 0.1$, Figure 7.3. When a panel contains one or more openings, it is even more difficult to evaluate its stiffness and failure mechanisms. In the next sections, a numerical analysis will be made on square panels with a square opening in the middle. Seismic loadings will be simulated statically by two diagonal compressive forces. Crack propagation from the

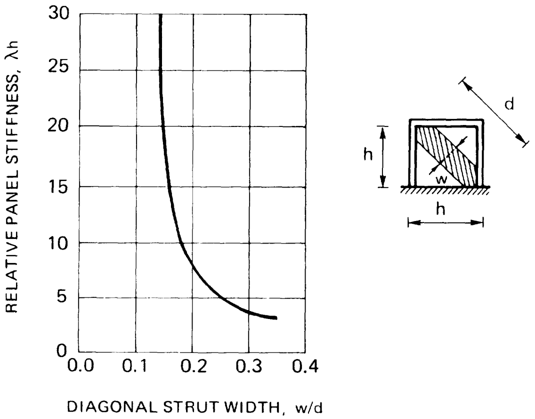

Fig. 7.2. Relative width of the fictitious strut as a function of the parameter λh defined in equation (7.1).

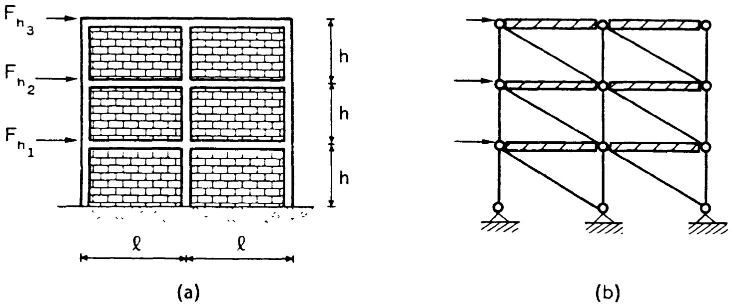

Fig. 7.3. Multistoreys infilled frame (a) and simulation by a network where the panels are replaced by diagonal struts (b).

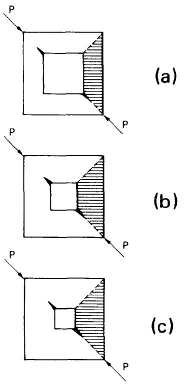

Fig. 7.4. Different panel opening sizes considered in the present analysis.

corners of the openings in Figures 7.4(a) to (c) will be analyzed step-by-step by application of the non-linear Strain Energy Density Theory [4, 5].

7.2. Variation in opening size

Three different panel opening sizes are considered, Figures 7.4(a) to (c). Because of symmetry, only one fourth of the panel needs to be analyzed. The finite element grid patterns that discretize the panels are shown in Figures 7.5(a) to (c). Three different ratios are assumed, $b/d = 1/2$, $2/3$ and $3/4$ where d is the panel half-diagonal and b is the difference between the half-diagonals of panel and opening. The initial crack length a_0 is assumed to be $b/4$ while the thickness of the panel is $t = 30\,\text{cm}$. The sizes will be geometrically scaled to study their influence on the mechanics of fracture. A more refined grid pattern around the crack tip is shown in Figure 7.6. Refer to Table 7.1 that summarizes the cases to be investigated. The three geometrical ratios,

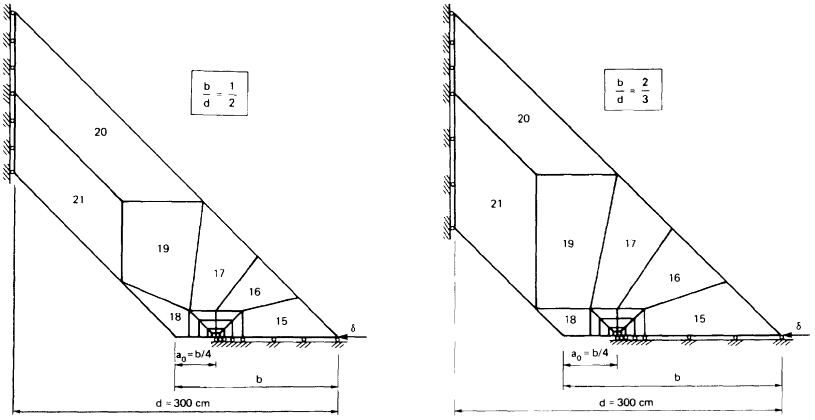

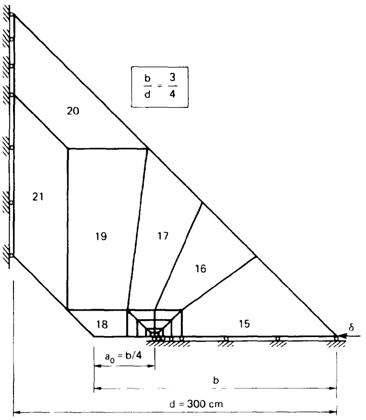

Fig. 7.5. (a) Finite element idealization of the panel in Figure 7.4(a). (b) Finite element idealization of the panel in Figure 7.4(b). (c) Finite element idealization of the panel in Figure 7.4(c).

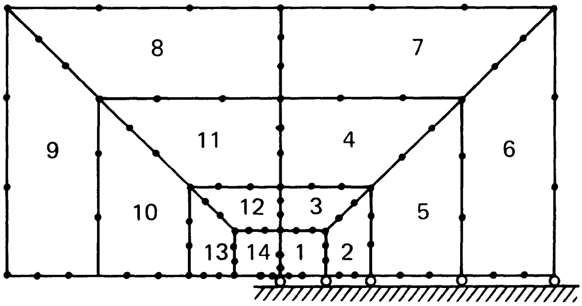

Fig. 7.6. Finite element mesh in the crack tip vicinity.

TABLE 7.1.
The five cases analyzed in this chapter, changing geometrical ratios and loading increments.

Case no.	Geometrical ratio b/d	Displacement increment $\Delta\delta$ (10^{-2} cm)	Symbol
I (1)	1/2	1	●
II (2)	2/3	1	⊙
III (3)	3/4	1	○
IV (4)	3/4	2	□
V (5)	3/4	4	△

b/d, in Figure 7.4 and three different loading increments are considered. The input parameter is the diagonal displacement of the load application point δ, Figure 7.7. The meshes and the deformed configurations related to Case (1) are illustrated in Figures 7.7(a) and (b). The load-displacement values and the crack growth increments are reported in Table 7.2 while the progressive crack lengths and the related strain energy density factors are reported in Table 7.3. In Tables 7.4, the damage level of the finite elements is reported according to equation (2.73) and for different loading increments. The load-displacement responses for a constant deflection increment of $\Delta\delta = 1 \times 10^{-2}$ cm and different geometrical shape factors b/d, are displayed in Figure 7.8. The more flexible panels correspond to low ratios of b/d and their load carrying capacities are also lower.

The ratio of stiffness loss by material damage to total stiffness loss is plotted against the imposed displacement, δ in Figure 7.9. The ratio reaches a maximum of about 50% and then decreases which shows that both material damage and crack growth are important. In Figure 7.10, the load P is plotted against the crack growth $a - a_0$. The post-collapse behavior is not given. However, subsequent loadings would lead to complete separation of the panel. The SR-curves for $b/d = 1/2$, 2/3 and 3/4 are displayed in Figure 7.11. There appears to be an optimum b/d ratio that maximizes subcritical crack growth. This is seen to occur at $b/d \simeq 2/3$.

7.3. Variation in loading step

In Figure 7.12, the load-displacement curves are displayed for $b/d = 3/4$ and three different displacement increments: $\Delta\delta = 1 \times 10^{-2}$, 2×10^{-2} and 4×10^{-2} cm. The results are not sensitive to changes in the load increment, $\Delta\delta$. The ratio of stiffness loss by material damage to total stiffness loss is plotted as a function of the displacement, δ in Figure 7.13. The trend is the same as that found in the preceding cases, but the decrease in damage is more rapid for the smaller load increments. The converse applies to the influence of crack growth. Shown in Figure 7.14 is the variation of the load P with crack

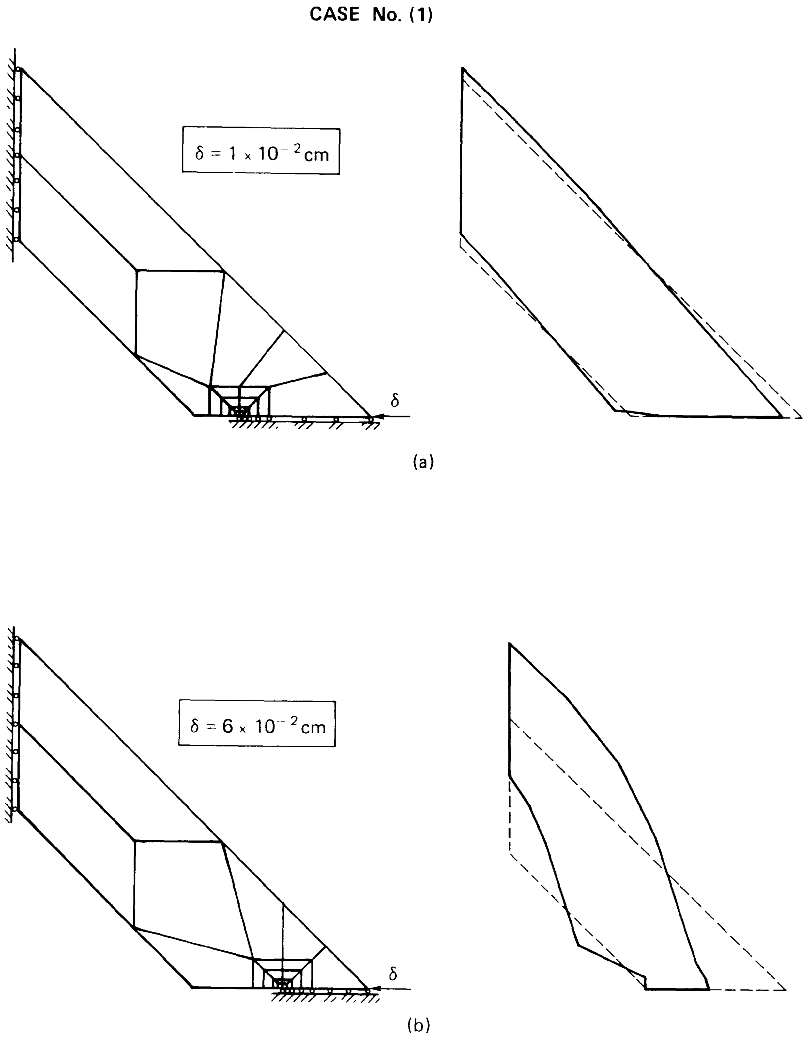

Fig. 7.7. Finite element mesh and deformed configuration related to the first (a) and sixth (b) loading step of Case No. 1 in Table 7.1.

growth $a - a_0$. These curves change more readily as $\Delta\delta$ is varied. Figure 7.15 gives a plot of S versus a by varying $\Delta\delta$. Large steps of $\Delta\delta$ tend to enhance brittle fracture by decreasing the amount of subcritical crack growth, but this effect is not pronounced.

TABLE 7.2.
Load, displacement and crack growth increment at each loading increment and for each case in Table 7.1.

Increment $j = 1, 2$, etc.	Load/Thickness P_j/t (kg/cm)	Displacement δ_j (10^{-2} cm)	Crack growth increment Δa_j (cm)
Case no. (1)			
1	387	1	0.364
2	758	2	1.260
3	1071	3	3.762
4	1284	4	8.579
5	1425	5	10.388
6	1464	6	14.982
Case no. (2)			
1	801	1	0.296
2	1596	2	0.868
3	2349	3	3.177
4	3044	4	4.923
5	3570	5	10.701
6	3924	6	13.094
7	4165	7	15.844
Case no. (3)			
1	1019	1	0.230
2	2036	2	0.647
3	3033	3	1.768
4	3972	4	4.630
5	4735	5	10.210
6	5286	6	13.015
7	5754	7	16.072
Case no. (4)			
1	2036	2	0.646
2	4006	4	3.357
3	5652	6	11.369
4	6876	8	17.112
Case no. (5)			
1	4014	4	3.347
2	7206	8	15.769

7.4. Size scale effect of panel with opening

Figures 7.16(a) to (c) inclusive summarize the *SR*-curves for different b/d and $\Delta\delta/d$ ratios. The amount of slow crack growth decreases as specimen size is increased with complete brittle fracture occurring at $d = 960$ cm.

Figures 7.17(a) to (e) inclusive give the dimensionless load-displacement results for the five cases in Table 7.1. The vertical lines locate global crack

TABLE 7.3.
Crack length and strain energy density factor at each loading increment and for each case in Table 7.1.

Increment $j = 1, 2$, etc.	Crack length a_j (cm)	Strain energy density factor S_j (kg/cm $\times 10^{-3}$)
Case no. (1)		
1	37.864	2.828
2	39.124	8.203
3	42.886	13.820
4	51.465	63.827
5	61.853	51.524
Case no. (2)		
1	50.296	2.299
2	51.164	6.128
3	54.341	10.674
4	59.264	22.301
5	69.965	56.929
Case no. (3)		
1	56.480	1.787
2	57.127	4.865
3	58.895	9.954
4	63.525	30.141
5	73.735	64.629
Case no. (4)		
1	56.896	4.858
2	60.253	15.005
3	71.622	64.007
Case no. (5)		
1	59.597	4.886
2	75.366	83.022

instability that corresponds to the strain energy density factor being critical and equal to $S_c = 8 \times 10^{-3}$ kg/cm. The maximum loads, $P_{\max}^{(2)}$ and $P_{\max}^{(3)}$ obtained respectively from Linear Elastic Fracture Mechanics and Limit Analysis are given in Table 7.5. The stress-intensity factors used in the calculation are given by

$$K_I = \frac{P}{b^{1/2}t} f\left(\frac{b}{d}, \frac{a_0}{b}\right) \tag{7.4}$$

in which $f(\frac{1}{2}, \frac{1}{4}) = 4.78$, $f(\frac{2}{3}, \frac{1}{4}) = 2.36$ and $f(\frac{3}{4}, \frac{1}{4}) = 1.71$.

An approximate evaluation of the limit load can be made by the scheme in Figure 7.18. This gives

TABLE 7.4(a).
Level of damage according to equation (2.73) in each finite element and at each loading increment. Case No. 1 in Table 7.1.

Damage element reference number	Increment $j = 1, 2$, etc. 1	2	3	4	5	6
1	–	14	25	25	25	25
2	–	–	10	25	25	25
3	–	–	5	13	13	13
4	–	–	–	–	3	3
5	–	–	–	6	20	25
6	–	–	–	–	–	8
7	–	–	–	–	–	–
8	–	–	–	–	–	–
9	–	–	–	–	–	–
10	–	–	–	–	–	–
11	–	–	–	–	–	–
12	–	–	–	–	–	–
13	–	–	–	–	–	–
14	–	–	11	21	25	25
15	–	–	–	–	–	–
16	–	–	–	–	–	–
17	–	–	–	–	–	–
18	–	–	–	–	–	–
19	–	–	–	–	–	–
20	–	–	–	–	–	–
21	–	–	–	–	–	–

TABLE 7.4(b).
The same as in Table 7.4(a). Case No. 2 in Table 7.1.

Damage element reference number	Increment $j = 1, 2$, etc. 1	2	3	4	5	6	7
1	–	10	23	25	25	25	25
2	–	–	5	21	25	25	25
3	–	–	3	9	9	9	12
4	–	–	–	3	8	9	–
5	–	–	–	4	19	25	25
6	–	–	–	–	8	20	25
7	–	–	–	–	3	6	–
8	–	–	–	–	–	–	–
9	–	–	–	–	–	–	–
10	–	–	–	–	–	–	–
11	–	–	–	–	–	–	–
12	–	–	–	–	–	–	–
13	–	–	–	–	–	–	–
14	–	–	6	18	25	25	25
15	–	–	–	–	–	–	–
16	–	–	–	–	–	–	–
17	–	–	–	–	–	–	–

TABLE 7.4 (b) (CONTINUED)

Damage element reference number	Increment $j = 1, 2$, etc. 1	2	3	4	5	6	7
18	–	–	–	–	–	–	–
19	–	–	–	–	–	–	–
20	–	–	–	–	–	–	–
21	–	–	–	–	–	–	–

TABLE 7.4 (c).
The same as in Table 7.4 (a). Case No. 3 in Table 7.1.

Damage element reference number	Increment $j = 1, 2$, etc. 1	2	3	4	5	6	7
1	–	5	18	25	25	25	25
2	–	–	–	14	25	25	25
3	–	–	2	8	12	–	4
4	–	–	–	3	10	15	–
5	–	–	–	–	15	25	25
6	–	–	–	3	12	22	25
7	–	–	–	–	6	–	–
8	–	–	–	–	–	–	–
9	–	–	–	–	–	–	–
10	–	–	–	–	–	–	–
11	–	–	–	–	–	–	–
12	–	–	–	–	–	–	–
13	–	–	–	–	–	–	–
14	–	–	–	13	24	25	25
15	–	–	–	–	–	–	–
16	–	–	–	–	–	–	–
17	–	–	–	–	–	–	–
18	–	–	–	–	–	–	–
19	–	–	–	–	–	–	–
20	–	–	–	–	–	–	–
21	–	–	–	–	–	–	–

TABLE 7.4 (d).
The same as in Table 7.4 (a). Case No. 4 in Table 7.1.

Damage element reference number	Increment $j = 1, 2$, etc. 1	2	3	4
1	5	25	25	25
2	–	8	25	25
3	–	11	21	25
4	–	4	16	25
5	–	–	18	25
6	–	2	17	25
7	–	–	11	–
8	–	–	–	–
9	–	–	–	–

TABLE 7.4 (d) (CONTINUED)

Damage element reference number	Increment $j = 1, 2$, etc. 1	2	3	4
10	–	–	–	–
11	–	–	–	–
12	–	–	–	–
13	–	–	–	–
14	–	10	25	25
15	–	–	–	–
16	–	–	–	–
17	–	–	–	–
18	–	–	–	–
19	–	–	–	–
20	–	–	–	–
21	–	–	–	–

TABLE 7.4 (e).
The same as in Table 7.4 (a). Case No. 5 in Table 7.1.

Damage element reference number	Increment $j = 1, 2$, etc. 1	2
1	25	25
2	7	25
3	11	25
4	4	23
5	–	25
6	2	24
7	–	19
8	–	–
9	–	–
10	–	–
11	–	–
12	–	6
13	–	–
14	10	25
15	–	–
16	–	–
17	–	–
18	–	–
19	–	–
20	–	–
21	–	–

$$P_{\max}^{(3)} = \frac{3}{80}\sigma_u d^2 \frac{(b/d)^2}{(2-b/d)} \tag{7.5}$$

The results in Figures 7.19(a) to (e) inclusive are normalized with respect to $P_{\max}^{(2)}$ obtained from Linear Elastic Fracture Mechanics and plotted against d.

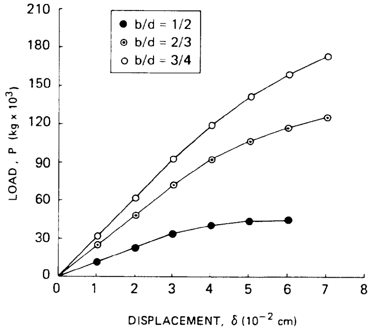

Fig. 7.8. Load-displacement diagrams for three different geometrical ratios *b*/*d* and $\Delta\delta = 1 \times 10^{-2}$ cm.

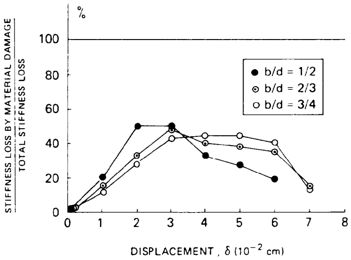

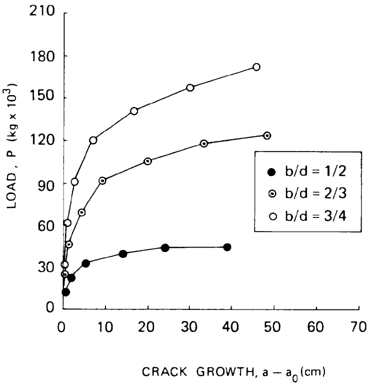

Fig. 7.9. Ratio of stiffness loss by material damage to total stiffness loss as a function of displacement, for three different geometrical ratios *b*/*d* and $\Delta\delta = 1 \times 10^{-2}$ cm.

Fig. 7.10. Load-crack growth diagrams for three different geometrical ratios *b*/*d* and $\Delta\delta = 1 \times 10^{-2}$ cm.

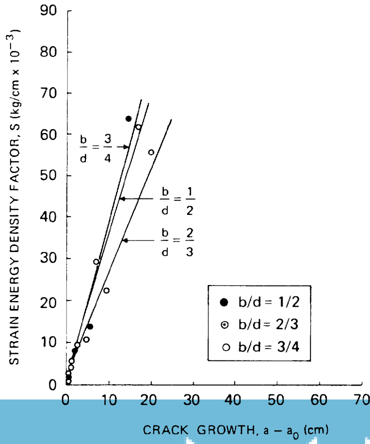

Fig. 7.11. Strain energy density factor versus crack growth for three different geometrical ratios *b*/*d* and $\Delta\delta = 1 \times 10^{-2}$ cm.

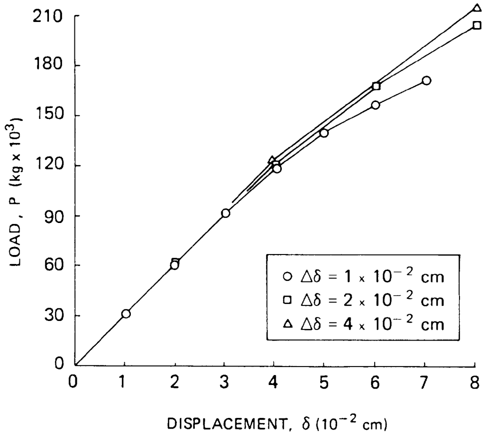

Fig. 7.12. Load-displacement diagrams for $b/d = 3/4$ and three different loading increments.

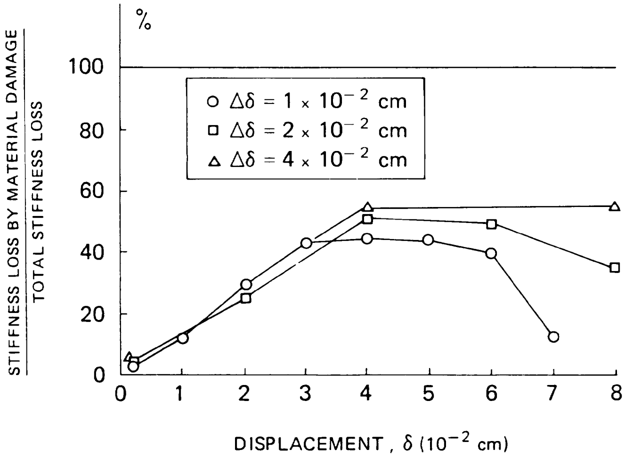

Fig. 7.13. Ratio of stiffness loss by material damage to total stiffness loss as a function of displacement, for $b/d = 3/4$ and three different loading increments.

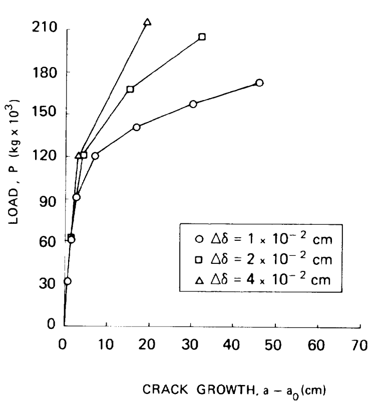

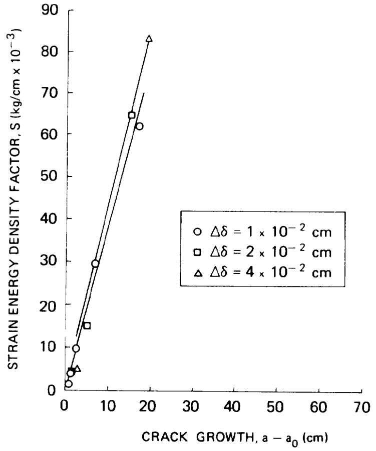

Fig. 7.14. Load-crack growth diagrams for three different loading increments and $b/d = 3/4$.

Fig. 7.15. Strain energy density factor versus crack growth for three different loading increments and $b/d = 3/4$.

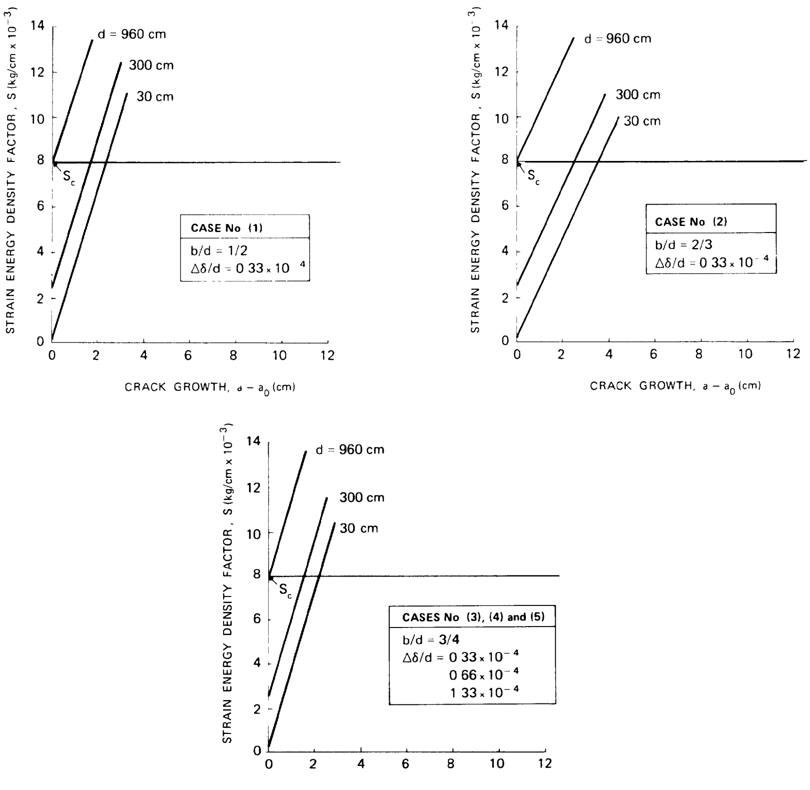

Fig. 7.16. (a) Straight line plots of strain energy density factor versus crack growth, varying the size scale of the panel. Case No. 1 in Table 7.1. (b) The same as in Figure 7.16 (a). Case No. 2 in Table 7.1. (c) The same as in Figure 7.16 (a). Cases No. 3, 4 and 5 in Table 7.1.

TABLE 7.5.

(a) Maximum load for different size scales and according to the various theories: Strain Energy Density Theory, Linear Elastic Fracture Mechanics, Limit Analysis. Case No. 1 in Table 7.1. (b) The same as in Table 7.5 (a). Case No. 2 in Table 7.1. (c) The same as in Table 7.5 (a). Case No. 3 in Table 7.1. (d) The same as in Table 7.5 (a). Case No. 4 in Table 7.1. (e) The same as in Table 7.5 (a). Case No. 5 in Table 7.1.

Case no. (1)

Size d, cm	30	120	300	960
$P^{(1)}_{\max}$ (SEDT), kg	412	5 250	20 625	63 058
$P^{(2)}_{\max}$ (LEFM), kg	348	2 787	11 015	63 058
$P^{(3)}_{\max}$ (Limit analysis), kg	180	2 880	18 000	184 320
$P^{(1)}_{\max}/P^{(2)}_{\max}$ ratio	1.18	1.88	1.87	1.00
$P^{(3)}_{\max}/P^{(2)}_{\max}$ ratio	0.52	1.03	1.63	2.92

Case no. (2)

Size d, cm	30	120	300	960
$P^{(1)}_{\max}$ (SEDT), kg	1 162	13 200	56 250	147 532
$P^{(2)}_{\max}$ (LEFM), kg	815	6 520	25 772	147 532
$P^{(3)}_{\max}$ (Limit analysis), kg	360	5 760	36 000	368 640
$P^{(1)}_{\max}/P^{(2)}_{\max}$ ratio	1.43	2.02	2.18	1.00
$P^{(3)}_{\max}/P^{(2)}_{\max}$ ratio	0.44	0.88	1.40	2.50

Case no. (3)

Size d, cm	30	120	300	960
$P^{(1)}_{\max}$ (SEDT), kg	1 462	16 800	71 250	216 540
$P^{(2)}_{\max}$ (LEFM), kg	1 196	9 570	37 828	216 540
$P^{(3)}_{\max}$ (Limit analysis), kg	486	7 776	48 600	497 664
$P^{(1)}_{\max}/P^{(2)}_{\max}$ ratio	1.22	1.75	1.88	1.00
$P^{(3)}_{\max}/P^{(2)}_{\max}$ ratio	0.41	0.81	1.28	2.30

Case no. (4)

Size d, cm	30	120	300	960
$P^{(1)}_{\max}$ (SEDT), kg	1 980	20 760	75 000	216 540
$P^{(2)}_{\max}$ (LEFM), kg	1 196	9 570	37 828	216 540
$P^{(3)}_{\max}$ (Limit analysis), kg	486	7 776	48 600	497 664
$P^{(1)}_{\max}/P^{(2)}_{\max}$ ratio	1.65	2.17	1.98	1.00
$P^{(3)}_{\max}/P^{(2)}_{\max}$ ratio	0.41	0.81	1.28	2.30

Case no. (5)

Size d, cm	120	300	600	960
$P^{(1)}_{\max}$ (SEDT), kg	33 000	135 000	360 000	216 540
$P^{(2)}_{\max}$ (LEFM), kg	9 570	37 828	107 000	216 540
$P^{(3)}_{\max}$ (Limit analysis), kg	7 776	48 600	194 400	497 664
$P^{(1)}_{\max}/P^{(2)}_{\max}$ ratio	3.45	3.56	3.36	1.00
$P^{(3)}_{\max}/P^{(2)}_{\max}$ ratio	0.81	1.28	1.82	2.30

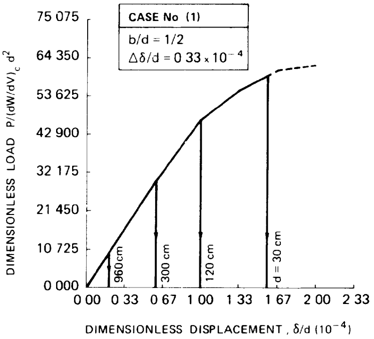
CASE No (1)
b/d = 1/2
Δδ/d = 0 33 x 10⁻⁴
DIMENSIONLESS LOAD P/(dW/dV)c d²
75 075
64 350
53 625
42 900
32 175
21 450
10 725
0 000
960cm
300 cm
120 cm
d = 30 cm
0 00
0 33
0 67
1 00
1 33
1 67
2 00
2 33
DIMENSIONLESS DISPLACEMENT , δ/d (10⁻⁴)

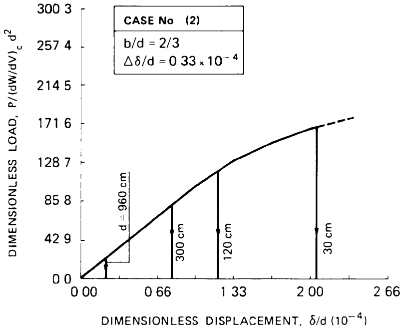
CASE No (2)
b/d = 2/3
Δδ/d = 0 33 x 10⁻⁴
DIMENSIONLESS LOAD, P/(dW/dV)c d²
300 3
257 4
214 5
171 6
128 7
85 8
42 9
0 0
d = 960 cm
300 cm
120 cm
30 cm
0 00
0 66
1 33
2 00
2 66
DIMENSIONLESS DISPLACEMENT, δ/d (10⁻⁴)

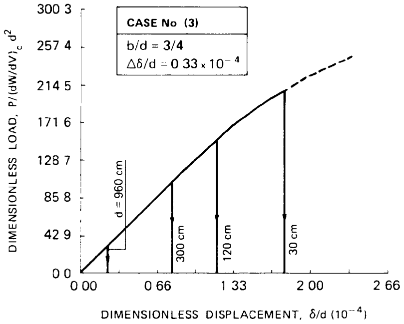
CASE No (3)
b/d = 3/4
Δδ/d = 0 33 x 10⁻⁴
DIMENSIONLESS LOAD, P/(dW/dV)c d²
300 3
257 4
214 5
171 6
128 7
85 8
42 9
0 0
d = 960 cm
300 cm
120 cm
30 cm
0 00
0 66
1 33
2 00
2 66
DIMENSIONLESS DISPLACEMENT, δ/d (10⁻⁴)

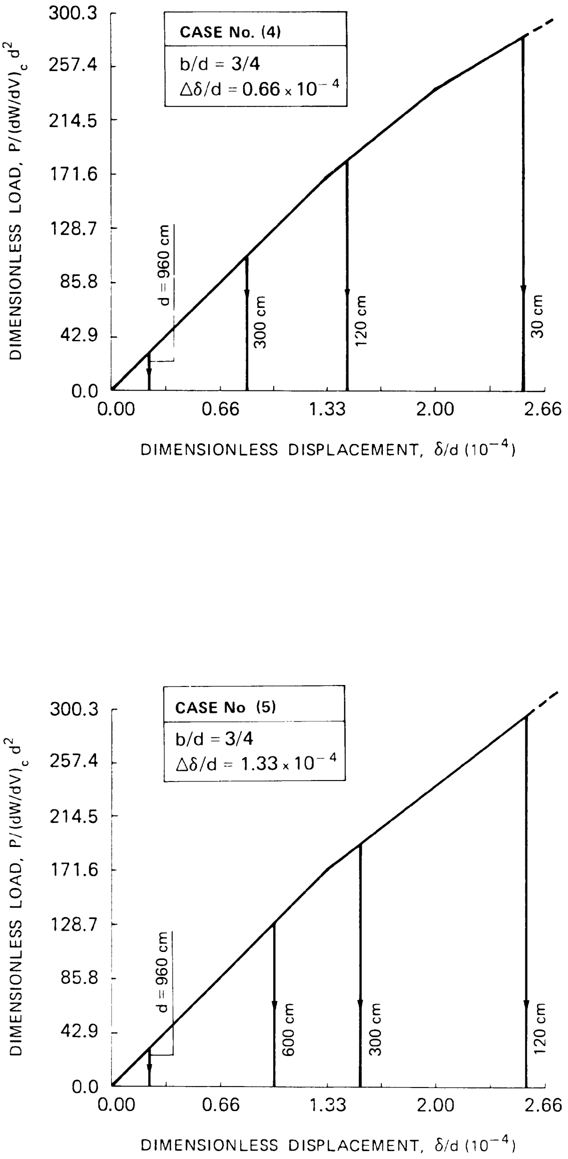

Fig. 7.17. (a) Dimensionless load-displacement diagrams, varying the size scale of the panel. Case No. 1 in Table 7.1. (b) The same as in Figure 7.17(a). Case No. 2 in Table 7.1. (c) The same as in Figure 7.17(a). Case No. 3 in Table 7.1. (d) The same as in Figure 7.17(a). Case No. 4 in Table 7.1. (e) The same as in Figure 7.17(a). Case No. 5 in Table 7.1.

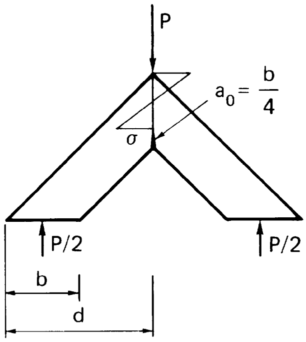

$$\sigma = \frac{M}{W} = \frac{\frac{1}{2}P\left(d - \frac{b}{2}\right)}{t\left(\frac{3}{4}b\right)^2 / 6}$$

Fig. 7.18. Approximate evaluation of the limit load at the ligament.

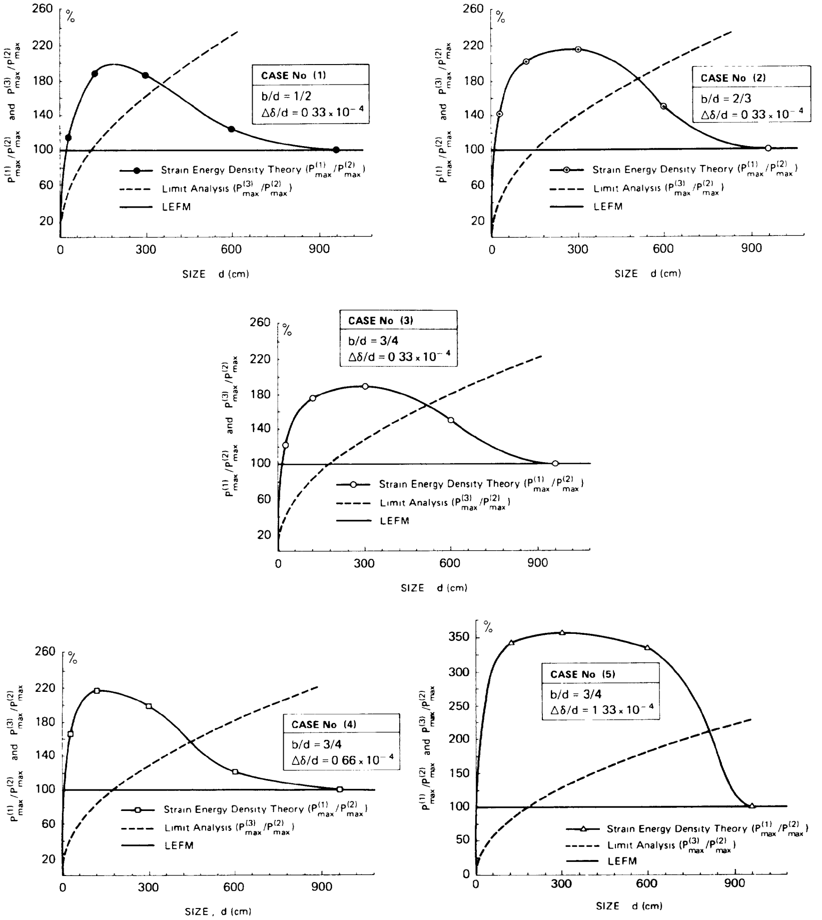

Fig. 7.19. (a) Maximum load predicted by Strain Energy Density Theory and by Limit Analysis referred to the critical load from LEFM. Case No. 1 in Table 7.1. (b) The same as in Figure 7.19(a). Case No. 2 in Table 7.1. (c) The same as in Figure 7.19(a). Case No. 3 in Table 7.1. (d) The same as in Figure 7.19(a). Case No. 4 in Table 7.1. (e) The same as in Figure 7.19(a). Case No. 5 in Table 7.1.

The strain energy density theory prediction shows that the normalized load rises with d to a maximum of $P^{(1)}_{\mathrm{max}}/P^{(2)}_{\mathrm{max}} \simeq 2.0$ and then decreases to unity. The ratio $P^{(1)}_{\mathrm{max}}/P^{(2)}_{\mathrm{max}}$ represents also the ratio of fictitious to real K_{IC}, which is larger than unity when the damage dissipation prevails over the size effect.

References

1. Stafford Smith, B., Lateral stiffness of infilled frames, Journal of the Structural Division, American Society of Civil Engineers, 88, pp. 183–199 (1962).
2. Stafford Smith, B., Behavior of square infilled frames, Journal of the Structural Division, American Society of Civil Engineers, 92, pp. 381–403 (1966).
3. Riddington, J.R. and Stafford Smith, B., Analysis of infilled frames subject to racking with design recommendation, The Structural Engineer, 55, pp. 263–268 (1977).
4. Sih, G.C. and Matic, P., A pseudo-linear analysis of yielding and crack growth: strain energy density criterion, Defects, Fracture and Fatigue, edited by G.C. Sih and J.W. Provan, Martinus-Nijhoff Publishers, The Hague, pp. 223–232 (1982).
5. Carpinteri, A. and Sih, G.C., Damage accumulation and crack growth in bilinear materials with softening: application of strain energy density theory, Journal of Theoretical and Applied Fracture Mechanics, Vol. 4, No. 2, pp. 145–160 (1984).

8

Fracture testing and design

8.1. Model scaling and physical similitude

Preliminary remarks. One of the major problems in analyzing the strength of materials is the so-called 'size effect'. Despite the numerous research efforts, this effect is still not completely understood. Two important aspects of size effects are:

(1) Uncracked structures show an increase in brittleness when their size is increased, and
(2) Notched (or cracked) structures become less sensitive to the presence of mechanical imperfections when their size is decreased and they tend to behave in a more ductile fashion.

These two effects have been known for a long time, but it is only recently that a consistent explanation could be given in terms of Fracture Mechanics concepts. The two fundamental failure modes known classically are brittle fracture and plastic collapse both of which may occur depending on the combination of the load and geometric variables. Although Plastic Limit Analysis can be applied to treat the failure of structures due to excessive distortion and Linear Elastic Fracture Mechanics to the onset of rapid fracture, both of these disciplines apply only at the global scale level. They cannot address failure by yielding and fracture [1–9] that is the rule in practice rather than the exception.

Materials with aggregates as concrete cannot be analyzed simply by applying the Linear Elastic Fracture Mechanics concept.* The difficulties lie in explaining the experimental results and in extrapolating them to the structural design of large structures that contain heterogeneity and nonlinearity behavior such as concrete. There are two fundamental reasons why cementitious materials cannot be treated by Linear Elastic Fracture Mechanics:

---

* Since the stress-intensity factor K_I [11] or K_{IC} is derived from a linear elastic analysis, it cannot be used to explain nonlinear effects at the crack tip due to change in specimen size.

(1) Slow crack growth, which occurs prior to unstable crack propagation such that the actual crack length at termination is not known, and
(2) Microcracking which occurs near the crack tip, where energy is dissipated due to plasticity as in the case of metallic materials.

The presence of mechanical defects such as cracks or notches is significant because they alter the local stress field. This effect interacts with specimen size as smaller specimens store less energy and tend to be more ductile while the opposite holds for the larger specimens. Peterson [10] has shown that below a certain size threshold the net section rupture stress coincides with the ultimate strength σ_u where the stress raisers are no longer sensitive.

The only theory that can consistently explain the nonlinear behavior of concrete from uniaxial data alone is based on the strain energy density concept [12–14]. It can predict crack initiation, slow growth and final termination without invoking arbitrary assumptions. The *SR*-curves* that consist of plotting the strain energy density factor S as a function of crack growth are straight lines for crack growth data that are highly nonlinear. This salient feature of the theory permits extrapolation of specimen sizes, loading rates or steps and material types to situations that are not tested. The examples presented in the earlier chapters of this book have demonstrated the versatility and usefulness of the *SR*-curves. The results are particularly pertinent for establishing design formulas.

Dimensional analysis. The size scale effect can be analyzed by resorting to dimensional analysis. Two of the important parameters that were used are the strain energy density function $[(\mathrm{d}W/\mathrm{d}V)] = [F]\,[L]^{-2}$, and the strain energy density factor $[S] = [F]\,[L]^{-1}$. When the structural size reaches certain upper limit, stable crack growth ceases to occur and the crack growth becomes catastrophic. Material inhomogeneity, of course, also interacts with the loading depending on the specimen or structure size which can vary from case to case. This is why it would be more consistent and less problematic to focus attention on the rate of energy dissipated and/or stored in a unit volume of material.

To start off with, the fundamental mechanical quantities to be defined are length $[L]$, force $[F]$ and time $[T]$. Consider a certain quantity $[Q] = [L]^{\alpha}[F]^{\beta}[T]^{\gamma}$. If the length unit of measure is multiplied by λ, the force unit of measure by ϕ and the time unit of measure by τ, then Q is multiplied by $\lambda^{\alpha}\phi^{\beta}\tau^{\gamma}$. Define three mechanical quantities Q_1, Q_2, Q_3 as follows:

$$[Q_1] = [L]^{\alpha_1}[F]^{\beta_1}[T]^{\gamma_1} \tag{8.1a}$$

---

* It should be cautioned that the crack-growth model used throughout this book assumes elastic unloading. Sih has shown in [14] that the assumption of plastic unloading will only alter the *SR*-curve results quantitatively but not qualitatively.

$$[Q_2] = [L]^{\alpha_2}[F]^{\beta_2}[T]^{\gamma_2} \tag{8.1b}$$

$$[Q_3] = [L]^{\alpha_3}[F]^{\beta_3}[T]^{\gamma_3} \tag{8.1c}$$

If the units of measure (L, F, T) are multipled by λ, ϕ, τ, then the units measuring Q_1, Q_2, Q_3 are multiplied by χ_1, χ_2, χ_3 so that

$$\chi_1 = \lambda^{\alpha_1}\phi^{\beta_1}\tau^{\gamma_1} \tag{8.2a}$$

$$\chi_2 = \lambda^{\alpha_2}\phi^{\beta_2}\tau^{\gamma_2} \tag{8.2b}$$

$$\chi_3 = \lambda^{\alpha_3}\phi^{\beta_3}\tau^{\gamma_3} \tag{8.2c}$$

It follows that

$$\ln\chi_1 = \alpha_1 \ln\lambda + \beta_1 \ln\phi + \gamma_1 \ln\tau \tag{8.3a}$$

$$\ln\chi_2 = \alpha_2 \ln\lambda + \beta_2 \ln\phi + \gamma_2 \ln\tau \tag{8.3b}$$

$$\ln\chi_3 = \alpha_3 \ln\lambda + \beta_3 \ln\phi + \gamma_3 \ln\tau \tag{8.3c}$$

which is a linear system of equations with unknowns $\ln\lambda$, $\ln\phi$ and $\ln\tau$. It admits one and only one solution, if and only if the coefficient determinant is different from zero:

$$D = \begin{bmatrix} \alpha_1 & \beta_1 & \gamma_1 \\ \alpha_2 & \beta_2 & \gamma_2 \\ \alpha_3 & \beta_3 & \gamma_3 \end{bmatrix} \neq 0 \tag{8.4}$$

Equation (8.4) when satisfied makes the three quantities Q_1, Q_2 and Q_3 dimensionally independent. They may thus be regarded as fundamental quantities.

Another equivalent definition of dimensionally independent quantities can be invoked. The three quantities Q_1, Q_2, Q_3 are dimensionally independent when any quantity $[Q_0] = [L]^{\alpha_0}[F]^{\beta_0}[T]^{\gamma_0}$ can have the same physical dimensions as the product $Q_1^{\alpha_{10}}Q_2^{\alpha_{20}}Q_3^{\alpha_{30}}$ for appropriate values of α_{10}, α_{20} and α_{30}. From equations (8.1), it follows that

$$\alpha_0 = \alpha_1\alpha_{10} + \alpha_2\alpha_{20} + \alpha_3\alpha_{30} \tag{8.5a}$$

$$\beta_0 = \beta_1\alpha_{10} + \beta_2\alpha_{20} + \beta_3\alpha_{30} \tag{8.5b}$$

$$\gamma_0 = \gamma_1\alpha_{10} + \gamma_2\alpha_{20} + \gamma_3\alpha_{30} \tag{8.5c}$$

which is a linear system with unknowns α_{10}, α_{20} and α_{30} and the transposed matrix D^T of the system in equations (8.3) as coefficient matrix. Equations (8.3) and (8.5) admit one and only one solution, if and only if the condition in equation (8.4) holds. There are only two fundamental quantities in the statical field: length $[L]$ and force $[F]$, since time does not enter. Under these considerations, it is possible to assert that stress, $[\sigma] = [L]^{-2}[F]$, length $[L]$ and time $[T]$ are dimensionally independent:

$$D = \begin{vmatrix} -2 & 1 & 0 \\ 1 & 0 & 0 \\ 0 & 0 & 1 \end{vmatrix} = -1 \neq 0$$

Buckingham's theorem. The mechanical behavior of a structural element and its collapse mechanisms can be scaled by a model provided that the size reduction is not too small. In the case of a cracked body, two different failure modes are possible:

(1) collapse at ultimate strength caused by the maximum normal stress σ with the crack considered as a weakening of the cross-section without including the local effects, and

(2) crack propagation fracture determined by the critical stress-intensity factor, K_{IC}, assuming that structure geometry and loadings are symmetrical with respect to the crack line. The two generalized forces are $[\sigma] = [L]^{-2}[F]$ and $[K_I] = [L]^{-3/2}[F]$.

The Buckingham's Theorem will now be applied to analyze a simple system that consists of a body symmetrically loaded with respect to the crack line. The material is homogeneous, isotropic and elastic-plastic. In one case, the yield strength σ_y will be used as reference and the other considers the tensile

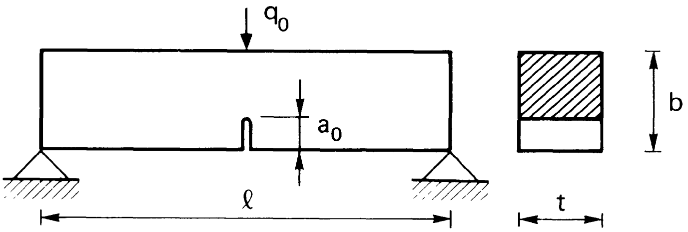

Fig. 8.1. Cracked body subjected to general loading.

strength σ_u. It is evident from Figure 1.3 that the two cases are the limits of an elastic-linear softening material.

Let q_0 be the load at final collapse for the cracked structure in Figure 8.1. This load is a function of several variables and can be expressed as

$$q_0 = F(q_1, q_2, \ldots, q_n; \quad r_1, r_2, \ldots, r_m) \tag{8.6}$$

where q_i are physical quantities with different dimensions and r_i are nondimensional numbers. Each quantity with certain dimensions appears just once in the function F. For example, in the case of an elastic-work-hardening material, q_1 could be the ultimate strength σ_u and r_1 the ratio of the yield strength σ_y to the ultimate strength; q_2 could be a linear size b of the structure in Figure 8.1; r_2, r_3, etc., the ratios of the other sizes, which are characteristic of the structural geometry with the reference size b; q_3 could be the fracture toughness K_{IC}; and so on. Consider now two dimensionally independent quantities q_1 and q_2. They are considered as fundamental quantities such that the product $q_1^{\alpha_{10}} q_2^{\alpha_{20}}$ has the same dimensions as q_0 for suitable values of α_{10} and α_{20}. In the same way, the product $q_1^{\alpha_{13}} q_2^{\alpha_{23}}$ can have the same dimensions as q_3, for suitable values of α_{13} and α_{23}, and so on. The function in equation (8.6) can therefore be transformed into

$$\frac{q_0}{q_1^{\alpha_{10}} q_2^{\alpha_{20}}} = G\left(q_1, q_2, \frac{q_3}{q_1^{\alpha_{13}} q_2^{\alpha_{23}}}, \ldots, \frac{q_n}{q_1^{\alpha_{1n}} q_2^{\alpha_{2n}}}; \quad r_1, r_2, \ldots, r_m\right) \tag{8.7}$$

The function F becomes G because of nondimensionalization. If the unit of measure of q_1 changes, G, being a nondimensional number, does not vary. Therefore, G is not really a function of q_1 nor of q_2. It is only a function of $(n - 2 + m)$ nondimensional numbers, and thus

$$\frac{q_0}{q_1^{\alpha_{10}} q_2^{\alpha_{20}}} = G(N_3, N_4, \ldots, N_n; \quad r_1, r_2, \ldots, r_m) \tag{8.8}$$

In the simple case of an elastic-perfectly plastic material in Figure 8.1, q_0 is given by

$$q_0 = F\left(\sigma_y, b, K_{IC}; \quad \frac{a_0}{b}, \frac{l}{b}, \frac{t}{b}\right) \tag{8.9}$$

where the initial crack length a_0 is also included. If σ_y and b are regarded as fundamental quantities, then equation (8.9) becomes

$$\frac{q_0}{\sigma_y^\alpha b^\beta} = G\left(\frac{K_{IC}}{\sigma_y b^{1/2}};\quad \frac{a_0}{b}, \frac{l}{b}, \frac{t}{b}\right) \tag{8.10}$$

where the function G depends on the geometry of structure and external loadings. It is possible to separate function G into two functions G_1 and G_2 as

$$\frac{q_0}{\sigma_y^\alpha b^\beta} = G_1\left(s, \frac{a_0}{b}\right) G_2\left(\frac{l}{b}, \frac{t}{b}\right) \tag{8.11}$$

The function G_1 governs the notch sensitivity phenomenon and is a function of the nondimensional number

$$s = \frac{K_{IC}}{\sigma_y b^{1/2}} \tag{8.12}$$

and of the relative crack length a_0/b. Note that both mechanical properties of the material and size of the body appear in s which will be referred to as the *brittleness number.*

Structural geometries. For the tension test in Figure 4.1, the stress-intensity factor is given by equation (4.1) from which it is possible to obtain the load at incipient fracture:

$$\frac{\sigma_{\max}^{(2)}}{\sigma_y} = s\left(\frac{\cos\dfrac{\pi}{2}\dfrac{a_0}{b}}{\dfrac{\pi}{2}\dfrac{a_0}{b}}\right)^{1/2} \tag{8.13}$$

The load corresponding to plastic collapse for the cracked section is

$$\frac{\sigma_{\max}^{(3)}}{\sigma_y} = 1 - \frac{a_0}{b} \tag{8.14}$$

In Figure 8.2, the nondimensional load at fracture is plotted as a function of the relative crack length a_0/b for different values of the brittleness number $s = K_{IC}/\sigma_y\sqrt{2b}$. The load at which plastic flow begins is also given. It is evident that the fracture data have no meaning for s higher than the critical value $s_0 \simeq 0.54$ since plastic collapse is the governing mechanism for $s > 0.54$.

For the three points bend test in Figure 3.1, the stress-intensity factor is given by equation (3.11) from which the load at incipient fracture is determined:

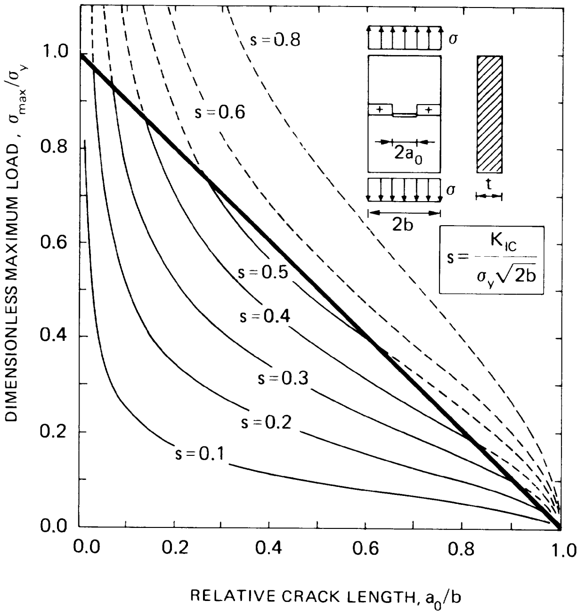

Fig. 8.2. Nondimensional load at fracture (thin line) and at plastic collapse (thick line) as a function of the relative crack length. Tension test.

$$\frac{P^{(2)}_{\text{max}}l}{\sigma_y b^2 t} = \frac{s}{f\left(\frac{a_0}{b}\right)} \tag{8.15}$$

The plastic collapse load obtained from the limit analysis is

$$\frac{P^{(3)}_{\text{max}}l}{\sigma_y b^2 t} = \left(1 - \frac{a_0}{b}\right)^2 \tag{8.16}$$

whereas the ultimate strength for an elastic material is

$$\frac{P^{(3)}_{\text{max}}l}{\sigma_u b^2 t} = \frac{2}{3}\left(1 - \frac{a_0}{b}\right)^2 \tag{8.17}$$

The data in Figure 8.3 are analogous to those in Figure 8.2. For an elastic-perfectly plastic material, fracture data are valid only if $s < 0.75$. The fracture curve is tangent to the plastic flow curve at $s = 0.75$. Since $0.75 > 0.54$, (fracture data limits of an elastic-plastic material), it can be asserted that the three

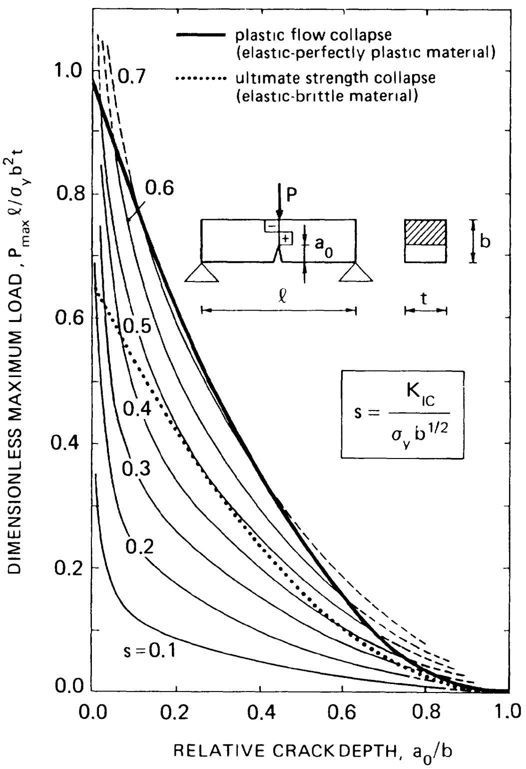

Fig. 8.3. The same as in Figure 8.2. Three point bend test.

point bend specimen is more sensitive to notch effects than the tension specimen if the material is elastic-perfectly plastic. The converse holds for an elastic-brittle material.

For the compact test in Figure 8.4, the stress-intensity factor is given by

$$K_I = \frac{Q}{b^{1/2}t} g\left(\frac{a_0}{b}\right) \tag{8.18}$$

in which

$$g\left(\frac{a_0}{b}\right) = 29.6\left(\frac{a_0}{b}\right)^{1/2} - 185.5\left(\frac{a_0}{b}\right)^{3/2} + 655.7\left(\frac{a_0}{b}\right)^{5/2}$$
$$- 1017\left(\frac{a_0}{b}\right)^{7/2} + 638.9\left(\frac{a_0}{b}\right)^{9/2}$$

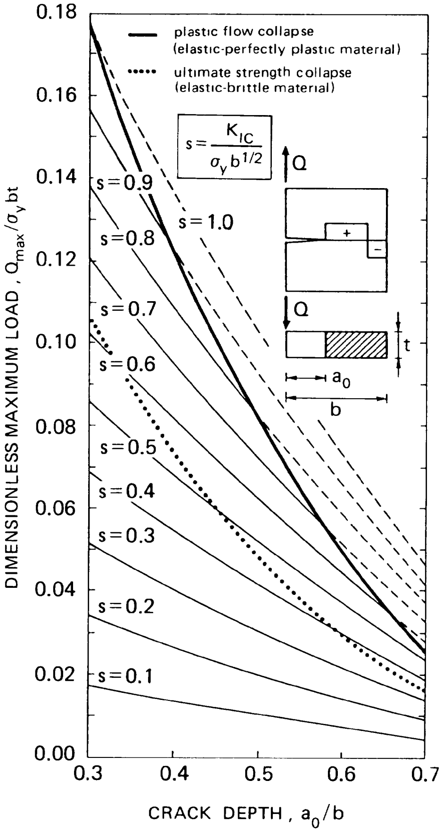

Fig. 8.4. The same as in Figure 8.2. Compact test.

for $0.3 \leqslant (a_0/b) \leqslant 0.7$. From equation (8.18), the crack extension force is obtained:

$$\frac{Q^{(2)}_{\max}}{\sigma_y b t} = \frac{s}{g\left(\dfrac{a_0}{b}\right)} \tag{8.19}$$

The plastic or ultimate strength collapse at the weakened section due to the eccentric load are given respectively by

$$\frac{Q^{(3)}_{\max}}{\sigma_y bt} = \left[\left(1 + \frac{a_0}{b}\right)^2 + \left(1 - \frac{a_0}{b}\right)^2\right]^{1/2} - \left(1 + \frac{a_0}{b}\right) \tag{8.20a}$$

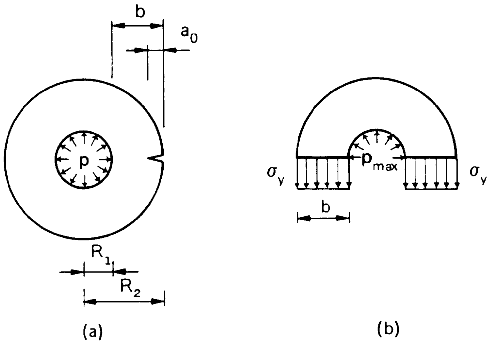

Fig. 8.5. Cracked cylinder pressure vessel (a). Plastic collapse of the uncracked vessel (b).

$$\frac{Q^{(3)}_{\max}}{\sigma_u bt} = \left(1-\frac{a_0}{b}\right)^2 \Big/ \left(2\frac{a_0}{b}+4\right) \tag{8.20b}$$

Fracture data in Figure 8.4 are significant up to $s \simeq 1.02$. Fracture collapse can occur in small specimens provided that the initial cracks are not too long. For $s = 0.9$, the relative crack length must be $a_0/b \lesssim 0.4$. The condition of small scale yielding, according to ASTM-E399 [11] however, calls for the opposite, i.e., for sufficiently long cracks with $a_0/b > 0.45$.

For the cracked cylinder pressure vessel in Figure 8.5(a), the pressure of plastic collapse of the uncracked vessel may be evaluated from Figure 8.5(b) as

$$p^{(3)}_{\max}/\sigma_y = \frac{R_2}{R_1} - 1 \tag{8.21}$$

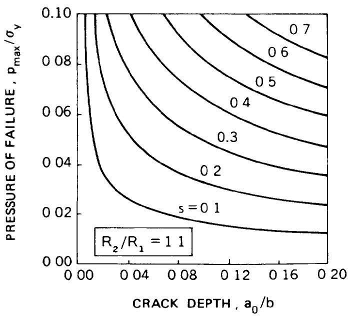

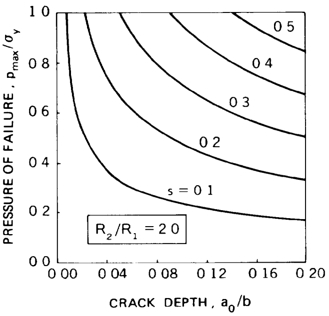

Fig. 8.6. Pressure of failure for the cracked cylinder vessel in Figure 8.5(a). The upper horizontal line represents plastic collapse of the uncracked vessel in Figure 8.5(b). $R_2/R_1 = 1.1$.

Fig. 8.7. The same as in Figure 8.6. $R_2/R_1 = 2.0$.

On the other hand, the pressure at which crack propagation begins for small cracks is found as

$$p^{(2)}_{\max}/\sigma_y = 0.25\left[\left(\frac{R_2}{R_1}\right)^2 - 1\right]\frac{s}{\sqrt{\dfrac{a_0}{b}}} \tag{8.22}$$

In Figure 8.6, the crack propagation curves are given for $R_2/R_1 = 1.1$ while the brittleness number, s, is varied. The upper horizontal line represents plastic collapse. With a crack depth of $a_0/b = 0.1$, the brittleness number must be higher than 0.60 in order for the Plastic Limit Analysis to be valid. It must be lower than 0.60 so that Linear Elastic Fracture Mechanics can be applied. Similar results are shown in Figure 8.7 for $R_2/R_1 = 2.0$. The transition brittleness number is approximately 0.42. Hence, ductility appears to be enhanced by raising the fracture toughness of the material and/or by reducing the sizes of the specimen.

Data obtained from the damage-crack growth model [12–14] in this book may be regarded as a generalization of the results based on the critical stress intensity factor concept. The brittleness number s, which governs the transition between plastic collapse and brittle fracture, can be related to the number defined in equation (3.10) [12]:

$$S^* = s^2\,\frac{(1+\nu)(1-2\nu)}{\pi} \tag{8.23}$$

Here, slow crack growth and material damage are not considered. That is, the relation $(\mathrm{d}W/\mathrm{d}V)_c = \sigma_u^2/2E$ has been used with the assumption that local and global crack instability occur simultaneously. This, of course, is an idealization that does not occur in nature.

Dugdale crack model. The Dugdale crack in an infinite sheet [15] considers a plastic zone, $r_y/(a + r_y)$ that varies as a function of the applied normal stress σ in Figure 8.8(a):

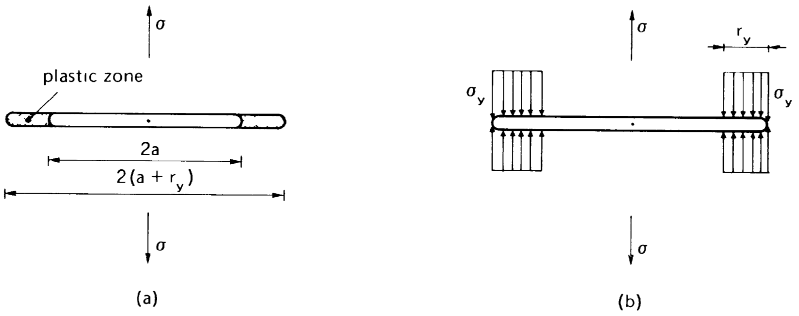

Fig. 8.8. Dugdale crack in an infinite sheet (a). Plastic pressure tending to close the fictitious crack (b).

$$\frac{r_y}{a+r_y} = 2\sin^2\left(\frac{\pi}{4}\frac{\sigma}{\sigma_y}\right) \tag{8.24}$$

According to equation (8.24), the stress σ achieves the yield strength σ_y when $r_y/a \to \infty$ and the plastic zone occupies the entire sheet. Suppose now that the plastic zone size is constant under the plane stress condition and given by

$$r_y = \frac{1}{2\pi}\left(\frac{K_{IC}}{\sigma_y}\right)^2 \tag{8.25}$$

and then consider the plastic collapse separately. The pressure in the plastic zone is σ_y that tends to close the fictitious crack of length $2(a + r_y)$ at distances $r < r_y$ from its tip, Figure 8.8(b).

Define a dimensionless fracture load, $\tilde{q}_0$ by ignoring the plastic deformation at the crack tip such that

$$\tilde{q}_0 = \frac{s}{g(\xi)} \tag{8.26}$$

where s is the brittleness number and g the function that depends on the structure and load geometry with ξ being the relative crack depth. The following assumptions will now be invoked to solve the problem in Figure 8.9(a):

(1) Replace the plastic pressure on the prospective crack surfaces in Figure 8.9(b) with the equivalent force F^*, and bending moment M^* shown in Figure 8.9(c).

$$F^* = -\sigma_y r_y t \tag{8.27a}$$

$$M^* = -\sigma_y r_y t\left(\frac{b}{2} - a - \frac{r_y}{2}\right) \tag{8.27b}$$

(2) Fracture collapse is to be evaluated at the tip of the fictitious crack of relative length

$$\xi^* = \xi + \frac{r_y}{b} = \xi + \frac{s^2}{2\pi} \tag{8.28}$$

The new fracture load, therefore, becomes

$$\tilde{q}_0 = \frac{1}{g(\xi^*)}\left[s - \frac{M^*}{\sigma_y b^2 t} Y_M(\xi^*) - \frac{F^*}{\sigma_y bt} Y_F(\xi^*)\right] \tag{8.29}$$

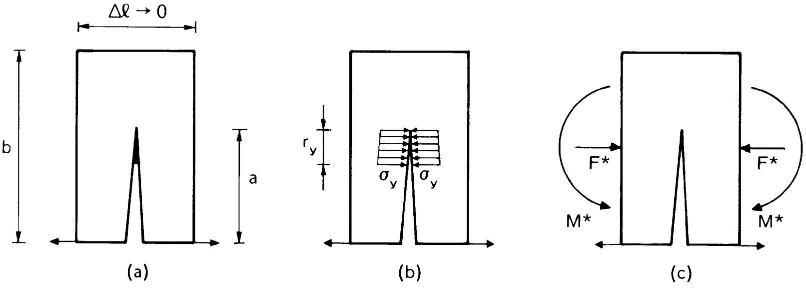

(a) (b) (c)

Fig. 8.9. Process zone (a). Plastic pressure (b). Equivalent force and moment (c).

where the functions Y_M and Y_F are given by equations (6.22) and (6.24). If equations (8.27) are put into equation (8.29), there results

$$\tilde{q}_0 = \frac{1}{g(\xi^*)}\left[s + \frac{s^2}{2\pi}\left(\frac{1}{2} - \xi - \frac{s^2}{4\pi}\right) Y_M(\xi^*) + \frac{s^2}{2\pi}\, Y_F(\xi^*)\right] \tag{8.30}$$

Figures (8.10) to (8.12) plot the fracture loads $\tilde{q}_0$ for the three point bend test, the four point bend test and compact tension test as a function of the real crack depth ξ while the brittleness number, s, is varied. As before, both plastic collapse and brittle fracture can occur depending on the value of s.

Galileo's early concept. As mentioned earlier, the concept of size effect is not new. In his fundamental volume 'Discorsi e dimostrazioni matematiche intorno a due nuove scienze attenenti alla mecanica e i movimenti locali' (1638), Galileo discussed size effect in relation to material strength of solids

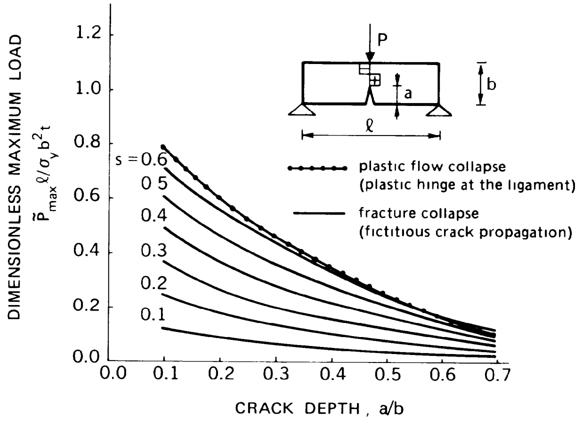

Fig. 8.10. Interaction between fracture and plastic collapse. Three point bending test.

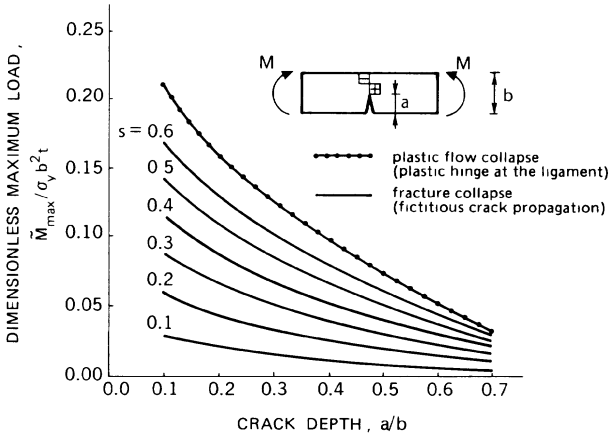

Fig. 8.11. Interaction between fracture and plastic collapse. Four point bending test.

subjected to their own weight, Figure 8.13(a). He observed that small models of machines are proportionally much stronger than full-scale machines. If only the shape were responsible for the strength, then any object could be reproduced at any scale level without sacrificing its strength. Quoting from his work: 'a horse will break its bone when falling from a height of three arms while a cat will not be injured falling from a height of eight or ten, neither a cricket from a tower, nor an ant falling from the moon . . . '. Galileo continues to argue that: 'Nature could not make trees of enormous magnitude because the branches would then break under their own weight . . . nor giant

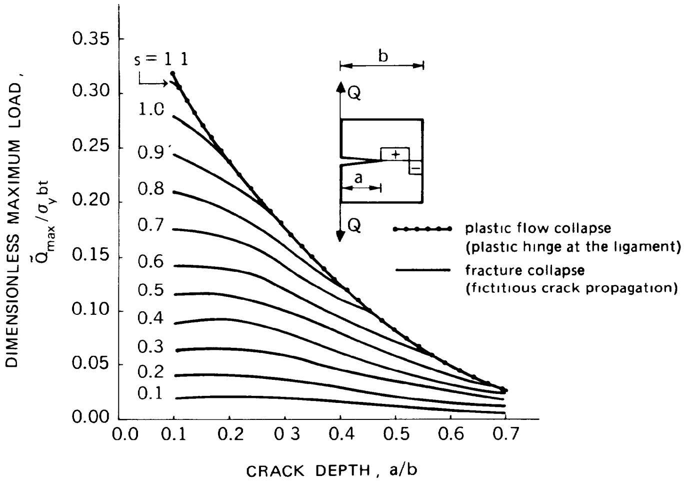

Fig. 8.12. Interaction between fracture and plastic collapse. Compact test.

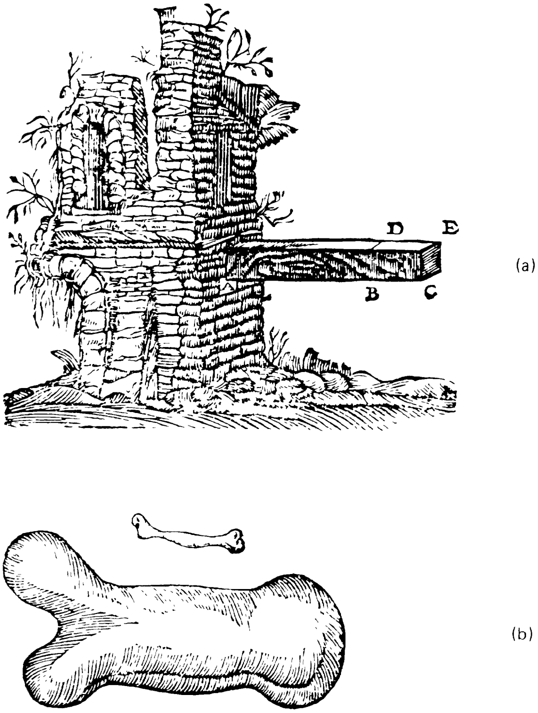

Fig. 8.13. Original drawings by Galileo: material strength of solids subjected to their own weight (a); size effect in relation to the animal bones (b).

men and animals, unless much harder and stronger materials or much less slender bones were used . . . '. Illustration for the less slender bone is given in Figure 8.13(b).

Galileo, of course, was not aware of Fracture Mechanics nor did he refer to the scale effects discussed in this book. He did consider the failure of solid bodies under their own weight by applying the stress criterion. If b is a characteristic length of the body and is allowed to vary as the shape is kept constant, then $P \sim b^3$, $A \sim b^2$ and $\sigma \sim P/A \sim b$. Since the weight P increases with the volume, the stress due to body weight increases proportionally with b and hence strength can be scaled in an inversely proportional manner with regard to b. His concept could be extended to failure based on stress-intensity factor criterion with $K_I \sim P/b^{3/2}$ leading to $K_I \sim b^{3/2}$. Hence, strength is inversely proportional to b with the exponent 1.5 which decreases more rapidly with size than strength as implied by Galileo.

8.2. Experimental investigation

Early work. The stress-intensity factor was first proposed by Griffith and later on advanced by Irwin [16]. Although the size effect was not resolved directly, it did call attention to the importance of treating defects that are inherent in the material and contribute to the change in failure modes as specimen sizes are altered. Of particular significance is the K_{IC}/σ_u ratio that serves as a measure of the sensitivity of materials to failure by crack propagation. The fact that K_{IC} applies only to specimens that are sufficiently thick has made investigators aware of the thickness effect in fracture mechanics.

It was as early as 1933 that Peterson [10] had commented that 'it seems that where stress concentration is not present the results are in most cases independent of size. However, with stress concentration present, the results of dynamic tests are quite different. Smaller specimens tend in general to give higher values of strength. The effect of time as reflected in the speed of testing is perhaps important where stress concentration is present'. In connection with Peterson's paper, Nadai [17] concludes that 'the conditions of similarity in fatigue tests probably depend on further mechanical or other factors not yet found or established, and it will be an interesting task, in the future, to search for these unknown variables or effects which seem to influence fatigue failures'. In retrospect, Nadai has already perceived that a more fundamental quantity would eventually be found to explain these seemingly different phenomena of failure behavior from a unique theory. The strain energy density theory* [18] discovered in 1973 by Sih has indeed opened the door to such a possibility. It has the capability to predict the failure of structural members with or without initial flaws under monotonic, fatigue and creep loading from uniaxial data alone.

More recently, Glucklich and Cohen [20] treated the problem of size effects and explained that 'specimen size (or, its energy-storage capacity) influences its brittle-ductile transition and strength. This effect is not the recognized statistical one, but derives from the strain energy in the system and concerns the stability of slow-growing cracks after nucleation. The thesis put forward is, therefore, that for a given temperature, strain rate and state of stress, ductility decreases with increasing size'. Although the work lacked quantitative assessment of actual problems, it does conceptually confirm the very basic idea of the strain energy density theory [18]. In relation to concrete materials, Kaplan [21] performed three and four point bending tests and determined the critical value of strain energy

* A corollary of this theory has recently been proposed by Sih [19] that can address the damage of every element for each load increment in the structure without having a prior knowledge of the constitutive relations in general other than the uniaxial data. This approach is particularly useful for analyzing the failure behavior of concrete and rock that cannot be explained by the theory of plasticity.

release rate, G_{IC} for different specimen sizes. The values of G_{IC} were found to vary widely with specimen size. He attributed the variation to nonlinear plastic effects and slow crack growth prior to the unstable crack propagation that are not included in the energy release concept of G_{IC}. The Linear Elastic Fracture Mechanics approach was already in suspect.

Similar works were also carried out by Romualdi and Batson [22] and by Glucklich [23] for reinforced concrete. They examined the crack arrest at the interface between concrete and steel and formed a series of tension tests with cracks of different length. The observed G_{IC} values increased with crack length. The conclusion was that G_{IC} is an increasing function of the crack length, instead of a material constant. Glucklich [23] considered dissipative effects at the crack tip in concrete as a result of microcracking rather than plastic flow. The heterogeneity of concrete was analyzed.

In 1969, Naus and Lott [24] determined the fracture toughness K_{IC} of Portland concrete by varying the water/cement ratio, air content, fine aggregate content, curing time, and maximum size of coarse aggregate. A consistent variation of K_{IC} was observed. Welch and Haisman [25] also explained that the K_{IC} and G_{IC} variations were caused by slow crack growth. Unlike the others, they claimed K_{IC} and G_{IC} to be 'material constants', and their being independent of the ultimate strength σ_u. Three point bending tests on cement pastes, mortars and concretes of different composition were also performed by Moavenzade and Kuguel [26]. The specimens (1 × 1 × 10 inches) might have been too small to provide reliable results. They found fracture toughness values decidedly higher for concretes than for mortars and pastes and offered the following explanation with regard to the presence of the aggregate: (1) it increases the microcracking and then scatters the available energy in a number of small streams (microcracks) rather than conveying it in a single large flow (macrocrack) and (2) it directly arrests the macrocrack run by a higher G_{IC}. These discrepancies have been accounted for by Sih [13, 14] applying the strain energy density theory. Additional works on mortar and concrete prisms in compression with an inclined crack were also done by Desayi [27].

Recent work. Shah and McGarry [28] studied the notch sensitivity problem in mortar and concrete and concluded that they are notch insensitive when the crack length is lower than a few centimeters. Brown [29] performed a series of bending tests and double cantilever beam tests using cement paste and mortar. The K_{IC} values when plotted against the nondimensional crack length a/b showed a great deal of scatter, Figure 8.14. Here, b is the beam height. Brown [30] also studied the resistance to crack propagation in glass-fiber-reinforced cement paste. A 'pseudo-toughness' was defined for this material and found to increase linearly with crack growth at a rate proportional to the fiber content. Such an increase was rapid and almost linear between 4 and 10 mm crack growth. Above 10 mm, the rate of increase

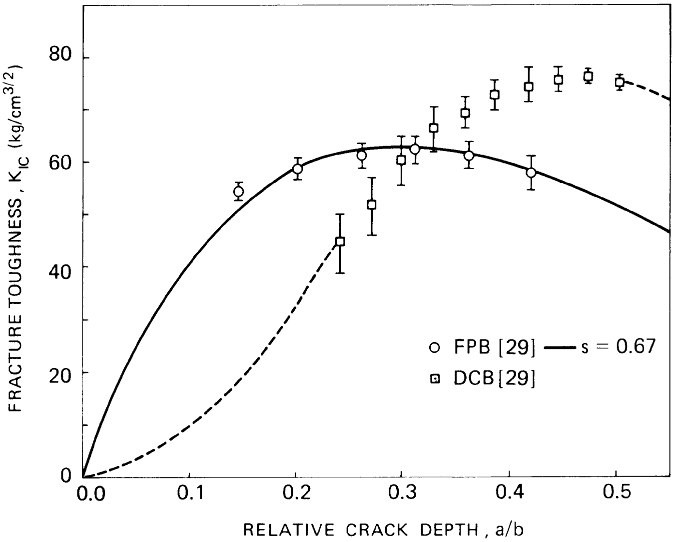

Fig. 8.14. Bell-shaped curves of fracture toughness versus relative crack depth according to the experimental data by Brown [29].

seemed to slacken with some results showing ill-defined plateaus. Brown and Pomeroy [31] concluded that the addition of aggregate not only tends to increase toughness, but also leads to a progressive increase in toughness as the crack grows. The increase in toughness is proportional to the aggregate content. A review of the foregoing works on concrete fracture testing has been made by Naus, Batson and Lott [32].

Further studies concerning notch sensitivity and specimen sizes were made in [33–35]. Walsh [33] assumed that the zone of stress disturbance is surrounded by an area in which the stresses are elastic in nature if the specimen is large enough. He attributed the K_{IC} variability to specimens being too small [33] rather than to 'slow crack growth'. Higgins and Bailey [34] performed fracture tests for a cement paste and obtained increasing K_{IC} values, as the specimen size increased. They deduced that Linear Elastic Fracture Mechanics is not applicable to hardened cement paste samples of the size used in their investigation, because the zone of stress perturbation around the crack tip is not small compared with the specimen and crack sizes. Schmidt [35] measured the fracture toughness, K_{IC}, of a calcareous rock (Indiana limestone) by three point bending tests and obtained K_{IC} values which increased with the crack length and the specimen width, up to a maximum value. The upper limit was considered to be the true value of K_{IC} in plane strain. Evans, Clifton and Anderson [36] studied on the plain and polymer impregnated mortars and showed that the fracture mechanics parameters are independent of the crack length for cracks larger than about 2 cm. Acoustic emission measurements indicated that the susceptibility to microcracking is substantially retarded by polymer impregnation.

Tests on mortar and concrete were carried out by Mindess and Nadeau [37] to find whether fracture toughness depended on the specimen thickness. No dependence was found due to the fact that concrete is a truly brittle material and the size of the plastic zone is negligible. Bear and Barr [38–40] suggested that two fracture tests should be performed with samples taken from concrete beams by a radial drill. In the bending test [39], they obtained K_{IC} values that increased with notch depth, while in the eccentric compression test [40], the K_{IC} values decreased. In the eccentric compression tests on circumferentially notched bars, they also observed that if a shallow notch is used, shear failure can occur prior to crack propagation. Henry and Paquet [41–43] published fracture toughness values of rocks that varied with porosity and temperature. Moreover, the rock anisotropy influenced the fracture behavior such that some planes are more susceptible to crack propagation. In addition to the usual bending tests, they proposed a particular Brazilian test with a pre-cracked disk [43]. Hillemeier and Hilsdorf [44] have reported fracture toughness of single concrete compounds, i.e., cement paste, aggregate and interface paste-aggregate. The eccentric force of the compact test was produced by a wedge, changing compression into traction loading, Figure 8.15, such that crack growth can be easily controlled. For cement paste, they obtained K_{IC} values that decreased with crack depth. Gjϕrv, Sϕrensen and Arnesen [45] observed how notch sensitivity decreased as the crack depth increased. In their opinion, this is due to the particular testing procedure and support conditions; consequently, it may not reflect the true behavior of the material. Cook and Crookham [46] performed four point bending tests on impregnated polymer concrete. For notch depth ratios greater than approximately 0.35, K_{IC} values decreased as crack lengths

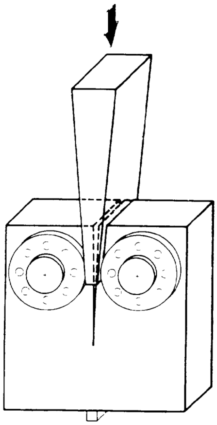

Fig. 8.15. Compact test where the eccentric force is produced by a wedge [44].

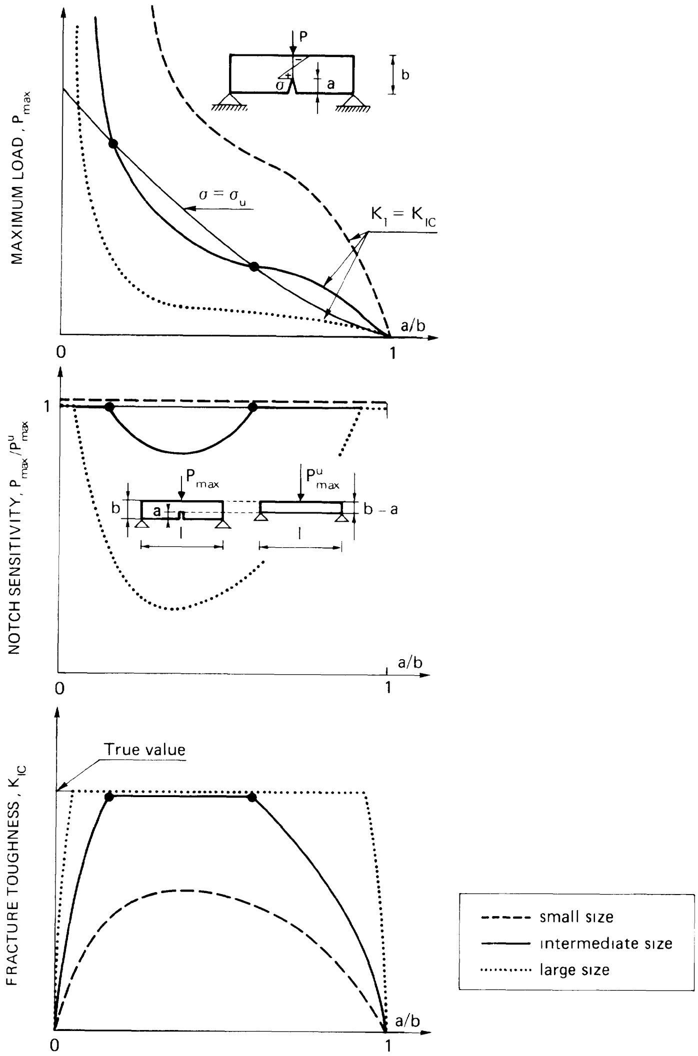

Fig. 8.16. Interaction between crack propagation ($K_I = K_{IC}$) and ultimate strength collapse ($\sigma = \sigma_u$): nondimensional maximum load (a), notch sensitivity (b) and fracture toughness (c).

increased. This phenomenon is caused by cracks that are either too short or too long. As a result, the collapse load takes precedence to fracture, Figure 8.16(a) to (c). Swartz, Hu and Jones [47] considered the method of compliance measurement as a suitable and convenient technique for monitoring crack growth in plain concrete beams subjected to repeated loads. They did not consider the fracture toughness parameter normally used as a pertinent material constant. Strange and Bryant [48] reported the results of their bending and tension tests on concrete, mortar and paste. Again, the fracture toughness K_{IC} did not remain constant but varied with specimen and crack size. The variations were small only when the cracks are sufficiently long. Their conclusion is that concrete can not be regarded as an ideal elastic homogeneous material. A region of non-elastic behavior must exist at the crack tip and linear elastic stress analysis is not valid. Sok and Baron [49] observed that the energy necessary for fracture increases as the crack propagates. A resistance-curve was introduced and regarded as a fracture material property. Swamy [50] presented a review of the experimental results regarding fracture toughness measurements in concrete materials. Values of G_{IC} and K_{IC} obtained by various investigators were tabulated. Additional criticisms of the Linear Elastic Fracture Mechanics theory was made by Ziegeldorf, Müller and Hilsdorf [51] with regard to notch sensitivity. They explained the increase in net failure stress of notched specimens as the notch depth increases, after passing through a minimum, Figure 8.16(b). A theoretical and experimental analysis of crack formation in concrete were presented later in [52]. The investigations indicate that cracks due to internal desiccation exist in concrete and form in the aggregates having a diameter larger than a critical size.

All of the aforementioned experimental findings confirmed that K_{IC} or G_{IC} cannot be regarded as constants for concrete-like materials. The material nonlinearity ahead of the crack and the process of slow crack growth must be treated in the theoretical model by a suitable failure criterion.

Further work. Additional studies were made by Carpinteri [1] on the notch sensitivity in fracture testing. The dimensional analysis was used with attention focused on the quantities $[\sigma] = [L]^{-2}[F]$ and $[K_I] = [L]^{-3/2}[F]$. A nondimensional brittleness number s, was introduced to define notch sensitivity. Inconsistencies in the experimental data such as

(1) increase and decrease in fracture toughness, K_{IC}, with crack length;
(2) increase in K_{IC} with specimen size and
(3) variation of K_{IC} with test geometry, were explained.

The experiments of Carpinteri [3, 53] involved in determining the fracture toughness parameters, K_{IC} and G_{IC}, for a Carrara marble, a mortar and two concretes with different maximum aggregate size. The three point bending test was used. The variations of K_{IC} in Figure 8.17 are caused by systematic errors rather than by true statistical fluctuations. There is, in fact, a trend in the results in terms of the relative crack depth for marble and concrete. The K_{IC} values increased for small crack depth a/b and decreased for large depth. Saouma, Ingraffea and Catalano [54] reexamined the results by Kesler, Naus and Lott [55] by considering the finite sizes of the specimens

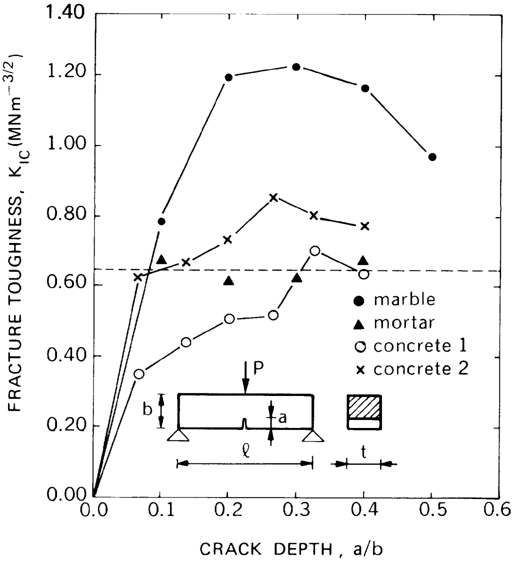

Fig. 8.17. Bell-shaped curves of fracture toughness versus relative crack depth according to the experimental results by Carpinteri [3, 53].

and showed that a single-parameter K_{IC} approach to crack propagation in concrete structures can be used within engineering accuracy.

The February 1980, issue No. 1, of the International Journal 'Cement Composites', edited by Dr. R.N. Swamy, was devoted to the fracture mechanics of fibre-reinforced concrete. Mai, Foote and Cotterell [56] presented an investigation on the size effects of asbestos-cellulose cement composite using three point notched bend beams with geometrically scaled dimensions from 1 to 8 except for thickness which was constant. It was found that the unit size beams of 25 mm depth were notch insensitive and failure occurred when the net section stress was equal to the modulus of rupture. For the large specimens, K_{IC} were much larger than those obtained for the smaller specimens. Theoretically speaking, the scaling of cracks in geometrically similar nonlinear elastic structures [57, 58] was also considered. Visalvanich and Naaman [59] presented fracture test data related to asbestos cement DCB specimens, Figure 8.18(a). They observed that the apparent critical stress-intensity factor increased rapidly and reached a plateau after a short crack extension. It decreased, however, as the crack reached about 14 inches. The $K_{IC}(a)$ data are shown in Figure 8.18(b). Petersson [60] determined the values of the critical strain energy release rate, G_{IC} for the three point bending and tensile specimens, Figure 8.19(a). The results appear highly affected by geometry and size, Figure 8.19(b). A fracture energy

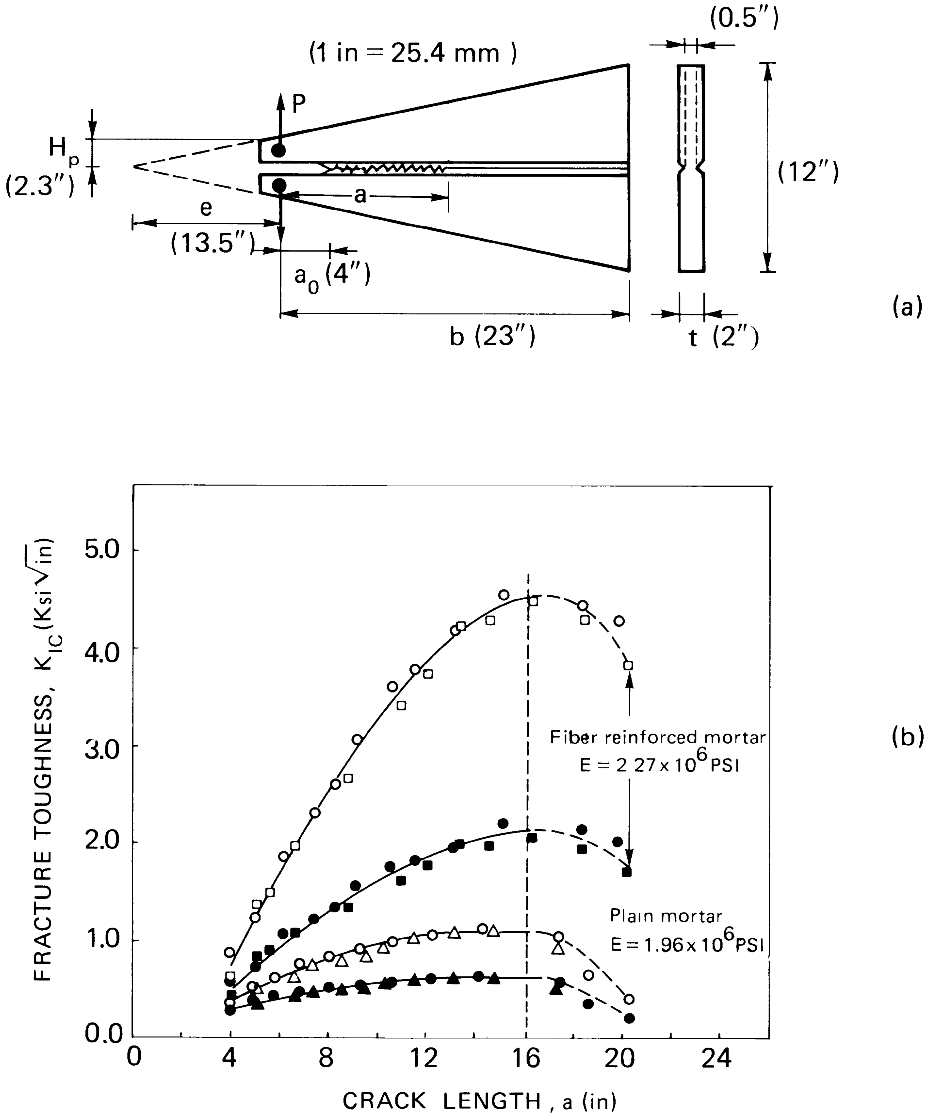

Fig. 8.18. Bell-shaped curves of fracture toughness versus relative crack depth according to the experimental results by Visalvanich and Naaman [59].

$$G_F = \frac{\int_0^{\delta_c} P d\delta}{(b - a_0)t} \tag{8.31}$$

was found to agree more favourably with the results, Figure 8.19(c). Arrea and Ingraffea [61] made a combined experimental and numerical investigation

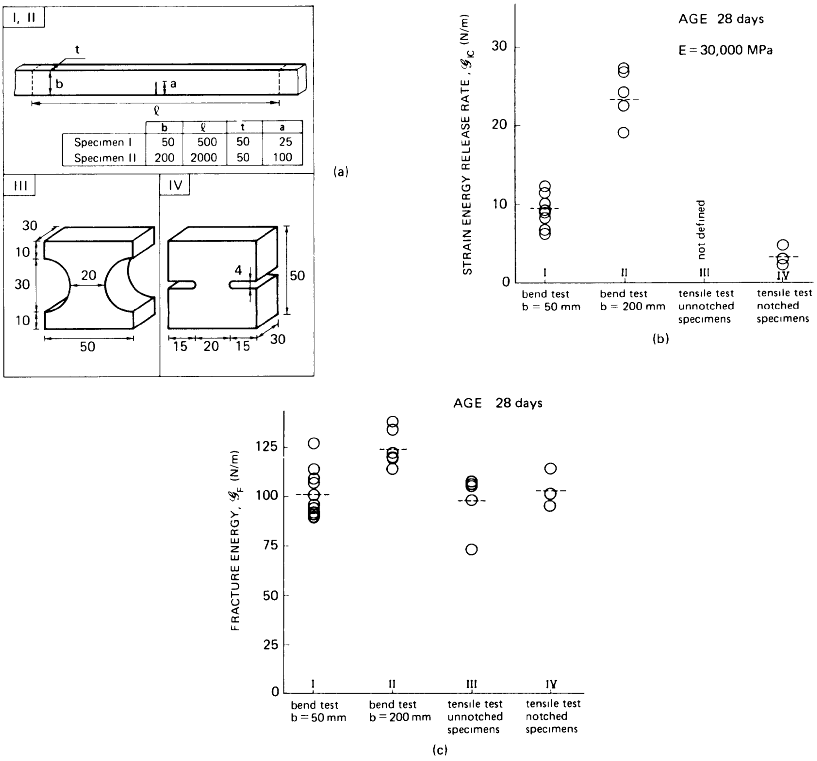

Fig. 8.19. Empirical fracture toughness parameters for the three point bending and tensile specimens in (a): strain energy release rate (b) and fracture energy (c) [60].

on mixed-mode crack propagation in mortar and concrete. The experimental program consisted of tests on three series of beams under a four-point loading system that created a high K_{II}/K_I ratio at the tip of a saw notch, Figure 8.20(a). As the crack propagated from the notch, this ratio decreased since the Mode I stress-intensity factor started to dominate. The crack trajectories were predicted exactly by the application of the Strain Energy Density Theory, Figure 8.20(b). The behavior of the beams was reproduced satisfactorily by the numerical analysis only when aggregate interlocking effects were included.

Hillerborg and Petersson [62] also proposed a method for determining the fracture energy, G_F of mortar and concrete by using the three point bend test of very slender notched beams. A recommendation is still being made by the R.I.L.E.M. 50-FMC Committee [63]. The results obtained at the ‘Istituto Sperimentale Modelli e Strutture’ in Bergamo (Italy) based on three point bend tests of concrete specimens with different width b and maximum particle size, $D_{\max}$ [64] are also worthy of mentioning in terms of

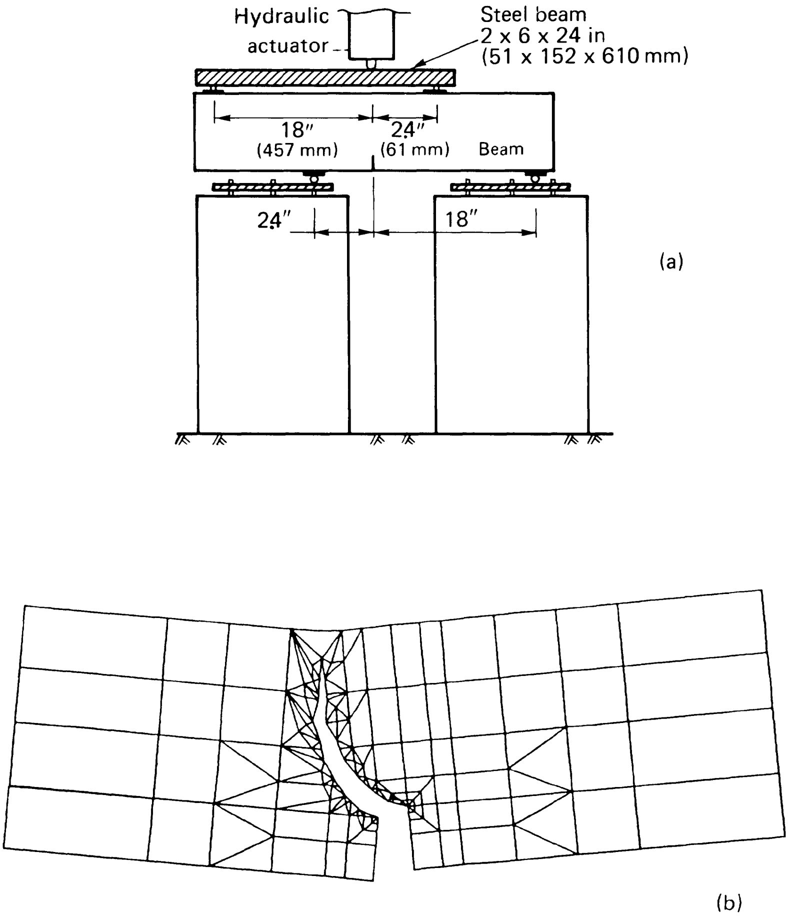

Fig. 8.20. Four-point loading system creating a high K_{II}/K_I ratio (a). Crack trajectory in the finite element mesh (b) [61].

dimensional analysis [65]. Figure 8.21 plots K_{IC} values against the relative crack depth a/b. By assuming that $K_{IC} = 164.7\,\mathrm{kg/cm^{3/2}}$, $D_{\max} = 25\,\mathrm{mm}$ and $\sigma_u = 50.36\,\mathrm{kg/cm^2}$, it is possible to obtain a brittleness number $s = 0.82$ for Specimen 1 and $s = 0.46$ for Specimen 2. Analogously, by assuming $K_{IC} = 158.2\,\mathrm{kg/cm^{3/2}}$, $D_{\max} = 120\,\mathrm{mm}$ and $\sigma_u = 46.68\,\mathrm{kg/cm^2}$, $s = 0.48$ is found for Specimen 3. The s number related to Specimen 1 is too high and therefore the reported K_{IC} values are meaningless, since ultimate strength collapse would have first occurred. K_{IC} does not appear to be a material constant but it reaches a maximum when the crack depth a/b, is equal to about 0.20. Decreasing the brittleness number of Specimens 2 and 3, the curves tend to become flat. Therefore, K_{IC} may be regarded as constant for increasingly larger intervals of the ratio a/b. The experimental values

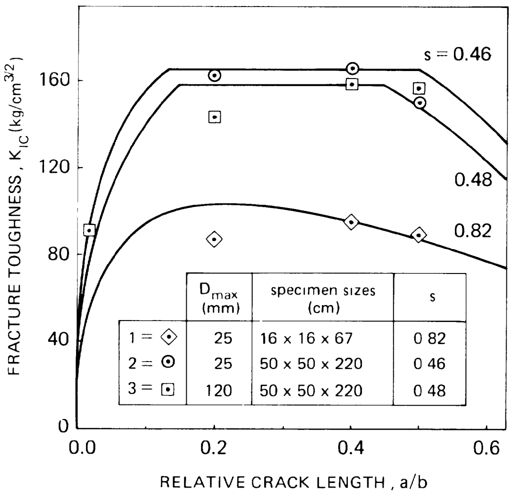

Fig. 8.21. Bell-shaped curves of fracture toughness versus relative crack depth according to the experimental data by Ferrara and Imperato [64].

pertaining to cracks of intermediate length are related to a crack propagation failure. A second report to R.I.L.E.M. 50-FMC Committee [66] contains additional results from six laboratories. The tests reported from the 'Istituto di Scienza delle Costruzioni' of the University of Bologna are very extensive, since they consist of seven different beam sizes, each with six different notch

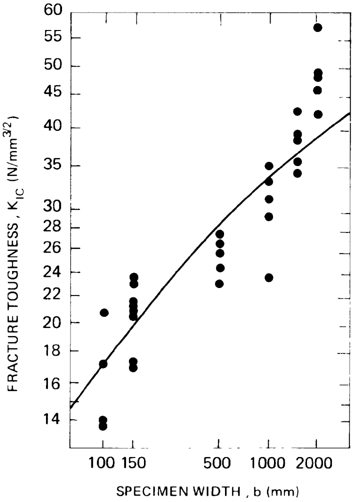

Fig. 8.22. K_{IC} values versus beam depth plot obtained at the 'Instituto di Scienza delle Costruzioni' of the University of Bologna (Di Leo).

depths, and three tests for each type of specimen making a total of 126 beams. The largest beam had a span of 2.5 m and a depth of 2 m. Only the smallest beams gave stable tests with a notch depth of 0.2 times the beam depth or more. The K_{IC} values are shown in Figure 8.22 as functions of the beam depth. They increase for increasing beam depths. Mindess [67] has recently prepared an extensive bibliography with nearly 500 references on the fracture of concrete and a host of experimental data [68].

It should now be clear that a valid K_{IC} value for concrete can be obtained only if the specimen size is prohibitively large. Smaller specimens, however, can be used for other materials such as mortar and cement paste. Concrete specimens are measurable in meters while cement paste specimens in centimeters. Brittle fracture therefore depends on scaling that is also a function of the heterogeneity of the material. Table 8.1 shows that strength σ_u and toughness K_{IC} may be regarded as independent properties. Their combination determines the brittleness of the material.

8.3. Statistical strength variation

Preliminary remarks. Strength is known to vary with specimen size, a phenomenon pointed out long ago by Weibull [69]. He used the weakest link concept for determining a critical imperfection in a given material, the size of which increases by increasing the volume. This is a simple model that does not account for details of the imperfections nor the constitutive relation of the material. Jayatilaka [70] and Freudenthal [71] considered a linear elastic material with a great number of embedded Griffith cracks and indicated that the variability of strength with specimen volume may be related to the probability density of crack size distribution. The strength size effect in structures with re-entrant corners was considered by Leicester [72] who included the effect of stress-singularity at the corner vertex. He showed that the strength size effect is due to the existence of one or more stress singularity sources in the body. These sources can arise from macroscopic notches or partially debonded interfaces. Bazant [73] also explained size effects in the brittle failure of concrete structures by application of Linear Elastic Fracture Mechanics and contrasted his results with those of Weibull.

TABLE 8.1.
Strength, toughness and brittleness of various materials.

	Strength (MN/m^2)	Toughness (MN/m$^{3/2}$)	Brittleness (m$^{-1/2}$)
Concrete	$\sigma_u = 3.57$	$K_{IC} = 1.96$	$\sigma_u/K_{IC} = 1.8$
Aluminium alloy	$\sigma_u = 500$	$K_{IC} = 100$	$\sigma_u/K_{IC} = 5$
Plexiglass	$\sigma_u = 33$	$K_{IC} = 5.5$	$\sigma_u/K_{IC} = 6$
Glass	$\sigma_u = 170$	$K_{IC} = 0.25$	$\sigma_u/K_{IC} = 680$

The purpose of this section is to extend the work in [72] to an ideal material with a random distribution of microscopical cracks, voids or inclusions. These heterogeneities will be assumed to be of regular polygonal shape. Other irregular shapes may also be considered. The Ramberg–Osgood stress-strain relation with power hardening is employed. Interactions between the geometrical shape of the polygonal voids, the nonlinearity of the matrix and the nature of the probability density of heterogeneity size distribution are considered. The Weibull modulus depends on the angle γ formed by the sides of the polygonal void, the exponent n in the Ramberg–Osgood relation, and the degree of the cumulative distribution function related to the defect size, N. The results show that the empirical Weibull assumption has a precise physical meaning in terms of physical defects in the material.

Structures with a dominant defect. Consider a two-dimensional linear elastic structure with an edge crack, Figure 8.23(a). Based on the results in [16], the symmetrical stress field around the crack tip can be described by

$$\sigma_{ij} = K r^{-1/2} F_{ij}(\theta) \tag{8.32}$$

where K is the stress-intensity factor and r, θ are the radial and angular coordinates, respectively. In general, the K-factor can be expressed as [74]:

$$K = \sigma b^{1/2} f_1(a/b) \tag{8.33}$$

where σ is the nominal stress, b is a characteristic size of the structure, f_1 is a shape-factor depending on the geometry of structure and on the crack size a. The stress at failure σ_f is reached when the K-factor is equal to its critical value, K_c:

$$\sigma_f = K_c b^{-1/2} \frac{1}{f_1(a/b)} \tag{8.34}$$

Taking the logarithms of both sides of equation (8.34) gives

$$\ln \sigma_f = [\ln K_c - \ln f_1(a/b)] - \tfrac{1}{2} \ln b \tag{8.35}$$

which takes the general form

$$\ln \sigma_f = A\left(K_c, \frac{a}{b}\right) - \tfrac{1}{2} \ln b \tag{8.36}$$

with A being a function that depends on the structure geometry, material and crack depth. Consider a set of geometrically similar structures, Figure 8.23(a). The strength $\ln \sigma_f$ is a linearly decreasing function with a slope of $-1/2$,

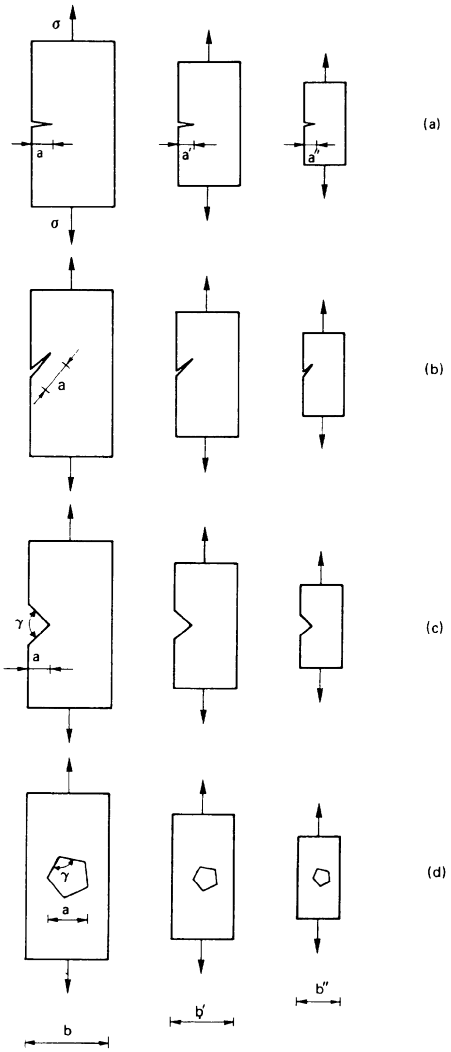

Fig. 8.23. Geometrically similar bodies with a dominant defect: opening crack (a), mixed mode crack (b), re-entrant corner (c) and polygonal cavity (d).

Figure 8.24(a). This means that if $b \rightarrow \infty$, then $\ln b$ tends to $+\infty$ and $\ln \sigma_f$ tends to $-\infty$ since $\sigma_f \rightarrow 0^+$. If $b \rightarrow 0^+$ with $\ln b$ tending to $-\infty$, then $\ln \sigma_f$ tends to $+\infty$ as $\sigma_f \rightarrow +\infty$. The horizontal line

$$\ln \sigma_f = \ln \sigma_u \tag{8.37}$$

represents the strength limit for $b \rightarrow 0^+$ in Figure 8.24(a). As already

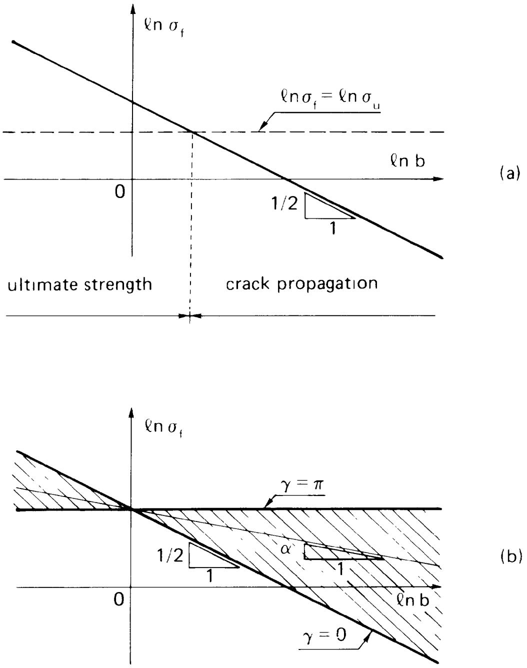

Fig. 8.24. Bi-logarithmic strength versus size diagram: interaction between ultimate strength collapse and crack propagation (a); attenuation of the strength decrease when the re-entrant corner angle increases (b).

mentioned, small size structure tends to fail by collapse rather than crack propagation.

Under a mixed mode loading, Figure 8.23(b), the crack tip stress field takes the form

$$\sigma_{ij} = \sum_{k=1}^{2} K_k r^{-1/2} F_{ij}^{k}(\theta) \tag{8.38}$$

where K_k ($k = 1, 2$) are the stress-intensity factors related to Mode I (opening) and Mode II (sliding) crack extension, respectively. As for the case of equation (8.33), they can be written as

$$K_k = \sigma b^{1/2} f_k(a/b); \qquad k = 1, 2 \tag{8.39}$$

A combination of K_k ($k = 1, 2$) is required to describe incipient fracture [75]:

$$H(K_I, K_{II}) = H_{cr} \tag{8.40}$$

An elliptic function H may be used [76]:

$$K_1^2 + qK_2^2 = K_c^2 \tag{8.41}$$

where q ($q \geqslant 0$) is a measure of the influence of Mode II crack extension. Inserting equation (8.39) in equation (8.41), it follows that

$$\sigma^2 b[f_1^2 + qf_2^2] = K_c^2 \tag{8.42}$$

A failure stress can thus be defined by equation (8.34) with

$$f = \sqrt{f_1^2 + qf_2^2} \tag{8.43}$$

Note that a straight line relation with a slope of $-1/2$ in the plane $\ln \sigma_f - \ln b$ still holds in mixed mode, Figure 8.24(a). The geometry of the crack, structure and load do not seem to come into play.

Consider now a two-dimensional linear elastic structure with a reentrant corner of angle γ, Figure 8.23(c). Williams [77] showed that when both notch surfaces are stress free, the symmetrical stress field at the notch tip is

$$\sigma_{ij} = K^* r^{-\alpha} F_{ij}^{(\gamma)}(\theta) \tag{8.44}$$

where the power α of the stress-singularity ranges from $1/2$ ($\gamma = 0$) to 0 ($\gamma = \pi$) as illustrated in Figure 8.25. If dimensional analysis is applied, an equation analogous to equation (8.33) may be found:

$$K^* = \sigma b^{\alpha} g_1(a/b) \tag{8.45}$$

When the angle γ vanishes, equation (8.45) coincides with equation (8.33). When $\gamma = \pi$, the stress-singularity disappears and the stress-intensity coefficient K^* assumes the physical dimensions of a stress and becomes proportional to the nominal stress σ. Leicester [72] showed that the failure stress σ_f corresponds to K^* becoming critical, i.e.,

$$\sigma_f = K_c^* b^{-\alpha} \frac{1}{g_1(a/b)} \tag{8.46}$$

In the logarithmic form, equation (8.46) is

$$\ln \sigma_f = B\left(K_c^*, \frac{a}{b}\right) - \alpha \ln b \tag{8.47}$$

in which

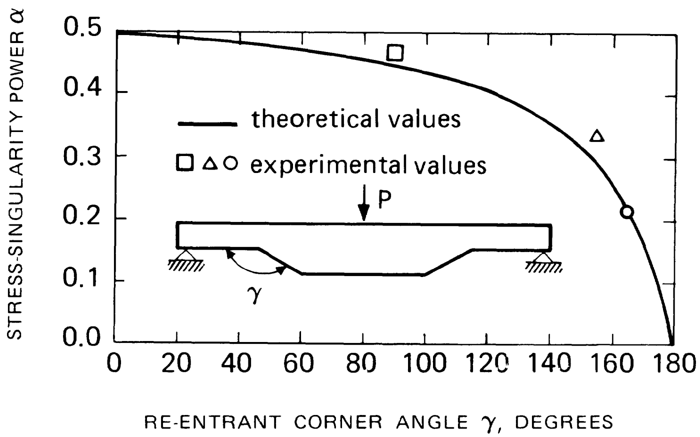

Fig. 8.25. Stress-singularity power versus re-entrant corner angle.

$$B\left(K_c^*, \frac{a}{b}\right) = \ln K_c^* - \ln g_1(a/b) \tag{8.48}$$

For a set of geometrically similar structures, Figure 8.23(c), the strength $\ln \sigma_f$ is a linear decreasing function of $\ln b$ with a slope of $-\alpha$ as shown in Figure 8.24(b). When $\gamma \to \pi$ or $\alpha \to 0$, the scale effect disappears and the straight line becomes horizontal. In this case, the equilibrium condition becomes

$$\sigma b = K^*(b - a) \tag{8.49}$$

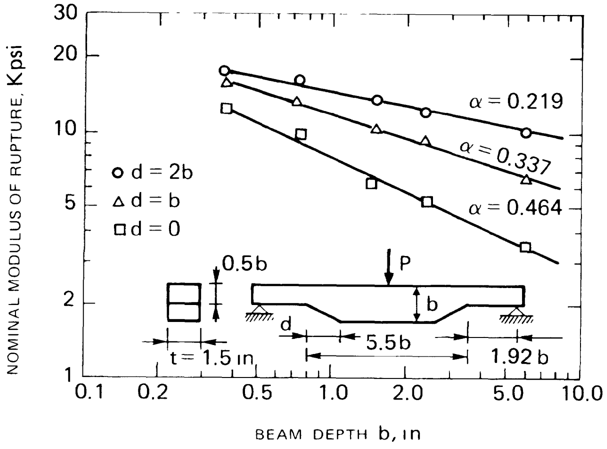

Fig. 8.26. Size effect on bending strength of timber beams with re-entrant corners [72].

and hence equation (8.45) gives

$$g_1(a/b) = \frac{1}{1-\frac{a}{b}} \tag{8.50}$$

When the notch depth a/b tends to zero, the shape-function $g_1(a/b) = 1$. The stress-intensity coefficient K^* coincides with the nominal stress σ as shown in equation (8.45). Experimental confirmations of the above concept are given in Figure 8.26 by Leicester [72] who tested geometrically similar timber beams with reentrant corners. Size effects of the type described above were observed. The rate of decrease in stength coincides with that predicted in Figure 8.25.

Consider a two-dimensional linear elastic structure with a polygonal void of regular shape and arbitrary number of sides M, Figure 8.23(d). The angle γ is a function of the number of sides, M, i.e.,

$$\gamma = \pi\left(\frac{M-2}{M}\right) \tag{8.51}$$

Every reentrant corner of the polygonal void is subjected to a mixed mode loading condition with a stress-singularity $r^{-\alpha}$. For a given external load, there is a corner tip which is subjected to the most severe stress field. If the load is increased progressively, the fracture condition will first be achieved at this tip. According to equation (8.47), the intercept is

$$B\left(K_c^*, \frac{a}{b}\right) = \ln K_c^* - \ln\sqrt{g_1^2 + q g_2^2} \tag{8.52}$$

The ln σ_f versus ln b diagram is linear with a slope $-\alpha$ for the case of polygonal cavity. $M = 2$ corresponds to a crack with $\gamma = 0$. For $M = \infty$, the polygonal cavity becomes a circular hole as equation (8.51) gives $\gamma = \pi$. In the latter case, the size effect vanishes and the ln σ_f versus ln b line becomes horizontal.

Structures with many imperfections. Two-dimensional structures with a multitude of cracks, voids or inclusions of a given size-distribution will be considered. The two assumptions made are

(1) the structure is macroscopically homogeneous and isotropic and

(2) the interaction between the imperfections is negligible.

A set of geometrically similar structures containing many cracks and/or

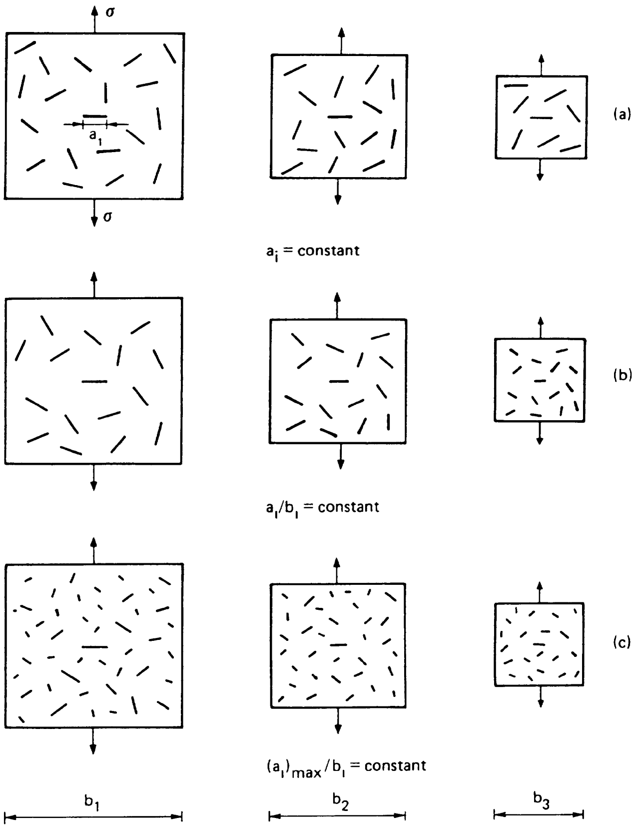

Fig. 8.27. Geometrically similar bodies with many random defects: constant defect size (a); defect size constant and proportional to the body size (b); defect size distribution of proportionality (c).

polygonal cavities of constant size a are considered, Figure 8.27(a). They may be regarded as specimens made of the same material. Their failure will be associated with imperfections oriented at a critical position. Figure 8.27(b) considers a set of geometrically similar structures, where the size of the imperfections is constant and proportional to the structural size. In this case, they cannot be considered as specimens of the same material. The strength size effect is represented by the $\ln \sigma_f$ versus $\ln b$ line with slope $-\alpha$. If the imperfections were of the same size, but with different shape (e.g., cracks and circular pores), the fracture condition must then be evaluated only for those with the maximum value for α $(0 \leqslant \alpha \leqslant 1/2)$. For imperfections with the most dangerous shape $(\alpha = \alpha_{\max})$ in Figure 8.27(c), the probability density $p(a)$ of size distribution is given in Figure 8.28(a). It can thus be said that if the size distribution $p(a)$ is such that the maximum size $a_{\max}$ is

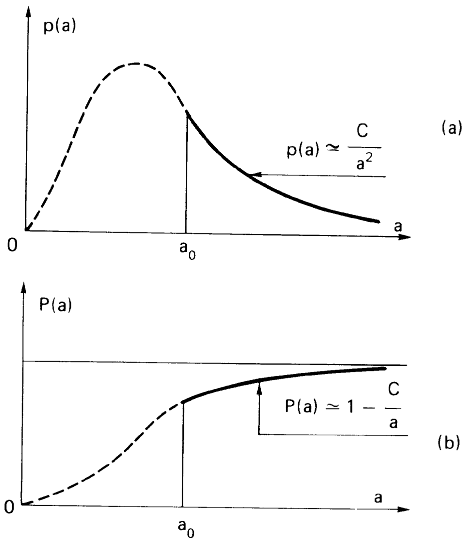

Fig. 8.28. Defect size distribution of proportionality: probability density (a) and cumulative distribution (b).

proportional to the linear scale b, then the strength size effect is represented by the $\ln \sigma_f$ versus $\ln b$ line diagram with a slope of $-\alpha_{\max}$. The above statement is somewhat restrictive and is valid only when the probability density of size distribution $p(a)$ possesses particular properties. If ρ is the density of the imperfections (number of imperfections per unit area), then the maximum size $a_{\max}$ can be defined as

$$\rho b^2 p(a_{\max}) \frac{1}{2\pi} \Delta a \Delta \beta = 1 \tag{8.53a}$$

The factor $(1/2\pi)$ pertains to all imperfections orientated at the angle β which are alike. If a geometrically similar structure of characteristic size kb is considered, there results

$$\rho (kb)^2 p(ka_{\max}) \frac{1}{2\pi} \Delta a \Delta \beta = 1 \tag{8.53b}$$

Since $a_{\max}$ is a function of ρ, b, Δa and $\Delta \beta$, it follows that equations (8.53) must be valid for any defect size a, i.e.,

$$\rho b^2 p(a) \frac{1}{2\pi} \Delta a \Delta \beta = 1 \tag{8.54a}$$

$$\rho k^2 b^2 p(ka) \frac{1}{2\pi} \Delta\alpha \Delta\beta = 1 \tag{8.54b}$$

From equations (8.54), it follows that

$$p(a) = k^2 p(ka), \quad \forall a \gg \bar{a}, \quad \forall k \in R^+ \tag{8.55}$$

Hence, p assumes the form

$$p(a) = \frac{C}{a^2}, \quad \forall a \gg \bar{a} \tag{8.56}$$

where C is a constant with the physical dimension of a length and $\bar{a}$ is the mean defect size. Equation (8.56) will be referred to as the defect size distribution of proportionality. The related cumulative distribution function P is

$$P(a) = \int_0^a p(x)\mathrm{d}x = \int_0^{a_0} p(x)\mathrm{d}x + \int_{a_0}^a \frac{C}{x^2}\,\mathrm{d}x \tag{8.57}$$

where a_0 ($a_0 \gg \bar{a}$) is the value beyond which the decreasing branch of function p can be approximated by equation (8.56). From equation (8.57), it is found that

$$P(a) = P_0 + \left[-\frac{C}{x}\right]_{a_0}^{a} = P_0 + \frac{C}{a_0} - \frac{C}{a} \tag{8.58}$$

For $a \to \infty$, the cumulative distribution $P(a) \to 1$ and

$$P_0 + \frac{C}{a_0} = 1 \tag{8.59}$$

From equations (8.58) and (8.59) it follows

$$P(a) = 1 - \frac{C}{a}, \qquad \text{for } a > a_0 \tag{8.60}$$

such that

$$C = (1 - P_0)a_0 \tag{8.61}$$

Generally speaking, the cumulative distribution function, P, can have the following form

$$P(a) = 1 - \frac{C}{a^N}, \qquad \text{for } a > a_0 \tag{8.62}$$

and

$$C = (1 - P_0)a_0^N \tag{8.63}$$

In this case, the strength size effect can be represented by the ln σ_f versus ln b line with a slope $-s_0$, i.e.,

$$s_0(\gamma, N) = \frac{\alpha(\gamma)}{N^{w_0}} \tag{8.64}$$

where the exponent w_0 depends on the density of imperfections, size distribution of the less dangerous defects, etc. The probability density of size distribution in the general case can be obtained from equation (8.62) as

$$p(a) = \frac{\mathrm{d}P}{\mathrm{d}a} = N\frac{C}{a^{N+1}}, \qquad \text{for } a > a_0 \tag{8.65}$$

which reduces to equation (8.56) when $N = 1$.

Up to this point, only cracks and cavities have been considered. Similar considerations can also be given to the case of inclusions. The probability density p and the cumulative distribution P may depend on the inclusion size with partial debonding, Figure 8.29. This assumption is realistic for concrete where cracks due to internal dessication and shrinkage occur, particularly for large aggregates [52]. In the case of circular inclusions [78], the strength size effect is represented by the ln σ_f versus ln b line with a slope of $-1/(2N^{w_0})$. The above model applies only to the size effects related to the first microcracking. In order to study the subsequent stages of material degradation, the stochastic process theory should probably be

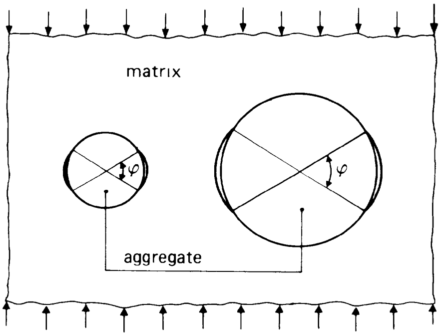

Fig. 8.29. Debonding cracks at the interface between matrix and aggregate.

applied despite Hatano's [79] claim that it does not apply to concrete.

The power hardening Ramberg-Osgood material with the stress-strain relation

$$\left(\frac{\epsilon}{\epsilon_0}\right) = \left(\frac{\sigma}{\sigma_0}\right)^n, \qquad 1 \leqslant n < \infty \tag{8.66}$$

may also be applied to study the state of affairs near a reentrant corner with angle γ. Hutchinson [80], and Rice and Rosengren [81] gave the stress-singularity* at the crack tip for this material as

$$\lambda = \frac{1}{n+1} \tag{8.67}$$

with λ as the exponent of r, i.e., $r^{-\lambda}$. When $n = 1$, the linear elastic behavior $\lambda = 1/2$ is recovered. When $n \to \infty$ and $\lambda \to 0$, a rigid-perfectly plastic material is obtained. The stress-singularity then vanishes and the plastic stress-intensity coefficient attains the physical dimensions of stress [5]. This limit case is analogous to a reentrant angle with $\gamma \to \pi$ in linear elasticity. For $\gamma > 0$ and $n > 1$, the symmetrical stress-field at the corner tip may be described as

$$\sigma_{ij} = K^* r^{-s_0} F_{ij}^{(\gamma, n)}(\theta) \tag{8.68}$$

in which the power s_0 is given by

$$s_0(\gamma, n) = 2\alpha(\gamma)\frac{1}{n+1} \tag{8.69}$$

The function $s_0(\gamma, n)$ is given in Figure 8.30.

Extending the single crack analysis given above to the case of many defects of a given size distribution in nonlinear materials, the strength size effect can be represented by the $\ln \sigma_f$ versus $\ln b$ line with a slope of $-s_0$. From equations (8.64) and (8.69), it is found that

$$s_0(\gamma, n, N) = \frac{2\alpha(\gamma)}{(n+1)N^{w_0}} \tag{8.70}$$

Equation (8.70) shows that size effect vanishes when $\gamma = \pi$ (circular pores), and/or when $n \to \infty$ (rigid-perfectly plastic material), and/or when $N \to \infty$

This result was based on the assumption that macro-plasticity occurs uniformly around the crack tip which is not always consistent with experimental observation. Hence, care must be exercised in not over-extending the application of the work in [80, 81].

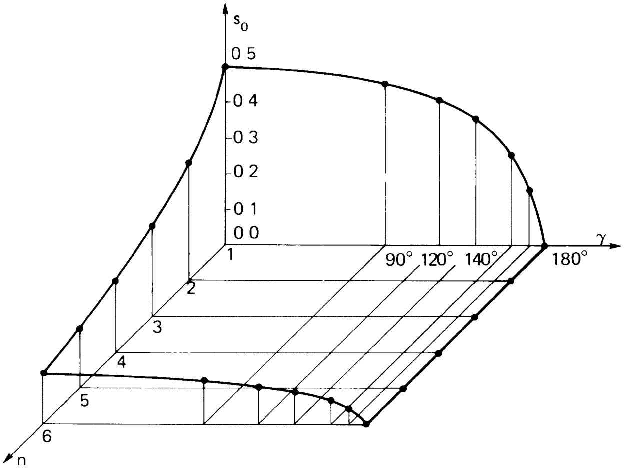

Fig. 8.30. Stress-singularity power as a function of re-entrant corner angle γ and material hardening exponent n.

(nearly constant defect size). On the other hand, the size effect becomes enormous when $N \to 0$ (very large dispersion in the imperfection size distribution). Owing to the form of equation (8.70), size effect can be annuled by proper combination of the angle γ, the hardening exponent, n, and the degree of defect size dispersion, N.

The two-dimensional treatment can be extended to three-dimensional structures with polyhedral cavities. Equation (8.70) can be generalized as

$$s_0(\Omega, n, N) = \frac{2\alpha(\Omega)}{(n+1)(N-1)^{w_0}} \tag{8.71}$$

in which $(N-1)$ instead of N has been written because equations (8.54) in three-dimensions yield

$$p(a) = k^3 p(ka), \quad \forall a \gg \bar{a}, \quad \forall k \in R^+ \tag{8.72}$$

and hence

$$p(a) = \frac{C}{a^3} \tag{8.73a}$$

$$P(a) = 1 - \frac{C}{2a^2} \tag{8.73b}$$

prevail for sufficiently large a. Here, Ω represents a reentrant solid angle and not its amplitude. A knowledge of the singular stress fields near a three-dimensional reentrant corner is, of course, required.

Weibull parameters. Many past investigations have applied equations (2.44) and (2.45) to study the implications of the Weibull theory in order to establish the relation between the Weibull modulus m and the shape of the defects, ductility of the material and dispersion of the defect size. Jayatilaka [70] and Freudenthal [71] used the model of cracks embedded in a linear elastic material to determine the Weibull modulus, m. Jayatilaka [70] found m to be a function of the degree N of the defect size cumulative distribution:

$$m = 2N \tag{8.74}$$

Freudenthal [71] found m to be a function of the coefficient of variation C_v of the defect size probability density:

$$m = \frac{2}{C_v} \tag{8.75}$$

By casting equation (2.43) into a logarithmic form

$$\ln \bar{\sigma}_f = \ln \left[\sigma_0 \Gamma \left(1 + \frac{1}{m} \right) f(m) \right] - \frac{1}{m} \ln V \tag{8.76}$$

and invoking the assumption of geometric similarity in two-dimensions, i.e., bodies with similar shape and constant thickness as shown in Figure 8.31, the result

$$\ln \bar{\sigma}_f = \ln \left[\sigma_0 \Gamma \left(1 + \frac{1}{m} \right) f(m) \right] - \frac{1}{m} \ln (kb^2 t) \tag{8.77}$$

is obtained such that

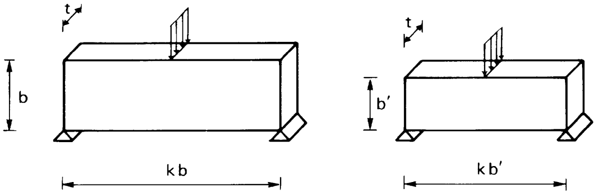

Fig. 8.31. Bodies with similar shape and constant thickness.

$$\ln \bar{\sigma}_f = D(\sigma_0, m) - \frac{2}{m} \ln b \tag{8.78}$$

in which

$$D(\sigma_0, m) = \ln \frac{\sigma_0 \Gamma\left(1 + \frac{1}{m}\right) f(m)}{(kt)^{1/m}} \tag{8.79}$$

Equations (8.78) and (8.79) can be compared with equations (8.80) and (8.81) for $N = 1$:

$$\ln \bar{\sigma}_f = B\left(K_c^*, \frac{a_{\max}}{b}\right) - s_0 \ln b \tag{8.80}$$

$$B\left(K_c^*, \frac{a_{\max}}{b}\right) = \ln \frac{K_c^*}{\sqrt{g_1^2 + q g_2^2}} \tag{8.81}$$

It follows that

$$m = 2/s_0 \tag{8.82}$$

$$\sigma_0 = \frac{K_c^* (kt)^{s_0/2}}{\Gamma\left(1 + \frac{s_0}{2}\right) f\left(\frac{2}{s_0}\right) \sqrt{g_1^2\left(\frac{a_{\max}}{b}\right) + q g_2^2\left(\frac{a_{\max}}{b}\right)}} \tag{8.83}$$

Equations (8.82) and (8.83) offer an interpretation of the Weibull parameters m and σ_0. Making use of equation (8.70), equation (8.82) gives

$$m = \frac{(n+1) N^{w_0}}{\alpha(\gamma)} \tag{8.84}$$

When $N = 1$, a minimum value of $m = 4$ is obtained. For glass, $m \simeq 2$ which means that $N < 1$. The crack size distribution therefore presents a large dispersion.

Experimental results. According to equation (8.70), the ln σ_f versus ln b line relationship should fit the experimental data with a negative slope of $-s_0$. When the dispersion of the imperfection size distribution is not very high, say $N \geqslant 1$, the theoretical upper bound $s_0 \leqslant 0.50$ is obtained which has rarely been exceeded by the available experimental data.

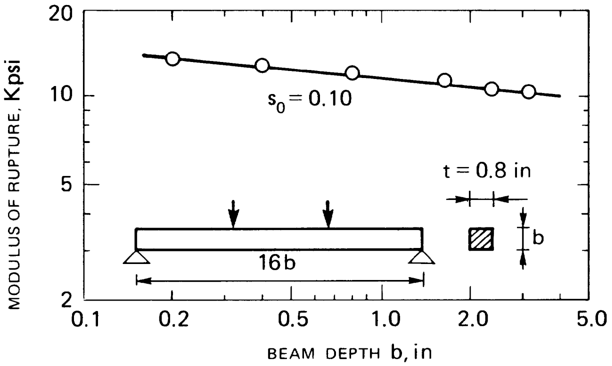

Fig. 8.32. Effect of size on bending strength of timber beams [82].

Figure 8.32 shows a typical size effect of this kind plotted from the data of Comben [82] for the bending strength of unnotched timber beams. For $s_0 = 0.10$, the defect shape is not very sharp and the defect size distribution has a small dispersion. A similar size effect is found in the yield stress of mild steel, which may be interpreted as the onset of microfracture. An example is given in Figure 8.33 [83]. The results by Strange and Bryant [48] are plotted in Figure 8.34. The flexural tensile strength decayed linearly with the beam width on the logarithmic scale for all four cementitious composites. Sabnis and Mirza [84] showed the same trend in Figure 8.35. The results obtained from the Brazilian test are in agreement, Figure 8.36. In the case of compressive strength [84], the decrease becomes bilinear, Figure 8.37. The "weakest link concept" may not be appropriate for analyzing the compressive failure of concrete where damage occurs in a progressive manner.

By regarding heterogeneity as imperfections, it is also possible to explain the effects of grain size on the tension strength of magnesium alloys at low temperatures [85]. Refer to the results in Figure 8.38.

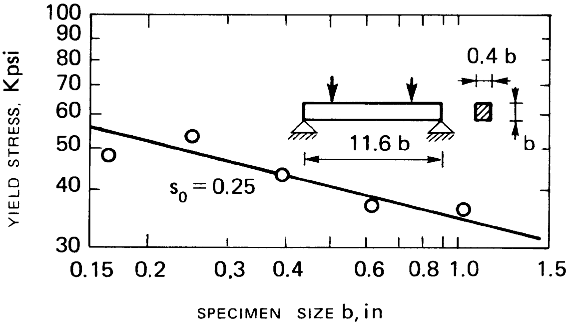

Fig. 8.33. Size effect on the yield stress of mild steel beams [83].

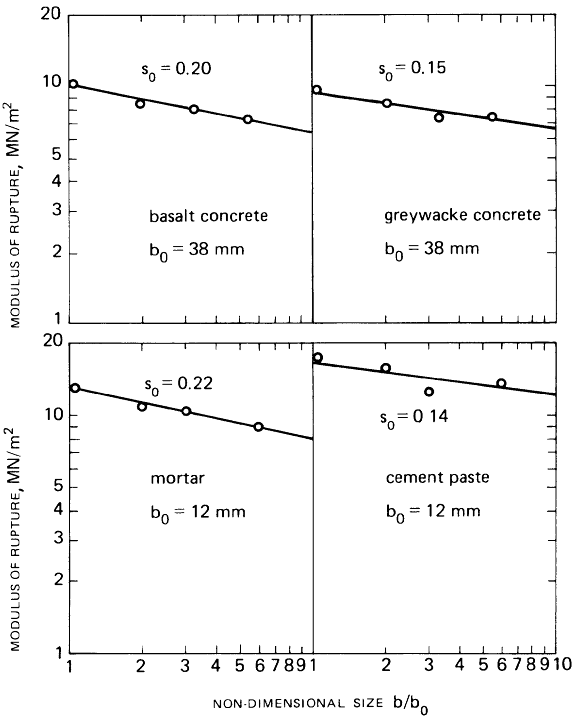

Fig. 8.34. Size effect on flexural tensile strength of cementitious materials [48].

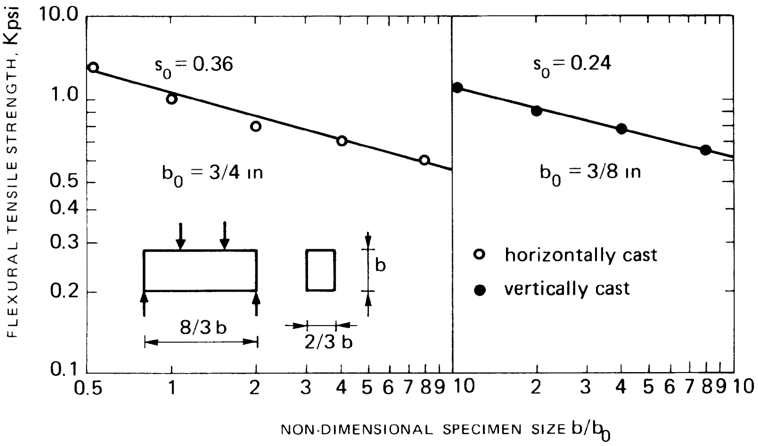

Fig. 8.35. Size effect on flexural tensile strength of concrete [84].

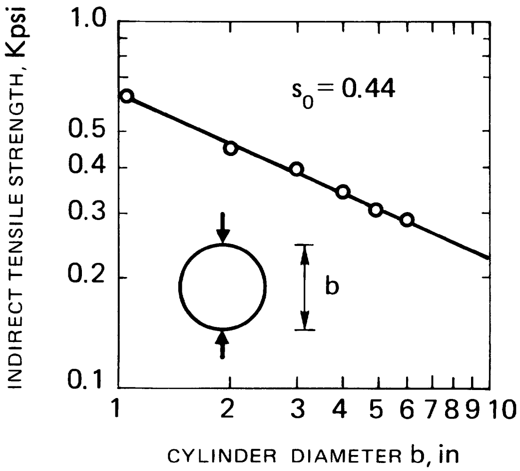

Fig. 8.36. Size effect on indirect tensile strength of concrete [84].

8.4. Simplified models

This section is concerned with a review of past works that utilize criteria such as localized strain, fictitious crack length, etc., for modeling the failure of specialized problems. Although these models are limited in application, they can be useful to explain the difference between local and global crack instability.

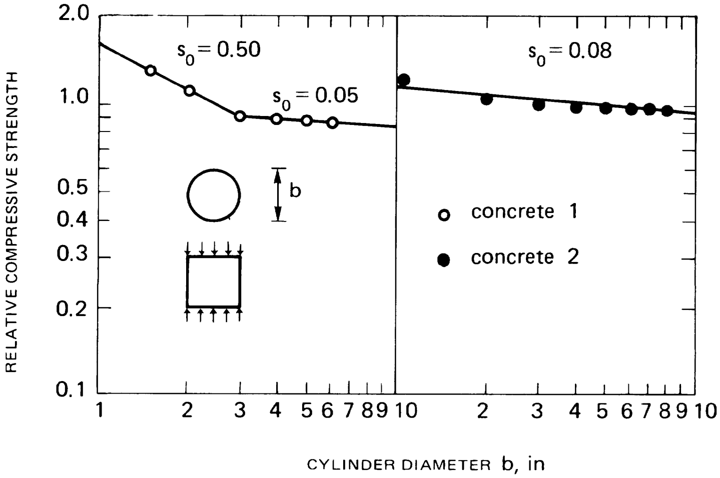

Fig. 8.37. Size effect on compressive strength of concrete [84].

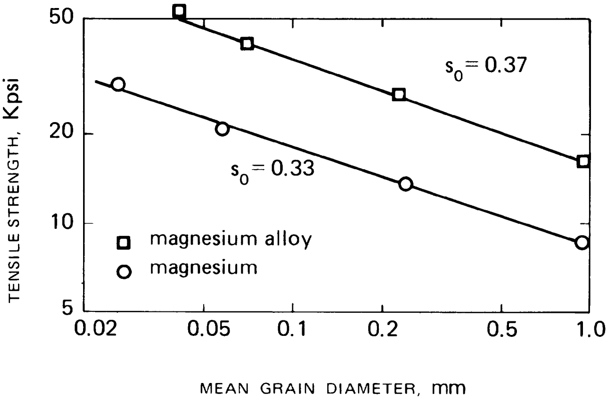

Fig. 8.38. Effect of grain size on tension strength of magnesium and magnesium alloy [85].

Localized strain. The concept of maximum localized strain is perhaps one of the most popular failure criteria simply because of its familiarity associated with the uniaxial test. The idea that damage is concentrated to a small material volume leading to eventual fracture has been suggested in [86]. The localization of strain in direct tensile tests on concrete was also given by Heilmann, Hilsdorf and Finsterwalder [87]. Their test results are

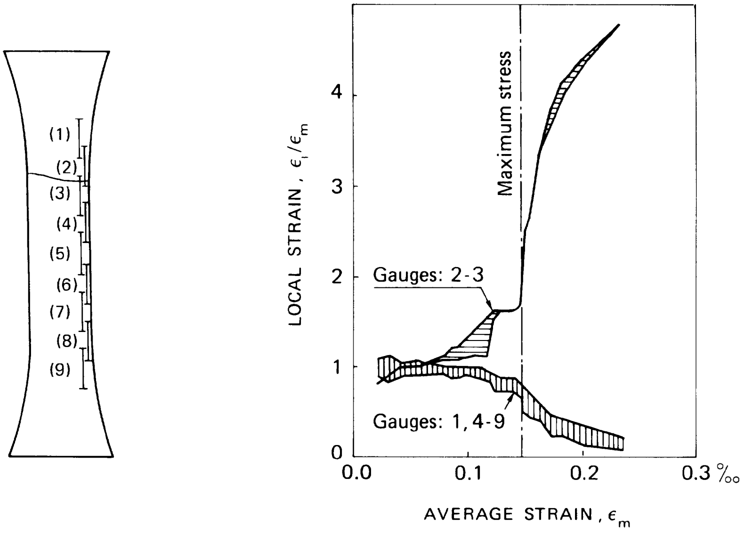

(a) (b)

Fig. 8.39. Localization of strain in direct tensile test (a) and local strains as functions of the mean strain of the specimen (b) [87].

shown in Figure 8.39. Strain gauges were glued at different positions on a 600 mm long concrete specimen with a cross-sectional area of $80 \times 150\,\mathrm{mm}^2$, Figure 8.39(a). The load was eccentrically applied so that it was possible to produce stable fracture. In Figure 8.39(a), the position of the final crack is shown. In Figure 8.39(b), the local strains are shown as functions of the mean strain of the specimen. The local strains are separated into two groups: one for the cross-section where the final crack develops (gauges 2–3) and the other for the material outside the position of the final crack (gauges 1, 4–9). As it can be seen from Figure 8.39(b), the strain measured by the gauges monitoring the final crack increases rapidly from the moment the maximum stress is reached. At the same time, the strain outside the fracture zone decreases. This implies that the fracture zone is localized in a very narrow band across the specimen.

As the width of the fracture zone in the loaded direction is relatively small, the fracture zone may be replaced by a narrow slit of width w [86] as shown in Figure 8.40. The total deformation of the specimen Δl then becomes:

$$\Delta l = \epsilon_0 l + w \tag{8.85}$$

where ϵ_0 is the strain in the material outside the fracture zone and l is the specimen length. From equation (8.85), it follows that the mean strain ϵ_m is given by

$$\epsilon_m = \frac{\Delta l}{l} = \epsilon_0 + \frac{w}{l} \tag{8.86}$$

After the maximum stress is reached, the elongation of the fracture zone affects the mean strain and hence the stress-strain curve of concrete may

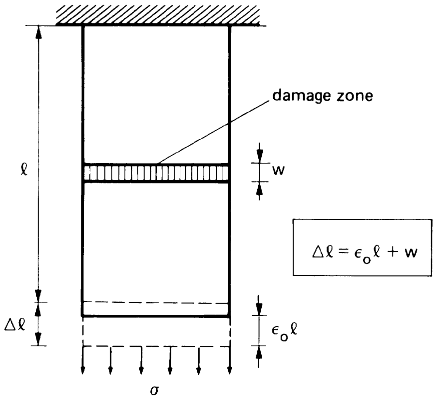

Fig. 8.40. Fracture zone represented as a narrow slit of width w.

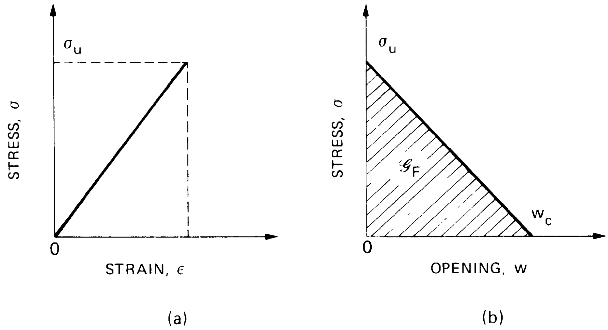

Fig. 8.41. Stress versus strain relation for the undamaged material outside the fracture zone (a) and stress as a function of fracture zone width (b).

depend on the specimen length. For this reason, Hillerborg, Modeer and Petersson [86] avoided using stress-strain curve as a material property. Instead, they proposed to use the stress and strain relation for the undamaged material outside the fracture zone in Figure 8.41(a) and that of stress as a function of fracture zone width in Figure 8.41(b).

It is important to note that the strain localization does not imply the change from a σ versus ϵ to a σ versus w relation as suggested by Hillerborg, Modeer and Petersson [86]. Rice [88, 89] pointed out that strain localization results from a low hardening modulus or a softening behavior in the σ versus ϵ relation. Also, Bazant and Oh [90], considered the fracture zone concept and used a finite width w_0 at the beginning of the loading process. They regarded w_0 as a material property and related it to a characteristic dimension $D_{\max}$ of the aggregates with $w_0 \simeq 3D_{\max}$. In this case, equation (8.85) becomes

$$\Delta l = \epsilon_0(l - w_0) + \epsilon_d w_0 \tag{8.87}$$

where ϵ_d is the strain in the damage zone that increases monotonically with load, while ϵ_0 decreases after reaching the ultimate stress σ_u. At fracture, equation (8.85) gives

$$\Delta l = w_c \tag{8.88}$$

whereas equation (8.87) yields

$$\Delta l = \epsilon_f w_0 \tag{8.89}$$

From equations (8.88) and (8.89), the expression

$$w_c = \epsilon_f w_0 \tag{8.90}$$

prevails that relates the critical crack opening displacement w_c to the fracture strain ϵ_f and characteristic crack band width w_0.

Cohesive force model. The three point bend specimen analyzed in chapter 3 is again considered, Figure 3.1. The material possesses ultimate tensile strength $\sigma_u = 31.90\,\mathrm{kg/cm^2}$, Young's modulus, $E = 365{,}000\,\mathrm{kg/cm^2}$, Poisson ratio, $\nu = 0.1$ and fracture energy, $G_F = 0.05\,\mathrm{kg/cm}$. These values correspond to Material 3 in Figure 2.29. The critical parameters for determining the onset of rapid crack propagation were the strain energy density factor $S_c = 8 \times 10^{-3}$ kg/cm and the fracture energy G_F that are related as

$$G_F = G_{IC} \simeq 2\pi S_c \tag{8.91}$$

The damage model presented in chapter 2 requires an additional material constant, the fracture strain ϵ_f, that is related to the critical crack opening displacement w_c and the crack band width w_0 through equation (8.90). Recalling from Figure 2.23 that

$$w_c = 2G_F/\sigma_u \tag{8.92}$$

the crack band width is thus obtained:

$$w_0 = \frac{2G_F}{\sigma_u \epsilon_f} \tag{8.93}$$

Using equation (8.91), equation (8.93) becomes

$$w_0 = \frac{2\pi S_c}{\left(\dfrac{dW}{dV}\right)_c} = 2\pi r_c \tag{8.94}$$

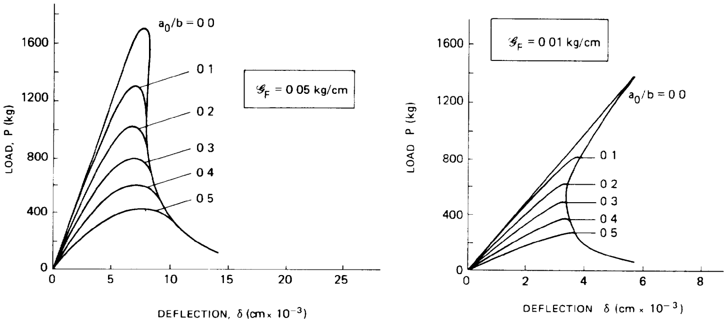

Fig. 8.42. Load-deflection curves for different initial crack depths: $G_F = 0.05$ kg/cm (a) and $G_F = 0.01$ kg/cm (b).

Equation (8.94) establishes the relation between the strain energy density theory [12] and crack band theory [90]. In the present case, $w_0 = 6.47$ cm which corresponds to about three times the aggregate size since $D_{\max} \simeq 2$ cm.

The load-deflection curves are displayed in Figure 8.42(a) for different initial crack depths and using the cohesive crack model [91]. The stiffness

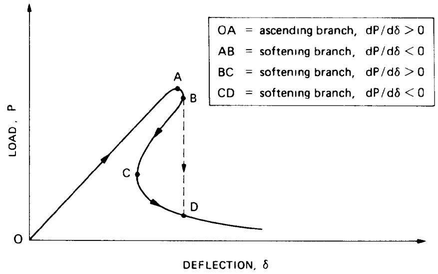

Fig. 8.43. Bifurcation of the global equilibrium.

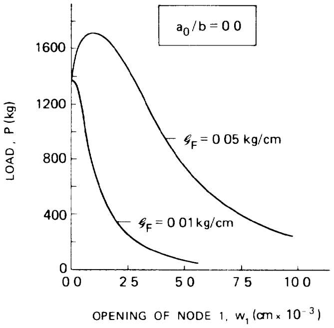

Fig. 8.44. Load versus crack mouth opening displacement.

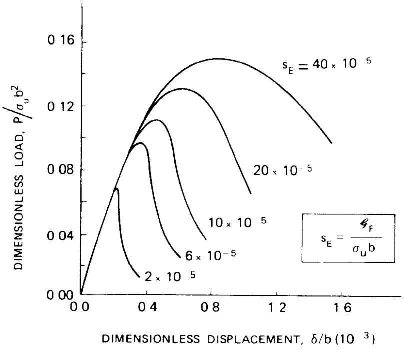

Fig. 8.45. Nondimensional load-deflection curves for different values of the nondimensional number $s_E = G_F/\sigma_u b = w_c/2b$.

and loading capacity of the specimen decrease with increasing initial crack depth. The load-deflection curves in Figure 8.42(b) pertain to $G_F = 0.01$ kg/cm. For small crack depths with $a_0/b \lesssim 0.2$, bifurcation occurs. A softening branch corresponding to $dP/d\delta > 0$ is obtained which could be defined as 'stable' according to the Drucker's Postulate. If the loading process is controlled by the deflection, the P versus δ curve will show a discontinuity in its loading capacity with global instability.

The catastrophic softening such as the third branch of the curve in Figure 8.43 is controlled by the crack mouth opening displacement w_1. As it is shown in Figure 8.44, the crack mouth opening displacement increases while the load P and the beam deflection δ decrease.

The nondimensional load-deflection curves are represented in Figure 8.45 for $a_0/b = \frac{1}{3}$ and different values of the nondimensional number

$$s_E = \frac{G_F}{\sigma_u b} = \frac{w_c}{2b} \tag{8.95}$$

which can be related to the brittleness number s when using a Dugdale type of cohesive model.* When the fracture energy G_F is very high as in fibre reinforced concrete, or when the beam size b is very small, the structural behavior is ductile. The opposite also holds.

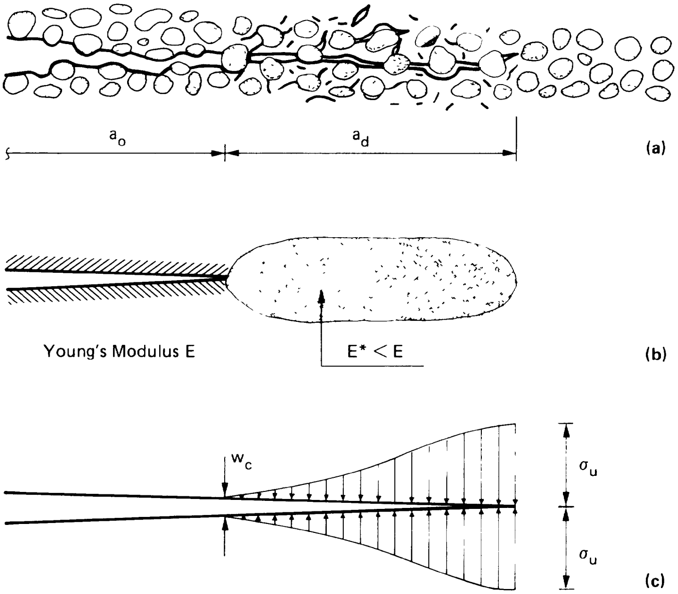

Fig. 8.46. Process zone at the crack tip of a concrete-like material (a). Damage zone ahead of the stress-free crack tip (b). Cohesive force distribution behind the fictitious crack tip (c).

---

* Recalling that $K_{IC} = \sqrt{G_F E}$, the relation is: $s_E = s^2 \cdot \epsilon_u$.

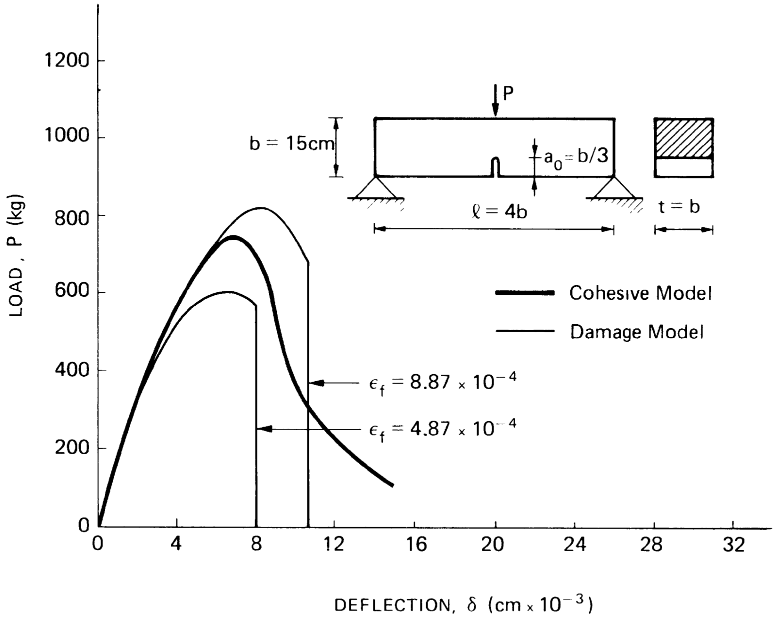

Fig. 8.47. Load-deflection curves obtained through the application of damage and cohesive models.

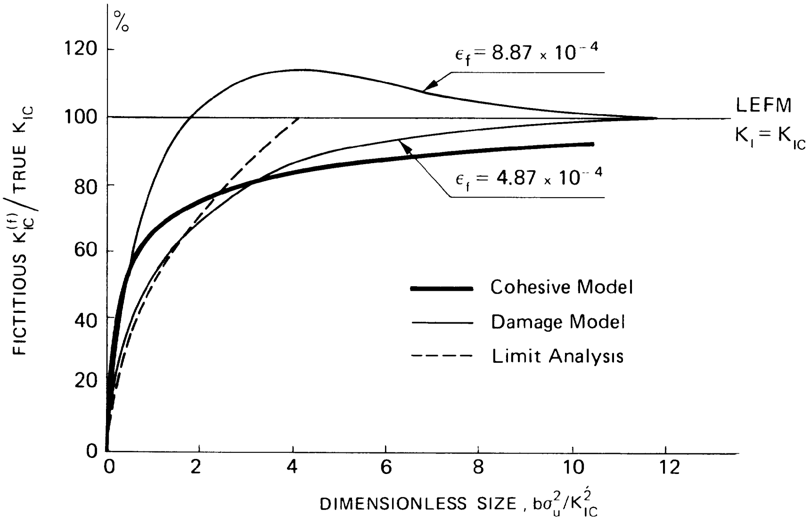

Fig. 8.48. Transition from structural instability to crack instability by varying the size scale.

Damage vs. cohesive force model. The process zone at the crack tip of a concrete-like material can be simulated in two ways as shown in Figures 8.46:

(1) with a damage zone ahead of the stress-free crack tip, Figure 8.46(b), and
(2) with a cohesive force distribution behind the fictitious crack tip, Figure 8.46:

The damage model requires an additional parameter, the fracture strain ϵ_f. Displayed in Figure 8.47 are the load-deflection curves for the beam in Figure 3.1. The damage model is seen to be sensitive to the variation in the fracture strain ϵ_f while the cohesive model does not contain this parameter. For average values of ϵ_f, however, the cohesive model solution is in agreement with that of the damage model, Figure 8.47.

Figure 8.48 displays the variations of $P^{(1)}_{\max}/P^{(2)}_{\max}$ with $1/s^2$, where s is the brittleness number. The maximum load computed from the damage or cohesive force model is $P^{(1)}_{\max}$ while $P^{(2)}_{\max}$ corresponds to that predicted from Linear Elastic Fracture Mechanics. The two extreme failure modes of ligament

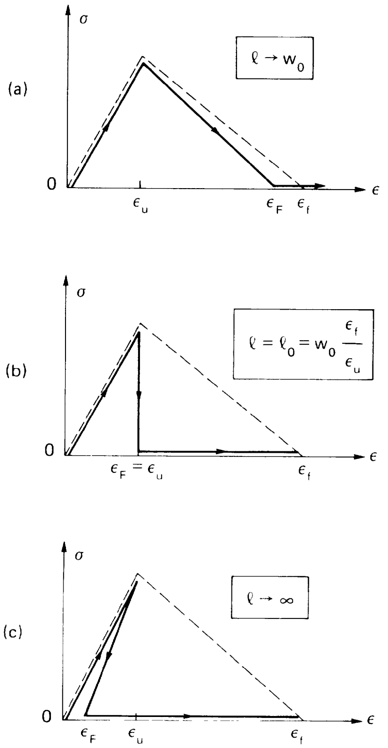

Fig. 8.49. Local (dashed line) and global (unbroken line) tensile softening behavior.

collapse and brittle fracture are thus connected by a smooth curve that accounts for the interaction of structure geometry, material type, loading step, etc. The results based on the cohesive force model are somewhat limited because it is based on a more simplified criterion of critical strain. One of the most serious limitations is the independency of load history effect which is an inherent feature of the material damage process.

Further insights into the bifurcation prediction [92–94] can be made. A failure parameter ϵ_F for the tensile specimen in Figure 8.40 can be obtained from equation (8.89):

$$\epsilon_F = \epsilon_f \frac{w_0}{l} \tag{8.96}$$

When $l \to w_0$, $\epsilon_F \to \epsilon_f$ and the softening behavior of the damage zone is reproduced by the specimen, Figure 8.49(a). For increasing specimen lengths l, the global softening behavior becomes more and more pronounced until the limit

$$l_0 = w_0 \frac{\epsilon_f}{\epsilon_u} \tag{8.97}$$

is reached which gives simply a vertical drop, Figure 8.49(b). Then, as l increases the global softening behavior becomes catastrophic with $d\sigma/d\epsilon > 0$. When $l \to \infty$, $\epsilon_F \to 0$ and the global softening branch tends to coincide with the rising portion of the σ versus ϵ curve, Figure 8.49(c). In conclusion, for $w_0 \leqslant l \leqslant l_0$, the softening behavior is unstable according to the Drucker's Postulate. For $l > l_0$, the softening behavior is even catastrophic and a strain-controlled loading process would produce a drop in the σ versus ϵ curve as in the case of $l = l_0$ in Figure 8.49(b).

References

1. Carpinteri, A., Size effect in fracture toughness testing: a dimensional analysis approach, Analytical and Experimental Fracture Mechanics, edited by G.C. Sih and M. Mirabile, Sijthoff and Noordhoff, pp. 785–797 (1981).
2. Carpinteri, A., Notch sensitivity in fracture testing of aggregative materials, Engineering Fracture Mechanics, 16, pp. 467–481 (1982).
3. Carpinteri, A., Static and energetic fracture parameters for rocks and concretes, Materials and Structures (RILEM), 14, pp. 151–162 (1981).
4. Carpinteri, A., Application of fracture mechanics to concrete structures, Journal of the Structural Division, American Society of Civil Engineers, 108, pp. 833–848 (1982).
5. Carpinteri, A., Plastic flow collapse versus separation collapse in elastic-plastic strain-hardening structures, Materials and Structures (RILEM), 16, pp. 85–96 (1983).

6. Carpinteri, A., Size effects in solid mechanics due to topology transformation during crack growth, Application of Fracture Mechanics to Materials and Structures, edited by G.C. Sih, E. Sommer and W. Dahl, Martinus Nijhoff Publishers, pp. 281–293 (1984).
7. Carpinteri, A., Marega, C. and Savadori, A., Ductile-brittle transition by varying structural size, Engineering Fracture Mechanics, 21, pp. 263–271 (1985).
8. Carpinteri, A., Size effects in material strength due to crack growth and material non-linearity, Theoretical and Applied Fracture Mechanics, 1, pp. 39–46 (1984).
9. Carpinteri, A., Scale effects in fracture of plain and reinforced concrete structures, Fracture Mechanics of Concrete: Structural Application and Numerical Calculation, edited by G.C. Sih and A. DiTommaso, Martinus Nijhoff Publishers, The Hague, pp. 95–140 (1984).
10. Peterson, R.E., Model testing as applied to strength of materials, Journal of Applied Mechanics, 1, pp. 79–85 (1933).
11. Standard Method of Test for Plane Strain Fracture Toughness of Metallic Materials, E 399–74, ASTM.
12. Carpinteri, A. and Sih, G.C., Damage accumulation and crack growth in bilinear materials with softening: Application of Strain Energy Density Theory, Journal of Theoretical and Applied Fracture Mechanics, Vol. 1, No. 2, pp. 145–160 (1984).
13. Sih, G.C., Mechanics of material damage in concrete, Fracture Mechanics of Concrete: Material Characterization and Testing, edited by A. Carpinteri and A.R. Ingraffea, Martinus Nijhoff Publishers, The Hague, pp. 1–29 (1984).
14. Sih, G.C., Non-linear response of concrete: Interaction of size, loading step and material property, Applications of Fracture Mechanics to Cementitious Composites, edited by S.P. Shah, Martinus Nijhoff Publishers, The Hague, pp. 3–23 (1984).
15. Dugdale, D.S., Yielding of steel sheets containing slits, Journal of Mechanics and Physics of Solids, 8, pp. 100–104 (1960).
16. Irwin, G.R., Analysis of stresses and strains near the end of a crack traversing a plate, Journal of Applied Mechanics, 24, pp. 361–364 (1957).
17. Nadai, A., Theory of flow and fracture of solids, McGraw-Hill Book Co., New York, Vol. I and II (1950).
18. Sih, G.C., Introductory chapters of mechanics of fracture, Vol. I to VII, edited by G.C. Sih, Martinus Nijhoff Publishers, The Hague (1973)–1981).
19. Sih, G.C., Mechanics and Physics of Energy Density Theory, J of Theoretical and Applied Fracture Mechanics, Vol. 4, No. 3 pp. 157–173 (1985).
20. Glucklich, J. and Cohen, L.J., Size as a factor in the brittle-ductile transition and the strength of some materials, International Journal of Fracture Mechanics, 3, pp. 278–289 (1967).
21. Kaplan, M.F., Crack propagation and the fracture of concrete, Journal of the American Concrete Institute, 58, pp. 591–610 (1961).
22. Romualdi, J.P. and Batson, G.B., Mechanics of crack arrest in concrete, Journal of the Engineering Mechanics Division, American Society of Civil Engineers, 89, pp. 147–168 (1963).
23. Glucklich, J., Fracture of plain concrete, Journal of the Engineering Mechanics Division, American Society of Civil Engineers, 89, pp. 127–136 (1963).
24. Naus, D.J. and Lott, J.L., Fracture toughness of Portland cement concretes, Journal of the American Concrete Institute, 66, pp. 481–489 (1969).
25. Welch, G.B. and Haisman, B., The application of fracture mechanics to concrete and the measurement of fracture toughness, Materials and Structures (RILEM), 2, pp. 171–177 (1969).
26. Moavenzadeh, F. and Kuguel, R., Fracture of concrete, Journal of Materials, 4, pp. 497–519 (1969).
27. Desayi, P., Fracture of concrete in compression, Materials and Structures (RILEM),

10, pp. 139–144 (1969).

28. Shah, S.P. and McGarry, F.J., Griffith fracture criterion and concrete, Journal of the Engineering Mechanics Division, American Society of Civil Engineers, 97, pp. 1663–1675 (1971).
29. Brown, J.H., Measuring the fracture toughness of cement paste and mortar, Magazine of Concrete Research, 24, pp. 185–196 (1972).
30. Brown, J.H., The failure of glass-fibre-reinforced notched beams in flexure, Magazine of Concrete Research, 25, pp. 31–38 (1973).
31. Brown, J.H. and Pomeroy, C.D., Fracture toughness of cement paste and mortars, Cement and Concrete Research, 3, pp. 475–480 (1973).
32. Naus, D.J., Batson, G.B. and Lott, J.L., Fracture mechanics of concrete, Fracture Mechanics of Ceramics, edited by R.C. Bradt, D.P.H. Hasselman and F.F. Lange, Vol. 2, Plenum Press, pp. 469–481 (1974).
33. Walsh, P.F., Crack initiation in plain concrete, Magazine of Concrete Research, 28, pp. 37–41 (1976).
34. Higgins, D.D. and Bailey, J.E., Fracture measurements on cement paste, Journal of Materials Science, 11, pp. 1995–2003 (1976).
35. Schmidt, R.A., Fracture-toughness testing of limestone, Experimental Mechanics, 16, pp. 161–167 (1976).
36. Evans, A.G., Clifton, J.R. and Anderson, E., The fracture mechanics of mortars, Cement and Concrete Research, 6, pp. 535–548 (1976).
37. Mindess, S. and Nadeau, J.S., Effect of notch width on K_{IC} for mortar and concrete, Cement and Concrete Research, 6, pp. 529–534 (1976).
38. Bear, T.J. and Barr, B., Fracture toughness tests for concrete, International Journal of Fracture, 13, pp. 92–96 (1977).
39. Barr, B. and Bear, T.J., A simple test of fracture toughness, Concrete, 10, pp. 25–27 (1976).
40. Barr, B. and Bear, T.J., Fracture toughness, Concrete, 11, pp. 30–32 (1977).
41. Henry, J.P. and Paquet, J., La tenacité des roches calcaires: influence des paramètres microstructuraux et de l'environment, Mechanics Research Communications, 4, pp. 193–198 (1977).
42. Henry, J.P., Paquet, J. and Tancrez, J.P., Experimental study of crack propagation in calcite rocks, International Journal of Rock Mechanics, Mining Science and Geomechanics, 14, pp. 85–91 (1977).
43. Henry, J.P. and Paquet, P., Résistance des Matériaux, C.R. Acad. Sc., Paris, 284, pp. 511–514 (1977).
44. Hillemeier, B. and Hilsdorf, H.K., Fracture mechanics studies on concrete compounds, Cement and Concrete Research, 7, pp. 523–536 (1977).
45. Gjϕrv, O.E., Sϕrensen, S.I. and Arnesen, A., Notch sensitivity and fracture toughness of concrete, Cement and Concrete Research, 7, pp. 333–344 (1977).
46. Cook, D.J. and Crookham, G.D., Fracture toughness measurements of polymer concrete, Magazine of Concrete Research, 30, pp. 205–214 (1978).
47. Swartz, S.E., Hu, K.K. and Jones, G.L., Compliance monitoring of crack growth in concrete, Journal of the Engineering Mechanics Division, American Society of Civil Engineers, 104, pp. 789–800 (1978).
48. Strange, P.C. and Bryant, A.H., Experimental tests on concrete fracture, Journal of the Engineering Mechanics Division, American Society of Civil Engineers, 105, pp. 337–342 (1979).
49. Sok, C. and Baron, J., Mécanique de la rupture appliquée au béton hydraulique, Cement and Concrete Research, 9, pp. 641–648 (1979).
50. Swamy, R.N., Fracture mechanics applied to concrete, Developments in Concrete Technology, Vol. 1, edited by F.D. Lydon, Applied Science Publishers LTD, pp. 221–281 (1979).

51. Ziegeldorf, S., Müller, H.S. and Hilsdorf, H.K., A model law for the notch sensitivity of brittle materials, Cement and Concrete Research, 10, pp. 589–599 (1980).
52. Ziegeldorf, S., Müller, H.S. and Hilsdorf, H.K., Effect of aggregate particle size on mechanical properties of concrete, Proceedings of the 5th International Conference on Fracture, Cannes, pp. 2243–2251 (1981).
53. Carpinteri, A., Experimental determination of fracture toughness parameters K_{IC} and J_{IC} for aggregative materials, Proceedings of the 5th International Conference on Fracture, Cannes, pp. 1491–1498 (1981).
54. Saouma, V.E., Ingraffea, A.R. and Catalano, D.M., Fracture toughness of concrete – K_{IC} revisited, Report 80-9, Department of Structural Engineering, Cornell University (1980).
55. Kesler, C., Naus, D. and Lott, J., Fracture mechanics – Its applicability to concrete, Proceedings of the International Conference on Mechanical Behavior of Materials, Vol. IV, pp. 113–124 (1971).
56. Mai, Y.W., Foote, R.M.L. and Cotterell, B., Size effects and scaling laws of fracture in asbestos cement, The International Journal of Cement Composites, 2, pp. 23–34 (1980).
57. Mai, Y.W. and Atkins, A.G., Scale effects and crack propagation in non-linear elastic structures, International Journal of Mechanical Science, 17, pp. 673–675 (1975).
58. Mai, Y.W. and Atkins, A.G., Crack propagation in nonproportionally scaled elastic structures, International Journal of Mechanical Science, 20, pp. 437–449 (1978).
59. Visalvanich, K. and Naaman, A.E., Fracture methods in cement composites, Journal of the Engineering Mechanics Division, American Society of Civil Engineers, 107, pp. 1155–1171 (1981).
60. Petersson, P.E., Crack growth and development of fracture zones in plain concrete and similar materials, Report TVBM-1006, Division of Building Materials, Lund Institute of Technology (1981).
61. Arrea, M. and Ingraffea, A.R., Mixed mode crack propagation in mortar and concrete, Report 81-13, Department of Structural Engineering, Cornell University (1982).
62. Hillerborg, A. and Petersson, P.E., Determination of the fracture energy of mortar and concrete by use of three-point bend tests on notched beams, Proposed RILEM Recommendation, 29th January, 1982.
63. Hillerborg, A., Concrete fracture energy tests performed by 9 laboratories according to a draft RILEM recommendation, Report TVBM-3015, Division of Building Materials, Lund Institute of Technology (1983).
64. Ferrara, G. and Imperato, L., Il parametro G_F nella meccania della frattura del calcestruzzo; influenza della geometria di prova e del tipo di aggregato, XI Congresso AIAS, Torino, pp. 189–200 (1983).
65. Carpinteri, An., Dimensional analysis implications of the fictitious crack model, Engineering Fracture Mechanics, 22, pp. 327–333 (1985).
66. Hillerborg, A., Additional concrete fracture energy tests performed by 6 laboratories according to a draft RILEM recommendation, Report TVBM-3017, Division of Building Materials, Lund Institute of Technology (1984).
67. Mindess, S., The cracking and fracture of concrete: an annotated bibliography, Fracture Mechanics of Concrete, edited by F.H. Wittmann, Elsevier Science Publishers B.V., pp. 539–661 (1983).
68. Mindess, S., Fracture toughness testing of cement and concrete, Fracture Mechanics of Concrete: Material Characterization and Testing, edited by A. Carpinteri and A.R. Ingraffea, Martinus Nijhoff Publishers, pp. 67–110 (1984).
69. Weibull, W., A statistical theory of the strength of materials, Swedish Royal Institute for Engineering Research, Stockholm (1939).
70. Jayatilaka, A.S., Fracture of Engineering Brittle Materials, Applied Science Publishers LTD, London (1979).

71. Freudenthal, A.M., Statistical approach to brittle fracture, Fracture: An Advanced Treatise, edited by H. Liebowitz, Vol. II, pp. 592–619 (1968).
72. Leicester, R.H., Effect of size on the strength of structures, Paper No. 71, Division of Building Research, Forest Products Laboratory, C.S.I.R.O., Melbourne (1973).
73. Bazant, Z.P., Size effect in blunt fracture: concrete, rock, metal, Journal of Engineering Mechanics, American Society of Civil Engineers, 110, pp. 518–535 (1984).
74. Sih, G.C., Handbook of Stress-Intensity Factors for Researchers and Engineers, Lehigh University (1973).
75. Carpinteri, A., DiTommaso, A. and Viola, E., Collinear stress effect on the crack branching phenomenon, Materials and Structures (RILEM), 12, pp. 439–446 (1979).
76. DiLeonardo, G., Fracture toughness characterization of materials under multiaxial loading, International Journal of Fracture, 15, pp. 537–552 (1979).
77. Williams, M.L., Stress singularities resulting from various boundary conditions in angular corners of plates in extension, Journal of Applied Mechanics, 19, pp. 526–528 (1952).
78. Viola, E. and Piva, A., Two arc cracks around a circular rigid inclusion, Meccanica, 15, pp. 166–176 (1980).
79. Hatano, T., Theory of failure of concrete and similar brittle solid on the basis of strain, International Journal of Fracture Mechanics, 5, pp. 73–79 (1969).
80. Hutchinson, J.W., Singular behavior at the end of a tensile crack in a hardening material, Journal of the Mechanics and Physics of Solids, 16, pp. 13–31 (1968).
81. Rice, J.R. and Rosengren, G.F., Plane strain deformation near a crack tip in a power-law hardening material, Journal of the Mechanics and Physics of Solids, 16, pp. 1–12 (1968).
82. Comben, A.J., The effect of depth on the strength properties of timber beams, Special Report No. 12, Department of Scientific and Industrial Research, London (1957).
83. Richards, C.W., Size effect in the tension test of mild steel, Proceedings of the American Society for Testing and Materials, 54, pp. 995–1000 (1954).
84. Sabnis, G.M. and Mirza, S.M., Size effects in model concretes? Journal of the Structural Division, American Society of Civil Engineers, 105, pp. 1007–1020 (1979).
85. Hauser, F.E., Landon, P.R. and Dorn, J.E., Fracture of magnesium alloys at low temperature, Journal of Metals, pp. 589–593 (1956).
86. Hillerborg, A., Modeer, M. and Petersson, P.E., Analysis of crack formation and crack growth in concrete by means of fracture mechanics and finite elements, Cement and Concrete Research, 6, pp. 773–782 (1976).
87. Heilmann, H.G., Hilsdorf, H.H. and Finsterwalder, K., Festigkeit und Verformung von Beton unter Zugspannungen, Deutscher Ausschuss für Stahl-beton, 203 (1969).
88. Rice, J.R., The localization of plastic deformation, Theoretical and Applied Mechanics, Proceedings of the 14th IUTAM Congress, Delft, pp. 207–220 (1976).
89. Needleman, A. and Rice, J.R., Limits to ductility set by plastic flow localization, Mechanics of Sheet Metal Forming, edited by Donald P. Koistinen and Neng-Ming Wang, Plenum Publishing Corporation, pp. 237–265 (1978).
90. Bazant, Z.P. and Oh, B.H., Concrete fracture via stress-strain relations, Report 81-10/665c, Center for Concrete and Geomaterials, Northwestern University (1981).
91. Carpinteri, A., Interpretation of the Griffith instability as a bifurcation of the global equilibrium, Application of Fracture Mechanics to Cementitious Composites, NATO-ARW, Sept. 4–7, 1984. Northwestern University, edited by S.P. Shah, Martinus Nijhoff Publishers, pp. 287–316 (1985).

92. Maier, G., On structural instability due to strain-softening, IUTAM Symposium on Instability of Continuous Systems, Herrenhalb (Germany), Springer Verlag, pp. 411–417 (1971).
93. Maier, G., Zavelani, A. and Dotreppe, J.C., Equilibrium branching due to flexural softening, Journal of the Engineering Mechanics Division, American Society of Civil Engineers, 99, pp. 897–901 (1973).
94. Bazant, Z.P., Instability, ductility and size effect in strain-softening concrete, Journal of the Engineering Mechanics Division, American Society of Civil Engineers, 102, pp. 331–344 (1976).

Subject index

Author index